JOINT LABORATORY OF OPTICS
FACULTY OF SCIENCE
PALACKÝ UNIVERSITY OLOMOUC

DOCTORAL THESIS

Forward physics with the ATLAS detector

Design of radiation resistant descendant of the ALFA detector, detector AFP

2018

Ing. Ladislav Chytka

Supervisor: Mgr. Tomáš Sýkora, Ph.D.

Study field: Applied Physics, full-time form

Bibliografické údaje

Autor:	Ing. Ladislav Chytka
Název práce:	Dopředná fyzika na detektoru ATLAS (Návrh radiačně odolného následovníka detektoru ALFA, detektor AFP)
Typ práce:	disertační práce
Pracoviště:	Společná laboratoř optiky, Přírodovědecká fakulta, Univerzita Palackého v Olomouci
Rok:	2018
Studijní obor:	Aplikovaná fyzika, prezenční forma
Vedoucí práce:	Mgr. Tomáš Sýkora, Ph.D.
Konzultanti:	RNDr. Karel Černý, Ph.D.
	Mgr. Libor Nožka, Ph.D.
Počet stran:	180
Přílohy:	1 CD/DVD
Jazyk práce:	anglický

Bibliograhic info

Author:	Ing. Ladislav Chytka
Title:	Forward physics with the ATLAS detector (Design of radiation resistant descendant of the ALFA detector, detector AFP)
Thesis type:	doctoral thesis
Department:	Joint Laboratory of Optics, Faculty of Science, Palacký University Olomouc
Year:	2018
Study field:	Applied Physics, full-time form
Supervisor:	Mgr. Tomáš Sýkora, Ph.D.
Advisors:	RNDr. Karel Černý, Ph.D.
	Mgr. Libor Nožka, Ph.D.
Page count:	180
Supplements:	1 CD/DVD
Thesis language:	English

Anotace

Dopředné detektory experimentů na urychlovačích částic umožňují detekovat a měřit částice vystupující ze srážky pod velmi malými úhly, které jsou zajímavé např. pro měření difrakčních procesů, při kterých nedojde k disociaci jedné nebo obou částic vstupující do srážky. Neustále se zvyšující luminozita v urychlovačových experimentech vede ke zvyšování počtu srážek, ke kterým dojde během jedné interakce dvou protiběžných shluků srážených částic. Pro rozlišení bodu, ze kterého pochází částice detekované dopřednými detektory, je proto nezbytný systém pro měření času letu detekovaných částic. Předkládaná práce čtenáři představí experiment ATLAS, jeho dopředné detektory a vybraná témata dopředné fyziky, shrnuje autorovu práci na simulacích dopředných detektorů experimentu ATLAS a dokumentuje autorovo přispění k vývoji systému měření času letu pro detektor AFP s časovým rozlišením pod 30 ps.

Synopsis

Forward detectors of high energy collider experiments allow to tag and measure remnants of a colliding particle moving in a very forward direction that are of interest e.g. for measurements of diffractive processes, where one or both colliding particles are not dissociated and continue in the forward direction. Ever increasing luminosity in collider experiments leads to increased pileup of interactions and a time-of-flight system is necessary for forward detectors in order to determine the primary interaction vertex of recorded particles. The presented work introduces the ATLAS experiment, its forward detectors and selected topics of forward physics, summarizes author's work on simulation of the ATLAS forward detectors and documents authors contribution to the development of AFP time-of-flight system with sub-30 ps time resolution.

Klíčová slova: čas letu; Čerenkovovo záření; MCP-PMT; SiPM; AFP; ATLAS; dopředná fyzika; difrakce v částicové fyzice

Keywords: time-of-flight; Cherenkov light; MCP-PMT; SiPM; AFP; ATLAS; forward physics; diffraction in high energy physics

I thank my wife, for she stood by me and supported me.

I thank my supervisor, for he guided my steps.

I thank my colleagues, for they provided help when I needed it.

I thank the following projects, for they provided means of nourishment for me and my research:
LM 2015058, CZ.02.1.01/0.0/0.0/16_019/0000754 and CZ.02.1.01/0.0/0.0/16_-013/0001403 of MSMT of Czech Republic
IGA_PrF_2018_009 of Palacký University

I hereby declare that I have completed this thesis including its appendices on my own and used solely the sources cited in the text and included in the bibliography list.

date of thesis submission author's signature

Contents

Introduction **1**

I Forward Physics with the ATLAS detector **3**

1 ATLAS and its forward detectors **5**
1.1 LHC . . . 5
1.2 ATLAS . . . 7
1.2.1 ATLAS coordinate system and notation . . . 11
1.2.2 ALFA . . . 12
1.2.3 AFP . . . 15

2 Forward physics **19**
2.1 Beam optics . . . 19
2.1.1 Linear optics of synchrotron . . . 20
2.1.2 LHC running scenarios . . . 21
2.2 Elastic and total cross section . . . 22
2.3 Diffraction . . . 24
2.4 Beyond the Standard Model . . . 27

II Simulation of the forward detectors **29**

3 Full simulation of the ATLAS forward region **31**
3.1 Model . . . 32
3.1.1 Magnetic fields description . . . 32
3.1.1.1 Field transformation . . . 33
3.1.2 Geometry . . . 33
3.2 Validation . . . 34
3.2.1 Event-by-event comparison . . . 36
3.2.2 Check of FLUKA field maps for Q1–Q3 . . . 40
3.2.3 Orbit correctors . . . 43
3.2.4 Field transformation . . . 43

4 ALFA simulation **45**
4.1 RP filler . . . 45
4.2 Influence of the ATLAS central magnetic field . . . 46
4.2.1 ATLAS magnetic field . . . 46
4.2.2 Effect of the field on proton propagation . . . 48
4.2.2.1 End of cavern . . . 48
4.2.2.2 ALFA position . . . 48
4.2.3 Effect on reconstructed tracks in ALFA . . . 50
4.2.3.1 Alignment . . . 52
4.2.3.2 Comparison of hits distributions . . . 55
4.2.3.3 Event-by-event comparison . . . 55
4.2.3.4 Non-corrected t distribution . . . 59
4.2.3.5 t distribution from the truth information . . . 59
4.2.4 Comparison to data . . . 61
4.2.4.1 Beam screen edge . . . 62
4.2.4.2 B-slope effect . . . 63
4.2.4.3 Comparison of hits distributions . . . 63
4.2.4.4 Detector resolution . . . 64
4.2.5 Summary . . . 64

5 AFP simulation **67**
5.1 Effect of a tilted Hamburg beam pipe window . . . 67

III Development of the AFP time-of-flight detector **71**

6 AFP ToF detector **73**
6.1 LQbars and Cherenkov light . . . 74
6.2 MCP-PMT photodetector . . . 78
6.3 Fast readout electronics . . . 80
6.3.1 Preamplifiers . . . 81
6.3.2 Constant fraction discriminator . . . 83
6.3.3 Trigger module . . . 85
6.3.4 HPTDC module . . . 86
6.3.5 Reference clock . . . 87
6.3.6 Data acquisition and detector control . . . 87

7 Beam test campaigns **89**
7.1 Experimental area . . . 89
7.2 Measurement scheme . . . 90
7.3 November 2014 . . . 93
7.3.1 SiT and ToF readout integration . . . 95
7.3.2 ToF performance . . . 95
7.3.3 SiPM time resolutions . . . 97
7.3.4 ToF efficiency and crosstalk . . . 97

7.4 September 2015 . . . 98
7.4.1 Comparison of signal amplitudes of different bars . . . 99
7.4.2 ToF performance . . . 99
7.4.3 SiPM time resolution . . . 102
7.4.4 RCE data . . . 103
7.4.5 Effect of an optical grease . . . 104
7.4.6 Matte bars . . . 106
7.4.7 Bar correlations . . . 107
7.5 2016 beam tests . . . 108
7.5.1 ToF performance . . . 109
7.5.2 ToF crosstalk . . . 111
7.5.3 ToF efficiency . . . 113
7.5.4 HPTDC contribution . . . 114
7.5.5 First Sensor SiPM . . . 115
7.6 2017 beam tests . . . 116
7.6.1 Performance of ALD coated MCP-PMTs . . . 116
7.6.2 Trigger module . . . 118
7.6.3 ToF in vacuum . . . 120
7.7 Summary . . . 120

8 Laser laboratory testing **123**
8.1 Measurement setup . . . 123
8.2 MCP-PMT characterization . . . 125
8.2.1 Uniformity of pixel response . . . 125
8.2.2 Time transit spread . . . 127
8.3 SiPM measurements . . . 128
8.3.1 Optical grease effect . . . 129
8.3.2 SiPM characterization . . . 131
8.3.2.1 Methods . . . 132
8.3.2.2 Results . . . 136
8.3.2.3 Discussion . . . 138
8.3.2.4 Summary . . . 139

9 Installation and commissioning **141**
9.1 Tests before installation . . . 141
9.2 Commissioning . . . 143
9.2.1 SiT-ToF correlation . . . 144
9.2.2 Efficiency . . . 144
9.2.3 HV and CFD threshold setting . . . 148
9.2.4 Timing performance . . . 148
9.3 Summary and outlook . . . 151

Conclusion **153**

A List of figures **157**

B List of tables **167**

C List of abbreviations **169**

References **171**

Publications **179**

Introduction

Forward detectors of high energy collider experiments allow to tag and measure remnants of a colliding particle propagating in the very forward direction, i.e. at very small angles with respect to the circulating beam. Such remnants are of interest e.g. for measurements of diffractive processes, where one or both colliding particles are not dissociated and continue in the forward direction. Especially in the case of the elastic scattering, important for the measurements of total interaction cross section, the forward detectors are of essence.

The presented thesis documents author's contributions to the project of ATLAS forward detectors and to the development of AFP time-of-flight detectors in particular:

1. Software development within the Athena framework of the ATLAS collaboration.

2. Simulation and analysis of forward physics processes potentially interesting for ALFA and AFP detector groups.

3. Participation in beam tests, data taking and analyses.

The first part introduces the LHC, ATLAS and its forward detectors, and gives an overview of accelerator and particle physics related to the measurements with the forward detectors. Necessary concepts of forward physics as well as notations used within the ATLAS collaboration are explained.

The second part covers the simulations. Following the work started in my diploma thesis, I extended and further validated the model of the ATLAS forward region for the use in the full Geant4 based simulation under the Athena framework. The Roman pot filler, serving to reduce the radio-frequency heating of the ALFA stations, was implemented into the ALFA model and the influence of the ATLAS central magnetic field on the ALFA measurement was evaluated. For the AFP, the effect of multiple scattering and hadronic showers due to a thin entrance window was studied.

The third and final part follows my trail in the development of the AFP time-of-flight (ToF) detector. The AFP ToF detector is introduced along with its components. Large part is devoted to beam tests and laboratory testing, where the performance of the developing ToF detector was evaluated. Finally, the ToF installation and commissioning in 2017 is described.

Abbreviations are part of experimentalists everyday life and it is often easy to confuse people outside one's work group. Therefore, the abbreviations appearing in the text are listed and explained in Appendix C.

Part I

Forward Physics with the ATLAS detector

Chapter 1

ATLAS and its forward detectors

A Toroidal LHC Apparatus (ATLAS) [1] is a general purpose high energy physics experiment and one of the four large experiments at the Large Hadron Collider (LHC) at the European Organization for Nuclear Research (CERN).

This chapter aims to provide a necessary overview of experimental facilities utilized for high energy physics research with a focus on the forward detectors of ATLAS. First, I need to mention the collider that provides ATLAS with particle collisions — the LHC.

1.1 LHC

The LHC accelerates protons and heavy ions delivered by the Super Proton Synchrotron (SPS) and brings them to collisions at its four interaction points (IPs). There are two beams circulating in the LHC — clockwise and anticlockwise — with a separate beam pipe for each of them all around the LHC ring, except for the IPs, where the two opposite-going beams share a common pipe [2].

The LHC started up in November 2009 and reached half its design pp center-of-mass energy and over half its design luminosity, i.e. 7 TeV (i.e. 3.5 TeV per proton) and $6 \cdot 10^{33}\,\mathrm{cm}^{-2}\mathrm{s}^{-1}$, in 2010. The energy increased in early 2012 to 8 TeV and was kept at this level until the first long shutdown (LS1) that started in 2013. The operations resumed in early 2015 at energy of 13 TeV. The nominal luminosity of $1 \cdot 10^{34}\,\mathrm{cm}^{-2}\mathrm{s}^{-1}$ was reached in 2016 and exceeded by a factor of two in 2017. Running at 13 TeV finishes at the end of 2018 followed by a second long shutdown (LS2), after which the nominal energy of 14 TeV should be reached [3, 4].

The proton beams at the LHC are not continuous. Instead, each beam consists of *bunches* of protons with exact bunch placement depending on so-called *fill scheme*. The bunches occupy so-called *buckets* — virtual moving slots around the LHC circumference with spacing given by the 400 MHz frequency of the electro-magnetic (EM) standing wave in the LHC radio-frequency (RF) cavities that accelerate the protons. The minimum bunch spacing is 25 ns, given by the Proton Synchrotron (PS) — the pre-stage of the SPS (the full CERN accelerator

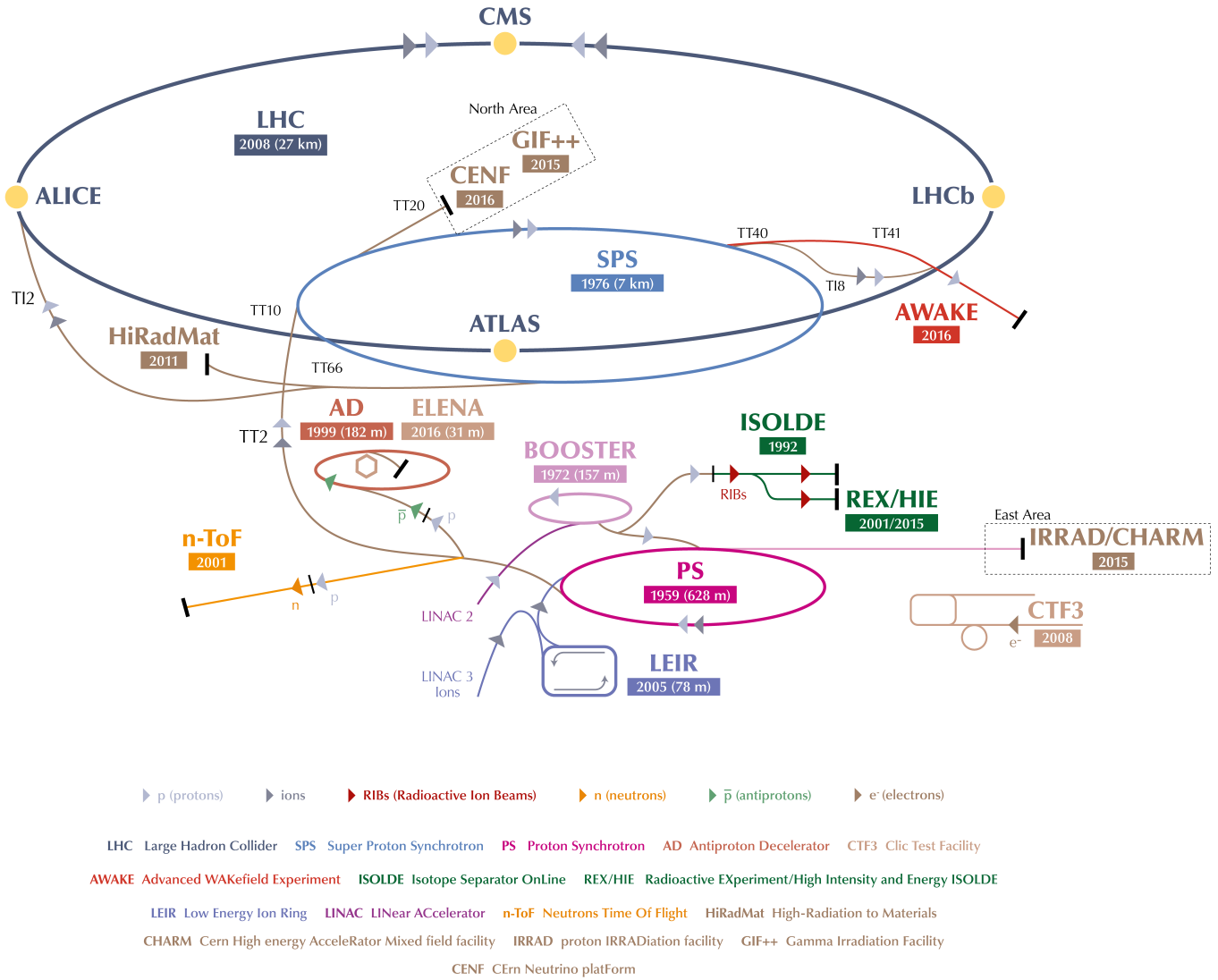

Figure 1.1: CERN accelerator complex [5].

complex is illustrated in Fig. 1.1) and it corresponds to the maximum instantaneous collision rate of 40 MHz [2]. An example of a bunch disposition at the LHC for a specific filling scheme is shown in Fig. 1.2.

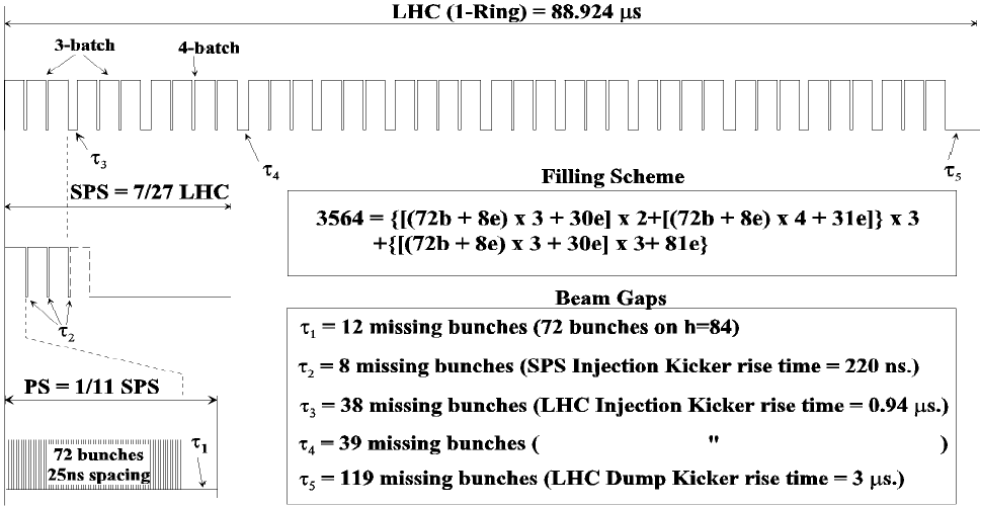

Figure 1.2: Bunch disposition of LHC, SPS and PS [2].

The two opposite-going beams are passing through each other at the interaction points and the bunches of protons in one beam are crossing bunches from the other beam. Duration of one *bunch crossing* (BX) is 1 ns [2]. The 25 ns bunch spacing in time corresponds to 7.5 m in distance. Therefore, the beams cannot collide head-on during the runs with large number of bunches since the LHC experiments are tens of meters long in the beam direction in order to capture most of the particles emerging from a single interaction point. Hence, there would be several interaction points 7.5 m apart within one experiment and the peripheral IPs would be effectively spoiling measurements of particles coming from the central IP. To avoid this, a *beam crossing angle* is introduced, as illustrated in Fig. 1.3.

The LHC bunches contain up to $1.15 \cdot 10^{11}$ [7] protons and to deliver the high luminosities, multiple proton collisions occur during a single bunch crossing leading to a *pileup* — multiple collisions recorded in a single event. An example of such an event is illustrated in Fig. 1.4.

1.2 ATLAS

The ATLAS was designed to perform measurements of wide variety of physics processes, ranging from precision measurements of Standard Model parameters to searches for new physics phenomena. The search for the Standard Model Higgs was of a special interest [1].

ATLAS installation in its cavern finished in early 2008 and commissioning using cosmic rays started in spring 2008. The beam commissioning started with

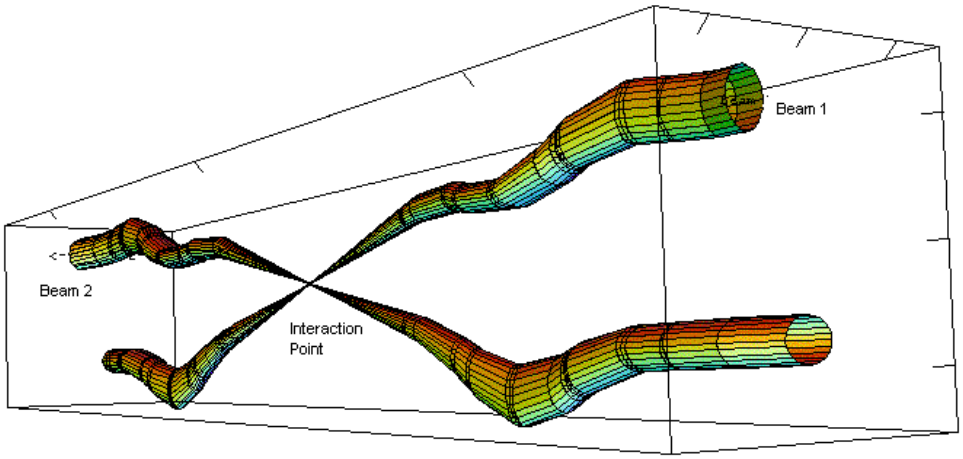

Figure 1.3: Visualization of the beam crossing at the IP1 [6].

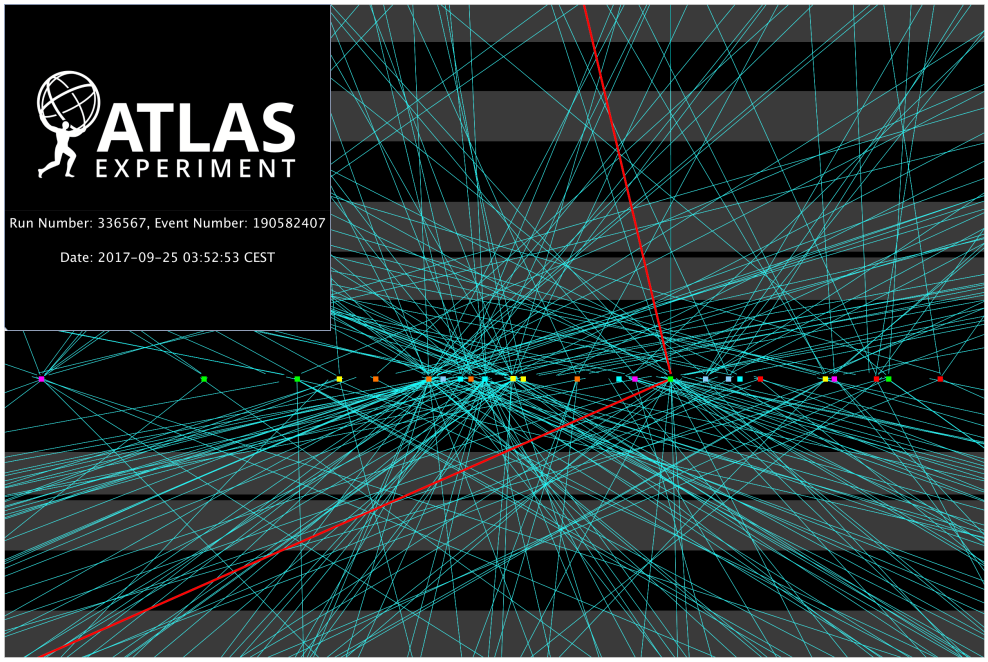

Figure 1.4: Event display of a $Z \to \mu\mu$ candidate with 24 accompanying vertices. Red lines represent tracks of reconstructed muons from the event of interest, while the blue lines show other reconstructed tracks. The grey horizontal stripes illustrate ATLAS tracker planes (ATLAS Experiment © 2018 CERN).

the LHC startup in November 2009.

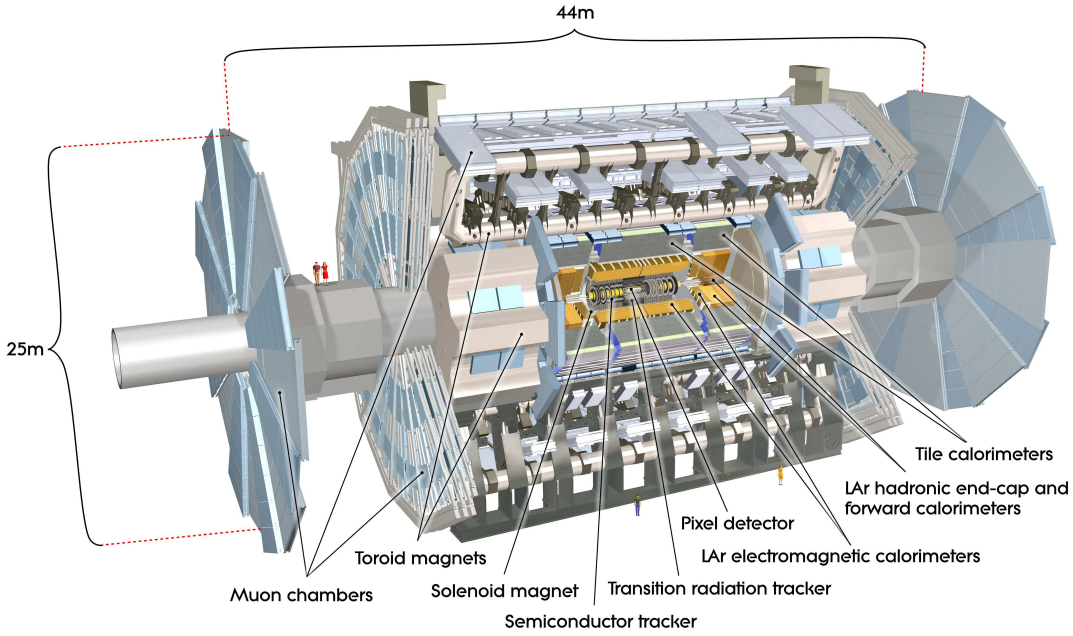

Figure 1.5: ATLAS experiment with a cut out part to see the inner composition of detector layers [1].

ATLAS design follows the usual layered structure of high energy physics collider experiments. Each layer consists of a barrel part and two end-cap parts, that together ensure that kinematics of particles emerging from the IP are well measured. The structure is shown in Fig. 1.5.

The innermost layer of ATLAS is the inner tracker followed by the electromagnetic (EM) calorimeter, the hadronic calorimeter and the muon system. The whole detector is 44 m long and 25 m high.

The inner tracker consists of 3 different types of detectors: semiconductor pixel detectors, semiconductor microstrip detectors and of straw tube transition radiation tracker (TRT). The inner tracker measures where the charged particles pass through, providing hits, from which particle tracks are reconstructed. It is designed to cope with more than 1000 tracks each 25 ns. The inner tracker is placed in the 2 T magnetic field of the ATLAS central solenoid. This enables determination of charged particles momenta. In 2014, during the LS1, an additional layer of pixel detectors — the Insertable B-layer (IBL) — was added to the inner tracker to improve the precision of the primary vertex reconstruction.

The sampling EM calorimeter uses liquid argon (LAr) as the active medium, in which the deposited energy is measured. Electrodes that collect the deposited charge, from which the energy is determined, are submerged in the LAr. A lead absorber plate is sandwiched in between electrodes from the neighboring LAr cells. The electrodes and absorber plates are folded into an accordion structure for the optimal coverage. The EM calorimeter also has finer structure than the

hadronic calorimeter placed above it. The thickness of the EM calorimeter is optimized to stop photons and electrons (and therefore to measure all their the kinetic energy).

Barrel hadronic calorimeter has a tiled structure composed of layers of steel (absorber) and layers of plastic scintillator (active medium). LAr calorimeter is used for the forward direction (i.e. for the particles having a small angle w.r.t. the proton beam) in the forward calorimeter (tubes filled with LAr with copper and tungsten in between) and also the inner part of the end-cap hadronic calorimeter (consisting of parallel copper wheels with LAr in between). The hadronic calorimeter is designed to contain hadronic showers for a precise jet reconstruction and measurement of missing energy.

As muons penetrate through all the layers described above, additional detector layers are added to allow a precise measurement of their momenta. Several detector types are used, commonly referred to as muon chambers. For the precision tracking, isolated drift tubes called Monitored Drift Tubes (MDTs) and multiwire proportional chambers with segmented cathodes called Cathode Strip Chambers (CSCs) are used. For triggering and additional tracking information, resistive plate chambers (RPCs) and thin gap chambers (TGCs) are utilized.

Apart from the main detector system, ATLAS is also equipped with detectors in the forward region, i.e. downstream from the IP in the direction of both beams. These forward detectors measure particles emerging from the IP at very small angle w.r.t. the beam. There are currently four sets of detectors installed in the forward region — LUCID, ZDC, AFP and ALFA. Figure 1.6 shows placement of the forward detectors (except for the AFP) on one side of the forward region. The detectors are placed symmetrically on both sides w.r.t. the IP.

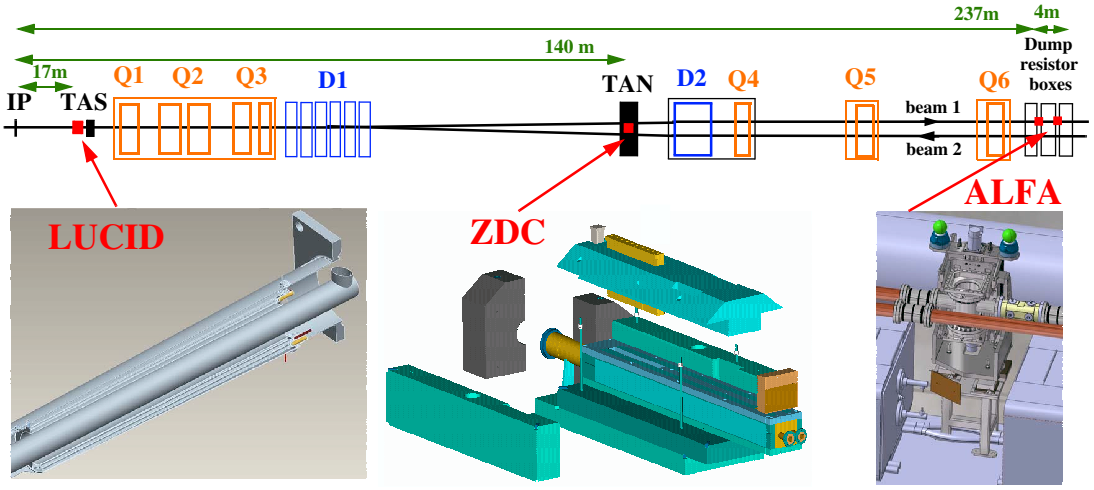

Figure 1.6: Placement of LUCID, ZDC and ALFA detectors in the forward region of ATLAS (one side) with a visualization of each detector. [1].

LUCID (Luminosity measurement using Cherenkov Integrating Detector) [8] provides online luminosity monitoring. There is one detector assembly on each

side placed between the muon wheels. Each assembly consists of 20 photomultipliers (PMTs) to detect Cherenkov light produced by scattered protons. The initial LUCID design used aluminum tubes filled with perfluorobutane gas as the Cherenkov radiator. The design was changed during LS1 and photomultiplier quartz windows with addition of quartz fiber bundles were used as the radiator in Run 2. LUCID provides relative luminosity measurement based on the measured rates of scattered protons.

The ZDC (Zero Degree Calorimeter) [9] is designed mainly to detect forward neutrons and photons. It is located in TAN (Target Absorber Neutral) absorber located at 140 m from the IP. The ZDC is formed by four tungsten blocks embedded with a matrix of quartz bars read out by PMTs.

The AFP (ATLAS Forward Proton) [10] aims to detect diffractive protons (i.e. protons that are not dissociated in a collision, but loose some energy). It is an upgrade project with the first set of detectors installed in the beginning of 2016 and the remaining detectors installed in 2017. The AFP detectors are fitted in Roman pot stations placed at 205 and 217 m from the IP on both sides. Each station is instrumented with 4 silicon tracker planes and the stations further from the IP (i.e. the far stations) are equipped by a time-of-flight (ToF) system.

ALFA (Absolute Luminosity For ATLAS) [P11] measures tracks of elastic protons in order to determine the luminosity and the total pp cross section. It utilizes tracking detectors build of cross stacked scintillating fibers read out by multiple anode PMTs (MAPMTs). The detectors are housed in the Roman pot stations placed originally at 237 and 241 m with the far stations moved to 245 m during LS1.

Before describing ALFA and AFP in more detail, I need to introduce the notation and the coordinate system commonly used within the ATLAS collaboration.

1.2.1 ATLAS coordinate system and notation

ATLAS uses right handed Cartesian coordinate system as illustrated in Fig. 1.7, with the origin in the IP, the z axis in the direction of the counterclockwise beam, y axis pointing towards surface and x axis oriented to the LHC center. The side with a positive z is called side A and the negative z side is side C [P2, 1].

The azimuthal angle ϕ is the angle around the beam axis with $\phi = 0$ in the direction of x axis. The polar angle θ is measured from the positive z axis. Apart from the polar angle, pseudorapidity $\eta = -\ln\tan\theta/2$ is commonly used to describe a particle direction w.r.t. the beam axis. It is useful in some cases to replace the polar and azimuthal angles by θ_x, defined as the angle between direction projection to $x-z$ plane and the z axis, and θ_y, being the angle between direction projection to $y-z$ plane and the z axis.

Quantities $\vec{p}_{\mathrm{T}}$, E_{T} and $\vec{E}_{\mathrm{T}}^{\mathrm{miss}}$, i.e. the transverse momentum, transverse energy and transverse missing energy, represent the part of the given physical quantity measured in the $x-y$ plane. The $\vec{p}_{\mathrm{T}}$ is the projection of $\vec{p}$ into the $x-y$ plane,

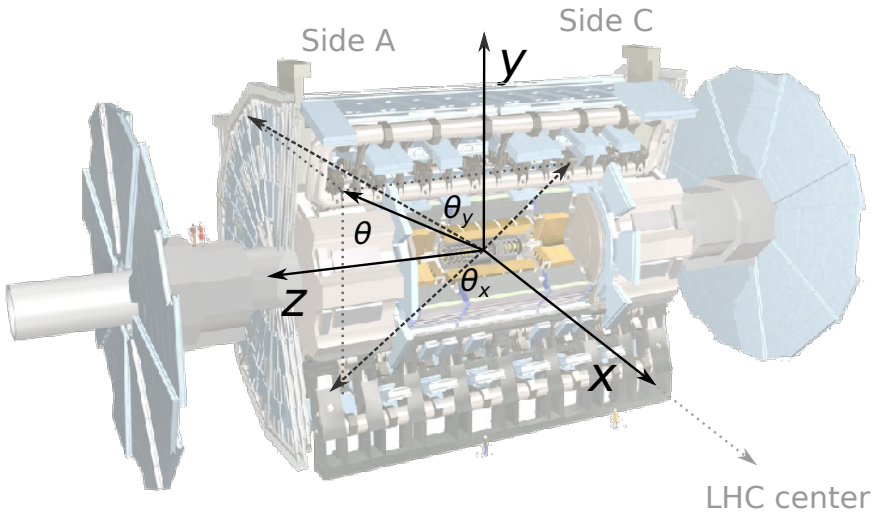

Figure 1.7: ATLAS coordinate system.

$E_{\mathrm{T}} = \sqrt{m^2c^4 + p_{\mathrm{T}}^2 c^2}$ and $\vec{E}_{\mathrm{T}}^{\mathrm{miss}} = -\sum_i \vec{p}_{\mathrm{T},i}$, where $\vec{p}_{\mathrm{T},i}$ is the $\vec{p}_{\mathrm{T}}$ of i-th recorded particle and the sum goes over all visible particles. A quantity often used for description of diffractive events is the fractional momentum loss ξ, defined as $\xi = \frac{p_{\mathrm{z}}^{\mathrm{in}} - p_{\mathrm{z}}^{\mathrm{out}}}{p_{\mathrm{z}}^{\mathrm{in}}}$, where $p_{\mathrm{z}}^{\mathrm{in}}$ is the z component of momentum of the proton before an interaction and $p_{\mathrm{z}}^{\mathrm{out}}$ is the z component of momentum of the proton after the interaction.

The number of interactions within one bunch crossing is distributed according to the Poisson distribution with the average number μ. The parameter μ is used to describe the amount of pileup for specific running conditions.

It is a common practice to label quantities related to the interaction point with a star, e.g. θ_x^* for the θ_x angle under which a particle is emerging from the IP.

Movable detectors in the forward region approach very closely to the beam. Since the beam profile determining the particle flux through such a detector can vary between runs, distance of the detector from the beam (especially the minimal allowed distance) is often given in multiples of the nominal beam width σ_{beam}.

1.2.2 ALFA

ALFA is designed to run with a special setting of the LHC magnets downstream from the ATLAS main detector that translates θ_x^*, θ_y^* angles of elastic protons into x, y positions of hits in ALFA, so-called parallel-to-point optics. This way, ALFA can measure the angles at the IP and calculate the total cross section from their distribution, as I explain in the next chapter.

ALFA consists of four stations located since Run 2 at 237 and 245 m (originally with the far stations in Run 1 at 241 m) from the IP. Each station houses two Roman pots equipped with detectors placed vertically, above and under the

beamline. Roman pots are movable in the vertical direction and can approach the beam closer than 1 mm from the beam center under the special run conditions. The placement of ALFA stations is illustrated in Fig. 1.8.

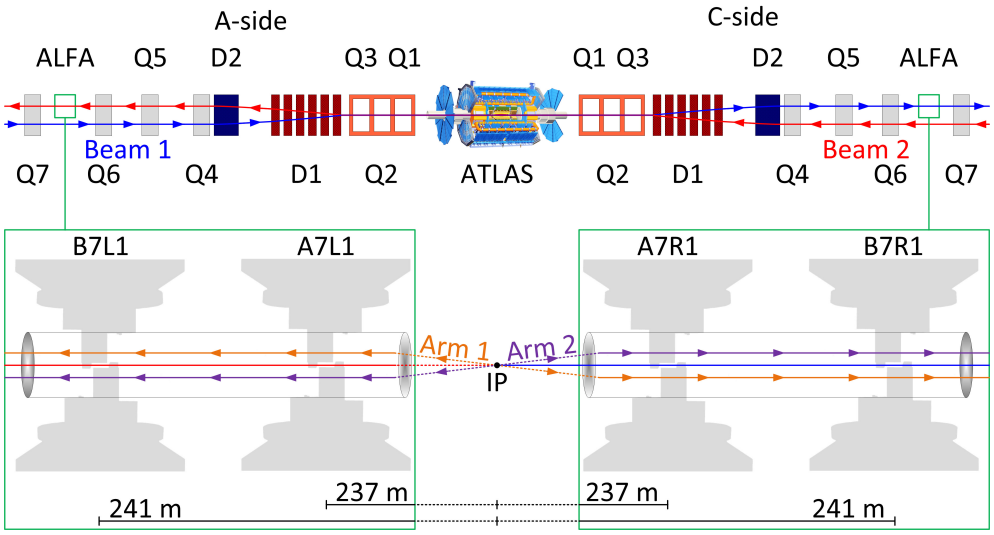

Figure 1.8: Schema of the ALFA placement. The lower part indicates the station names and positions in Run 1 [P11].

Each Roman pot (shown in Fig. 1.9) is equipped with two sets of detectors — a main detector (MD) and two overlap detectors (ODs). Both MDs and ODs are scintillating fiber detectors. Both use 0.5×0.5 mm^2 fibers scintillating in blue light. The fibers are aluminum coated to minimize crosstalk between them. In addition, plastic scintillator tiles are added to the MD and both ODs to provide trigger signal. Figure 1.10 illustrates how detectors from both Roman pots in a station approach the beam and shows the photograph of one detector assembly.

The MDs serve to reconstruct the tracks of elastically scattered protons, while the ODs from the two Roman pots in a station overlap each other to provide distance of the upper and lower detectors using beam halo protons.

The scintillating fibers in MDs are glued at 45° angle to a titanium support plate, as illustrated in Fig. 1.10. There are two sets of fibers glued to one support plate, one perpendicular to the other, with 64 fibers in a set. To minimize the amount of material in the way of protons, there is a machined triangular cut out in the MD support plates and thinned wall of the Roman pots in the shape of MD sensitive area. There are 20 fiber layers in total, 10 layers per inclination. The fibers are staggered between layers in order to achieve the design resolution of 30 µm [P11].

The OD fibers are all glued horizontally. The fibers are stacked in 3 layers of 30 fibers each and staggered by third of the fiber thickness in each layer. The distance between the upper and lower MD is measured with the precision of 10 µm [P11].

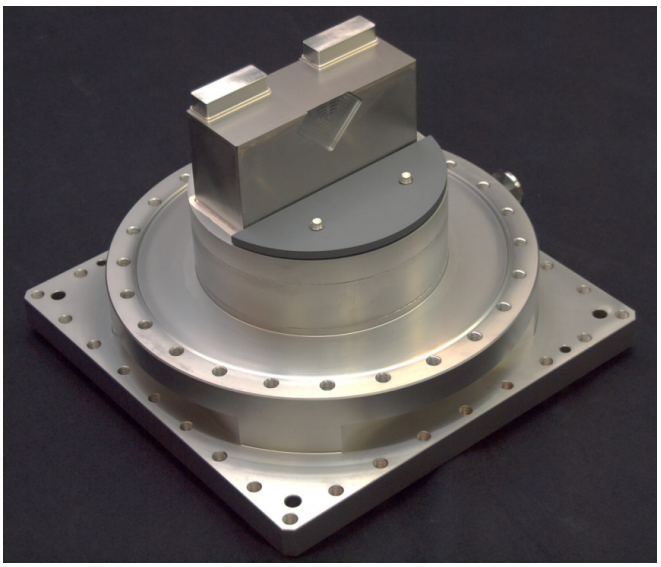

Figure 1.9: ALFA Roman pot [P11]. The two rectangular extensions at the top cover the OD detectors, while the MD is placed in the large box beneath with the sensitive area behind the diamond-shaped thinned wall.

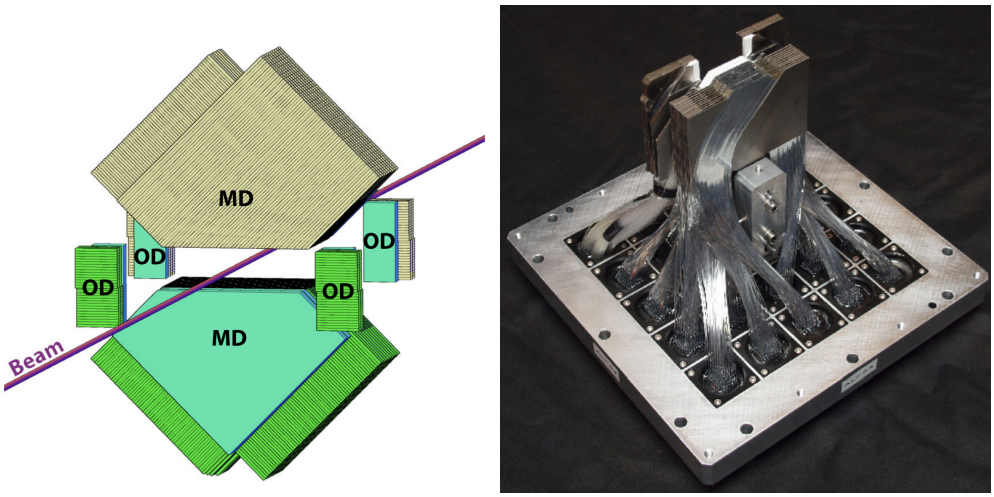

Figure 1.10: *Left:* Schematic view of the ALFA station instrumentation (copyright CERN, CC-BY-4.0 license). *Right:* Photograph of the ALFA detector assembly [P11].

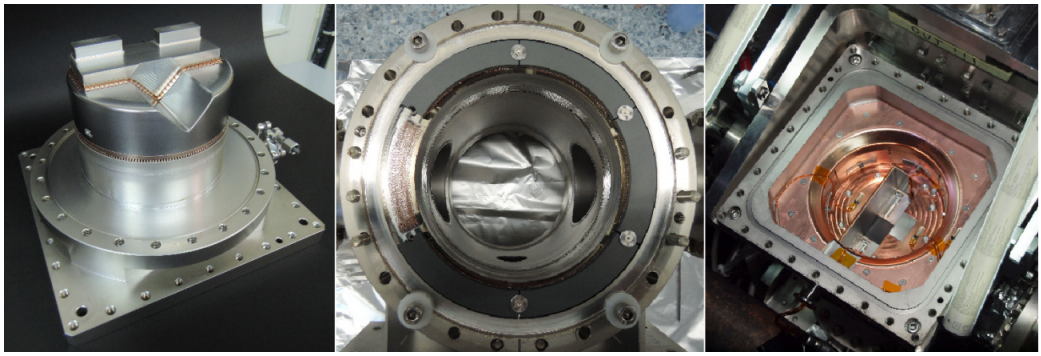

Figure 1.11: Modifications of the ALFA pot and station to lower RF heating. *Left:* RP filler placed on the original pot; *middle:* ferrite ring attached to the station flange; *right:* added copper inside the pot to improve heat transfer [P11].

During Run 1, ALFA observed high temperatures of up to 45 °C in the Roman pots and found the main cause of heating to be RF losses induced by the beam in the ALFA pots. As the beam intensity was to rise in Run 2, several measures were taken to reduce the RF heating, as illustrated in Fig. 1.11. Main modification was the addition of the Roman pot (RP) filler to remove the cavities in the ALFA stations with sharp steps in the beam pipe inner surface experienced by the RF field of the beam. The RP filler is made of titanium and connected by copper-beryllium springs to the original RP. Other upgrades include improved heat transfer inside the RP by adding a copper foil and change in ferrites. The original semi-circular piece of ferrite was removed and a new ring of ferrites was added to the flange to further reduce RF heating.

1.2.3 AFP

The AFP tags and measures protons that lost small fraction of their energy, but were not dissociated in a collision. Typically, this is the case in diffractive events, where the AFP provides valuable sign of such event and provides information about the fractional momentum loss ξ.

The AFP has evolved from the FP220 and FP420 projects with the intent to use the so-called Hamburg beam pipe, illustrated in Fig. 1.12, for detector housing. Whole assembly was to be mounted on a table with a movement in the horizontal direction and there were supposed to be bellows on both ends of the assembly to allow for this movement. The main advantage of this housing is that it provides a large space for detectors with reasonable space requirements.

The design of the Hamburg beam pipe was later modified to account for RF losses and an induced heating of the housing. Sharp steps in the inner beam pipe profile at ends of detector pockets were inclined and also the end parts of the beam pipe were changed to have conical shape. Despite the changes, it was later decided not to pursue the Hamburg beam pipe design, but rather to use Roman pots, as they were already operating at the LHC.

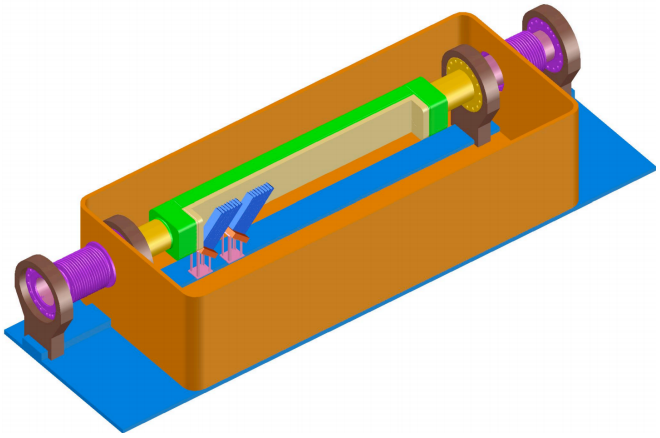

Figure 1.12: Hamburg beam pipe with QUARTIC detectors enclosed in the secondary vacuum vessel [11].

In the final configuration, the AFP is build of four stations at 205 and 217 m from the IP, as illustrated in Fig. 1.13. There is one horizontal Roman pot per station and all the Roman pots are instrumented with a silicon tracker detector (SiT) consisting of 4 detector planes. The Roman pots in the far stations are in addition equipped with a time-of-flight (ToF) system. A schematic view and a photograph of a far station instrumentation is shown in Fig. 1.14.

The SiT detector utilizes 3D pixel sensors developed and manufactured by CNM (Centro Nacional de Microelectronica, Barcelona, Spain) and FBK (Fondazione Bruno Kessler, Trento, Italy). Each sensor has 16.8×20 mm^2 area and 336×80 pixels with pixel size of 50×250 µm^2. The sensors are read out by the FE-I4B chip developed for the IBL, where the same pixel sensors are used. The sensors and readout chips are mounted on carbon fiber reinforced aluminum plates tilted at 14° to improve the resolution in the x coordinate. The sensors are staggered in y direction for the optimal y resolution. The achieved spatial resolution is 3 µm in x and 30 µm in y [10, 13].

The ToF system is needed in the high pileup environment of the LHC to discriminate e.g. double diffractive events, in which both protons survive the collision. It is based on Cherenkov photons emitted by a proton passing through quartz bars. The bars are L-shaped in order to fit into the limited space of the Roman pot, and they serve as both the Cherenkov radiator and light guide. There are 16 bars in total divided into 4 rows, called *trains*. A passing proton traverses 4 bars in a train and time of arrival is measured for each of them. Cherenkov light is detected by a Micro-channel Plate PMT (MCP-PMT) with a segmented anode providing 4×4 readout channels. The selected PMT is Photonis XPM85112 with 6 µm pores, 30 ps time transit spread (TTS) and an ALD (atomic layer deposition [14]) coated MCP for extended lifetime. MCP-PMT output is processed by amplifiers, constant fraction discriminator (CFD) and digitized by High Performance Time to Digital Converter (HPTDC) [15]. ToF

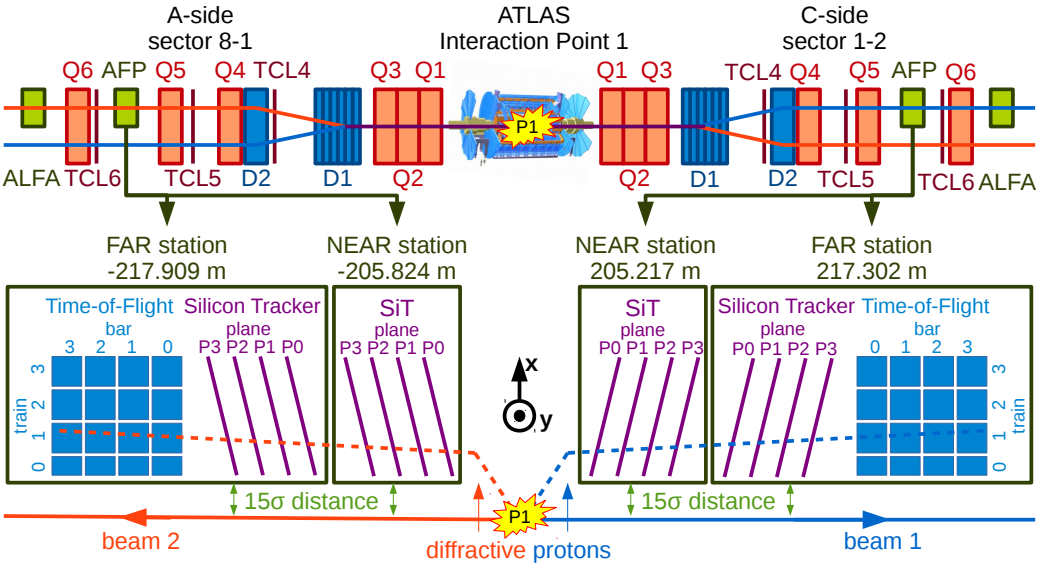

Figure 1.13: Schema of the AFP placement and instrumentation [12].

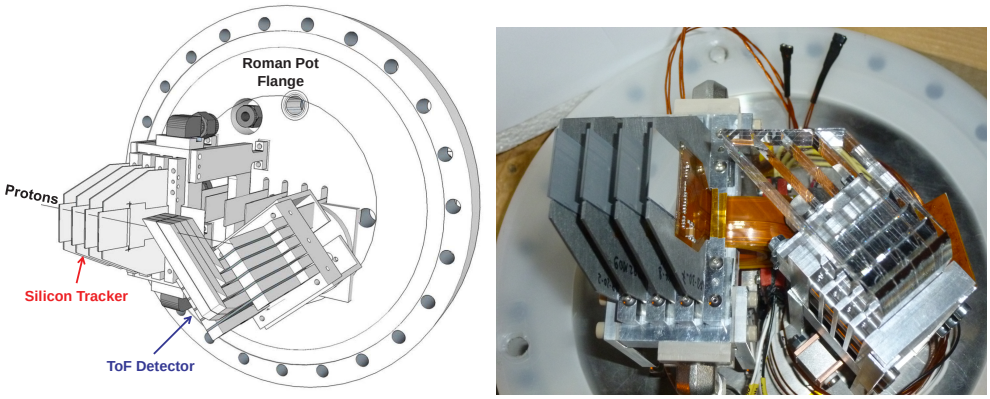

Figure 1.14: *Left:* Schematic view of the AFP far station instrumentation [12]. *Right:* Photograph of the AFP detector assembly [12].

achieved 20 ps time resolution during beam test campaigns [P14].

The AFP Roman pots enclosing the detector packages have thinned window with 300 µm thickness on sides and bottom, where the measured diffractive protons pass, in order to minimize a proton scattering on the steel. The window is shown in Fig. 1.15. There is a vacuum (10–40 mbar) inside the Roman pots in order to minimize interactions of protons with gas and to limit the stress caused by a different pressure on the sides of the thinned window with the ultra-high vacuum of the LHC beampipe ($1 \cdot 10^{-11}$–$1 \cdot 10^{-10}$ mbar [2]).

First two stations of the AFP were installed during the year end technical stop of the LHC in early 2016 on side C of ATLAS. The two stations were equipped with the SiT trackers only. The AFP was successfully commissioned in this configuration during the LHC intensity ramp up after the technical stop and operated in two special low-μ runs as well as normal high-μ runs at a distance

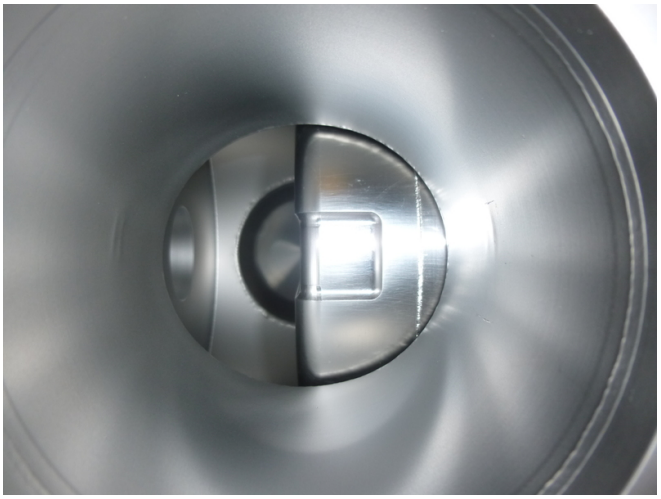

Figure 1.15: View of the Roman pot inserted in the beampipe [12].

from the beam down to $20\,\sigma_{\text{beam}}$ (about 3 mm).

The remaining stations together with ToF detectors were installed during the extended year end technical stop in the beginning of 2017. The AFP was qualified for insertions at $12\sigma_{\text{beam}} + 0.3\,\text{mm}$ (about 1.5–2.7 mm) and inserted on a regular basis during physics runs. The ALD coated MCP-PMTs were not ready at that time and ToF was installed with 10 µm pore MCP-PMTs without the ALD coating with a planned replacement during the next year end technical stop. However, ToF operated at a low efficiency and issues with new Photonis MCP-PMTs were observed during 2017 beam tests. It was decided in the beginning of 2017 to remove ToF and reinstall it when ready during a technical stop. Photonis delivered another set of MCP-PMTs in beginning of June 2018 and it was immediately tested. However, one of the PMTs was not able to operate in the vacuum, so ToF is currently not installed in the LHC tunnel.

Chapter 2

Forward physics

Forward detectors provide valuable information about a proton or protons that were not dissociated in a collision. This information is of interest especially in the case of elastic scattering and diffractive interactions, where zero or only small amount of energy is lost by the protons. Elastic scattering allows to measure total interaction cross section through the optical theorem, while diffraction is useful for probing the proton structure at low momentum transfers.

Both ALFA and the AFP are placed such that there are magnets between them and the IP. ALFA runs with a special magnets setting that allows it to determine angles at which protons leave the IP. The AFP is designed for measurements of the momentum loss ξ from position spread caused by dipole magnets. In both cases, knowledge of beam optics is needed for a successful operation and data analysis.

2.1 Beam optics

Figure 2.1 shows schema of magnets in the forward region between the IP and about 270 m. In this region, there are two dipole bending magnets — D1 (composed of six parts) and D2. There are two separate beam pipes for the two beams traveling in the opposite directions at the major part of the LHC circumference. However, the beams need to occupy a single beam pipe in the IPs to allow for collisions. The two dipoles are bending the beams at the transition from the two beam pipes (one for incoming and one for outgoing beam) to the one and back.

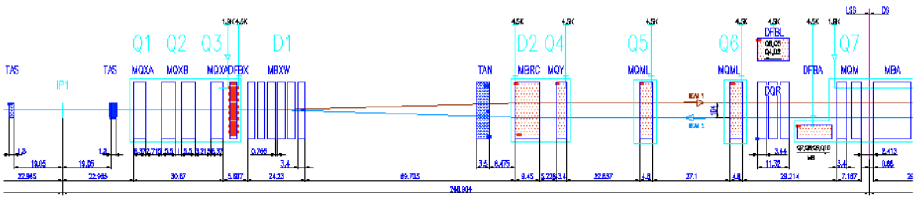

Figure 2.1: Schema of magnets in the forward region between the IP and about 270 m [16].

Beam focusing is performed by seven quadrupole magnets Q1–Q7, where Q2 and Q7 are composed of two parts. Q1–Q3 are the inner triplet quadrupole magnets responsible for the strong focusing of incoming beams in the IP down to the width of few tens of micrometers in transverse plane for high luminosity collisions.

In addition, there are five horizontal and six vertical orbit correctors (so-called kickers) in the region. These are again dipole magnets and are used to introduce the beam crossing angle before the IP and compensate it after the IP. They can also be used to introduce a bump for enhanced ξ acceptance of forward detectors [17].

Acceptance of the forward detectors is, apart from the optics itself, affected also by finite apertures of elements of the forward region — mainly by the magnets and the collimators. There are three sets of collimators with jaws movable in the horizontal (x) direction in the ATLAS forward region — TCL4 at 150 m, TCL5 at 190 m and TCL6 at 220 m from the IP.

2.1.1 Linear optics of synchrotron

A synchrotron, such as the LHC, has mostly periodic structure of bending dipoles and strongly focusing quadrupoles filled in by higher order magnets, RF cavities, beam insertion and dump systems, collimators and, of course, experiments. A charged particle motion in a synchrotron is governed in a linear approximation by the Hill's equation (written in the Frenet-Serret reference frame of the nominal particle) [18]

$$\frac{\mathrm{d}^2 u(s)}{\mathrm{d}s^2} + K_\mathrm{u}(s) u(s) = 0, \tag{2.1}$$

where s is the distance along the nominal particle trajectory and u is a perpendicular coordinate, i.e. x or y, and $K_\mathrm{u}(s)$ is a periodic function representing beam focusing properties of magnets.

A solution of Hill's equation can be written in a form of *betatron oscillations*

$$u(s) = \sqrt{\epsilon}\sqrt{\beta_\mathrm{u}(s)}\cos\left(\psi_\mathrm{u}(s) + \phi_\mathrm{u}\right), \tag{2.2}$$

where ϵ is the beam *emittance*, i.e. the size of the beam in the phase space (u, u') with $u' = \frac{\mathrm{d}u(s)}{\mathrm{d}s}$, $\beta_\mathrm{u}(s)$ is the *beta function*, determining the beam size and divergence at a given point s, $\psi_\mathrm{u}(s)$ is the phase and ϕ_u is the initial phase. The phase is given by the beta function as $\psi_\mathrm{u}(s) = \int_0^s \frac{\mathrm{d}s}{\beta_\mathrm{u}(s)}$.

It is also possible to calculate the transport of a charged particle through individual elements of the synchrotron. It is convenient to use the matrix representation, similar to the ray optics matrix formalism, and write

$$\begin{pmatrix} u(s) \\ u'(s) \end{pmatrix} = \mathcal{M} \begin{pmatrix} u(s_0) \\ u'(s_0) \end{pmatrix} = \begin{pmatrix} m_{11} & m_{12} \\ m_{21} & m_{22} \end{pmatrix} \begin{pmatrix} u(s_0) \\ u'(s_0) \end{pmatrix}. \tag{2.3}$$

Each element can be described by a matrix and to calculate the transport of the particle from the origin to a given point s at the synchrotron, it is only needed to multiply individual matrices in the order of elements they represent

$$\begin{pmatrix} u(s) \\ u'(s) \end{pmatrix} = \mathcal{M} \begin{pmatrix} u(0) \\ u'(0) \end{pmatrix} = \mathcal{M}_n \mathcal{M}_{n-1} \dots \mathcal{M}_2 \mathcal{M}_1 \begin{pmatrix} u(0) \\ u'(0) \end{pmatrix}. \tag{2.4}$$

This is of course equivalent to Eq. 2.2 and it can be shown that

$$\mathcal{M}_{0\to s} = \begin{pmatrix} \sqrt{\frac{\beta(s)}{\beta(0)}} \left(\cos\psi(s) + \alpha(0)\sin\psi(s)\right) & \sqrt{\beta(s)\beta(0)}\sin\psi(s) \\ \frac{(\alpha(0)-\alpha(s))\cos\psi(s) - (1+\alpha(0)\alpha(s))\sin\psi(s))}{\sqrt{\beta(s)\beta(0)}} & \sqrt{\frac{\beta(0)}{\beta(s)}}\left(\cos\psi(s) - \alpha(s)\sin\psi(s)\right) \end{pmatrix} \tag{2.5}$$

where $\beta(s) = \beta_{\mathrm{u}}(s)$, $\alpha(s) = -\frac{1}{2}\frac{\mathrm{d}\beta(s)}{\mathrm{d}s}$ and $\psi(0) = 0$.

In the case of diffractive or other off-nominal-momentum particles, the relative momentum difference ξ needs to be taken into the calculation. A deviation of such particles from the nominal trajectory is characterized by the dispersion function $D_{\mathrm{u}}(s)$. Hill's equation in such a case becomes inhomogeneous differential equation and a particular solution is added to the Eq. 2.2 in the form $D_{\mathrm{u}}(s)\xi$. The transport matrix becomes 3×3 matrix

$$\begin{pmatrix} u(s) \\ u'(s) \\ \xi \end{pmatrix} = \mathcal{M}(s) \begin{pmatrix} u(s_0) \\ u'(s_0) \\ \xi \end{pmatrix} = \begin{pmatrix} m_{11} & m_{12} & D_{\mathrm{u}}(s) \\ m_{21} & m_{22} & D'_{\mathrm{u}}(s) \\ 0 & 0 & 1 \end{pmatrix} \begin{pmatrix} u(s_0) \\ u'(s_0) \\ \xi \end{pmatrix}, \tag{2.6}$$

where $D'_{\mathrm{u}}(s) = \frac{\mathrm{d}D_{\mathrm{u}}(s)}{\mathrm{d}s}$.

2.1.2 LHC running scenarios

The LHC runs most of the time with the aim to provide the highest possible luminosity due to the focus on rare processes. A luminosity $\mathcal{L}$ is related to the rate of interactions $\frac{\mathrm{d}N}{\mathrm{d}t}$ through the total interaction cross section σ_{tot} as

$$\frac{\mathrm{d}N}{\mathrm{d}t} = \mathcal{L}\sigma_{\mathrm{tot}}. \tag{2.7}$$

The luminosity in an interaction point of a collider such as the LHC is given by numbers of particles N_1, N_2 in bunches of the two colliding beams, by the revolution frequency f, the number of colliding pairs of bunches N_{b} and the area of the overlap of the bunches. Assuming, for illustration, a head-on collision of beams with the same profile given by widths in the perpendicular axes σ^*_{x}, σ^*_{y} (the star is used for the value at the IP, e.g. $\sigma^*_{\mathrm{x}} = \sigma_{\mathrm{x}}(s_{\mathrm{IP}})$), the luminosity is given [19] by

$$\mathcal{L} = \frac{N_1 N_2 f N_{\mathrm{b}}}{4\pi\sigma^*_{\mathrm{x}}\sigma^*_{\mathrm{y}}}. \tag{2.8}$$

The revolution frequency is given by the LHC circumference and cannot be altered. The number of colliding bunches can be adjusted by the filling scheme, with the upper limit of about 2800 given by the minimum bunch spacing and necessary gaps for injection and extraction. The nominal number of protons per bunch is 10^{11} [2].

The beam profile is determined by the beam optics in use. A beam width in the u axis, where again u stands for x or y, at a given point s at the LHC circumference can be calculated from the value of the beta function at this point $\sigma_{\mathrm{u}}(s) = \sqrt{\epsilon\beta_{\mathrm{u}}(s)}$. Therefore, $\sigma^*_{\mathrm{u}} = \sqrt{\epsilon\beta^*_{\mathrm{u}}}$.

Beams can be separated in special runs, meaning that the longitudinal axes of the two beams are not crossing, but are few σ apart, so that only the peripheral part of the beam profiles interact. This is done to achieve a lower pileup (μ) with the same optics as for the high luminosity runs.

There are 3 basic running scenarios from the point of view of the forward detectors:

- *Low β^*, high μ* — normal run conditions. β^* down to 35 cm and μ up to 50 provide high luminosity for searches and measurements of rare processes. The AFP participates during normal runs, but most of the processes of interest require good pileup rejection, hence the ToF system is needed.

- *Low β^*, low μ* — the AFP special runs. β^* as in the normal runs and μ from about 0.01 to 3, providing clean samples for diffractive studies as well as for inelastic pileup modeling and studies of underlaying event.

- *High β^*, low μ* — ALFA special runs. Runs with β^* of 90–2500 m for measurements of luminosity and the total pp cross section. For the simultaneous determination of σ_{tot} and $\mathcal{L}$, ALFA needs an access to protons scattered elastically at very small angles (Mandelstam $-t < 10^{-3}\,\mathrm{GeV}^2$). Therefore, the high β^* is needed, since $-t_{\mathrm{min}} \sim (\beta^*)^{-1}$. Single diffraction and central exclusive production can be also studied with the ALFA detector using the data taken in this running scenario.

2.2 Elastic and total cross section

The total pp cross section is an important parameter of strong interaction. It is not predicted by the theory, but needs to be measured whenever a higher energy becomes available. Experiments show that it increases with the center-of-mass energy $\sqrt{s}$. Theory predicts so-called Froissart-Martin bound that states that the total cross section cannot rise faster than $\ln^2 s$ [20].

The total cross section can be determined from elastic scattering using the optical theorem from the quantum theory of scattering [P4, 20]

$$\sigma_{\mathrm{tot}} = 4\pi\,\mathrm{Im}\,f_{\mathrm{el}}(t)\Big|_{t=0}, \tag{2.9}$$

where $f_{\mathrm{el}}(t)$ is the elastic scattering amplitude and t is the Mandelstam squared four-momentum transfer variable. For small angles, Mandelstam t is related to the scattering angle at the IP θ^* as $t \approx -(p\theta^*)^2$, where p is the size of the 3-momentum of the incident proton.

Therefore, it is possible to determine the total cross section from the extrapolation of the measured differential elastic cross section $\frac{\mathrm{d}\sigma}{\mathrm{d}t}$ to $t = 0$. Two methods are commonly used [P4]. First, the luminosity dependent method

$$\sigma_{\mathrm{tot}}^2 = \frac{16\pi}{1+\rho^2}\frac{\mathrm{d}\sigma_{\mathrm{el}}}{\mathrm{d}t}\Big|_{t=0} = \frac{16\pi}{1+\rho^2}\frac{1}{\mathcal{L}}\frac{\mathrm{d}N}{\mathrm{d}t}\Big|_{t=0}, \tag{2.10}$$

where $\rho = \frac{\mathrm{Re}\, f_{\mathrm{el}}(t)}{\mathrm{Im}\, f_{\mathrm{el}}(t)}$. It can be used when an independent measurement of the luminosity is available.

Second is the luminosity independent method that utilizes simultaneous measurement of elastic and inelastic rate

$$\sigma_{\mathrm{tot}}^2 = \frac{16\pi}{1+\rho^2}\frac{1}{N_{\mathrm{el}}+N_{\mathrm{inel}}}\frac{\mathrm{d}N}{\mathrm{d}t}\Big|_{t=0}. \tag{2.11}$$

ALFA published measurements of the total cross sections at $\sqrt{s} = 7\,\mathrm{TeV}$ [P5] and at $\sqrt{s} = 8\,\mathrm{TeV}$ [P8] using the luminosity dependent method. The measurement is based on the determination of the differential elastic cross section $\frac{\mathrm{d}\sigma}{\mathrm{d}t}$ using the measurement of protons positions in ALFA detectors. Four-momentum transfer t is calculated from $t = -(p\theta^*)^2$. The angle θ^* is reconstructed using the knowledge of the beam optics transport matrix and the hit positions in the ALFA detectors. ALFA uses mainly the subtraction method [P4], utilizing the matrix element $m_{12} = \sqrt{\beta_{\mathrm{ALFA}}\beta^*}\sin\psi_{\mathrm{ALFA}}$ on the two sides of ATLAS (A and C) to compute θ^*_{u} from the u coordinate of the hit, where u is x or y, as

$$\theta^*_{\mathrm{u}} = \frac{u_{\mathrm{A}} - u_{\mathrm{C}}}{m_{12,\mathrm{A}} + m_{12,\mathrm{C}}}. \tag{2.12}$$

The differential elastic cross section is determined by scattering amplitudes of strong nuclear interaction and electromagnetic Coulomb interaction:

$$\frac{\mathrm{d}\sigma}{\mathrm{d}t} = \frac{1}{16\pi}\left|f_{\mathrm{N}}(t) + f_{\mathrm{C}}(t)e^{i\alpha\phi(t)}\right|^2, \tag{2.13}$$

where $f_{\mathrm{N}}(t)$ and $f_{\mathrm{C}}(t)$ are the amplitudes of strong interaction and Coulomb interaction, respectively, α is the fine structure constant and $\phi(t)$ is a phase induced by the long range Coulomb interaction. The expression can be expanded and parametrized [P4] as

$$\begin{aligned}\frac{\mathrm{d}\sigma}{\mathrm{d}t} &= \frac{4\pi\alpha^2\hbar^2c^2}{|t|^2}G^4(t) \\ &\quad - \sigma_{\mathrm{tot}}\frac{\alpha G^2(t)}{|t|}\left(\sin(\alpha\phi(t)) + \rho\cos(\alpha\phi(t))\right)\exp\frac{-B|t|}{2} \\ &\quad + \sigma_{\mathrm{tot}}^2\frac{1+\rho^2}{16\pi\hbar^2c^2}\exp(-B|t|),\end{aligned} \tag{2.14}$$

where $G(t)$ is the electric form factor of the proton and B the nuclear slope parameter. The term on the first line corresponds to the Coulomb interaction, the one on the second line to the Coulomb-nuclear interference and the third line is due to the strong interaction.

The measured differential elastic cross section at 8 TeV is plotted in the left part of Fig. 2.2 together with the fit using the theoretical prediction (Eq. 2.14), from which the total cross section and the nuclear slope parameter B are extracted.

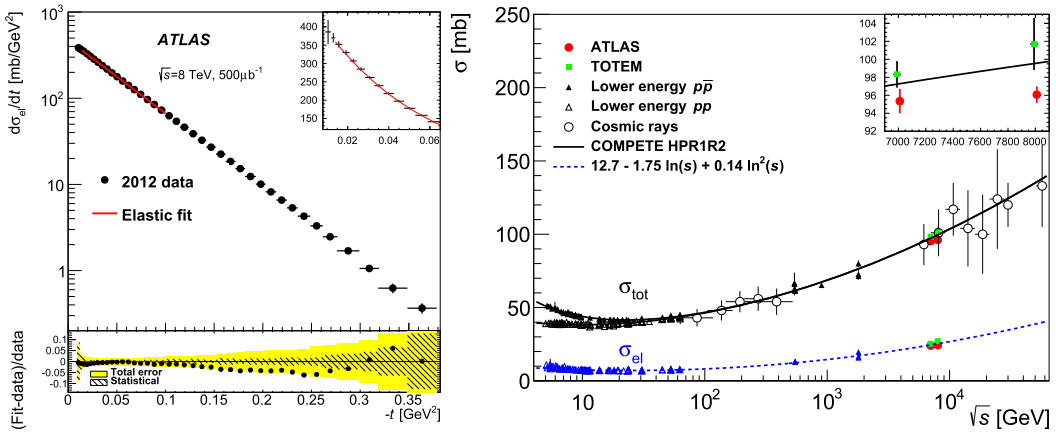

Figure 2.2: *Left:* Differential elastic cross section measured by ALFA with the fit using the theoretical prediction with free parameters σ_{tot} and B. The lower part shows the relative difference between the fit and the data with the yellow area representing the total uncertainty and the hatched area the statistical uncertainty. *Right:* Compilation of total and elastic cross section results as a function of the center-of-mass energy [P8].

Dependence of the total and elastic cross section on the center-of-mass energy is shown in the right part of Fig. 2.2 using data from lower energy pp and $p\bar{p}$ experiments, data from ALFA and TOTEM at 7 TeV and 8 TeV and from cosmic ray observatories.

2.3 Diffraction

Diffractive events are characterized by an exchange of vacuum quantum numbers ($J^{PC} = 0^{++}$). The incoming protons may be dissociated in the process, but the energy of the outgoing protons, proton and dissociated system, or two dissociated systems is almost equal to that of the incoming protons.

Diffraction in the wave optics occurs e.g. when light encounters a black disc. A typical pattern is produced on a distant screen with a forward peak followed by series of minima and maxima. A similar pattern, shown in Fig. 2.3, is observed in the differential cross section $\frac{\mathrm{d}\sigma}{\mathrm{d}t}$ of elastic proton-proton (pp) scattering,

where t is again the Mandelstam variable representing squared four-momentum transfer [21].

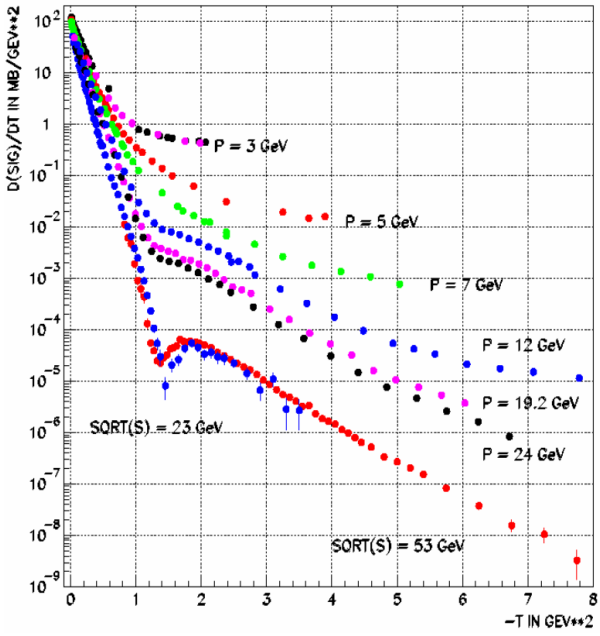

Figure 2.3: Proton-proton elastic cross section as a function of t for various energies in a collision. P stands for the momentum of the incoming proton in a fixed target experiment and $\sqrt{s}$ is the center-of-mass energy in pp collision [21].

Depending on the number of dissociated partons, it is possible to classify diffractive events as elastic scattering (no dissociation), single dissociation and double dissociation, as illustrated in Fig. 2.4. A typical sign of a diffractive event is that the outgoing particles are well separated in phase space, mostly observed in a form of a large rapidity gap (LRG). It is also possible to produce particles centrally as is shown in Fig. 2.5, such production is called central diffraction.

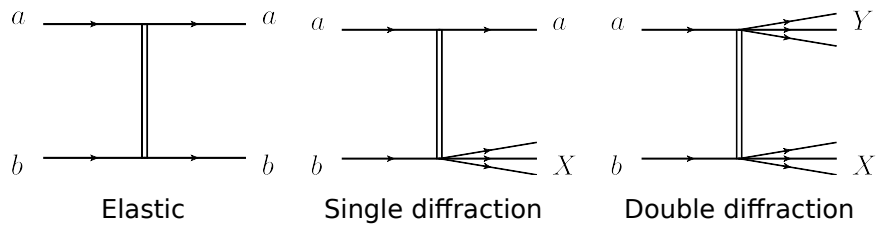

Figure 2.4: Illustration of elastic scattering, single and double diffractive dissociation [10].

There are two distinct regimes in which the diffraction manifests itself. At low momentum transfers, the so-called soft diffraction takes place. Since no hard scale is present, it is not possible to use the perturbative quantum chromodynamics (pQCD) and phenomenological models such as Regge theory are used.

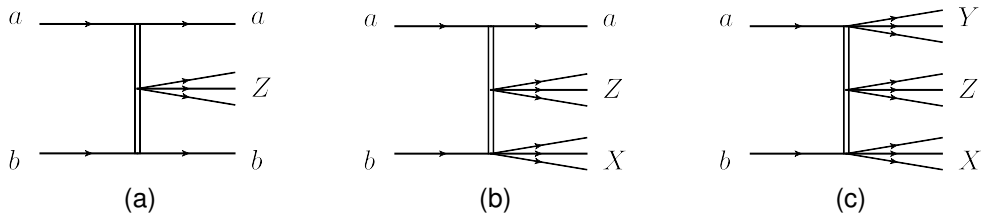

Figure 2.5: Illustration of central diffraction with (a) intact protons, (b) single dissociation, (c) double dissociation [10].

At high momentum transfers, hard diffraction is observed, with a presence of a hard scale.

Regge theory describes hadron-hadron scattering in terms of exchange of so-called *Regge trajectories*. Bound states of spherically symmetrical potentials represent poles in partial wave amplitude for a given integer angular momentum l. Regge treated l as a complex number, which leads, for well behaved potentials, to a line on which the poles lie. In such a case, a Regge trajectory can be parametrized as $\alpha(t) = \alpha(0) + \alpha' t$. It turns out that all known resonances lie on trajectories with the *intercept* $\alpha(0) \leq 0.5$. However, since total cross section $\sigma_{\text{tot}} \underset{s\to\infty}{\sim} s^{\alpha(0)-1}$, it should drop with increasing center-of-mass energy s, which is inconsistent with measurements, as shown in the previous chapter. An additional trajectory with intercept $\alpha(0) \approx 1$ was introduced to address the discrepancy and it was named *pomeron*. It is the pomeron that is exchanged in diffractive processes [20, 21].

Hard diffraction can be described using the perturbative QCD with the pomeron being a compound object represented in the lowest order by a pair of gluons. In this regime, it is possible to measure diffractive parton distribution function (DPDF) of proton and probe the composition of pomeron. Examples of hard diffractive processes are shown in Fig. 2.6.

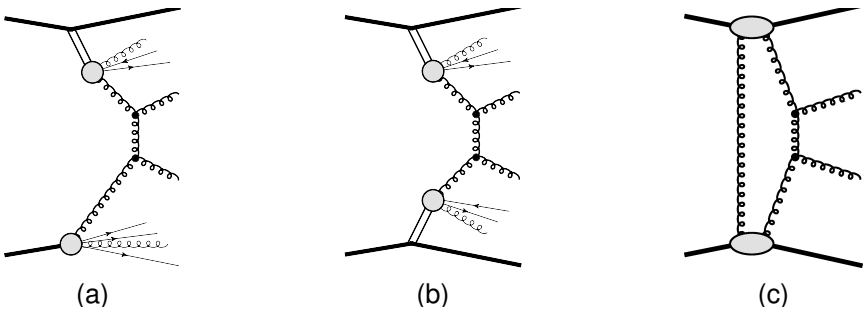

Figure 2.6: Feynman diagrams of hard diffraction processes — (a) diffractive deep inellastic scattering (DDIS), (b) double pomeron exchange (DPE), (c) central exclusive production (CEP) [10].

A typical signature of a diffractive event is a large rapidity gap observed in energy deposits in calorimeters. This can be used to discriminate diffractive

events. However, the gap can be filled in hadron-hadron colliders by interactions of spectator partons of the colliding hadrons, resulting in additional final state particles depositing energy in the calorimeters. The fraction of diffractive events with the preserved rapidity gap is given by the *rapidity gap survival probability*, denoted as S^2, with the measured value of $S^2 = 0.16 \pm 0.09$ at the LHC [22].

Forward detectors, especially the AFP, provide an additional tag of a proton or protons together with measurement of ξ. The single arm of the AFP (the two detectors on one side of ATLAS forward region) installed in 2016 enabled an extension and improvement of ATLAS single diffraction (SD) studies, including soft diffraction, SD jet, two jet (jet-gap-jet) and photon+jet production as well as SD W and Z production. Such processes can be studied to measure pomeron flux, S^2 or pomeron composition and to tune Monte Carlo simulations [23, 24]. Apart from normal high luminosity runs, AFP also took data in two low pileup runs with $\mu = 0.03$ and $\mu = 0.3$ with total integrated luminosity of $0.5\,\mathrm{pb}^{-1}$.

The second arm installed in 2017 provided the tag of the second outgoing proton, enabling to add central diffraction studies, like DPE production of jets and photon+jet. Three special runs took place during 2017 with $\mu = 0.05$, 1 and 2, providing very clean samples for model testing, DPDF and pomeron quark and gluon content studies.

Rare processes, like CEP, require much higher statistics, requiring data from high luminosity running. The AFP allows to suppress background in such runs by requiring two tagged protons. The comparison of the primary vertex z position reconstructed by the inner tracker of ATLAS to the vertex z position calculated from the AFP ToF system reduces the background by an additional factor of up to 10, assuming 10 ps time resolution [23].

2.4 Beyond the Standard Model

The AFP provides a useful tool for background rejection also in other processes with intact protons in the final state. An example of such a process is diphoton scattering or diphoton production of a WW or ZZ pair, as illustrated in Fig. 2.7. Cross sections of such processes depend on the strength of the quartic coupling and therefore it is possible to probe an anomalous quartic coupling predicted by some extensions of the Standard Model. A proton tag (even without the ToF information), together with reconstructed bosons, may be sufficient for background suppression, provided that the the anomalous coupling is strong enough [25].

Figure 2.7 also shows two possible production mechanisms of a new particle X, diphoton interaction and CEP. The AFP can provide measurement of the mass of the produced particle based on the proton momenta loss. This is especially useful for a search for an invisible particle. The AFP is able to reconstruct the missing mass of such a particle in range of about 300–1300 GeV, depending on how close the AFP is inserted to the beam, as illustrated in Fig. 2.8 [10, 26].

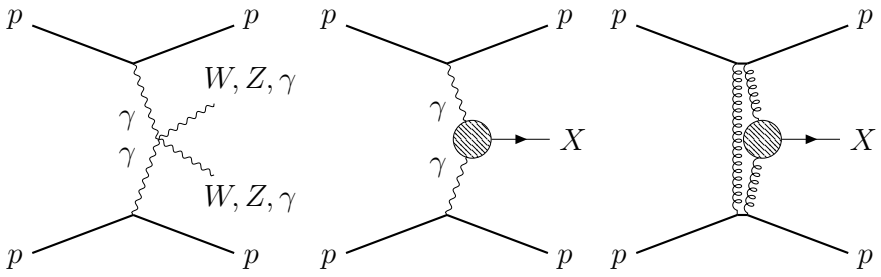

Figure 2.7: Feynman diagrams of processes with a potential to probe beyond the Standard Model physics. From left to right: diphoton production of diphoton, WW or ZZ; diphoton production of an invisible particle X; CEP of an invisible particle X.

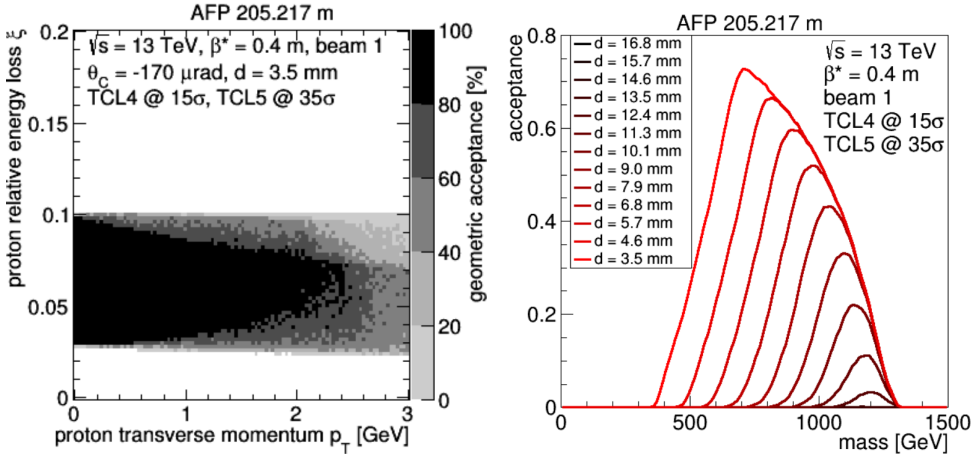

Figure 2.8: Geometric (*left*) and mass (*right*) acceptance of the AFP [26].

Part II

Simulation of the forward detectors

Chapter 3

Full simulation of the ATLAS forward region

In this chapter, I introduce the packages that allow full Geant4 [27] based simulation of particles entering the very forward region of the ATLAS experiment. Such simulations are useful for the forward detectors of ATLAS. I started the work on the packages already as a part of my master's thesis and I extended the functionality as a part of my ATLAS qualification task. I have documented the packages in an ATLAS note [P7], on which this chapter is based. I omit here the parts describing how to use the code under the Athena framework of ATLAS, as an interested reader can refer to the note [P7] or dedicated TWiki page [P6].

Forward detectors usually use just a mapping tool to calculate particles positions and their momenta at the distance of the detector from the interaction point of ATLAS (IP). Such a tool takes either particles from a particle generator or particles simulated by Geant4 inside of ATLAS volumes and calculates needed positions and momenta using matrices that describe magnets optics in the forward region. Examples of such mapping tools under Athena are `ForwardTransport`, `ForwardTransportFast` [28], `ALFA_BeamTransport` [29], `FPTracker` [30] and `FNTracker` [31] (the later three are now deprecated and replaced by the two former).

I describe here an approach using a Geant4 based simulation to transport particles from the IP to the location of a forward detector. There are several advantages of this approach. First, whole simulation runs under Geant4 and therefore simultaneous simulation of multiple forward detectors is naturally possible. Second, also secondary particles emerging in the forward region are simulated. For example, showers developing on beam screens of magnets can be studied. And third, it is possible to move and rotate magnets and vary their fields to study effect of such displacements and field differences. There is also one disadvantage, though — speed. While using e.g. `ForwardTransport` is fast and processing of thousand events takes a few seconds, using the full simulation is much slower, thousand events on the same computer may take few hours when using the full list of physics processes of Geant4.

3.1 Model

The model of the forward region (`ForwardSimulation`) consists of modeled beam pipe elements and the corresponding magnetic fields. It is divided into three packages:

- `ForwardRegionGeoModel` — GeoModel [32] description of the beam pipe elements,
- `ForwardRegionMgField` — magnetic fields definitions for the forward region,
- `ForwardRegionProperties` — the helper C++ class for passing properties from job option to `ForwardRegionMgField`.

Two approaches of description of the beam pipe elements are possible and implemented — GeoModel, implemented by me, and AGDD [33] (Atlas Generic Detector Description), implemented by a CERN summer student Knut Dundas Moraa. I document here only my contribution, the AGDD model is described in the note [P7]. The field description package is common for both approaches.

3.1.1 Magnetic fields description

The description of magnetic fields of magnets in the forward region is provided in the package `ForwardRegionMgField`. Two ways of configuration of the fields are possible — twiss files and the `magnets.dat` file.

The `magnets.dat` file contains a field strength value (i. e. magnetic induction value for dipoles or induction gradient for quadrupoles) for each magnet in the forward region. While this was useful for an early implementation and code tuning, it is not very practical for studies with a magnet setting being used for particular LHC running conditions. Still, the file can be used for a simple modification of the magnets optics, for example to study the effect of field value differences/uncertainties.

The setting of magnets, i. e. the optics of the LHC, is provided by optics experts in a form of so-called *twiss files*.

The twiss files contain $k_i L$ values (where k_i is i-th normalized, momentum independent magnetic moment and L is length of the magnet) and magnet lengths, and from these values, B field inductions and induction gradients used by the `ForwardRegionMgField` package are calculated (p_0 is the proton nominal momentum set in the job option file):

$$B_0[\mathrm{T}] = \frac{k_0 p_0[\frac{\mathrm{GeV}}{\mathrm{c}}]}{0.299792458}, \qquad g\left[\frac{\mathrm{T}}{\mathrm{m}}\right] = \frac{k_1 p_0[\frac{\mathrm{GeV}}{\mathrm{c}}]}{0.299792458}. \tag{3.1}$$

The field of the dipoles is described analytically for both D1, D2 and horizontal orbit correctors — $\vec{B} = (0, B_0, 0)$. For the vertical orbit correctors, the perpendicular bending plane is needed — $\vec{B} = (B_0, 0, 0)$.

The inner triplet quadrupole magnets (Q1–Q3) fields are described in two ways — analytically and by measured field maps taken from the FLUKA simulation of ATLAS [34], which were originally taken as more realistic. These field maps are renormalized to the field gradient from a given file (either twiss or `magnets.dat`). Since the maps contain the B field vector sampled on the mesh in the x-y plane, the bilinear interpolation is used to obtain the vector in between the mesh points. However, since the FLUKA field maps are anyway constructed from analytical description up to about 24 mm from the magnet axis and most protons in acceptance of the forward detectors do not pass further from the axis, it was decided to use analytical description as the default one. Furthermore, I observed transport errors in order of microns for high-ξ protons when crossing angle of the beams was present in the IP due to imprecision caused by the bilinear interpolation. Since the FLUKA maps are not really needed anymore and also due to performance issues (the field value is evaluated several times per event in given magnet), I did not implement higher order interpolation for these maps.

Other quadrupole fields are described analytically — $\vec{B} = (gy, gx, 0)$, where g is the field gradient.

3.1.1.1 Field transformation

The real LHC magnets are placed with a certain precision and small shifts and rotations occur. In Geant4 based simulation, it is possible to simulate such transformation of fields. In `ForwardSimulation` packages, this feature is implemented for dipole bending magnets D1, D2 and quadrupole magnets Q1–Q7.

Since the current implementation of the field manager in Athena does not allow to rotate and move a field with the geometric volume it is assigned to, proper field transformation needs to be calculated and applied to the field. In addition, GeoModel volumes need to be moved to correspond to the transformed field. Only small rotations are expected, therefore, besides shifts, only a rotation around the x axis is applied to the volume of the magnet. The used simplification applies only to GeoModel volumes, the field itself is transformed including all rotations.

3.1.2 Geometry

The model contained in the `ForwardRegionGeoModel` package describes elements of the beam pipe using Geometry Kernel Classes (usually called GeoModel) [32]. The beam pipe elements are build from 19 to 269 m on both sides of the IP. The model is composed of three basic volume types — a tube with circular, elliptical and recticircular (intersection of a circle and a rectangle such that a circle with flats on top and bottom or left and right side is created, see Fig. 3.2) aperture. It is possible to describe most beam pipe elements (sometimes with certain level of approximation) by one of these three volume types. In

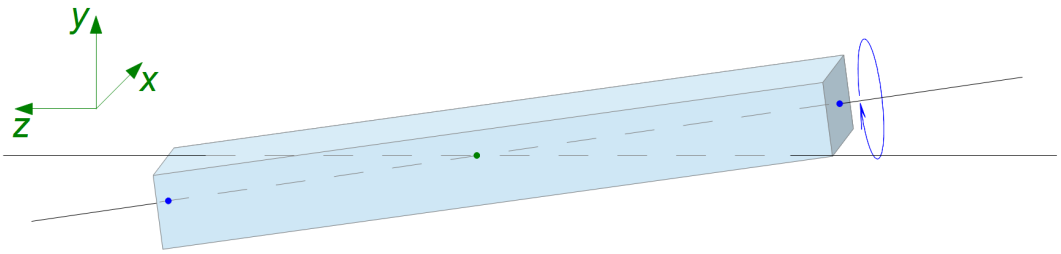

Figure 3.1: Illustration of the field transformation. Input parameters for the transformation are marked — start point, end point and rotation angle around the magnet axis. Point in the center shows the point around which the magnet is rotated.

addition, transition piece from one to two beam pipes — "trousers" — located at 140 m and TCL (by default only TCL5 at 184 m) collimator models are build. The VP1 [35] visualization is shown in Fig. 3.3.

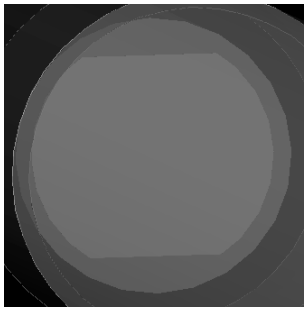

Figure 3.2: Visualization of recticircular volume with flats on top and bottom.

Positioning and apertures of beam pipe elements are based on the information contained in the *Layout Database* [36]. Wall thicknesses of elements are based on drawings from CERN Drawing Directory [37], except for magnets, where the wall thickness is increased 10 times to emulate the existing dead material of the magnets and to prevent holes.

3.2 Validation

I performed several simulations in order to validate the model. First, the nominal proton trajectory was checked against MadX [38]. This was shown already in my master's thesis and the results did not change during later code modifications and extensions. The difference between `ForwardSimulation` and MadX was shown to be less than 0.08 µm [P7].

The results of validation improved for diffractive protons after the extension of the model and several bug fixes. The event-by-event comparison was done again using `ALFA_BeamTransport` and I show results below.

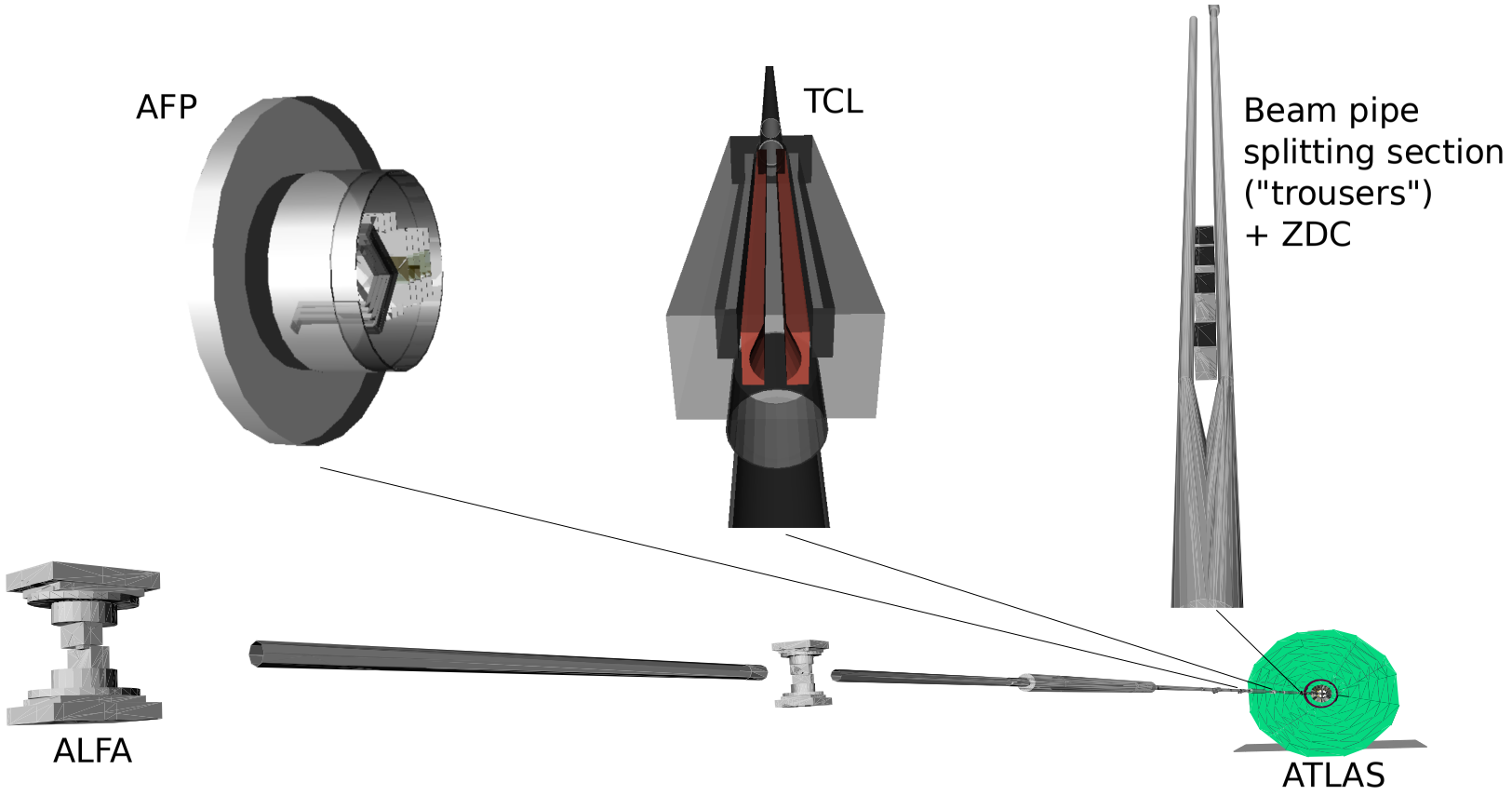

Figure 3.3: Visualization of the forward region model — one side with ALFA, AFP and ATLAS.

Also, the use of the FLUKA maps describing the fields of the quadrupoles Q1–Q3 was revisited and deprecated based on the test results. The new features of the model that could affect the proton transport were validated as well.

3.2.1 Event-by-event comparison

I checked how well diffractive protons are transported. For this purpose, I transported the same set of protons from the IP to $|z| = 237.403$ m (position of the inner ALFA station) using the full simulation of the forward region beam pipe and `ALFA_BeamTransport` package (which was validated against Mad-X [29]). Then, I compared x and y positions of the corresponding protons after transport.

For the comparison, I used the 3.5 TeV optics with $\beta^* = 90$ m. I have transported $1 \cdot 10^5$ protons for each outgoing beam with energy in the range $[3.0, 3.5]$ TeV with step of 0.02 TeV, pseudorapidity η in the range $[10, 18]$ with step of 0.2 and φ angle in the interval $[0, 2\pi)$ with 100 samples for each energy and pseudorapidity setting. The purged physics list (i.e. all relevant physics processes except for transport and magnetic bending were turned off) was used to only simulate transport of protons, so that physics processes do not smear the transported positions in the full simulation. This also significantly lowered required computing resources used by the full simulation and therefore enabled to simulate such a large sample.

There are some differences between the coordinate systems used by the full simulation and `ALFA_BeamTransport`. While in the full simulation, the beam 1 corresponds to proton beam propagating in the negative z direction, in `ALFA_BeamTransport` it is the beam 2 which travels in the negative z direction, which means that sign of z coordinate for `ALFA_BeamTransport` output needs to be reversed for comparison.

There is also a shift in the x coordinate. `ALFA_BeamTransport` takes coordinates x and y relative to a nominal proton trajectory, which results in 97 mm shift in x when compared to the full simulation, as the nominal proton position corresponds to x = -97 mm at 237.403 m from IP. For the y coordinate there is no shift or sign change [P2].

The differences of coordinate systems are summarized in Table 3.1.

Table 3.1: Coordinate system differences between `ALFA_BeamTransport` and the full simulation at the position of ALFA stations.

Beam 1	Beam 2
$x_{\text{FullSim}} = x_{\text{ALFA\_BT}} - 97$ mm	$x_{\text{FullSim}} = x_{\text{ALFA\_BT}} - 97$ mm
$y_{\text{FullSim}} = y_{\text{ALFA\_BT}}$	$y_{\text{FullSim}} = y_{\text{ALFA\_BT}}$
$z_{\text{FullSim}} = -z_{\text{ALFA\_BT}}$	$z_{\text{FullSim}} = -z_{\text{ALFA\_BT}}$

In Figure 3.4, there are shown positions of protons after the transport by the `ALFA_BeamTransport` (for readability, only the protons generated with $\eta = 10$ are shown). They form ellipses, which center depends on proton energy

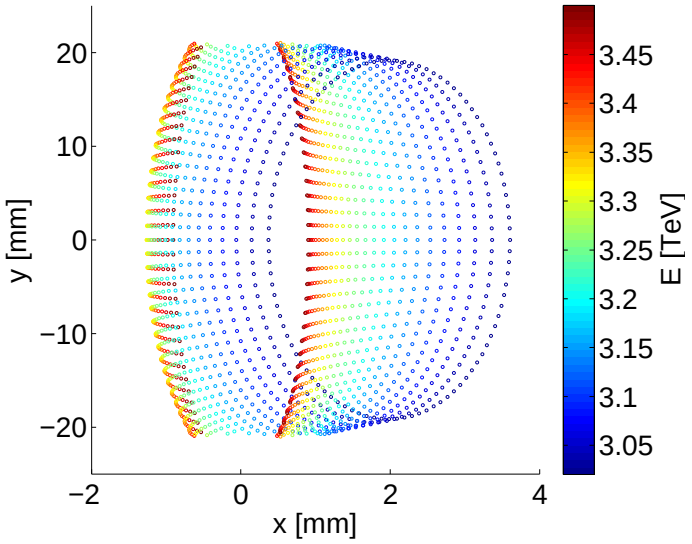

Figure 3.4: Positions of protons with $\eta = 10$ and different energy after the transport by the `ALFA_BeamTransport` at $z = 237.403$ m. Axes are not to scale. The cut top and bottom are caused by apertures of beam elements (for the given optics, mostly by the aperture of the Q6 magnet).

and major and minor axes depend on pseudorapidity. A lower energy value means a higher x coordinate of the center and a lower pseudorapidity value means longer axes of ellipses (for a given energy).

In histograms which follow, I use some abbreviations. I use length of radius vector in xy plane — r — and differences between the full simulation and `ALFA_BeamTransport` in x, y and r. The differences are labeled $\Delta x, \Delta y$ and Δr. I define these abbreviations as:

$$\begin{aligned} r &= \sqrt{x^2 + y^2} \\ \Delta x &= x_{\text{FullSim}} + 97 \text{ mm} - x_{\text{ALFA\_BT}} \\ \Delta y &= y_{\text{FullSim}} - y_{\text{ALFA\_BT}} \\ \Delta r &= \sqrt{\Delta x^2 + \Delta y^2} \end{aligned} \tag{3.2}$$

where the subscript FullSim corresponds to the full simulation and ALFA_BT to the `ALFA_BeamTransport`.

The coordinates x and y in histograms correspond to coordinates of `ALFA_BeamTransport`. Also when talking about the z coordinate, I mean the z coordinate in `ALFA_BeamTransport`, unless stated otherwise.

The results of the comparison are shown in Figures 3.5–3.8. Figure 3.5 shows distributions of differences between the full simulation and `ALFA_BeamTransport` in x and y coordinate of protons transported to $|z| = 237.403$ m from the IP.

It is visible that in x, there is a shift of $-0.06\,\mu$m and an absolute difference of

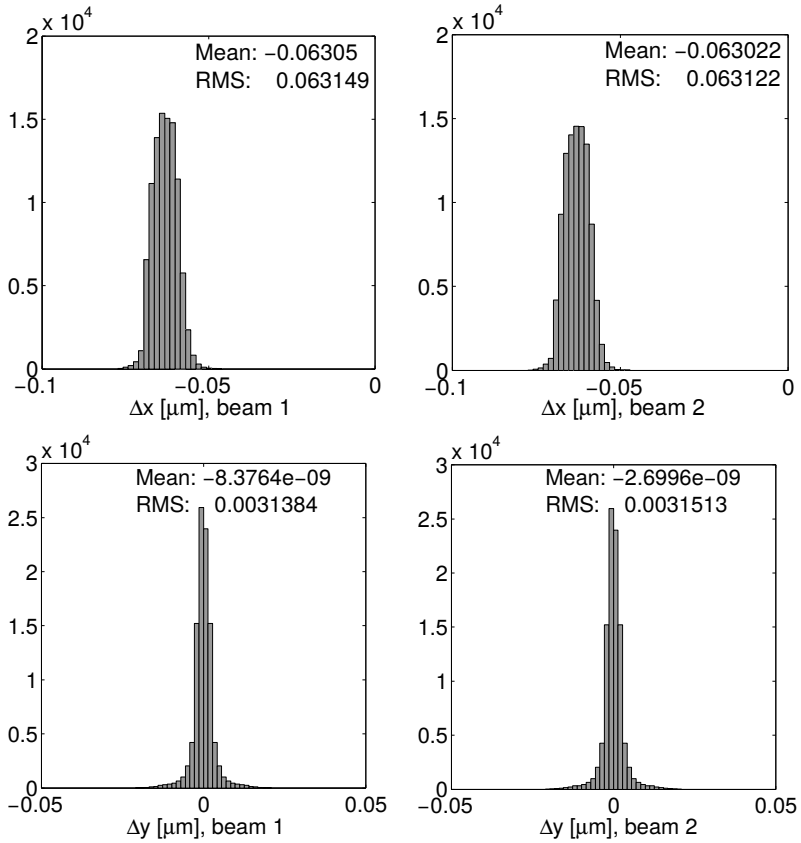

Figure 3.5: Histograms of the differences between the full simulation and `AL-FA_BeamTransport` in x (up) and y (down) for the beam 1 (left) and the beam 2 (right).

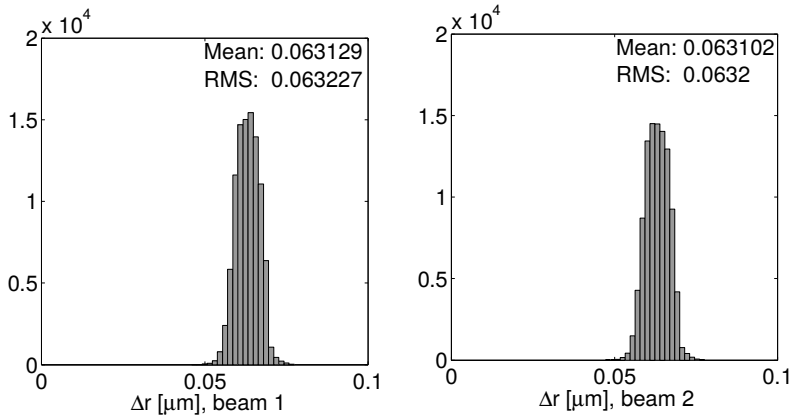

Figure 3.6: Histograms of the differences between the full simulation and `AL-FA_BeamTransport` in r for the beam 1 (left) and the beam 2 (right).

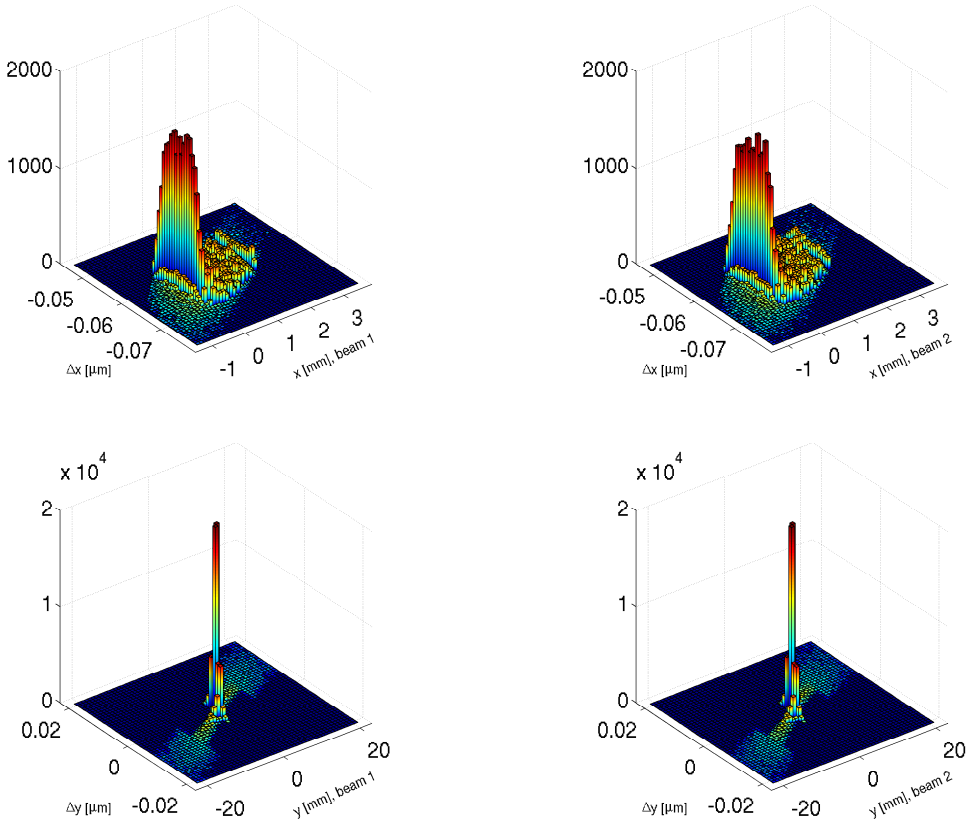

Figure 3.7: Histograms of the differences between the full simulation and `ALFA_BeamTransport` in x (up) and y (down) with corresponding coordinate value for the beam 1 (left) and the beam 2 (right).

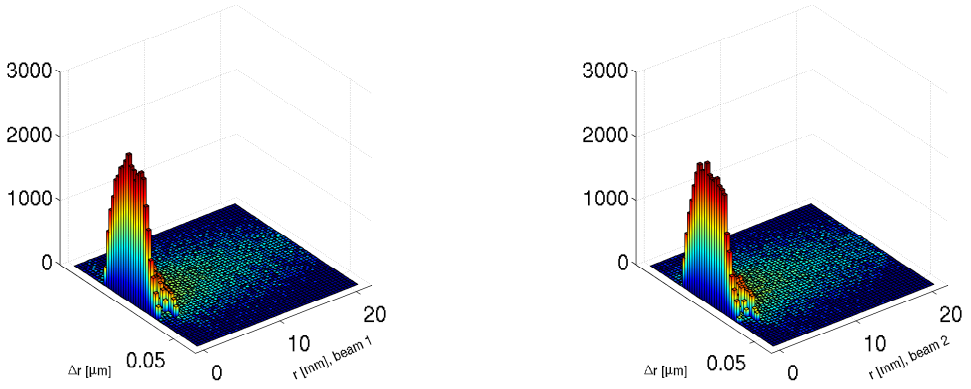

Figure 3.8: Histograms of the differences between the full simulation and `ALFA_BeamTransport` in r with corresponding value of r for the beam 1 (left) and the beam 2 (right).

less than 0.1 µm. The reason for the shift is that the nominal proton x coordinate at $|z| = 237.403$ m is not exactly -97 mm. This could be caused basically by two reasons — either there is an error in a dipole field or a dipole placement, or the nominal proton's x coordinate really slightly differs from the -97 mm. The second option is most likely right, because in the Mad-X survey file, the x position of a nominal proton is actually by 0.06 µm more than -97 mm. As far as the absolute difference is concerned, it could be caused either by errors in the quadrupole fields or by differences between these two models of transport.

In the y coordinate, there is no measurable shift and the absolute difference is less than 0.03 µm. Again this difference could be caused by quadrupole field errors or differences between the models.

In Fig. 3.6, there is the distribution of the radius vector length difference. This distribution comprises both differences in x and y. It peaks at 0.06 µm, which corresponds to the shift in x and maximum difference is again less than 0.1 µm.

Figures 3.7 and 3.8 show bivariate histograms of difference in x, y and r with dependence on the corresponding coordinate x, y or r.

In case of the x coordinate, the histogram peaks for $x = 0$ mm. This is caused by the fact that density of points actually drops with increasing x. This fact is visible also on lowering density of peaks for growing x coordinate. The x coordinate of point is influenced mostly by proton energy. The higher value of x corresponds to the lower energy value. There is a clear correlation between Δx and x.

In y coordinate, there can again be seen a linear dependence of Δy on y for the given energy. Only this time different proton energy causes different angle of the line of dependence.

Figure 3.8 again comprises differences in x and y.

3.2.2 Check of FLUKA field maps for Q1–Q3

When checking how protons are transported from the IP to the AFP position for different values of relative energy loss ξ and transverse momentum p_{T}, I noticed the following strange behavior. I used `ForwardSimulation` with purged physics list (only transport was to be simulated) to transport protons from the IP up to AFP. One expects that protons starting at the IP (without smearing) with given ξ, p_{T} and uniform φ form an ellipse after transport. However, as you can see in Fig. 3.9, flat sections start to appear in ellipses for $p_{\mathrm{T}} = 2$ GeV and $\xi > 0.11$.

These flats are caused by a drop in gradient of magnetic intensity when going further from the magnet axis. The reason for this drop is bilinear interpolation that I was using to calculate values in between the mesh points of the field map used to describe the field. The problem occurs mostly in Q2 magnet, where the limiting distance from the magnet axis (in perpendicular plane to the magnet axis, which is parallel with the z axis) is around 24 mm.

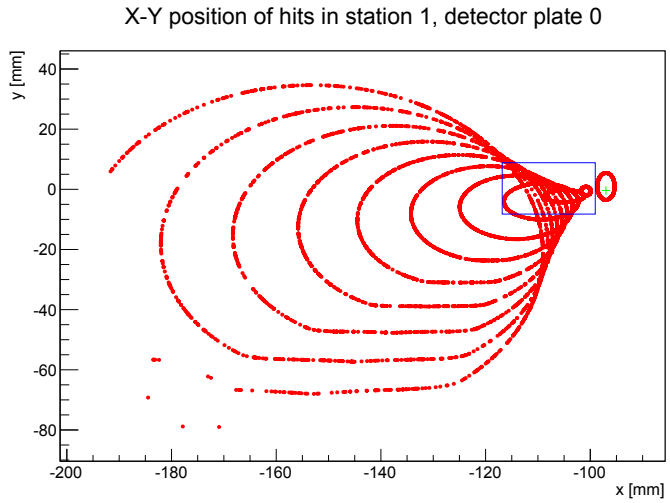

Figure 3.9: Transported protons positions at position of the first AFP station ($z = 204$ m), $\xi = 0.29, 0.26, 0.23, 0.20, 0.17, 0.14, 0.11, 0.09, 0.06, 0.03, 0$, $p_{\mathrm{T}} = 2$ GeV with purged physics list (transport only). The blue rectangle represents the AFP geometrical acceptance, the green cross marks center of the beam.

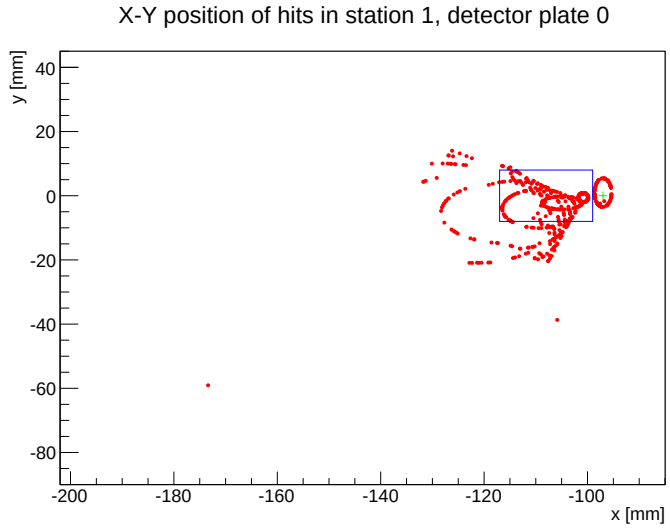

Figure 3.10: Transported protons positions at position of the first AFP station ($z = 204$ m), $\xi = 0.29, 0.26, 0.23, 0.20, 0.17, 0.14, 0.11, 0.09, 0.06, 0.03, 0$, $p_{\mathrm{T}} = 2$ GeV with default physics list. The blue rectangle represents the AFP geometrical acceptance, the green cross marks center of the beam.

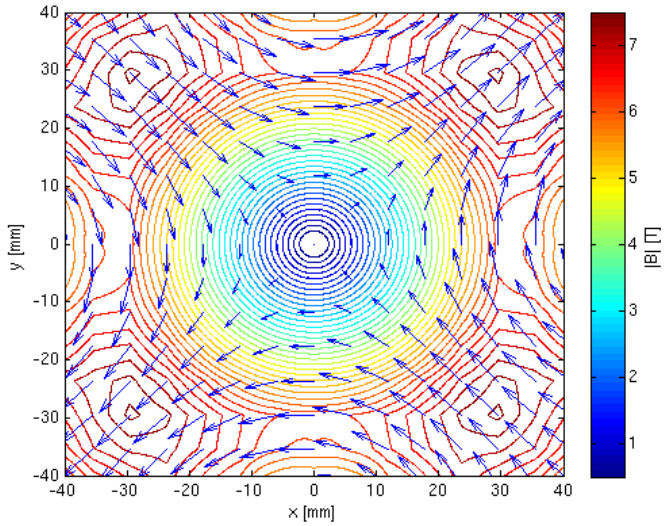

Figure 3.11: Visualization of the Q2 magnet field map. Contours show the value of the magnetic induction, arrows show the value and direction of the magnetic induction in the mesh points of the map.

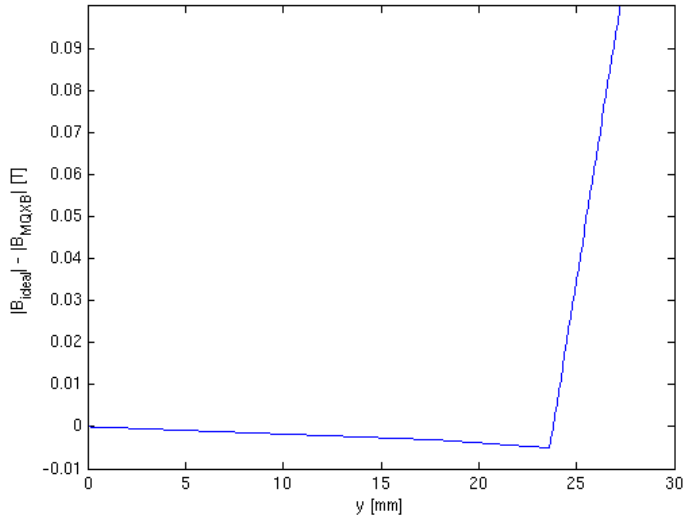

Figure 3.12: Difference between the magnetic induction value calculated by interpolating the field map and that of the ideal (analytical) quadrupole for $x = 0$.

I can illustrate this behavior on the visualization of the field map in Fig. 3.11. It is visible that at the distance of about 24 mm, shape of the contours starts to differ from ideal circles of analytical quadrupole description ($\vec{B} = (gy, gx, 0)$, where g is the field gradient). For the Q2 quadrupole, this distance is still not fully outside of the magnet aperture (recticircular aperture with flats parallel with y axis and maximum widths $d_x = 48$ mm, $d_y = 57.8$ mm).

The difference from the analytical quadrupole itself is not a problem, as it is expected (the quadrupole is not ideal). The problem is shown in Fig. 3.12 — there is a sharp drop of the magnetic induction value caused by the bilinear interpolation. The field changes too quickly to be well approximated by bilinear interpolation.

However, it can be shown that, even though particles affected by the interpolation effect are not lost in the Q2 aperture, they are lost further downstream. For this purpose, I run again the simulation of protons with the same setting that was used to produce Fig. 3.9, except for physics list — this time, the default physics list was used. Figure 3.10 shows the result — the protons that formed the flats in ellipses are lost during transport. The protons do not form such a nice ellipses any more. The reason is that protons do not interact just with the beam pipe elements, but also with the imperfect vacuum inside the tubes, which causes scattering of some protons.

Due to the effects shown here and since it turned out that the FLUKA maps are constructed from the analytical description up to about 24 mm from the magnet axis and most protons in acceptance of the forward detectors do not pass further from the axis, it was decided to use the analytical description as the default one.

3.2.3 Orbit correctors

To verify orbit correctors implementation, I transported 10^5 protons from the IP to the position of ALFA stations using Mad-X and full simulation; in both cases with optics that contained active orbit correctors — for the comparison, the 7 TeV, $\beta^* = 0.55$ m optics were used. The setup was the same as described in Sec. 3.2.1, except for the optics, corresponding proton energies and the number of generated protons. I subtracted the resulting x and y positions obtained by Mad-X from those obtained by full simulation.

The differences are plotted in Fig. 3.13. It is visible, that the overall difference is less than 1 µm and in x it is even less than 0.2 µm.

3.2.4 Field transformation

As described in Sec. 3.1.1.1, the magnetic field of magnets in the forward region can be moved and rotated in such a way, it corresponds to a misaligned magnet placement. From the input, consisting of a magnet start and end positions and its rotation around its axis, transformation matrix is calculated and applied to

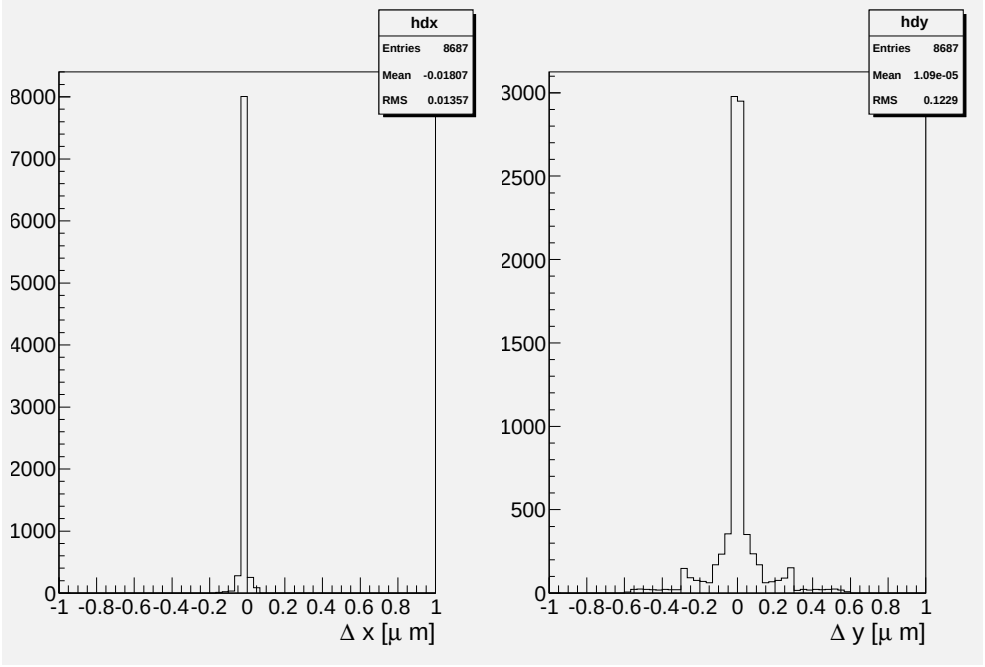

Figure 3.13: Differences in transported positions between Mad-X and the full simulation using 7 TeV, $\beta^* = 0.55$ m optics with a beam crossing.

the ideal field of the magnet.

The B field vector is insensitive to translations. To validate the applied rotations, I wrote out components of magnetic induction vector in the D1b dipole magnet. I applied unrealistically large rotations, so that the effect is easily visible and compared the B field value in the simulation with a computation by hand.

Several cases were tested for a dipole field $\vec{B} = (0, B_0, 0)$:

- no rotations with corresponding no change in the field;
- rotation around the magnet axis (paralel with z axis in this case) with expected magnetic induction vector $\vec{B} = (-B_0 \sin\varphi, B_0 \cos\varphi, 0)$, where φ is rotation angle;
- rotation around the x axis with $\vec{B} = (0, B_0 \cos\varphi_x, -B_0 \sin\varphi_x)$, where $\sin\varphi_x = \frac{\Delta y}{l}$ with Δy being the difference of end and start y position of the magnet and l being the length of the magnet (the rotation is set through setting of the magnet end points);
- rotation around both the magnet and the x axis: $\vec{B} = (-B_0 \sin\varphi, B_0 \cos\varphi \cos\varphi_x, -B_0 \cos\varphi \sin\varphi_x)$;
- rotation around the y axis, which has no effect on the induction vector paralel with the axis.

All tested cases shown full agreement with expected B field values.

Chapter 4

ALFA simulation

4.1 RP filler

The Roman pot fillers installed in all ALFA stations during the LS1 of the LHC were designed to reduce the radio frequency heating of the Roman pots by the proton beam. Each RP filler consists of two copper supports mounted on the preexisting Roman pot and a titanium cylindrical cover with a triangular groove. The cover is equipped with copper-beryllium springs that ensure electrical contact with the existing structure (as shown in Fig. 1.11).

I implemented the model of the RP fillers into the GeoModel implementation of the Roman pots under the Athena framework. The model is based on the technical drawings of the RP filler design. The visualization of the RP filler model is shown in Fig. 4.1.

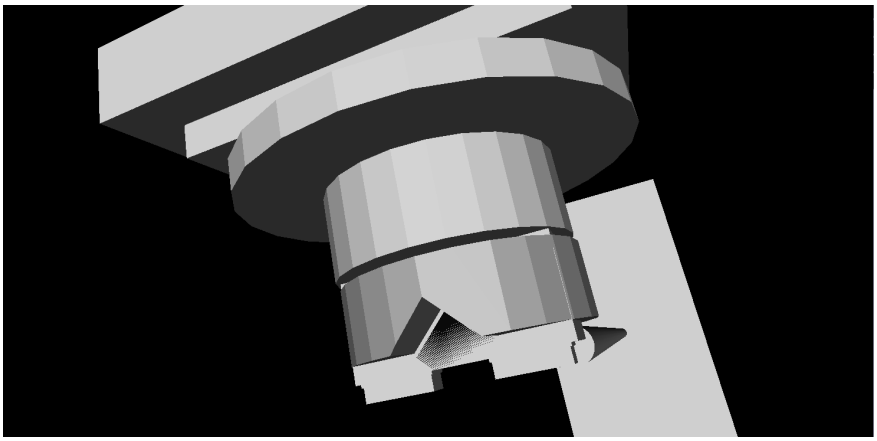

Figure 4.1: VP1 [39] visualization of the ALFA Roman pot (light gray in the foreground) with the RP filler (dark grey).

The model was needed to evaluate the influence of the added material on the ALFA measurements. I produced Monte Carlo samples with and without the RP fillers and the samples were analyzed by a CERN summer student Thomas

Keck. He showed that while the protons outgoing from the IP are unaffected by the RP fillers, the rate of the secondary particles increases and the energy deposited by the secondaries in the ALFA stations is greater by a factor of 5 [40].

4.2 Influence of the ATLAS central magnetic field

Protons leaving ATLAS interaction point in the forward direction are under influence of the magnetic field of the inner tracker solenoid and muon system toroids [1]. I assessed the effect of the ATLAS central magnetic field on measurements of the ALFA detector.

The field effect was evaluated using Monte Carlo (MC) simulation produced in the common ATLAS simulation framework, Athena. A sample of protons going in the forward direction was generated at the ATLAS IP, simulated inside the ATLAS beam pipe, transported or simulated through the Long Straight Section 1 (LSS1) of the LHC until it reached the ALFA detectors and simulated hits were recorded. Each simulation was run twice — once with the magnetic field of ATLAS detector switched on and second with the field switched off.

Several cases were simulated, first, without considering the effect of the ALFA detectors track reconstruction (only recording the precise positions of protons at the end of the ATLAS cavern and right before the first ALFA detector) and second, using the ALFA reconstruction and analysis chain.

To simulate propagation of the protons through the LSS1, I used two tools — `ForwardTransport` and `ForwardSimulation`.

4.2.1 ATLAS magnetic field

The ATLAS magnetic system comprises a solenoid with a 2 T axial magnetic field, a barrel toroid of about 0.5 T and two end-cap toroids with about 1 T field strength. Apart from these active magnets, ferromagnetic structures also affect the total magnetic field of ATLAS.

The fields of the solenoid and the toroids were measured and fitted, and a field map was created based on these measurements by ATLAS magnet systems experts [1]. The field map in the inner detector volume is based only on the fit of the measurement, since the precision is high enough. For the calorimeters and the muon system, calculations and simulations are tuned to the measured points. The complete field map of the ATLAS magnetic field was then produced by connecting all the parts. For more details, see Chap. 2 of the ATLAS overview paper [1].

The visualization of the complete field map is in Fig. 4.2 and 4.3. In all simulations described in this chapter, the field map was read from the conditions database, using tag "BFieldMap-FullAsym-09-solTil3", which corresponds to the latest available field map.

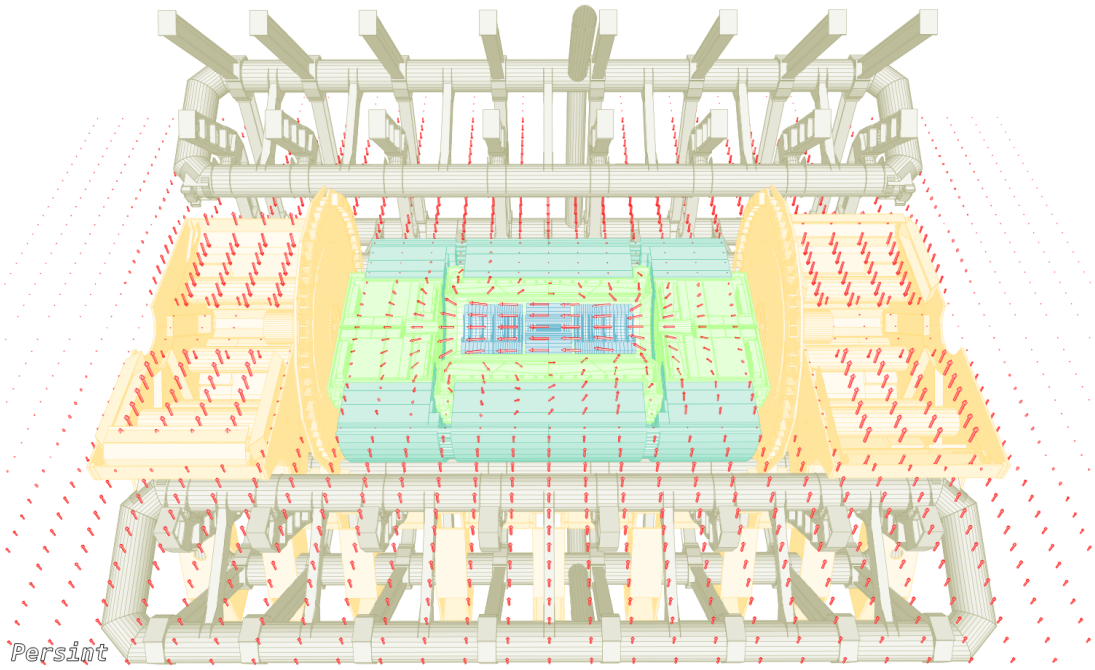

Figure 4.2: Persint [41] visualization of the ATLAS magnetic field — $y = 0$ plane.

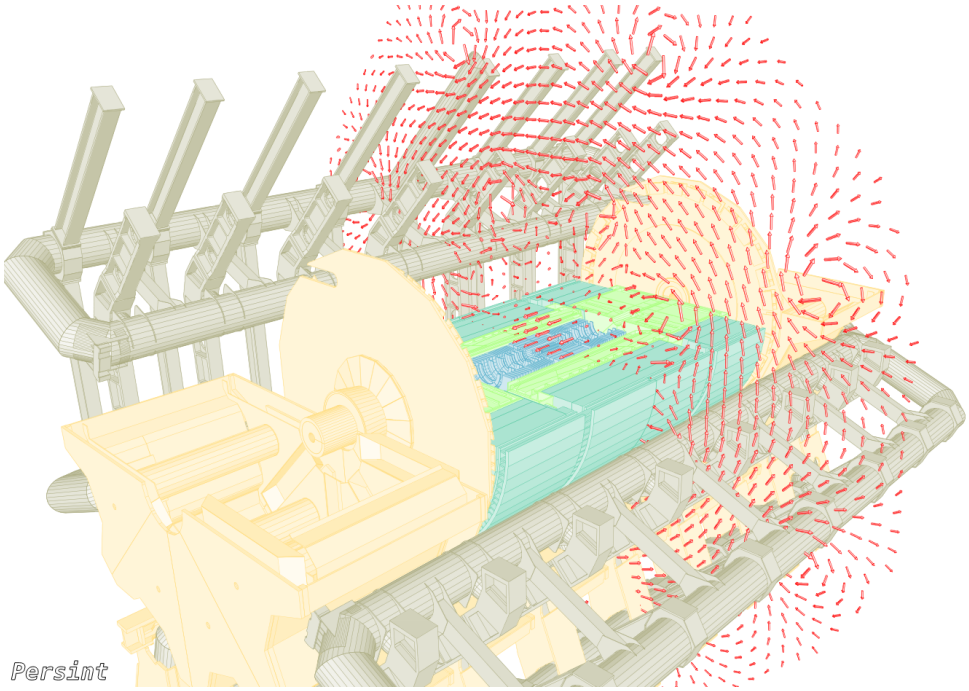

Figure 4.3: Persint [41] visualization of the ATLAS magnetic field — $z = 0$ plane.

The field is not ideal due to a non-perfect placement of magnets and the real coil geometry, and the field map accounts for that. Also, the solenoid axis is tilted ($\theta_x = -0.1\,\text{mrad}$, $\theta_y = 0.2\,\text{mrad}$) and shifted ($\Delta x = 0.3\,\text{mm}$, $\Delta y = -2.4\,\text{mm}$, $\Delta z = 0.5\,\text{mm}$) with respect to the axis of the circulating beams (the LHC coordinate system) [42].

4.2.2 Effect of the field on proton propagation

To see the effect of the real field of ATLAS (as is described by the field map), I simulated a special case of elastic sample — protons were generated with the constant energy of 3.5 TeV, the φ angle uniformly distributed from 0 to 2π and the pseudorapidity η in range 8 to 17 with a constant step in the θ angle. Such protons form ellipses in the perpendicular plane as they fly away from the IP. I ran a simulation using `ForwardSimulation` package, once with the magnetic field in ATLAS switched on and once with the field off. When small amount of protons (20 per each η value) is selected, it is possible to visualize how protons with different φ propagate with and without the presence of the magnetic field. For the study, the 3.5 TeV $\beta^* = 90$ m optics was used.

4.2.2.1 End of cavern

First, I have recorded positions of the protons as they leave the ATLAS cavern, i.e. at 22.5 m from the IP. Visualization of selected protons is in Fig. 4.4. The recorded positions of the two simulation outputs (one with the field on, one with the field off) are overlaid. Since the nominal proton (i.e. the proton leaving the IP with nominal energy and zero deflection) was also affected by the field, the position of the nominal proton was subtracted in case of simulation with the field on, such that the shown positions are plotted in the reference frame of the nominal beam (the nominal beam offset is corrected for by the alignment procedure of the ALFA detectors).

There are visible differences between the field on and the field off case. The differences are not caused by a simple rotation around the beam axis, as one would get for a solenoid field with the axis parallel with the beam axis. Also, the differences are asymmetric, as can be seen, for example, from the points in circles.

Histograms with the position differences for the full sample of 10 thousand events are plotted in Fig. 4.5. The differences are of the order of few microns here, however, this is for the end of cavern positions, i.e. very close to the IP.

4.2.2.2 ALFA position

Since the differences in proton positions with and without central magnetic field were very small at the end of the ATLAS cavern, it was interesting to see how this changes at the position of ALFA detectors, i.e. 237 m from the IP. Parameters

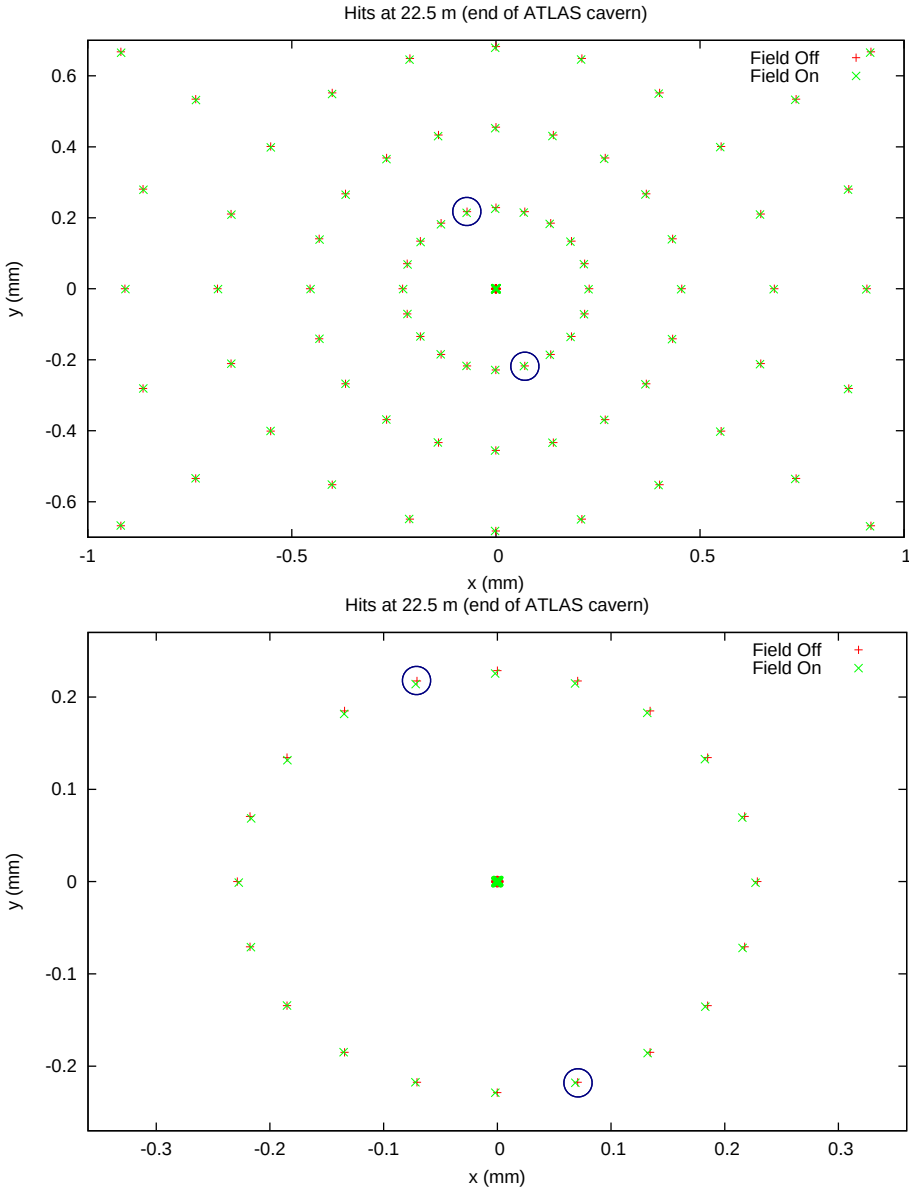

Figure 4.4: Transported protons of beam 1 at the end of cavern, for the magnetic field of ATLAS switched on (green) and for the field off (red). The bottom picture is the zoomed in central part of the upper picture. Two points are circled to provide a reference.

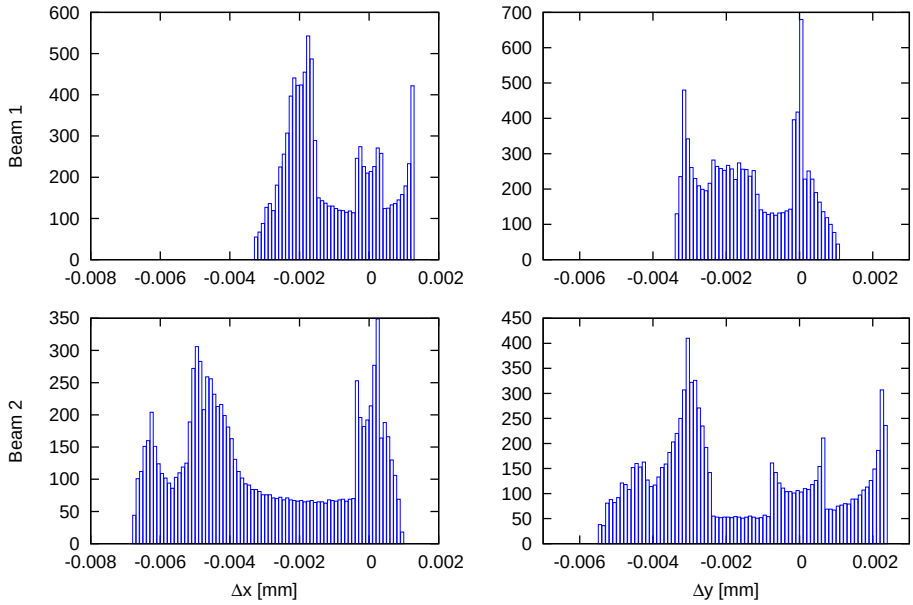

Figure 4.5: Differences of proton positions at the end of cavern for the magnetic field of ATLAS switched on and for the field off.

of the simulation were the same as in the previous subsection, only the proton positions were recorded at 237 m from the IP.

Visualization of the same selection of protons as before is in Fig. 4.6. The observed behavior is very similar to the case of the end of ATLAS cavern, however, the scale is now much larger in the y coordinate.

To see the magnitude of the effect, I plot the histograms of the position differences in Fig. 4.7. It is visible, that the difference in x coordinate is still of the order of microns, but the y coordinate differs by tens of microns.

4.2.3 Effect on reconstructed tracks in ALFA

In the previous section, the effect of the ATLAS magnetic field on forward protons was shown using artificially generated events. Here I present results of a more realistic case — I generated elastically scattered protons and ran the simulation including also the ALFA detectors.

For this simulation, I generated 100 thousand elastic protons. I set the total cross section $\sigma_{\text{tot}} = 95\,\text{mb}$ and the nuclear slope $B = 20\,\text{GeV}^{-2}$.

This time, the `ForwardTransport` was used to transport the protons from the end of ATLAS cavern to the position before the ALFA stations. In addition, the physics list was purged, so that only hadronic ionization was being simulated, to minimize random smearing. The ionization was required so that there would be an energy deposition in ALFA detector fibers and a track reconstructed.

Again, two simulations were run to produce two MC samples — one with the field in the central region switched off and the second with the field on (using again the field map tagged as "BFieldMap-FullAsym-09-solTil3").

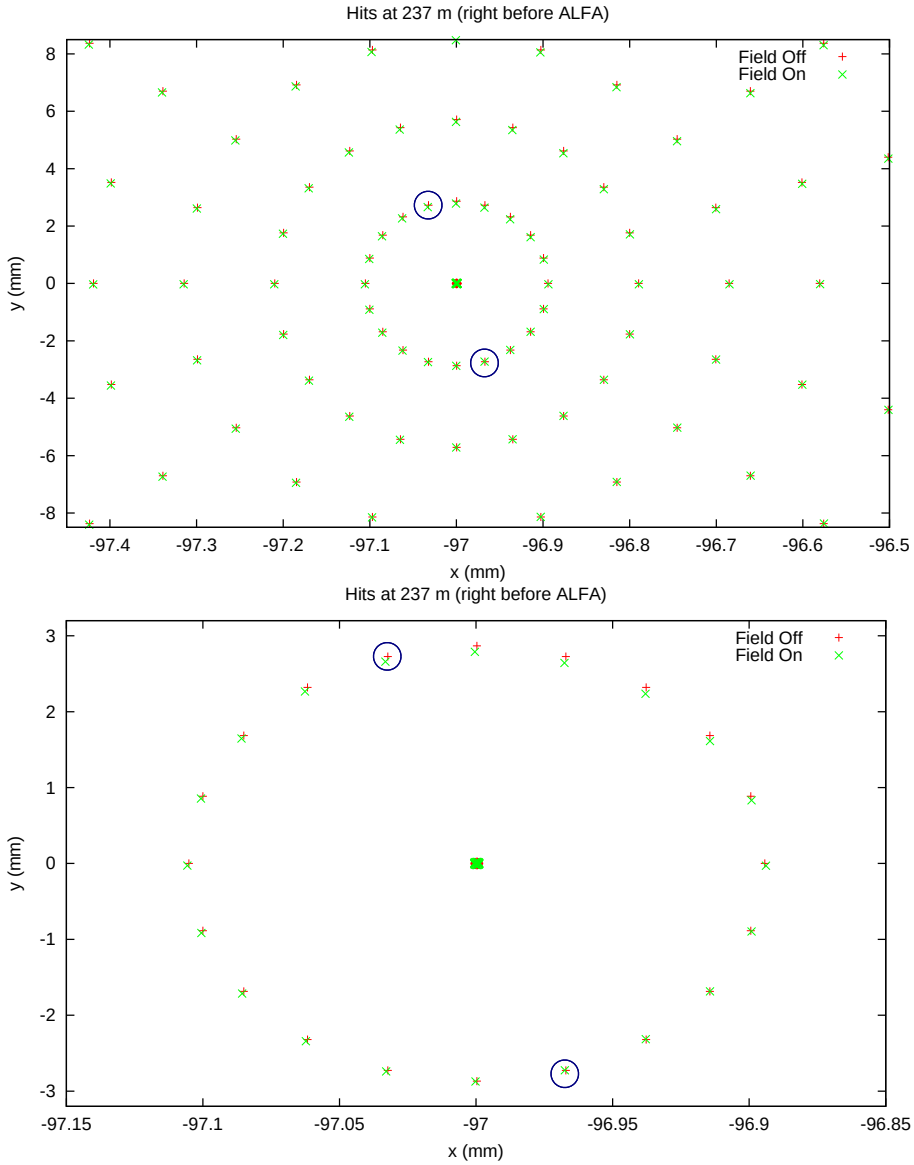

Figure 4.6: Transported protons at the 237 m from the IP, beam1 for the magnetic field of ATLAS switched on (green) and for the field off (red). The bottom picture is the zoomed in central part of the upper picture. Two points are circled to provide a reference.

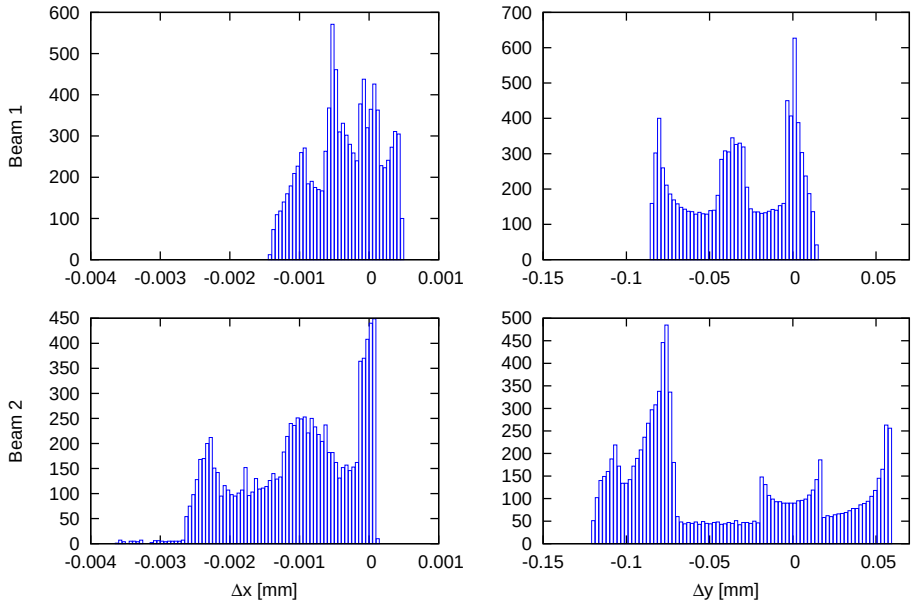

Figure 4.7: Differences of proton positions at the 237 m from the IP for the magnetic field of ATLAS switched on and for the field off.

Both samples were pre-processed, as much as possible, in the same way as the data from 191373 run [P4]. The bunch crossing identification, good lumiblocks selection and L1 triggering on elastic arms were removed since these criteria only apply to data and the generated events contain only elastic protons.

The pre-processing chain is shown in Fig. 4.8. The good luminosity selection was skipped, as already mentioned. The distance measurement was replaced by taking the distances of the detectors, as were set in the simulation. Remaining steps — alignment, selection of best tracks and edge fitting — were done separately for the sample with the field on and the sample with the field off.

4.2.3.1 Alignment

ALFA detectors are moving in the vertical direction w.r.t. the beam and operate close to the beam only for periods of data taking in special runs. A mapping between the local coordinate system of the detectors and the global beam coordinate system needs to be found for each ALFA run. The distance from the IP is fixed, but a vertical and a horizontal offset, as well as a rotation of each station needs to be determined.

For the study of the B field influence, the alignment was done using the same procedure as for the analysis of 191373 run [P4]. First, the horizontal offset was calculated, which provides horizontal offset and rotation angle of each detector based on the profile of the hit pattern in each detector. Second, the vertical alignment was done and vertical offset was obtained. The vertical alignment utilizes symmetry of the hit pattern of elastic protons with respect to the beam center. Finally, the alignment optimization was run, which yields corrected dis-

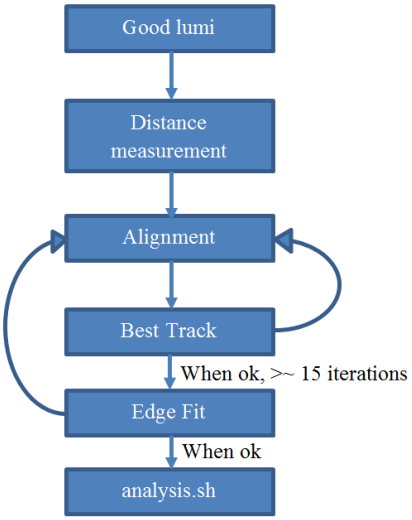

Figure 4.8: ALFA chain block diagram.

tances and vertical offsets. One station is selected as the reference, for which the distance is fixed and the other distances and offsets are optimized using recorded tracks. The offsets, angle and distance are schematically drawn in Fig. 4.9.

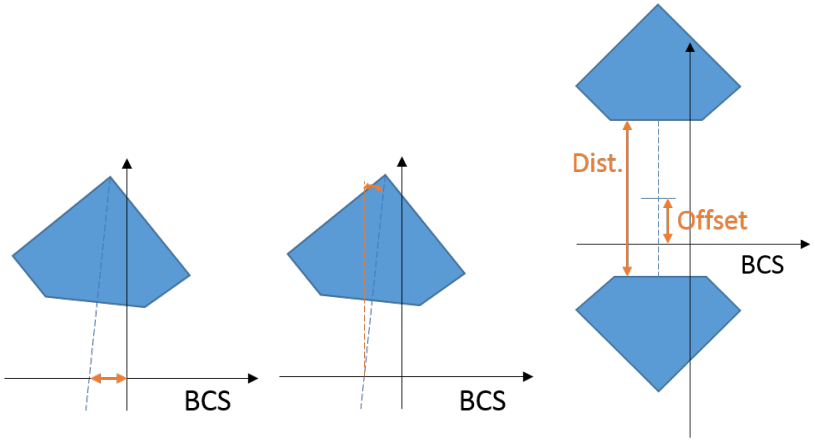

Figure 4.9: Alignment illustration. Left to right: horizontal offset, rotation angle, vertical distance and offset.

After the complete alignment was calculated, the best track algorithm was run. The algorithm goes through the events with multiple reconstructed tracks in an ALFA detector and selects the track that matches the best the tracks in the other detectors in one arm.

With the selected best tracks, the alignment is rerun. The best track algorithm is then repeated, the alignment is rerun and so on until the alignment parameters converge. Then, the edge fitting procedure is applied to get more precise selection criteria for events within detectors acceptance. After the edges are found, several iterations of the alignment and the best track selection are

Table 4.1: Results of horizontal alignment showing offset in mm for both samples. MC truth column contains offsets that were set in both simulations.

Detector	MC Truth	Field On	Field Off
B7L1U	0.326	0.318	0.318
B7L1L	-0.366	-0.363	-0.363
A7L1U	0.629	0.622	0.622
A7L1L	0.373	0.376	0.376
A7R1U	0.263	0.261	0.258
A7R1L	0.392	0.399	0.396
B7R1U	0.414	0.411	0.407
B7R1L	0.493	0.498	0.494

Table 4.2: Results of horizontal alignment showing rotation angle in rad for both samples. MC truth column contains angles that were set in both simulations.

Detector	MC Truth	Field On	Field Off
B7L1U	0.0051	0.00484	0.00480
B7L1L	0.0004	0.00062	0.00039
A7L1U	0.0029	0.00271	0.00270
A7L1L	0.0017	0.00202	0.00188
A7R1U	0.0004	0.00029	0.00049
A7R1L	-0.0001	0.00075	0.00067
B7R1U	0.0036	0.00374	0.00394
B7R1L	-0.002	-0.00191	-0.00196

Table 4.3: Results of vertical alignment showing optimized distance in mm for both samples. MC truth column contains distances that were set in both simulations. The reference station is underlined.

Detector	MC Truth	Field On	Field Off
B7L1	11.922	11.889	11.889
A7L1	12.430	12.430	12.430
A7R1	12.308	12.321	12.283
B7R1	11.936	11.963	11.927

Table 4.4: Results of vertical alignment showing offset in mm for both samples. MC truth column contains offsets that were set in both simulations. The reference station is underlined.

Detector	MC Truth	Field On	Field Off
B7L1	0.098	0.108	0.050
A7L1	0.007	0.066	0.006
A7R1	0.012	0.019	0.055
B7R1	0.057	0.049	0.083

repeated. For the Monte Carlo samples, only 3 iterations were needed. The final values for each sample are compared with the simulation input in Tab. 4.1–4.4.

4.2.3.2 Comparison of hits distributions

To estimate the effect of the central detector field on ALFA, I first compared distributions of hits positions. Output files from the simulation contained reconstructed positions of hits for all ALFA detectors (the 8 pots) in their local coordinate system. I calculated the hits positions in the beam coordinate system using the obtained alignment parameters. As I obtained different alignment parameters for the two samples (with and without magnetic field of the central detector), I applied the alignment separately for the two samples.

I selected events that contained reconstructed hits for all detectors belonging to one of the two elastic arms (the so-called 4/4 selection, i.e. all detectors in pots 0, 2, 5 and 7 or all detectors in pots 1, 3, 4 and 6). Hits selected by the best track algorithm were further considered in the events that passed the 4/4 selection. Events then had to pass cuts selecting hits lying at least 60 µm above the detector edge (removing fake hits) and at least 1 mm below the so-called beam screen edge (the shadow of the Q6 quadrupole aperture, therefore removing the showers from the magnet aperture).

The x and y hits distributions for all detectors are plotted in Figs. 4.10, 4.11. In y distribution, there is a visible bin migration. Apart from that, the distributions agree well.

4.2.3.3 Event-by-event comparison

Next, I compared reconstructed hit positions on an event-by-event basis. The alignment was applied in the same way as for the distributions comparison and also the selection criteria were the same with one addition — only events, where a hit was reconstructed for the both field on and field off case, were considered.

For each event, the difference between the hit position in the field on and the field off sample is plotted ($\Delta x = x_{\text{fieldOff}} - x_{\text{fieldOn}}$, $\Delta y = y_{\text{fieldOff}} - y_{\text{fieldOn}}$) in Fig. 4.12 and 4.13. The figures show rather large difference — in order of tens of microns.

The shapes of the difference distributions are coming from the placement of the fibers in ALFA detectors as is illustrated in Fig. 4.14. When the fibers were placed ideally in the model (all the fibers in one plane parallel with each other, same offset between neighboring fibers), the difference distribution was close to expected Gaussian, except it contained only certain discrete values. With the realistic fibers placement (based on measured fibers slope and offset), the differences were smeared in a non-trivial way.

To better understand why there were quite large differences in the event-by-event comparison while the distributions agree rather well, I have plotted positions of hits without a counterpart in the other sample in Fig. 4.15. There is a visible shift of hits in one sample with respect to the other in the y direction.

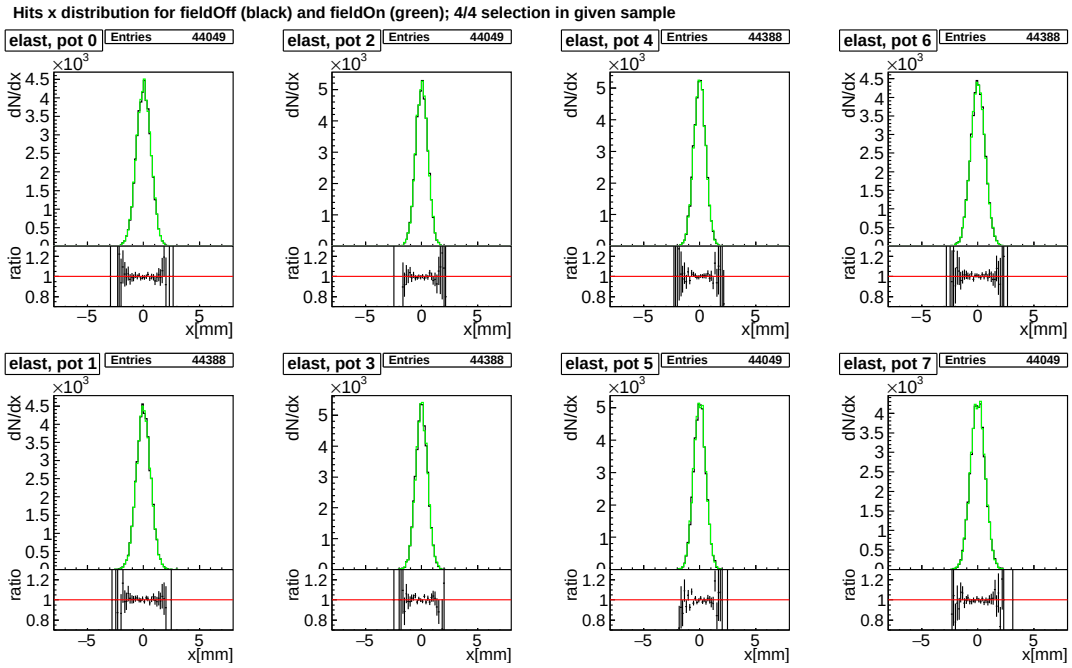

Figure 4.10: Comparison of x distributions of hits passing selection criteria for the sample with the field off (black) and on (green). Bottom graph under each histogram plots ratio in a given bin (excluding empty bins).

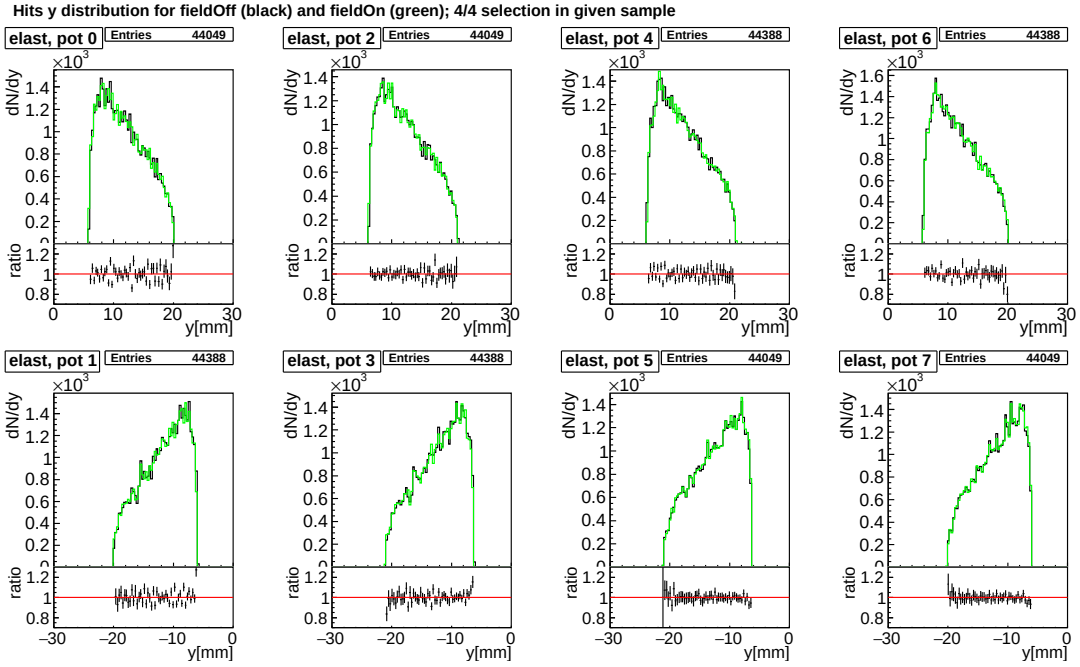

Figure 4.11: Comparison of y distributions of hits passing selection criteria for the sample with the field off (black) and on (green). Bottom graph under each histogram plots ratio in a given bin (excluding empty bins).

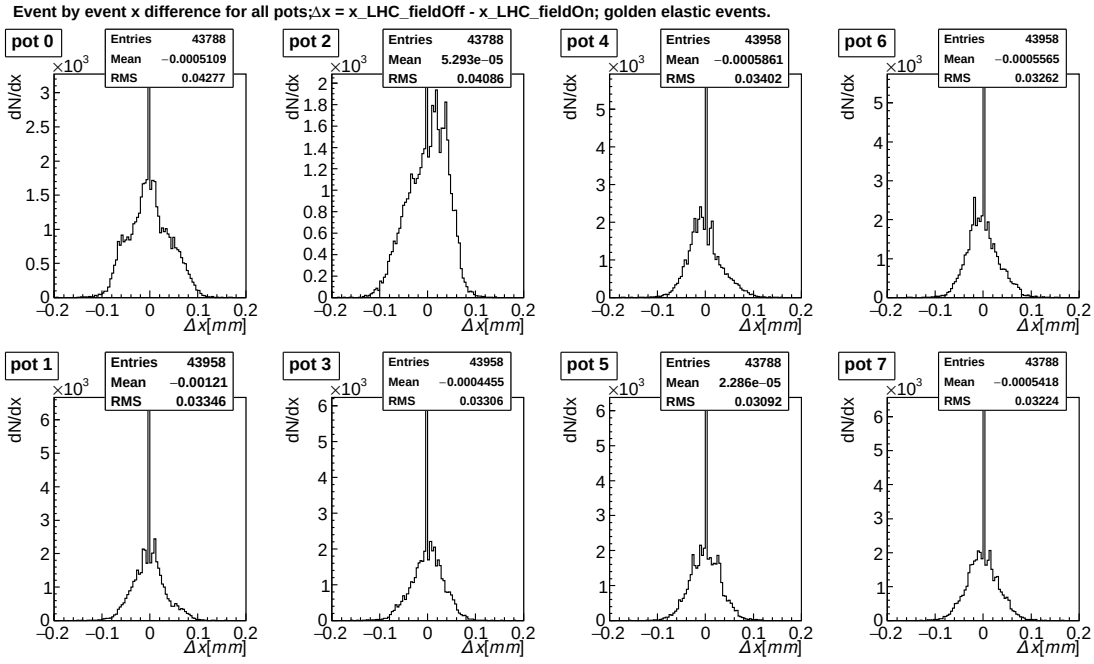

Figure 4.12: Event-by-event comparison — the difference between hit position in the field on and the field off sample ($\Delta x = x_{\text{fieldOff}} - x_{\text{fieldOn}}$).

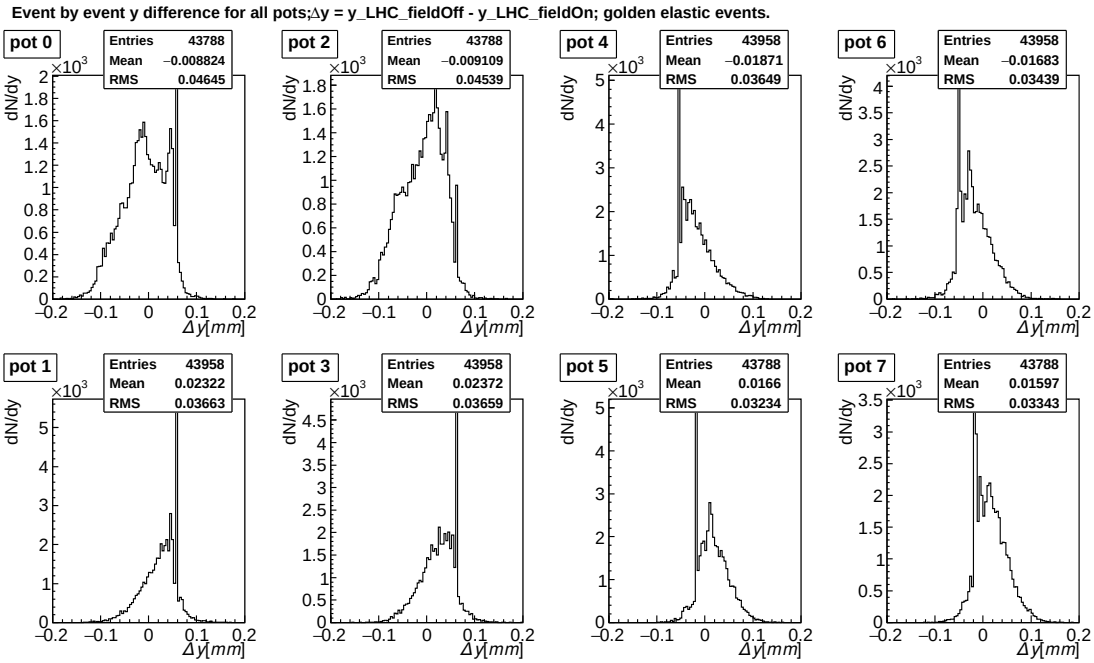

Figure 4.13: Event-by-event comparison — the difference between hit position in the field on and the field off sample ($\Delta y = y_{\text{fieldOff}} - y_{\text{fieldOn}}$).

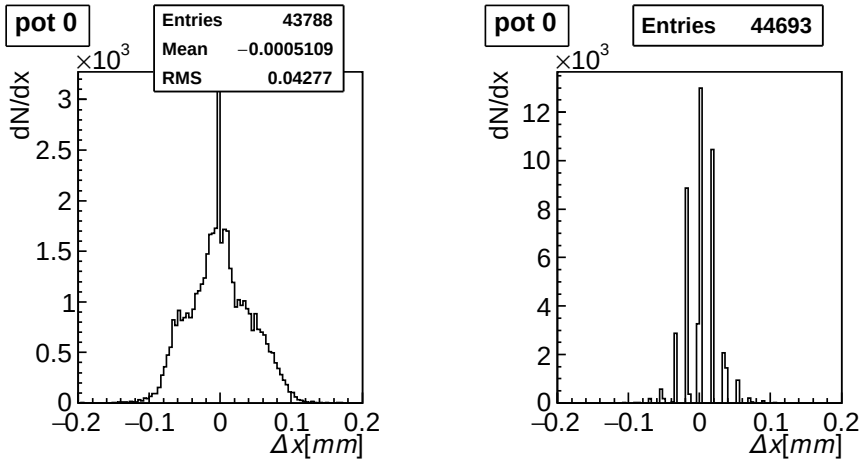

real geometry **ideal geometry**

Figure 4.14: Event-by-event x difference for the pot 0 with the real fiber placement (left) and the ideal fiber placement (right).

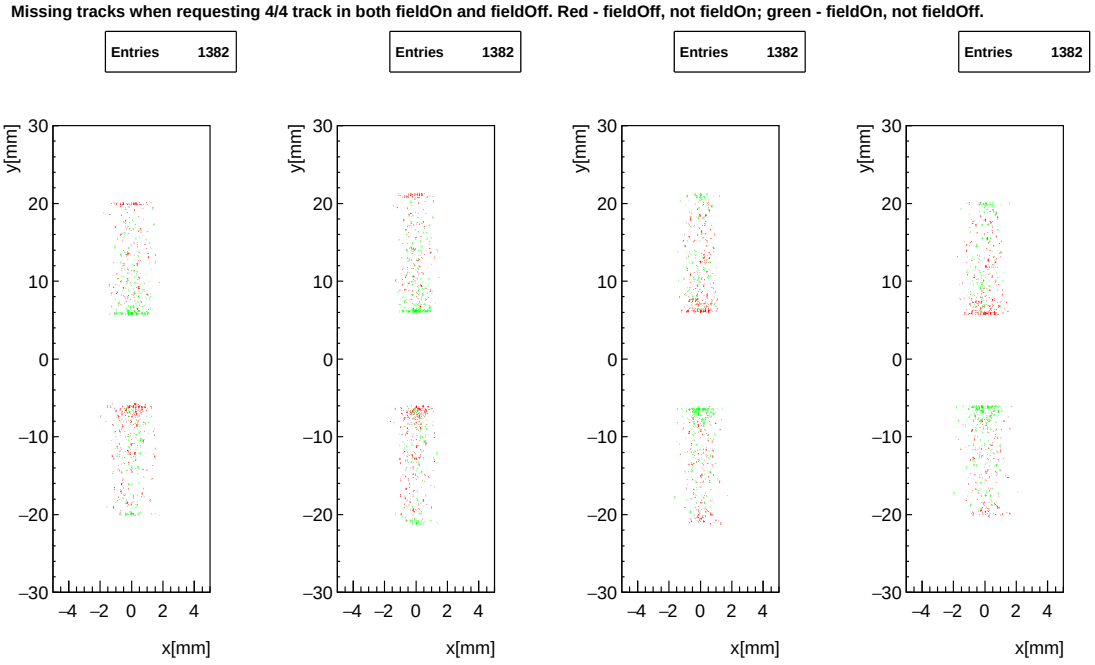

Figure 4.15: Positions of hits in events with a 4/4 track in the field off sample, but no 4/4 track in the field on sample (red), and in events with a 4/4 track in the field on sample, but no 4/4 track in the field ff sample (green).

The shift goes in the opposite direction on the left side than on the right side from the IP for a given sample. The hits shown in Fig. 4.15 are not included in the event-by-event difference (since one of the samples is missing a 4/4 track in a given event), but they are filled in the hits distributions.

4.2.3.4 Non-corrected t distribution

Finally, I have compared also the reconstructed t values without applying further corrections (acceptance, unfolding). The result for the subtraction method is in Fig. 4.16. The results show a rather good agreement of distribution and 3 % difference on the event-by-event basis, which is on the level of precision of the method for ALFA detectors.

Figure 4.17 shows the comparison of migration between MC truth and reconstructed t values for the two samples.

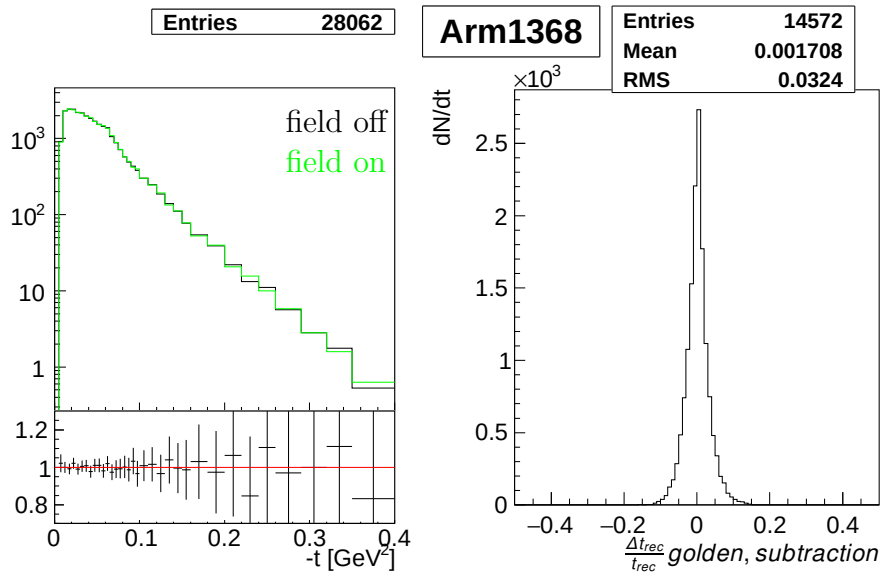

Figure 4.16: Raw t comparison. Left: reconstructed t spectrum for both samples without corrections. Right: event-by-event comparison of the reconstructed t values.

4.2.3.5 t distribution from the truth information

From the results in Fig. 4.16, 4.17, it is unclear, whether the observed difference is originating entirely from the reconstruction precision (and is therefore already included in systematic error estimation) or if it is largely coming from the field effect. To answer this, I looked at how the t distribution reconstructed from the true transported proton positions before the first ALFA station looks like. I compared the t distributions obtained this way for the sample with the field off and for the sample with the field on.

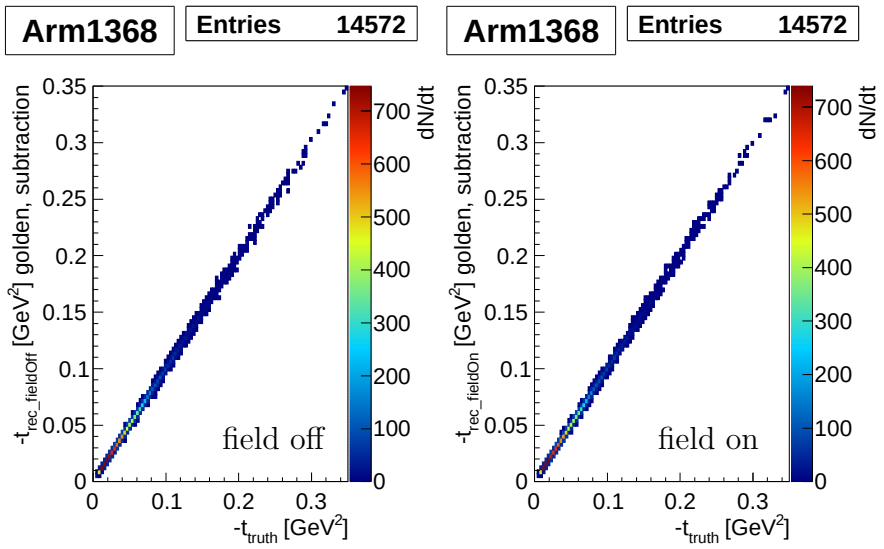

Figure 4.17: Migration between the true (generated) t values and the values reconstructed by the ALFA detectors for the two samples with the field off and on.

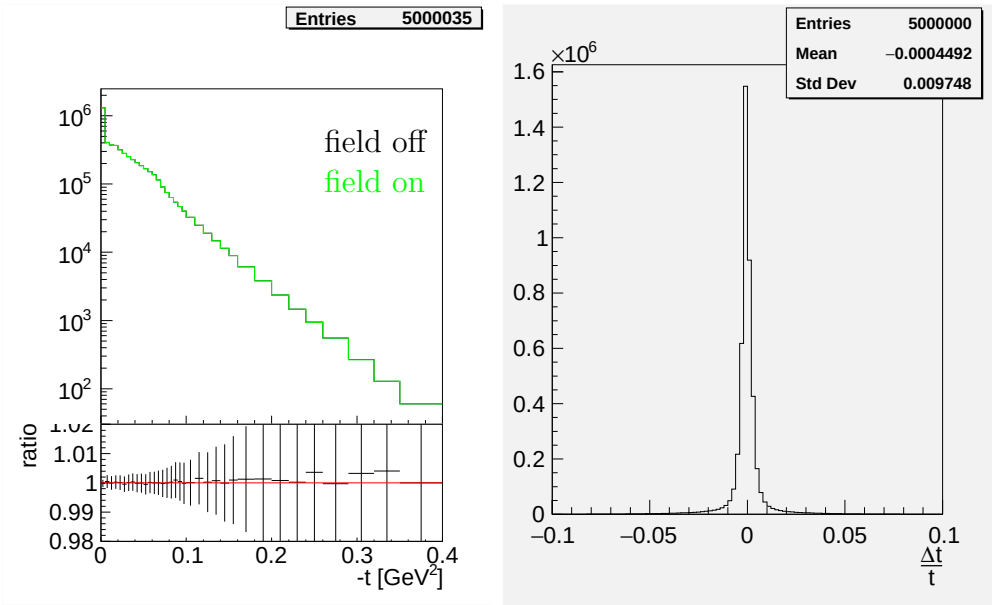

Figure 4.18: Raw t spectrum reconstructed from the true positions of transported protons. Left: reconstructed t spectrum for both samples without corrections; ratio subplot has now smaller scale. Right: event-by-event comparison of the reconstructed t

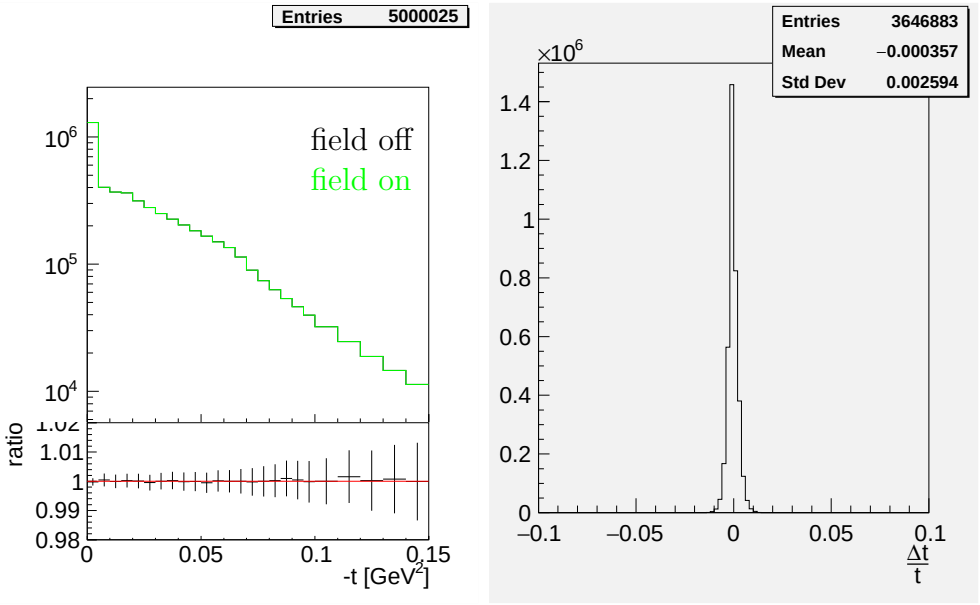

Figure 4.19: Raw t spectrum reconstructed from the true positions of transported protons in the range ALFA uses for fitting. Left: reconstructed t spectrum for both samples without corrections. Right: event-by-event comparison of the reconstructed t for $-t \in [0.05, 0.15)$ GeV^2.

The result is in Fig. 4.18. The distributions agree very well and there is 1 % difference on event-by-event basis. Event-by-event comparison, however, show a rather large tails and it turns out that they are caused by very small t values, where the numerical precision of the division dominates. Therefore, I have considered values of $-t > 0.05$ GeV^2. To better describe the effect on ALFA measurement, I have also limited $-t < 0.15$ GeV^2 to consider only the range of values that was used by ALFA for fitting of the corrected distribution and obtaining total cross section measurement. The result of the comparison after the cuts is shown in Fig. 4.19. The event-by-event comparison now agrees within 0.3 %.

4.2.4 Comparison to data

The next step was to compare the simulation with the real data. To study the effect of the field on the ALFA reconstructed events, I took x and y hits distributions from the data from the 191373 run used for the published measurement of the total cross section at $\sqrt{s} = 7$ TeV [P4, P5]. Histograms of these distributions for each of the ALFA detectors were then compared to two simulation samples (one with the magnetic field of the central detector switched on, the other with the field off) using the same binning and normalization factor such that I obtain the same integral of a given histogram.

To compare the simulation to the data, more events needed to be simulated and simulation input parameters were set such that they correspond to the measured values in the data. For this simulation, I generated 5 million elastic protons. I set the total cross section $\sigma_{\text{tot}} = 95.35\,\text{mb}$ and the nuclear slope $B = 19.73\,\text{GeV}^{-2}$.

The `ForwardTransport` was used to transport the protons from the end of the ATLAS cavern to the position before the ALFA stations. This time, the full physics list was used for simulation of the ALFA stations to describe the data.

Again, two simulations were run to produce two MC samples — one with the field in the central region switched off and the second with the field on (using again the field map tagged as "BFieldMap-FullAsym-09-solTil3").

Both samples were pre-processed, as much as possible, in the same way as the data from 191373 run.

Before I show the results of the comparison, I need to address few issues, that were observed.

4.2.4.1 Beam screen edge

When I applied the so-called beam screen edge cut, that is supposed to remove the showers from the Q6 magnet aperture in data, I have observed that the position of the edge was different for the data and MC samples, as illustrated in Fig. 4.20. Though in the MC samples, the showers from the Q6 magnet beam screens were not present because of the use of the `ForwardTransport` package, shadow of the beam screens was still present and could have been, therefore, fitted. The shadow is visualized in Fig. 4.21 using the EasyTracker [43] program.

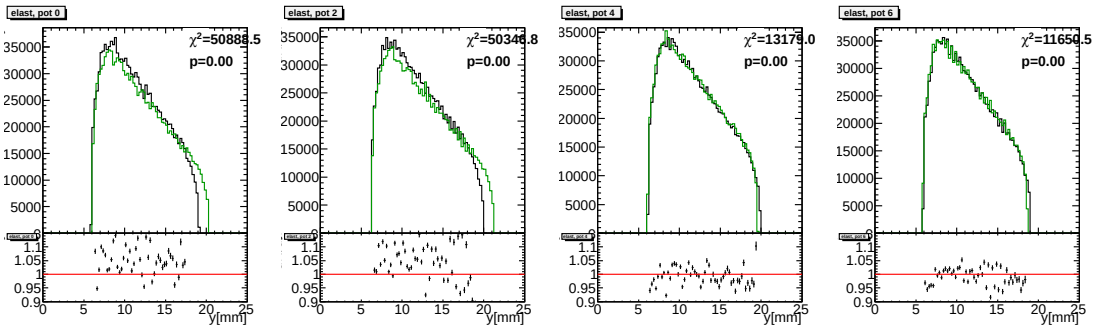

Figure 4.20: Illustration of the beam screen edge effect – the edge fitting procedure returns 1 mm different beam screen edge position (which is used to cut the y distribution) for data (green) and MC sample (black) in detectors on the left side.

As it turned out, the different beam screen edge position can be explained by a misalignment of the Q6 magnet. Indeed the alignment survey file of magnets in LSS1 from Dominique Missiaen confirmed that the Q6 beam screens are mis-

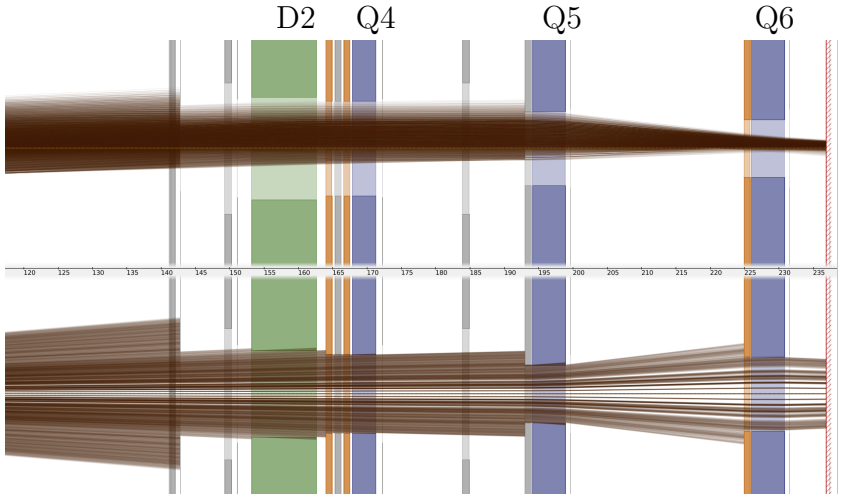

Figure 4.21: EasyTracker [43] visualization of the Q6 beam screen edge. Top: horizontal projection, bottom: vertical projection.

aligned in vertical direction. The misalignment is 1.08 to 1.65 mm, which agrees very well with the observed difference.

To solve this difference, I applied the beam screen edge values obtained from the data also on the MC samples. Since the distributions were cut 1 mm from the edge and the MC samples did not contain showers from the beam screens, it was possible to safely use also hits closer than 1 mm to the beam screen edge shadow in the MC samples.

4.2.4.2 B-slope effect

The nuclear slope, or B-slope, affects the shape of the pattern in ALFA detectors and therefore the width of the distributions of the basic variables — x, y, θ_x, θ_y.

In the first samples I produced to compare with the data, I have set B-slope parameter value to 20 GeV^{-2}. To check the effect of the nuclear slope, I have then re-weighted the sample to correspond to B = 19.5 GeV^{-2} and B = 19.73 GeV^{-2}. Result for the x distribution of hits in pot 0 is shown in Fig. 4.22. It is visible that for B = 20 GeV^{-2} the ratio of the distributions is clearly banana shaped as the MC distribution is narrower than the data one. The ratio straightens as the B-slope value lowers. Here, the value of 19.5 GeV^{-2} seems as the best one, however, it is not only the B-slope that affects the width of the distributions, but there can be also contribution of different resolution of the ALFA detectors in the simulation or a misalignment. Therefore, the measured value of 19.73 GeV^{-2} was used for the final produced samples to be compared with the data.

4.2.4.3 Comparison of hits distributions

Result of the comparison of the MC samples to data for the first detector is shown in Fig. 4.23 . Visually the agreement is rather satisfactory, however this does not allow to tell whether the data agrees better with the field on or the field

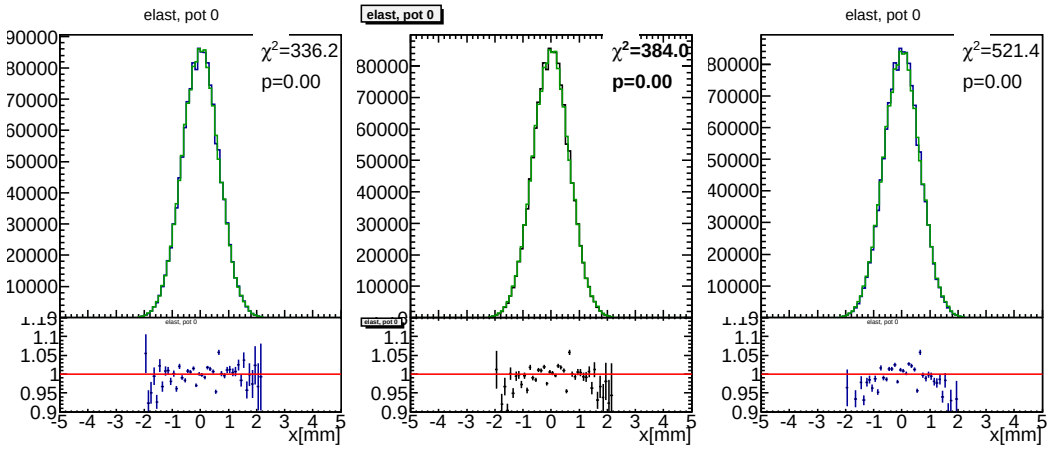

B = **19.5** GeV^{-2}, **19.73** GeV^{-2}, **20** GeV^{-2}

Figure 4.22: Effect of the B slope on the x distribution of hits in ALFA pot 0 in the MC sample (black) compared to the data sample (green). The bottom part of each histogram shows ratio of the counts in each bin for MC over data.

off sample. Also the ratios of histograms show very similar behavior for both samples. There is a visible migration between bins in both samples with respect to data, especially for the y distribution.

To say, which sample is describing the data better, I applied the χ^2 test and relevant values are shown in Fig. 4.23. However, from the χ^2 values, it can only be concluded that the simulation does not describe the data well enough.

4.2.4.4 Detector resolution

I compared the resolutions of the ALFA detectors in the simulation with the values obtained for the 191373 data, as a possible source of discrepancy. For the simulation, I used two methods — first, a difference between the position measured in the outer station and the projection of the position from the inner to the outer station (the same method as used for the data [P4]), and second, resolutions of individual detectors were obtained using the truth information about the hit positions and then quadratically added to compare with the convolved resolution of the inner and outer detector. The results are in Tab. 4.5. The results using the first method are labeled MC1 and the second MC2.

The two methods for determining the resolution in the simulation agree well and also there is no significant difference between the two samples (field on and off). There is a considerable difference between the simulation and the data, though.

4.2.5 Summary

The presented study aimed to evaluate the effect of the magnetic field of the inner detector and muon system of the ATLAS experiment on measurement of

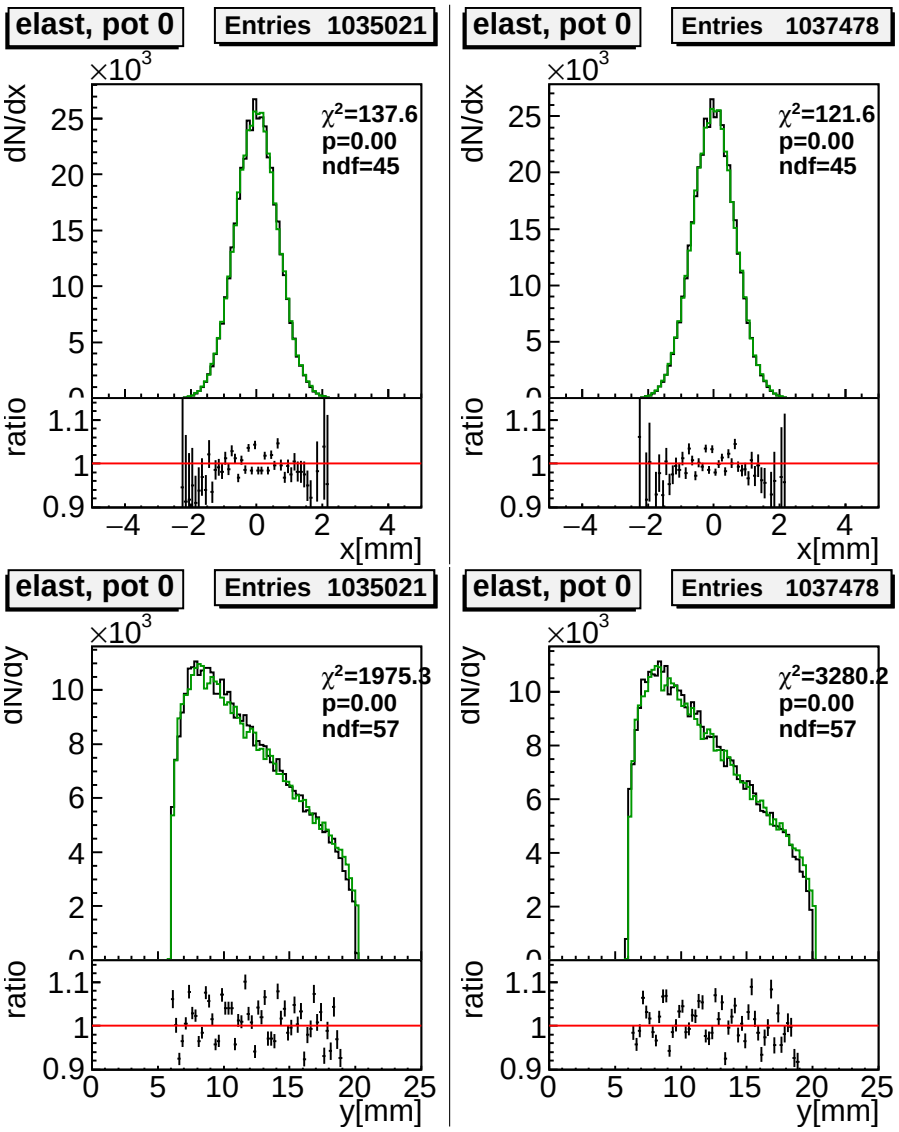

Figure 4.23: Comparison of the MC and the 191373 data distributions. Upper row: x distributions; lower row: y distributions. Left column: MC sample with the field off; right column: MC sample with the field on. Black: MC; green: data.

Table 4.5: Comparison of resolutions of the ALFA detectors in the simulation and in the data.

		MC Field off		MC Field on	
Armlet	Data	MC 1	MC2	MC1	MC2
ALFA1-ALFA3	43	42.0	42.2	42.0	42.4
ALFA2-ALFA4	41	39.0	38.8	39.0	38.9
ALFA7-ALFA5	41	39.1	39.1	39.2	39.1
ALFA8-ALFA6	39	35.1	35.0	35.2	35.0

the ALFA detector. The study utilized the ATLAS simulation framework to assess the field influence.

First, a simple study was done using protons transported from the IP to the end of the ATLAS cavern and to the position of ALFA stations. It showed that the field affects the nominal particles, which results in a shift of order of tens of microns in y direction at the ALFA position. Also a spread in positions was observed of up to 50 microns in the y direction.

After the initial study, I produced MC samples better corresponding to the real ALFA data, including the ALFA detectors, and I processed the samples, as much as possible, in the same way as the data from 191373 run. One sample included the central field while the second did not. I have then compared the obtained reconstructed positions of tracks in the detectors. Here, the comparison of distributions showed a very small difference between the samples, however, comparison on event-by-event basis resulted in 30 to 45 microns RMS difference. To show, what this means for the ALFA measurement, I have also compared t distributions reconstructed by the subtraction method. Again, the distributions were very much compatible and the event-by-event comparison showed 3 % difference. This value, however, contains also the precision of the reconstruction. Therefore, I have also compared the t values reconstructed by the subtraction method from the true positions of tracks, from which I conclude that the effect of the field on the t measurement of elastic protons is 0.3 %.

To support the simulation results I attempted to compare the simulation samples and the 191373 run data. Visual distribution agreement is good, but χ^2 tests showed that both samples are not describing the data well enough to draw conclusions about a sample being closer to the data. A discrepancy was found in the resolution of detectors, suggesting that a finer description of the detectors would be needed.

Chapter 5

AFP simulation

5.1 Effect of a tilted Hamburg beam pipe window

The Hamburg beam pipe was considered as a housing for AFP detectors. The initial design, illustrated in Fig. 1.12, offered rectangular detector pockets. Such solution presents a sharp step in aperture to the circulating beam, which leads to RF heating. Therefore, a modified Hamburg beam pipe with angled sides of the detector pockets tilted at the angle of 11° was proposed, as illustrated in Fig. 5.1.

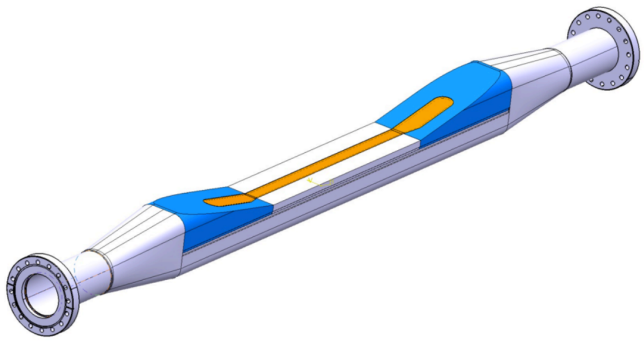

Figure 5.1: Modified Hamburg beam pipe design. The orange area marks the thinned steel window [44].

The tilted pocket wall significantly reduces the RF losses as was demonstrated in a simulation [44]. However, the material in the way of the measured diffractive protons is increased. I performed a set of simulations to evaluate the effect of the added material and hence the scattering of the diffractive protons.

The scattering was simulated under the Athena framework. The model of SiT tracker detectors was utilized, consisting at the time of 5 SiT planes each, with 40 µm thick Si sensor and 50 µm thick carbon support. The Hamburg beam pipe thinned window was represented by two thin steel plates (one before and

one after the SiT) — thicknesses of 0.3 mm and 0.4 mm were simulated. There were two sets of SiT detectors and thin steel plates in the simulation, placed 8 m apart. I produced a sample of 10^4 events for each of five angles of the detector pocket wall tilt in the range 11–90° (measured with respect to the beam axis z). Each event initiated with a 6 TeV proton propagating in the z direction. For the evaluation of the scattering, only transport, multiple scattering and hadronic ionization (needed to register proton hits in the SiT planes) were simulated. The resulting θ distribution and the development of the mean θ value are plotted in Fig. 5.2.

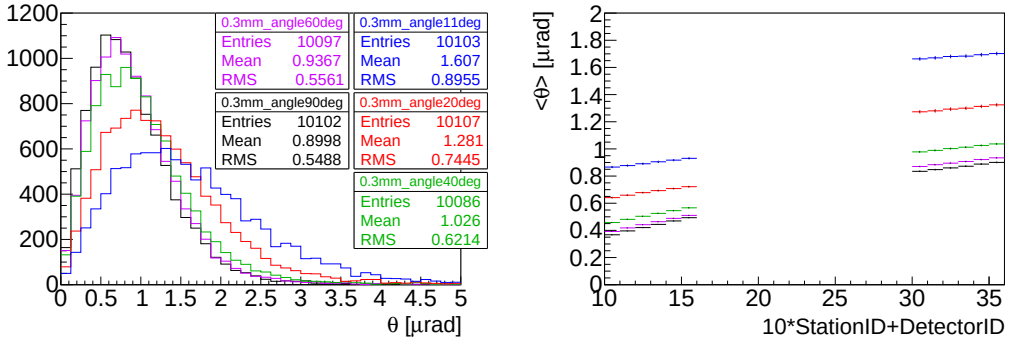

Figure 5.2: Scattering angle distributions after the last SiT plane (*left*) and the development of the mean scattering angle at individual SiT planes (*right*) for 0.3 mm thick window tilted at angles 11–90°.

It is visible that the scattering angle increases with the decreasing value of the tilt angle, as expected, since the more the plate is tilted, the more material is traversed by a proton. Also the right part of the figure shows the steady increase of the scattering angle within each SiT assembly and much more pronounced step at the steel plates. The mean value of the scattering angle is evaluated for the two thicknesses and for all the angles in Tab. 5.1.

Table 5.1: Mean scattering angle $\langle\theta\rangle$ after the last SiT plane for 0.3 mm and 0.4 mm thick window tilted at angles 11–90°.

	$\langle\theta\rangle$ [μm] for thickness	
Tilt angle [°]	0.3 mm	0.4 mm
11	1.61	1.81
20	1.28	1.43
40	1.03	1.12
60	0.94	1.01
90	0.90	0.96

The added material also increases probability that a hadronic shower develops within the set of detectors in an event. To evaluate how the fraction of events depends on the steel plate tilt, I have rerun the simulation with the default

Geant4 physics list enabled and calculated the amount of shower events in each case. The result is shown in Fig. 5.3. The fraction is almost doubled comparing the 90° case to the 11° case with the results of the later being 2.6 % for the 0.3 mm steel and 5.6 % for the 0.4 mm steel.

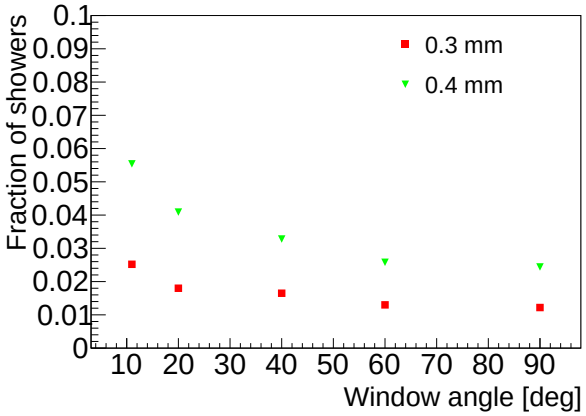

Figure 5.3: Fraction of events with showers as a function of the window tilt angle.

Part III

Development of the AFP time-of-flight detector

Chapter 6

AFP ToF detector

A good pileup rejection significantly improves ability of the AFP to provide precision measurements for studies of processes described in Sections 2.3 and 2.4. A central diffraction event, like a central exclusive production or a double pomeron exchange, can be mimicked by e.g. two single diffractive interactions occurring simultaneously due to pileup, as illustrated in Fig. 6.1.

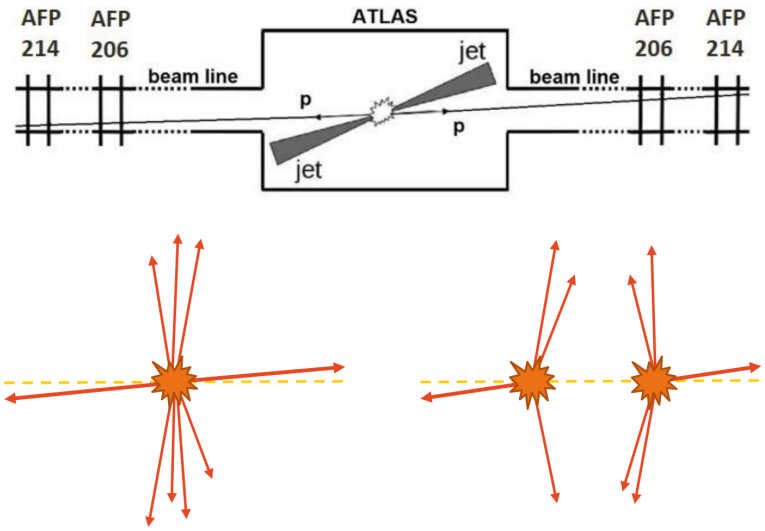

Figure 6.1: Illustration of a central diffraction event and two single diffraction events producing the same signature in AFP.

The two cases — a CD event and two SD events — can be distinguished using the z position of the vertex from which the protons originated. Primary vertices of particles with tracks in ATLAS are reconstructed using the inner tracker. As for the protons, it is possible to determine a difference in time-of-flight of the two protons Δt using the time-of-flight system installed in the AFP far stations. The protons travel at velocity unmeasurably smaller than the speed of light, therefore, the z position of the vertex can be calculated as $z_{\mathrm{ToF}} = \frac{1}{2}c\Delta t$ and pileup background can be suppressed by matching z_{ToF} to the z positions of vertices reconstructed by the inner tracker.

There were two ToF detectors being developed for use in the Hamburg beam pipe — QUARTIC (QUARtz TIming Cherenkov) [11] and GasToF (Gas Time-of-Flight) [45]. Both utilized MCP-PMT photodetector to detect Cherenkov photons produced by a proton, but used a different medium as the names suggest. GasToF used a gas container, while QUARTIC proposed 32 straight fused silica bars tilted at their Cherenkov angle per detector (two QUARTIC detectors are shown in blue in Fig. 1.12).

Roman pots provide limited space and the design of detectors needed to be modified to fit in. The ToF detector was based on QUARTIC with the straight bars replaced by L-shaped bars and original two-inch MCP-PMT by newly available one-inch MCP-PMT.

6.1 LQbars and Cherenkov light

L-shaped bars, called LQbars, were introduced to fit the ToF detector inside the Roman pot aiming to preserve advantages of QUARTIC, mainly the multiple measurements per proton and the compensation of time of flight for successive bars due to the tilt at the Cherenkov angle. LQbars were extensively simulated in Geant4 [27] and further optimizations were introduced that enabled to surpass QUARTIC design performance by 10–40 % [P3].

The AFP ToF is based on Cherenkov effect — a charged particle traversing a medium at a speed greater than the speed of light in the medium emits light [46]. The emitted light forms a cone with a specific angle between the direction of the particle and that of the emitted photon

$$\cos\theta_{\mathrm{C}} = \frac{1}{\beta n} \tag{6.1}$$

where β is the ratio of the particle velocity to the speed of light in vacuum and n is the refraction index of the medium.

The spectral intensity of the produced light is proportional to $\frac{1}{\lambda^2}$, where λ is the wavelength of the produced light, and further modified by transmission of the radiator material [47]. A prediction of light spectrum of an LQbar is plotted in Fig. 6.2b.

An LQbar is build from a radiator part and from a light guide part, as is illustrated in Fig. 6.3. The two parts are made of Suprasil (fused silica) glass glued together using Epotek 305 UV transparent epoxy glue [48]. Individual LQbars form 4×4 matrix that is held together with an MCP-PMT in an aluminum or plastic holder. It is customary in the AFP to call four consecutive bars in the proton direction a *train*. Trains are numbered from the bottom of the pot (top part in Fig. 6.3a) towards the MCP-PMT. Bars within one train are labeled A–D.

The radiator part is placed at the Cherenkov angle θ_{C} with respect to the incoming protons direction (Fig. 6.3b). The edge of the radiator is cut such that the edge is parallel with the protons, while the other end of the radiator towards

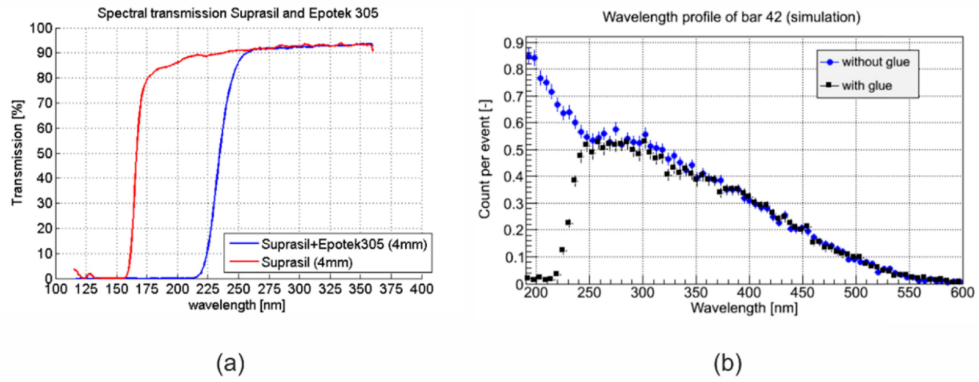

Figure 6.2: (a) Measured spectral transmissivity of Suprasil and Epotek 305 glue, (b) Light spectrum at the output of an LQbar (simulation) [P9].

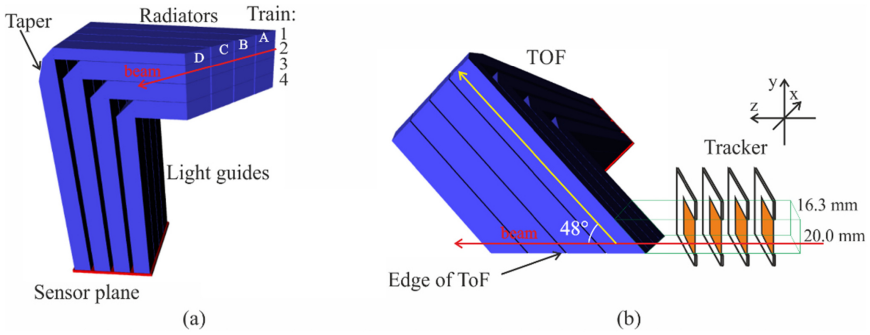

Figure 6.3: (a) Geometry of LQbars assembly in ToF, (b) LQbars with tracker planes (not in scale) [P14].

the light guide is cut at 45° in the perpendicular plane and the cut is coated with aluminum to reflect the photons from the radiator to the light guide. This is the only coated part of the LQbars, all the other faces are polished and the total reflection condition is met for the Cherenkov photons (the critical angle for transition from Suprasil to vacuum is approximately 45°).

The purpose of the radiator tilt at θ_C is to compensate the time of flight of a proton by the length of the radiator such that the direct photons arrive at the end of the light guide at the same time within one train, as illustrated in the left part of Fig. 6.4. The time of flight t_p of the highly relativistic proton between any two points along its path exactly compensates the additional time t_γ it takes a photon generated in the first point to reach the end of radiator compared to the photon generated in the second point, since (using Eq. 6.1)

$$t_p = \frac{l_p}{\beta c} = \frac{l_\gamma}{\beta c \cos\theta_C} = \frac{\beta n l_\gamma}{\beta c} = t_\gamma. \tag{6.2}$$

A different situation is depicted in the right part of Fig. 6.4. The measurement of two protons with a different y coordinate yields a time offset, since the photons generated by the proton closer to the edge propagate through the ra-

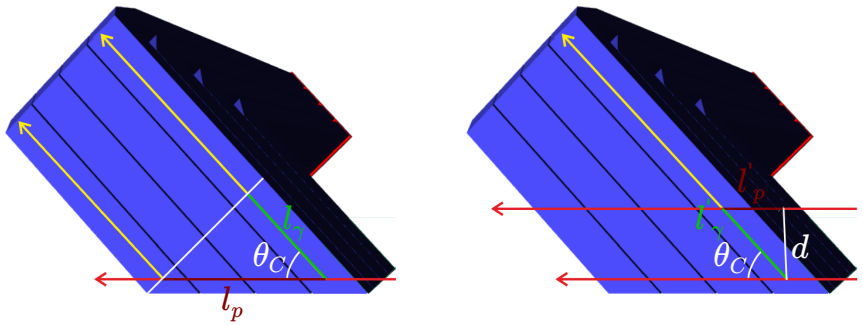

Figure 6.4: Calculation of the time offset compensation.

diator longer than the photons generated further from the edge. The offset is partially compensated by the prolonged time of flight of the proton further from the edge and the resulting offset can be calculated as

$$\Delta t = t'_\gamma - t'_\mathrm{p} = \frac{n l'_\gamma}{c} - \frac{l'_\mathrm{p}}{c} = \frac{nd}{c \sin\theta_\mathrm{C}} - \frac{d}{c \tan\theta_\mathrm{C}} = \frac{d}{c \sin\theta_\mathrm{C}} \left(n - \cos\theta_\mathrm{C}\right), \quad (6.3)$$

which yields

$$\frac{\Delta t}{d} = \frac{n - \cos\theta_\mathrm{C}}{c \sin\theta_\mathrm{C}} \approx 3.5\,\mathrm{ps\,mm^{-1}}. \quad (6.4)$$

The offset can be corrected for using the track position information from SiT. It was not corrected for during the beam test measurements with an SiPM as the time reference, however it is straightforward to calculate that the resulting mixture distribution over the interval of 3 mm (given by the SiPM radiator cross section) results in a contribution to the time resolution of about 3 ps (added in quadrature):

$$\sigma^2 = \sigma_0^2 + \sigma_\mathrm{mix}^2 = \frac{1}{3}\int_{-1.5}^{1.5} \left(\mu(x)^2 + \sigma_0^2\right) \mathrm{d}x = \frac{1}{3}\int_{-1.5}^{1.5} \left(\frac{\Delta t}{d} x\right)^2 \mathrm{d}x + \sigma_0^2, \quad (6.5)$$

where the first integral is the formula for the variance of a mixture distribution [49] with the dependence of the mean value given by $\mu(x)$ and the variance of a single distribution σ_0^2. The normalization is the length of the interval. The contribution of the mixture to the time resolution σ_mix can be evaluated using Eq. 6.4

$$\sigma_\mathrm{mix} = \sqrt{\frac{1}{3}\int_{-1.5}^{1.5} \left(\frac{\Delta t}{d} x\right)^2 \mathrm{d}x} \approx 3\,\mathrm{ps}. \quad (6.6)$$

The edge cut improves photon collection near the edge as the part of the Cherenkov cone in the direction of the edge cut would be lost without it. However, with the edge cut, the incident angle of the photons from this part of the cone is larger than the critical angle and the photons are reflected.

The dimensions of the bars are determined by the MCP-PMT pixel size, active area of SiT and the expected distribution of diffractive protons. In case of

radiators, the PMT pixel size determines the width of the bars along the z axis so that the radiator width matches the 6 mm width of the light guide. ToF needs to cover the full SiT area, which constrains mainly the x dimension of the bars, with the second constrain given by the diffractive protons distribution — rates in the bars need to be approximately equal. This results in the selected x dimensions illustrated in Fig. 6.5 — trains 1, 2, 3, 4 have thickness in x of 2 mm, 4 mm, 5 mm, 5.5 mm, respectively.

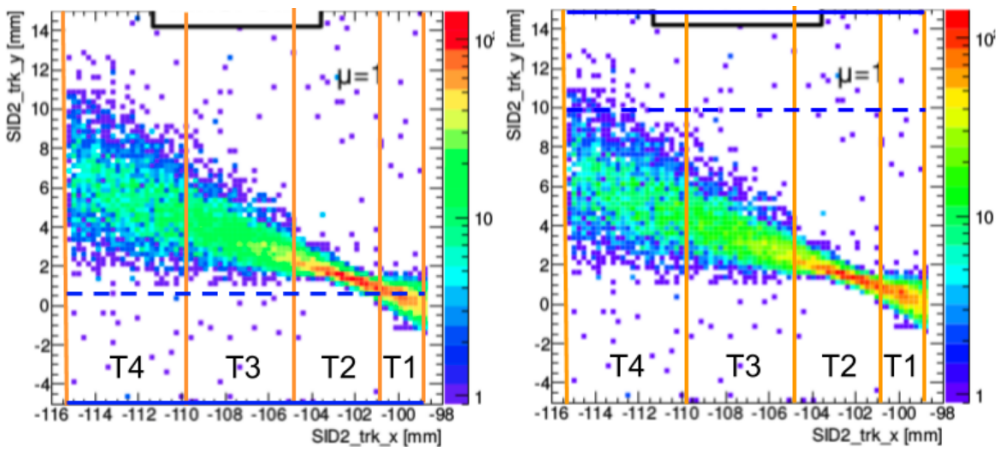

Figure 6.5: Distribution of diffractive protons in AFP tracker acceptance (simulation) with overlaid ToF bars for the A side (*left*) and the C side (*right*). T1–T4 stand for train 1–4, solid blue line represents the edge cut and dashed blue line is placed at 5 mm from the edge.

Light guides are rectangular with cross section of $5 \times 6\,\mathrm{mm}^2$ (trains 1–3) and $5.5 \times 6\,\mathrm{mm}^2$ (train 4) given by the MCP-PMT pixel size and the construction of the holder. Radiators thinner than the light guide have a *taper* at the end towards the radiator as illustrated in Fig. 6.6. The taper straightens a path of a significant part of photons that bounce at the walls of the radiator, thus reducing time smearing of the photons arrival [P3].

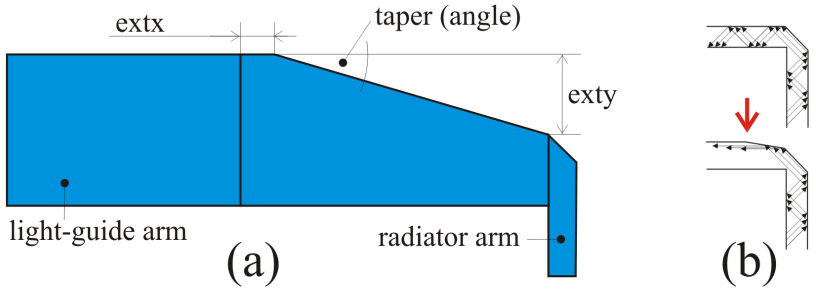

Figure 6.6: Light guide taper [P3].

The final design of the aluminum holder is build from a triangular base with cut corners, three pillars that hold rectangular PMT holder and two pillars are

extended to support also the assembly of plates that holds the LQbars. The plates have machined grooves, in which the LQ bars sit. The holder grooves (illustrated in Fig. 6.7) are machined such that the contact surface is minimized. There are two thick plates on each side of the plates assembly with the bars and 3 thin plates in between. There are four M3 threaded rods going through all the plates with metal spacers fitted on the rods in between the plates. The four rods are secured in the thick plate sitting on the two extended pillars and all the other LQbar holding plates are freely movable on the rods. There is another aluminum plate placed over the other thick plate with the four rods holding it in place. In the middle of this end plate is an M6 screw that is used to secure the bars once they are inserted. The holder is visible in the photograph of ToF and SiT assembly in Fig. 6.7.

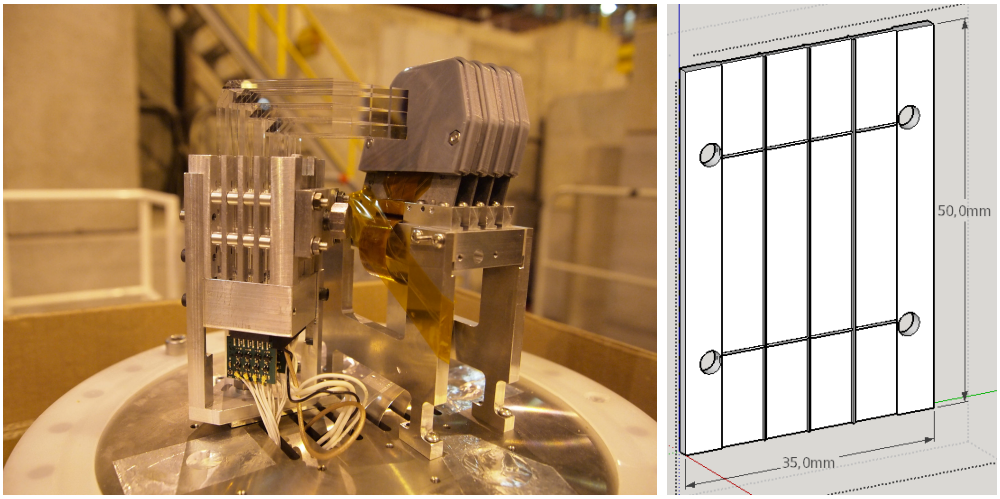

Figure 6.7: *Left:* Assembled ToF detector prototype with SiT tracker planes (with protective covers) on the Roman pot flange. *Right:* SketchUp [50] model of a holder plate with grooves.

6.2 MCP-PMT photodetector

An MCP-PMT is a compact photomultiplier that uses a micro-channel plate (MCP) for electron multiplication. A schema of operation is sketched in Fig. 6.8.

A photon hits a photocathode, as in a conventional PMT, and emits an electron with a probability given by the quantum efficiency of the photocathode used. The electron is then accelerated by an electric field towards the MCP.

MCP is made of a material with high resistance that is filled with small inclined channels (6–20 µm in diameter), as illustrated in Fig 6.9. Typically, multiple MCPs are stacked in so-called multi-chevron configuration. Channels represent typically about 60 % of MCP surface area. A very high voltage of about 1.5–2.5 kV is applied over the MCPs, providing an accelerating electric field. An

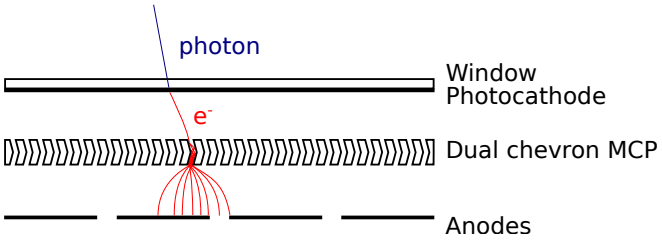

Figure 6.8: Schema of an MCP-PMT.

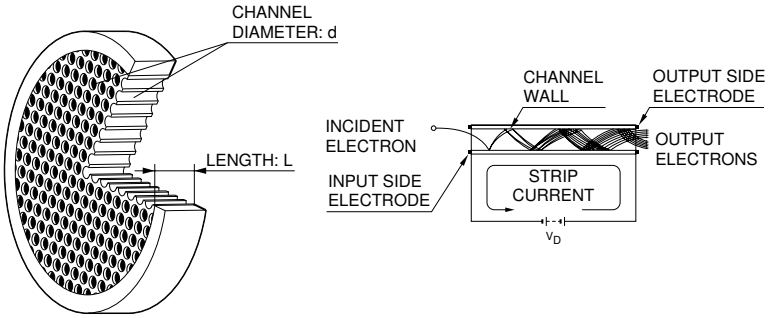

Figure 6.9: Schematic structure of MCP [51].

electron is multiplied by a factor of order up to about 10^7. Electrons emitted by the MCPs are then guided by a weaker electric field towards a single or multiple anodes, where they are collected and a negative pulse is produced at the output.

The electric fields in the 3 regions of propagation are created by applying high voltages between metal plates represented by the photocathode, conductive coatings on top and bottom of MCP and the anodes. Typically, a resistive voltage divider (with the 1:10:1 ratio in case of the AFP MCP-PMTs) is used to provide appropriate potentials.

An important characteristic of MCP-PMT for time of flight purposes is the time transit spread (TTS). It is the variation in signal propagation time through the MCP-PMT for the case of single photoelectron (i.e. one electron generated by a photon in the photocathode). The TTS considers only the main peak of the time distribution, as illustrated in Fig. 6.10. The main peak is approximately Gaussian with the tail toward higher times being prolonged by electrons that do not hit a micro-channel in the MCP directly, but are scattered into it. Some electrons that hit the MCP in between micro-channels can even bounce off and end up in a micro-channel further away due to the electric field.

For a higher illumination, time resolution of an MCP-PMT improves as

$$\sigma = \sqrt{\frac{\sigma_{\mathrm{TTS}}^2}{N_{\mathrm{pe}}} + \sigma_{\mathrm{const}}^2}, \tag{6.7}$$

where N_{pe} is the mean number of produced photoelectrons and σ_{const} is the contribution of an irreducible internal electronic jitter [52].

A crosstalk is also of importance in case of multi-anode MCP-PMTs. As the

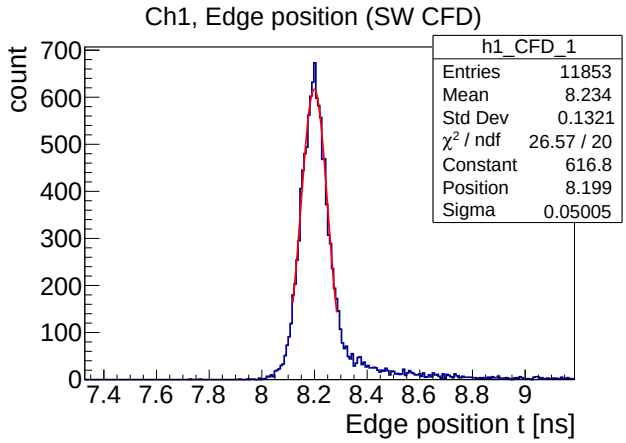

Figure 6.10: Time distribution of single photoelectron pulses produced by Photonis XPM85112 MCP-PMT illuminated by a femtosecond laser.

anodes are placed next to each other, a signal from one channel can influence measurement of neighboring channels. Two main sources of crosstalk are always present — charge sharing and capacitive coupling. Charge sharing happens when a signal from a single MCP micro-channel is collected by multiple anodes, as illustrated in Fig. 6.8. Since the anodes are thin metal plates with a dielectric in between, they represent a capacitance (of the order of picofarad) in between them. This results, for a pulsed signal, in transfer of small amount of signal into neighboring channels.

The AFP ToF utilizes Photonis miniPlanacon XPM85112 [53] (Fig. 6.11) with the reduced anode gap for a minimal charge sharing. Active area of $25 \times 25\,\mathrm{mm}^2$ is divided into 4×4 pixels, to which the LQbars are matched. First versions used in beam tests and for the installation in 2017 had 10 µm MCP pores and expected lifespan in terms of collected charge of about $1\,\mathrm{C\,cm^{-2}}$. Lately also 6 µm pore MCP-PMT with atomic layer depostion (ALD) coating became available, promising up to $10\,\mathrm{C\,cm^{-2}}$ lifespan, as the ALD coating on top of the MCP layer protects photocathode from bombardment by ions freed from the MCP pores [14].

The MCP-PMT is held in the middle part of the aluminum holder shown in Fig. 6.7. In 2018, also a plastic 3D printed version of the MCP-PMT housing was incorporated into the ToF holder allowing easier changes of the design.

6.3 Fast readout electronics

The MCP-PMT output is read out by an electronic chain designed with an aim to minimize the induced electronic jitter that affects timing performance of the ToF system. The schema of the readout chain is illustrated in Fig. 6.12. The signal is amplified by a set of broadband preamplifiers (PAs) with a variable gain up to 20 dB per stage. Next, a constant fraction discriminator (CFD) is used to

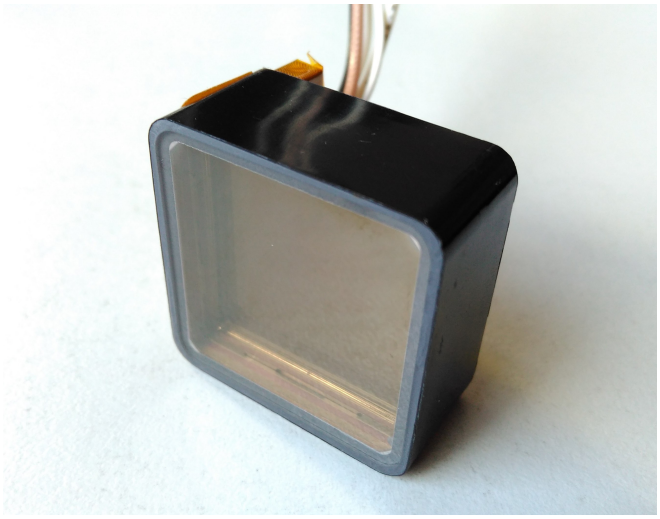

Figure 6.11: Photograph of a Photonis XPM85112 MCP-PMT.

obtain a sharp stable square pulse needed for a digitizer, that provides digital information to be stored. The selected digitizer is based on the HPTDC chip developed at CERN and the data acquisition (DAQ) is handled by RCE system interfaced to the central ATLAS DAQ [10, 15, 54].

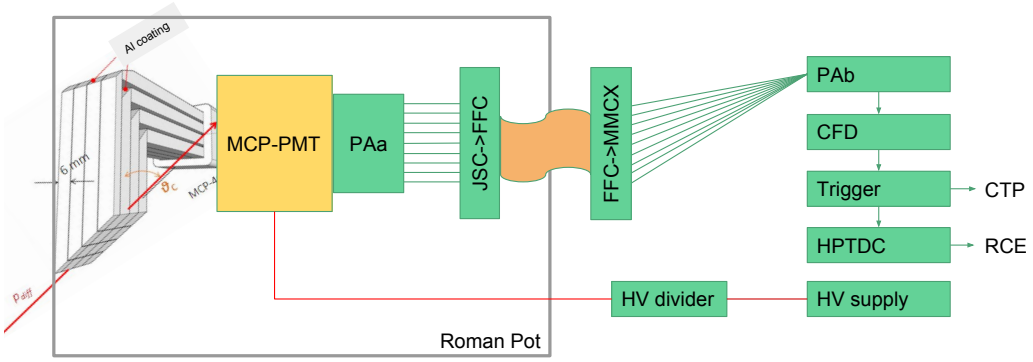

Figure 6.12: Schema of ToF readout electronics.

The PAb, CFD, trigger and HPTDC modules are installed in a NIM crate located at the foot of the AFP station base, about 1 m below the Roman pot.

6.3.1 Preamplifiers

The PMT output pulse amplitude is of the order of millivolts when measured over 50 Ω load. Since the usable range of input pulses to the CFD is about 200–1800 mV, the PMT output needs to be amplified before the CFD.

The first stage preamplifier (PAa) is connected directly at the backplane of the MCP-PMT. It consists of two 8 channel boards fitted with PSA4-5043+ low noise InGaP broadband amplifier and it was designed by Stony Brook University

(SBU). PAa boards are powered by 5 V provided via its coaxial output from the second stage preamplifier (PAb).

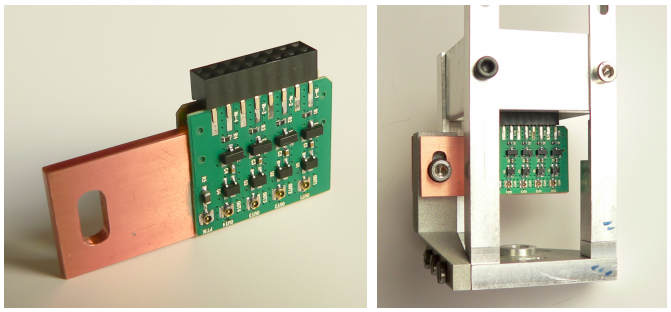

Figure 6.13: The first stage preamplifier (PAa) board with the heat sink (courtesy off Vladimír Urbášek).

PAa boards are placed in the secondary vacuum of the Roman pot. Therefore, the boards are very well thermally insulated and heat removal needs to be addressed. I participated in designing of the heat sink designed and manufactured at Joint Laboratory of Optics (JLO) in Olomouc. The heat sink is shown in Fig. 6.13. The first part of the heat sink is made of a 2 mm thick copper plate on which the two PCB boards of one PAa are glued on using a thermally conductive glue. Two copper plates are mounted by screws to the aluminum pillar that widens at its bottom (to form an upside down "T") to maximize contact with the ToF holder base, to which the "T" is screwed. To avoid ground loops, a thermally conductive electrically insulating tape is inserted between the copper plates and the pillar, and the screws holding the plates are fitted with a plastic pad.

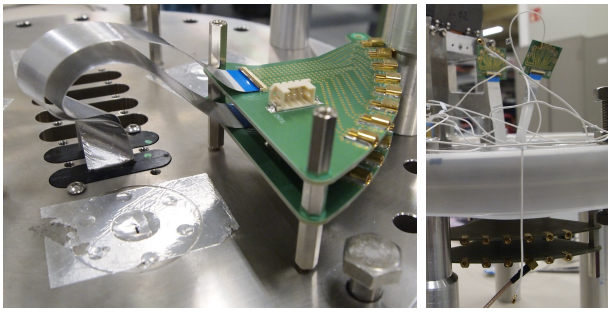

Figure 6.14: Feedthrough for signal lines and thermistors from the PAa. *Left:* outside of the Roman pot, *right:* whole feedthrough assembly with the inside of the pot at the top.

Vacuum feedthroughs are needed to extract the signal from the Roman pot. Flat flexible cables (FFCs) with potted sealing cap are used for this purpose. PCBs for interconnections from the PAa to the FFC and from the FFC further on were designed and assembled at JLO. The PAa is fitted with Murata JSC

connectors and 10 cm JSC-JSC cables are used to connect PAa to the feedthrough PCB inside the pot. On the outside of the pot, crescent shaped PCBs are placed, fitted with MMCX connectors for signal outputs and a 4 pin JST connector for the thermistor readout.

The second stage of amplifier (PAb) is needed to obtain a signal amplitude within the range needed for the CFD. The PAb is based on ADL5611 operational amplifier complemented by a variable attenuator. The original design from Stony Brook University was later modified at the JLO. The current version of PAb assembly consists of two NIM modules per ToF detector fitted with 8 single channel PAb cards each.

Figure 6.15: The PAb module.

In 2018, also the third stage amplifier (PAc) was designed and manufactured at CERN to allow operation of the MCP-PMT at lower gain in order to improve the high rate capability of the PMT and prolong the lifetime. This also required much better RF shielding of the analog signal path from the MCP-PMT up to the output of the PAc. The shielding was designed by the University of West Bohemia in Pilsen in cooperation with the JLO in Olomouc.

6.3.2 Constant fraction discriminator

CFDs are designed to correct for a time walk that occurs when a time of arrival of a variable amplitude pulse is determined when the pulse crosses a specified threshold. In such a case, two pulses of the same shape and peak time, but with a different amplitude, are measured at different times, hence the time walk. A CFD typically produces a square pulse of a fixed amplitude when an input pulse exceeds the preset fraction of its amplitude, as illustrated in Fig. 6.16. The output square pulse is no longer subject to a time walk when its time of arrival is measured at a fixed threshold.

The CFD is typically implemented using a splitter to divide input signal in two. One is delayed by a delay line, while the other part is inverted and attenuated. Two parts are then summed and the output pulse is generated when the combined signal crosses zero. The attenuation and the delay line length need to be tuned for a given pulse shape to produce the output at the optimal

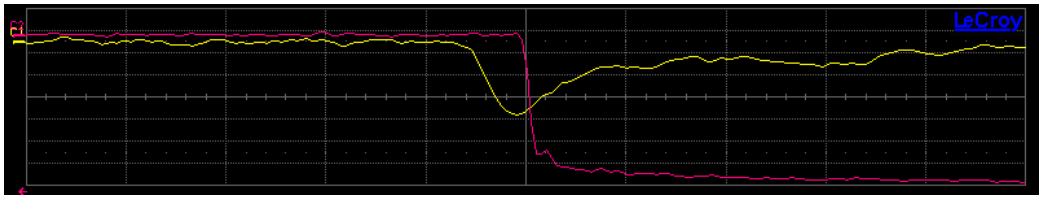

Figure 6.16: Oscilloscope view of an MCP-PMT pulse (C1, yellow, 50 mV/div) and CFD output pulse (C2, magenta, 70 mV/div). Time scale set to 2 ns/div.

fraction of a pulse amplitude. The timing performance for an MCP-PMT pulse and different fractions is illustrated in Fig. 6.17, where a software implementation of the CFD was used to measure the time of arrival at a varying fraction of the peak amplitude on the same sample of MCP-PMT pulses and the time resolution was determined for each fraction.

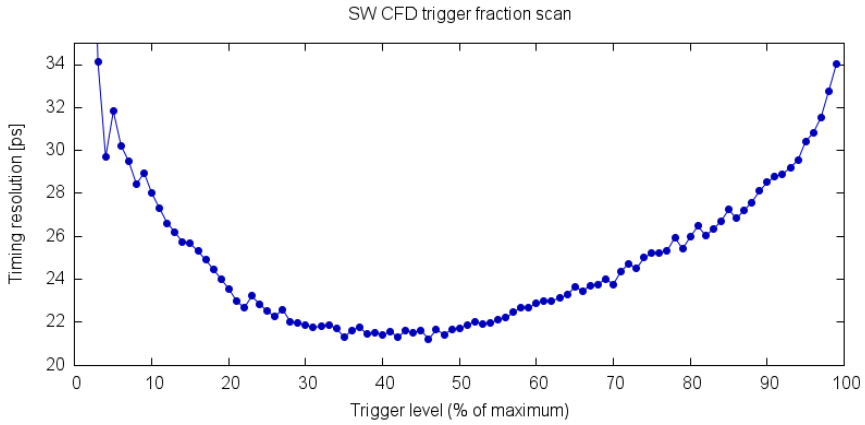

Figure 6.17: Simulation of the CFD constant fraction setting (labeled as the trigger level) impact on the time resolution of ToF (courtesy of Tomáš Komárek). The same set of MCP-PMT signal was processed using the software (SW) CFD with varying constant fraction setting for the pulse edge time extraction and the time resolution was evaluated for each setting.

Initial design of the CFD used in the AFP ToF was prepared by the Université Catholique de Louvain and further developed by the University of Alberta. The final version comprises NIM modules with 8 single channel cards plugged in a common motherboard. Each CFD card recieves a signal from an SMA input and provides an LVPECL differential output for further processing and a NIM output (on a LEMO 00 connector) for laboratory testing. The CFD fraction is set to 42 % for MCP-PMT signals, corresponding to the optimal timing performance, as illustrated in Fig. 6.17. Apart from the main CFD function, a fixed threshold comparator (configurable via I^2C) is used to filter noise and time-over-threshold (ToT) functionality is implemented, translating the input signal amplitude into the length of the output square pulse. The time resolution smearing, due to the

residual time walk and the electronic jitter, is less than 5 ps.

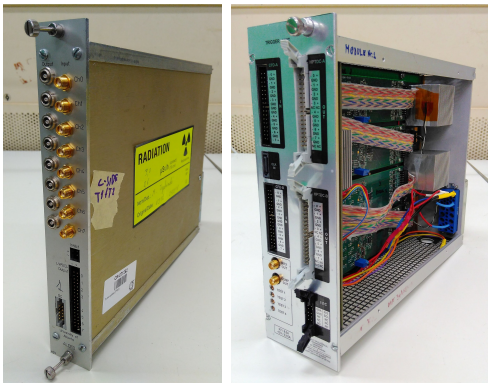

Figure 6.18: The CFD module (*left*) and the trigger module (*right*).

6.3.3 Trigger module

The AFP needs to provide a trigger information to the central trigger processor (CTP) of ATLAS so that the forward proton tag can be added to the lowest level (Level 1 or L1) trigger decision. There are two sources of trigger in AFP that can be used — SiT and ToF.

SiT uses a configurable coincidence of multiple planes responses to generate the trigger. While this is a good option for low μ runs, SiT trigger saturates at high pileup runs due to its dead time of about 10 bunch crossings (BX = 25 ns), depending on the SiT readout settings.

The trigger module for ToF was initially designed at the Stony Brook University and further developed at the JLO in Olomouc and at the University of West Bohemia in Pilsen. The main purpose of the module is to provide a trigger output signal whenever a proton passes through ToF. The module consists of four identical trigger boards for individual trains and a motherboard that combines the output of all the trigger boards and accordingly produces NIM output on two output SMA connectors.

Each trigger board acts as a coincidence unit with a selectable number of bars that need to fire within one train in order to produce output trigger signal. The coincidence is implemented using an RF combiner and comparator with a tunable threshold to set N out of 4 ($N/4$) coincidence. The coincidence level is configurable via I^2C. Apart from providing partial trigger output, the trigger boards also gates signals from the CFD to the HPTDC module to limit the rate. The trigger board passes through the signals from bars within one train only if the preset $N/4$ coincidence is fulfilled. In addition, signals are required to arrive in 1 ns window within each bunch crossing.

The trigger signal must arrive into the ATLAS CTP within the maximum allowed latency of about 2 µs. Considering the proton flight time from the IP to the AFP far station (217 m apart) of 724 ns, propagation delay in ToF of less

than 5 ns, cabling from the Roman pot to the NIM crate adding 10 ns and trigger module logic adding less than 10 ns, the maximum time of the signal propagation to the CTP located in the USA15 service cavern near the IP and of the processing the signal before the CTP is about 1.25 µs. An air-core coaxial cable (RFS HCA78-50J [55]) was selected for its high propagation velocity of 93 % of the speed of light in vacuum and a low attenuation. There is one pair of 330 m long air-core cables routed between the USA15 and the AFP far station on each side. The delay introduced by the air-core cable is 1180 ns, leaving about 70 ns for the signal processing at the CTP side, currently realized by a NIM discriminator module that produces a proper NIM pulse from the trigger pulse smeared after the air-core cable propagation. The individual latency contributions are summarized in Tab. 6.1 for clarity.

Table 6.1: The AFP trigger signal latency.

Path	Delay [ns]
Proton flight (217 m)	724
Propagation delay in ToF	< 5
Cabling from RP to NIM crate	< 10
Air-core cable (330 m)	1180
Signal processing before CTP	< 50
Total delay	< 1969

A compatible fully digital solution using an FPGA (field-programmable gate array) was implemented at the University of West Bohemia in Pilsen.

The trigger module was not ready for the installation with ToF in 2017. Instead, a similar functionality was programmed by Paul Davis in the FPGA of the HPTDC module, but since the trigger module is also designed to limit the rates at the HPTDC module input, it was only a temporary solution.

6.3.4 HPTDC module

Time digitization module was developed by the University of Alberta. It is based on the High Performance Time-to-Digital Converter (HPTDC) ASIC chip developed at CERN [54]. Each module has 12 LVPECL input channels and contains three HPTDC chips and FPGA that handles the data flow.

The intrinsic time resolution of the current HPTDC module was measured in a University of Alberta laboratory to be 16 ps. This adds a significant deterioration to the ToF resolution. Development of an HPTDC successor, the picoTDC, is currently finishing and a module based on the picoTDC should add less than 3 ps.

Each HPTDC chip is able to handle up to 8 MHz continuous rate per channel with possible short bursts [10]. This is on par with expected rate of diffractive protons in the AFP: assuming the collision rate up to 40 MHz with an average

pileup of about 40 and about 2 % probability [56] of a proton hitting the AFP in a collision, one can estimate about 30 MHz rate over the whole ToF and 8 MHz per train. This is the reason for the gating of signals at the trigger module.

The Time-over-Threshold extracted from the pulse length is recorded in the FPGA of the HPTDC. The HPTDC module also serves as the I^2C master, providing the configuration to the CFD and the trigger modules. Since all the modules operate in a radiation environment, I^2C commands are sent periodically in order to minimize an impact of a single event upset.

6.3.5 Reference clock

The ToF detectors on the two sides of ATLAS need to be very precisely synchronized to be able to pinpoint the primary vertex z position. A clock distribution system with less than 3 ps clock jitter is used to provide clock signal for the HPTDC and the trigger module.

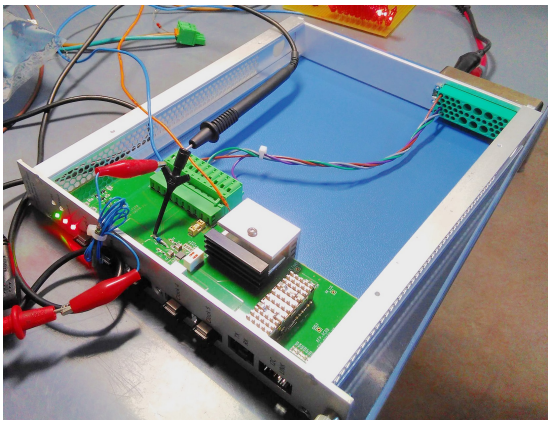

Figure 6.19: The clock distribution reciever module under laboratory testing.

The clock distribution uses the LHC clock as the source of the clock signal at 40.087 MHz. The system is based on a phase locking loop. The signal is distributed from the ATLAS service cavern (USA15) to the two AFP stations with ToF detectors via optical fibers and a second set of fibers is providing a loopback for the phase matching back in the USA15. A variable fiber optic delay line is used to match the phase of the two return signals. The clock receiver module (Fig. 6.19) then converts the optical signal to the needed differential LVPECL clock signal.

6.3.6 Data acquisition and detector control

The AFP uses a DAQ system based on the Reconfigurable Cluster Element (RCE) developed at the Stanford Linear Accelerator Complex (SLAC). The RCE is handling data received by the High Speed Input/Output (HSIO) board. The HSIO serves as an interface and receives data from SiT planes and HPTDC

modules on modified gigabit Ethernet ports and the RCE manages their transfer to the central ATLAS DAQ system.

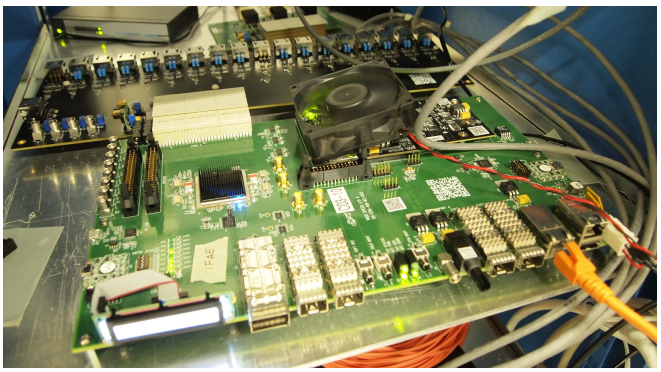

Figure 6.20: High Speed Input/Output board with Reconfigurable Cluster Element mezzanine (the small black board with the fan on top).

The powering of detectors, station movement, monitoring and logging of the position, temperatures, voltages and currents etc. is managed by the Detector Control System (DCS). An interlock system is implemented to prevent a damage to detectors. Operation ranges are defined for most monitored quantities and appropriate warnings and errors are produced when a quantity falls out of its defined range. E-mail and SMS notifications are in place to assure timely response of a shifter, the AFP on-call person or experts.

Chapter 7

Beam test campaigns

The AFP detectors were tested with a hadron beam during several beam test campaigns. At first, SiT and ToF, were tested separately and in later stages, the full readout chain, including the RCE, was utilized and SiT and ToF detectors took combined data.

In this chapter, I describe beam tests in which I participated, with the focus on the ToF detector. All these tests took place at the CERN North Area site, at the CERN building 887.

7.1 Experimental area

The North Area experimental hall 887 is divided into smaller beam areas by concrete blocks as visible in Fig. 7.1. There are four beam lines in the hall — H2, H4, H6 and H8 [57]. Each beam line serves several beam areas.

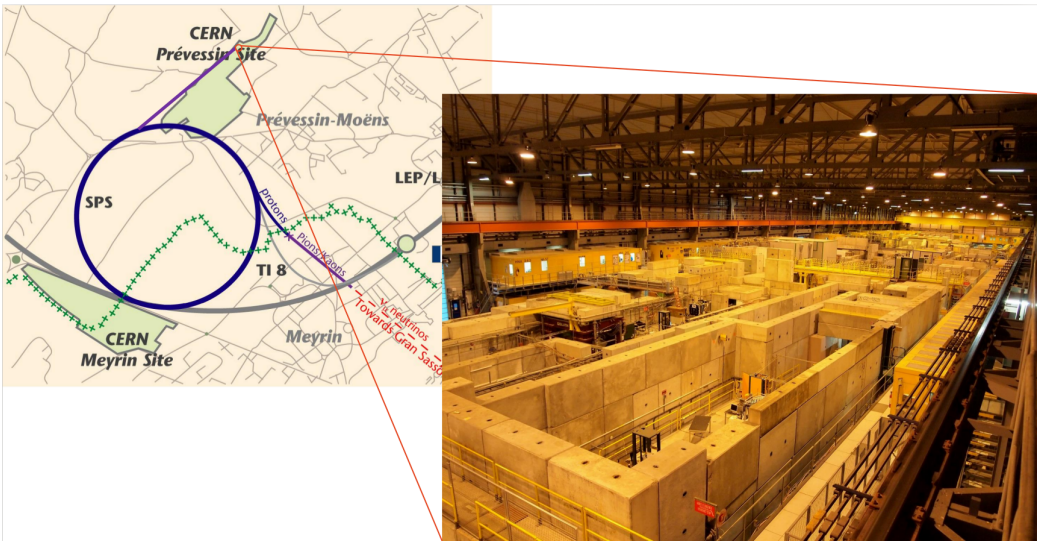

Figure 7.1: CERN North Area experimental site.

All AFP beam tests, I describe in this chapter, were performed on the H6

beam line. There are two beam areas used for short term experiments in the beam line. H6 provides a high energy secondary beam with particle momentum up to 205 GeV/c. The beam was mostly composed of 120 GeV π^+ pions for the AFP beam tests. Optics of the beam line, as well as beam intensity, can be adjusted and about 2 cm wide beam with a high intensity was pursued in the AFP beam tests.

The pion beam is produced by the primary proton beam extracted from the SPS and impacting on the T4 target composed of beryllium and lead [57]. The secondary beam of a desired momentum is extracted by a combination of a dipole magnet and a slit in an absorber. The pions are delivered during the proton beam extraction with a limited duration of about 4–10 s. An extraction accompanied by the secondary beam being delivered to the beam test areas is called a *spill*. The frequency of spills is given by the current SPS operation scheme, so-called *supercycle* that governs where the SPS is delivering protons. Duration of a supercycle is about 25–120 s and usually one or two spills are delivered to targets in one supercycle. A course of a supercycle with two spills is visualized in Fig. 7.2. Particles are delivered to the North Area beam lines on the falling edge of the yellow line.

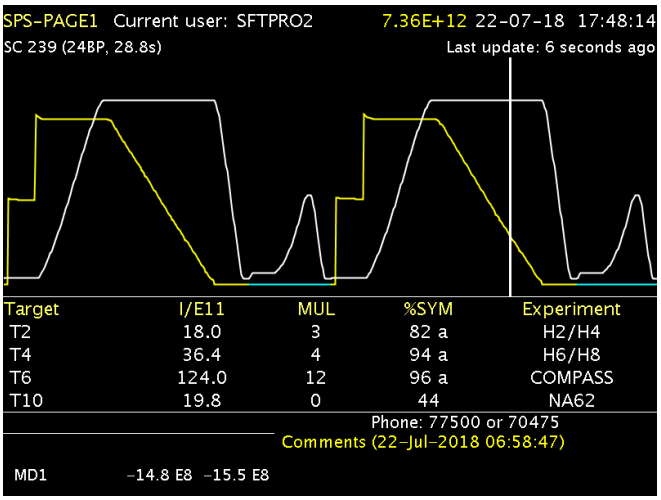

Figure 7.2: Monitoring screen of the SPS showing a course of a supercycle with two spills. The white line plots the field intensity of the SPS bending magnets and the yellow line the proton beam intensity [58].

7.2 Measurement scheme

A general measurement scheme and the experimental setup was very similar throughout all the beam tests I describe here, although parts of the setup changed as necessary for particular goals of a given beam test. An experimental setup consisting of four tracker planes, two ToF detectors and two SiPM timing reference detectors is shown in Fig. 7.3.

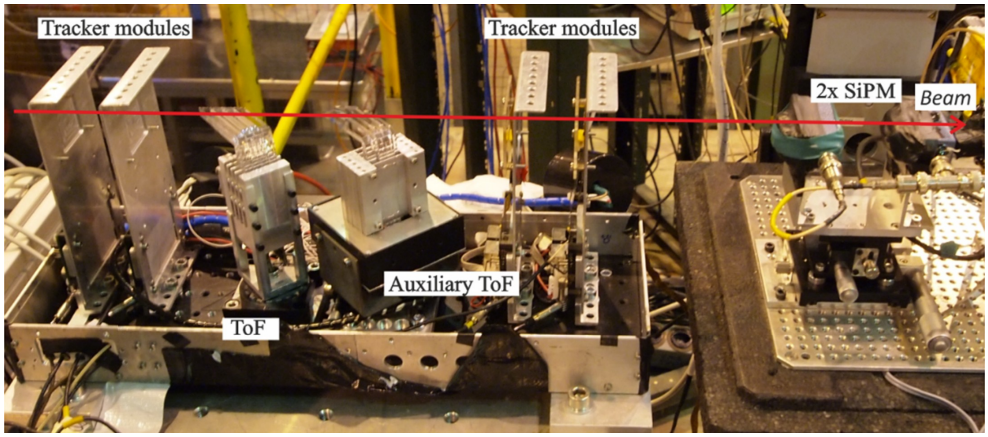

Figure 7.3: Beam test experimental setup [P14].

Tracker planes were initially mounted on machined aluminum plates as shown in Fig. 7.3. These were later inclined to measure how the resolution improves and finally also carbon fiber reinforced aluminum plates of the final SiT holder design were tested. SiT measurements focused on spatial resolution as well as optimization of the charge readout. In later beam tests, the tracker was mostly used for the alignment of ToF.

Various versions of ToF prototype were tested in beam tests. Main focus was on time resolution of the whole ToF system, however to optimize the resolution, it was needed to study the interplay of individual components. Different versions of bars were tested, individual bars and single trains were measured to understand crosstalk, several ToF holder designs were used, optical separation of bars was studied and several MCP-PMTs were utilized.

SiPM detectors were used as a timing reference. They composed of 3 cm long fused silica bar with a cross section of $3 \times 3\,\mathrm{mm}^2$ oriented along the beam and a SiPM (Silicon Photomultiplier) chip placed on the rear face of the bar, optically coupled by an optical grease. At first, 3.5×3.5 mm^2 SiPMs produced by STMicroelectronics (NRD09_1, $58 \times 58\,\mu\mathrm{m}^2$ cell size) were used and later also 3×3 mm^2 SiPM manufactured by FBK (SiPM-NUV3S [59], $40 \times 40\,\mu\mathrm{m}^2$ cell size) and by SensL (MicroFC-SMA-30050 [60], $50 \times 50\,\mu\mathrm{m}^2$ cell size) were tested as possible replacements. One to four SiPM detectors were used at the same time during beam test campaigns. Initially the SiPMs were mounted to the same table as the ToF and SiT detectors. Later a motorized X-Y translation movable stage (PI stage) was used to position the SiPM detectors horizontally and vertically with respect to the rest of the setup.

The full overview of a beam test area with all commonly used components is shown in Fig. 7.4. AIDA telescope was used on several occasions as a reference tracking detector for SiT with a micrometer precision in both perpendicular axes. The PAb, CFD, HPTDC and later on also the trigger modules were placed in the depicted NIM crate together with a high voltage power supply for the MCP-PMT. The main setup was placed on the heavy duty movable table to

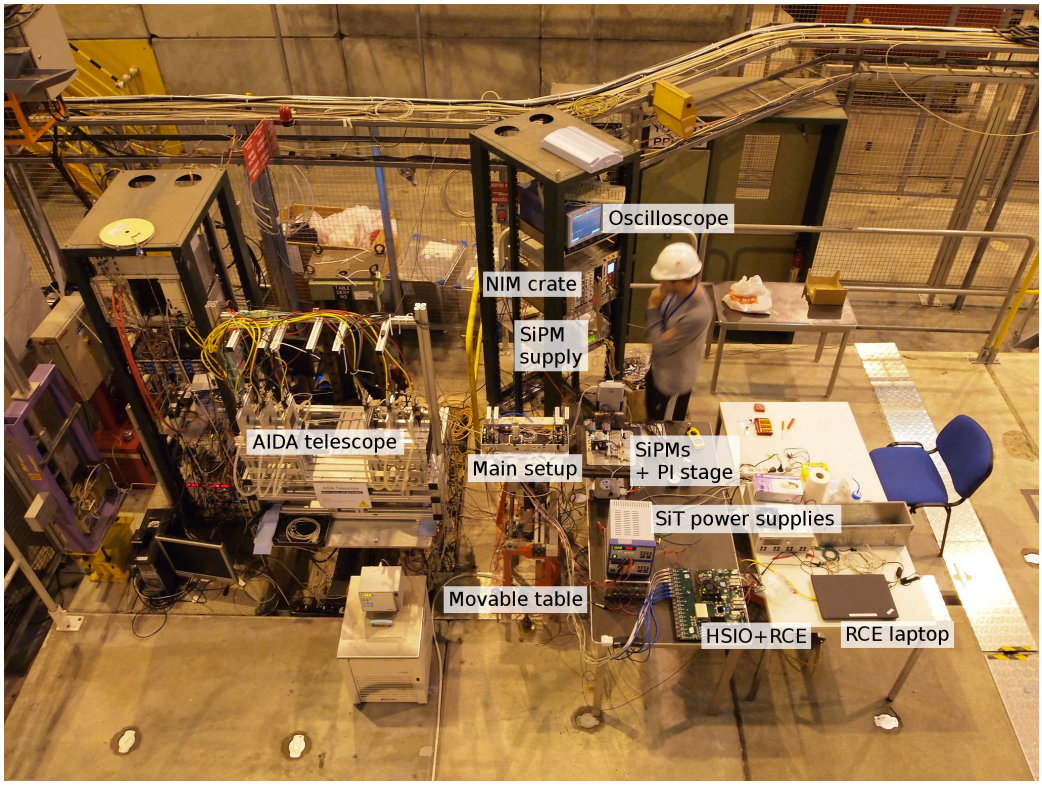

Figure 7.4: Beam test area (H6B) overview.

allow an optimization of the setup positioning within the beam. All the sensitive detectors were roughly aligned using a self leveling cross line laser tool and the beam was used for the fine alignment.

Both MCP-PMT and SiPM detectors need to operate in dark. An aluminum box with the optical breadboard as a base, depicted without its cover in Fig. 7.3, was used in all beam tests. The box consists of the breadboard base, feedthrough side panels and the box cover, being the largest part of the box. Additionally, the box is sealed by black tape and covered by a black drape to increase its light-tightness. In later beam tests, also the AFP Roman pot was used as a housing.

The readout chain for ToF was essentially the same in the beam tests as the final AFP electronics chain described in Sec. 6.3 with some different prototype versions of the modules being used during a particular beam test. In addition, the same readout chain was used also for the SiPM detectors. Measurements can be divided in two groups based on the DAQ device — oscilloscope measurements and RCE measurements.

A fast oscilloscope was used to capture full MCP-PMT waveforms and to measure the time resolution of ToF without the influence of the HPTDC. Only a part of the readout chain was used in such measurements. Only the PAa and PAb amplifiers were used for the measurements capturing the full waveform (so-called *raw measurements*) and the CFDs were usually added for the time resolution studies (*CFD measurements*).

The RCE was used to record both SiT and ToF data. These were used for the ToF alignment as well as measurements of timing resolution including the HPTDC contribution, efficiency of the ToF channels and their crosstalk.

7.3 November 2014

The first beam test I participated in, was focused on the integration of SiT and ToF readouts. The operation of the first LQbar ToF prototype, finding the optimal operation voltage of the MCP-PMT and the first timing resolution measurement were also of great interest. Four trains consisting of two bars each were prepared by the JLO workshop, the mechanical construction by the SBU and the Photonis MCP-PMT was provided by the University of Texas in Arlington (UTA). The H6B beam area was available for the AFP tests for one week. A photograph of the experimental setup without the box cover is in Fig. 7.5. Apart from this main setup, also LGAD and diamond detectors were tested as an alternative timing detectors and SAMPIC was tested as an alternative time digitizer (utilizing sampling of waveforms instead of the CFD and the edge timing).

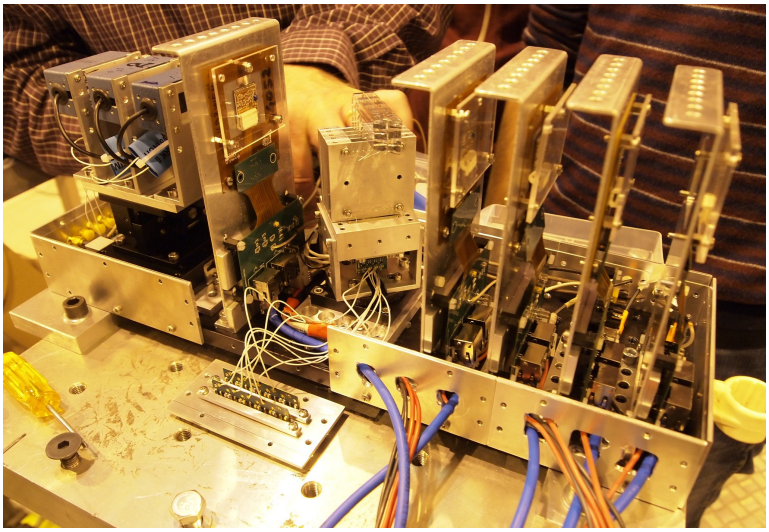

Figure 7.5: November 2014 beam test experimental setup.

In this beam test, all the detectors were enclosed in the aluminum box. The ToF detector was placed on a rotary stage to adjust the bar angle to match the Cherenkov angle. Three STM SiPMs with quartz bars were mounted on a manual X-Y translation stage to adjust the SiPM position with respect to a ToF train. Most measurements were performed with SiPMs aligned with the ToF train 2. The thicknesses (in x) of trains were different from the final design — train 1 utilized radiator bars 3 mm thick and the all the other trains comprised 5 mm thick radiator bars. Only the train 1 had the taper.

Figure 7.6: Oscilloscope screenshot from the CFD test. Two CFD output channels (magenta and cyan) and the trigger pulse (green) are recorded. The two histograms show time difference between the leading edge of the CFD output w.r.t. the trigger pulse leading edge (at 50 % level).

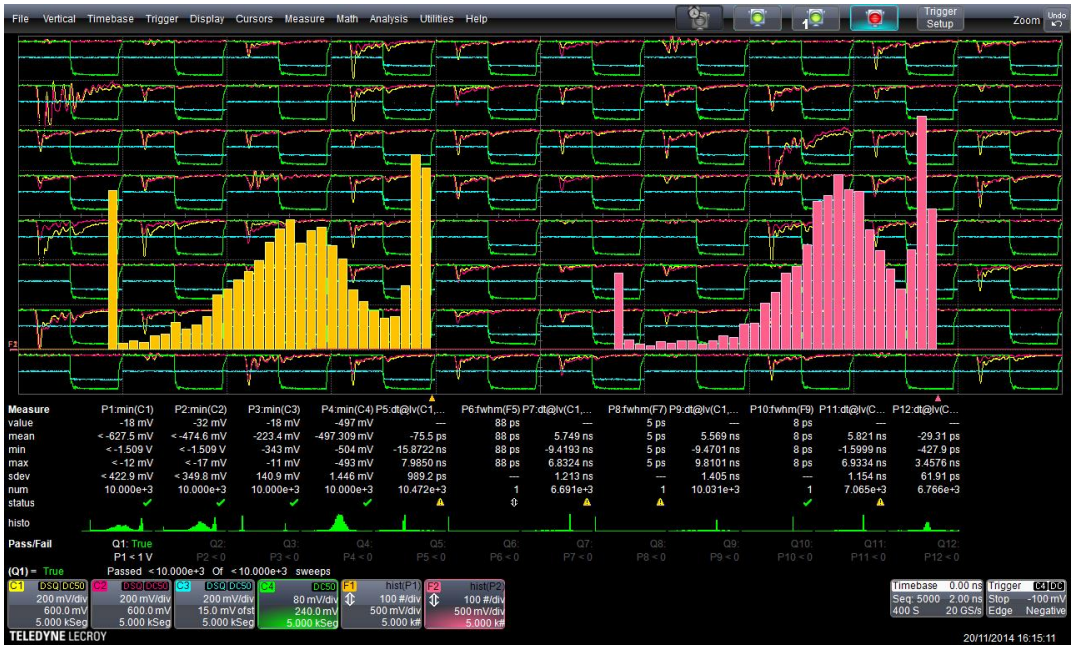

Figure 7.7: Oscilloscope screenshot from the HV optimization. The oscilloscope is triggered by an SiPM passed through the CFD (C4, green) and raw signals from two ToF bars are recorded (C1, yellow and C2, magenta). The two histograms represent the amplitude distribution of the C1 and C2 inputs with matching colors, each bin corresponds to 50 mV. Both histograms show an acceptable signal separation from the pedestal.

I helped with preparation of the beam test, the data taking with the oscilloscope and the oscilloscope data analysis. The experimental setup was assembled and individual electronic components were tested in the week before the beam test campaign. Figure 7.6 illustrates the test of the CFD channels. A timer module (CAEN N93B) was used as a pulse generator that triggered the oscilloscope (LeCroy SDA760Zi-A) and a discriminator module (LeCroy 4608B). The discriminator provided two short signals that were fed into two CFD channels under test and the CFD outputs were observed by the oscilloscope. The amplitudes and the shapes of the CFD output signals were observed and time differences between the leading (falling) edges of two CFD outputs and the trigger pulse were compared. The shapes of the histograms in Fig. 7.6 show non-negligible timing jitter of the discriminator.

Just before the start of the beam test campaign, all the equipment was moved to the beam test site and the test setup with all the readout electronics, including the oscilloscope and the RCE, were installed in the beam area H6B. A remote control was set up for the oscilloscope, the high voltage (HV) power supply for the MCP-PMT, the low voltage (LV) supply for SiPMs, and for the RCE, so that they could be controlled from the associated control hut of the beam area.

The beam test started by bringing all the detectors alive, locating the beam and aligning the detectors to the beam. The SiPM voltage was set initially to 30 V and later optimized to 30.7 V. The HV for the MCP-PMT was tuned to achieve a good separation of the signal pulses from the noise pedestal, while staying within the voltage range given by the CFD dynamic range, as illustrated in Fig. 7.7. The optimal HV value of 1850 V was found for the tested MCP-PMT.

7.3.1 SiT and ToF readout integration

The integration of readout of SiT and ToF detectors using the RCE was successful and common data were taken and analyzed as illustrated in Fig. 7.8. Several issues were encountered and solved, e.g. deteriorated timing due to the HPTDC measuring on a trailing edge, instead of a leading edge, caused by swapped CFD output polarity; and a light leak in the box, solved by a careful covering of slits and feedthroughs by a black tape and putting the black drape over the setup. Data with the oscilloscope were initially taken in parallel, using RF splitters at the PAb outputs to provide signals for the full readout chain as well as for the oscilloscope. Later during the beam test, the splitters were removed, since double peaks in timing distributions were observed and attributed to reflections in the splitters.

7.3.2 ToF performance

The first timing results were obtained from the histograms set up in the WaveStudio control software of the oscilloscope during the CFD measurements. The full width at half maximum (FWHM) of distributions of a time difference between

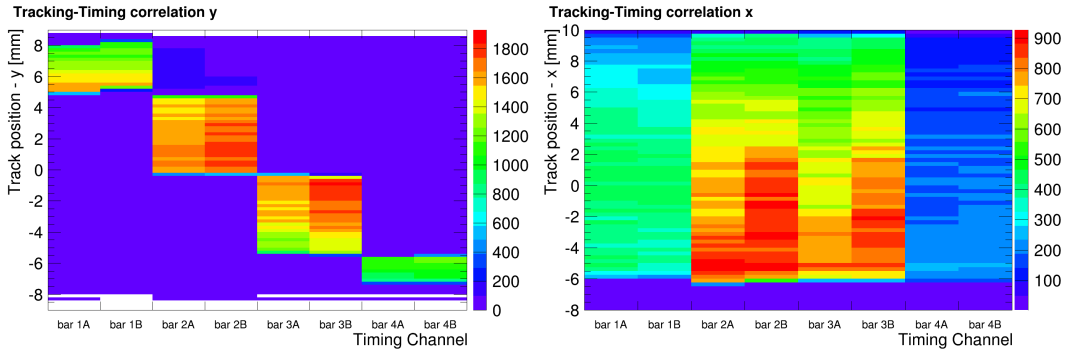

Figure 7.8: Correlation between the reconstructed SiT track position and response in ToF channels for the x (*right*) and y (*left*) coordinate. The MCP-PMT HV was set to 1800 V [P10].

a bar and the triggering SiPM was measured in range 70–90 ps including the contribution of the SiPM time resolution (of about 30 ps FWHM). This corresponds, for a Gaussian distribution (since FWHM $\approx 2.35\sigma$), to σ of 27–36 ps per bar with the SiPM contribution subtracted (in quadrature, assuming no correlations).

The observed time distributions are approximately Gaussian with abundance of events in the tail towards later times, as illustrated in Fig. 7.9. I compared fitting using a single Gaussian and a sum of multiple Gaussians. Already two Gaussians describe the obtained time distribution well, as illustrated in the figure. The asymmetric tails can be explained by delayed pulses forming a second Gaussian distribution with delayed mean time of detection. These can occur when a low number of photoelectrons is produced at the MCP-PMT photocathode and the photoelectrons do not hit MCP pores directly.

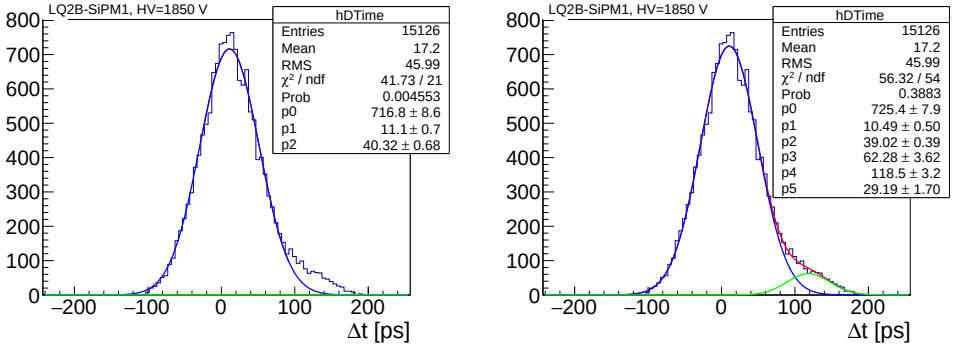

Figure 7.9: Example of time distribution obtained for bar 2B w.r.t. SiPM1 with Gaussian fit (*left*) and fit by sum of two Gaussians (*right*).

Although the double Gaussian fit describes the distribution better, the simple Gaussian fit of the central part (~ 1.5 FWHM) was used for the time resolution analysis later on. The reason was mainly that the double Gaussian fit was

unstable and sensitive to fluctuations in the tail. Also, the tail represents a small part of events (about 8 % in the case in Fig. 7.9).

7.3.3 SiPM time resolutions

The time resolutions of the three SiPMs were determined so that the SiPM trigger contribution could be subtracted from the time resolutions of the bars. Oscilloscope data with the three SiPMs connected were taken and time distributions of the three possible time differences were plotted and their width determined. The individual SiPM time resolutions were then determined from the set of equations

$$\begin{aligned} \sigma_{12}^2 &= \sigma_1^2 + \sigma_2^2 \\ \sigma_{13}^2 &= \sigma_1^2 + \sigma_3^2 \\ \sigma_{23}^2 &= \sigma_2^2 + \sigma_3^2 \end{aligned} \tag{7.1}$$

where $\sigma_i j$ is the width of the distribution of time differences between i-th and j-th SiPM and σ_i is intrinsic time resolution of an i-th SiPM.

The measurement yielded

$$\begin{aligned} &\sigma_{12} = 17.4\,\text{ps}, \quad \sigma_{23} = 16.6\,\text{ps}, \quad \sigma_{13} = 14.5\,\text{ps}, \quad \text{for LV} = 30.3\,\text{V} \\ &\sigma_{12} = 14.5\,\text{ps}, \quad \sigma_{23} = 14.9\,\text{ps}, \quad \sigma_{13} = 12.3\,\text{ps}, \quad \text{for LV} = 30.7\,\text{V} \\ &\sigma_{12} = 14.0\,\text{ps}, \quad \sigma_{23} = 11.5\,\text{ps}, \quad \sigma_{13} = 11.9\,\text{ps}, \quad \text{for LV} = 31.0\,\text{V} \end{aligned} \tag{7.2}$$

I get the resolutions of the individual SiPMs by solving the Eq. 7.1

$$\begin{aligned} &\sigma_1 = 10.9\,\text{ps}, \quad \sigma_2 = 13.6\,\text{ps}, \quad \sigma_3 = 9.5\,\text{ps}, \quad \text{for LV} = 30.3\,\text{V} \\ &\sigma_1 = 8.4\,\text{ps}, \quad \sigma_2 = 11.8\,\text{ps}, \quad \sigma_3 = 9.1\,\text{ps}, \quad \text{for LV} = 30.7\,\text{V} \\ &\sigma_1 = 10.2\,\text{ps}, \quad \sigma_2 = 9.7\,\text{ps}, \quad \sigma_3 = 6.2\,\text{ps}, \quad \text{for LV} = 31.0\,\text{V} \end{aligned} \tag{7.3}$$

It is visible that the SiPM1 reaches its optimal performance around 30.7 V, while the other SiPMs need higher bias voltage. Most of the time, the SiPM1 was used as the reference and therefore the voltage of 30.7 V was used as the optimum. Also, higher voltages lead to increase of the SiPM output pulse amplitude outside of the usable CFD dynamic range and even over the saturation level of PAb ($\sim$1.8 V).

7.3.4 ToF efficiency and crosstalk

The ToF efficiency and crosstalk were analyzed from the RCE data [P10]. Events with a single track in the SiT detector were selected. The efficiency was calculated as the fraction of events with the track pointing to a given ToF channel, in which the ToF channel responded. The crosstalk estimate was obtained by requiring a track pointing to a neighboring, next-to-neighboring... channel and counting in what fraction of such events a given ToF channel responded. The results are plotted in Fig. 7.10. It is visible that with increasing HV the efficiency, but also

the crosstalk increases. It is worth noting that the bars of train 1, i.e. the only bars with the taper in this beam test, manifest much higher efficiency at the lower voltages, while the crosstalk behavior is similar to the rest of bars. During the tests, it was tried to remove the optical crosstalk between the trains by optical isolation using a mylar foil. This did not lead to a significant improvement and it was concluded that the main crosstalk source is at the MCP-PMT — possibilities being a light leaking into a neighboring channel at the MCP-PMT faceplate, charge sharing between multiple anodes and capacitance coupling of the anodes.

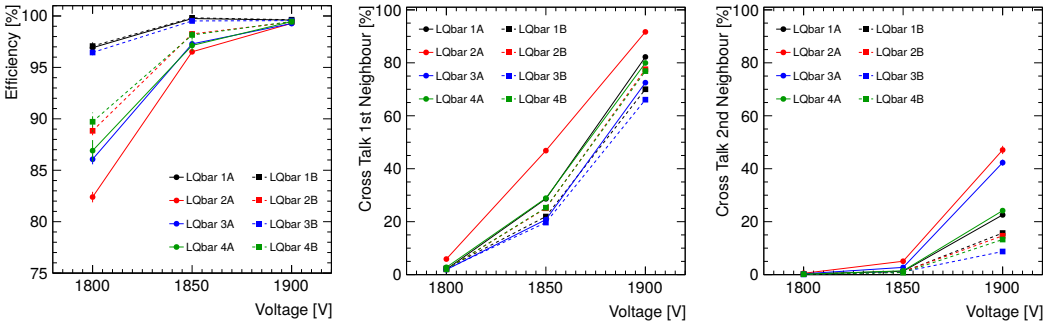

Figure 7.10: Efficiency (*left*) and mean crosstalk from the neighboring channels (*middle*) and next-to-neighboring channel (*right*) as a function of HV for all bars [P10].

7.4 September 2015

The next beam test focused on tuning and measuring properties of SiT and ToF detectors. Spatial resolution of SiT was measured with 14° tilt foreseen for the final version, a range of bias voltages was tested and charge readout was tuned for the optimal resolution [P10]. The ToF was tested with a new MiniPlanacon MCP-PMT loaned to the AFP by Photonis and, for a direct comparison, also the previously used MCP-PMT from UTA was utilized. New sets of bars and options for an optical coupling of the LQbars to the MCP-PMT front face were tested as well as x dependence of time resolution.

The beam test took place in the H6A beam area during two weeks in the second half of September 2015. The setup was essentially the same as before with the exception of SiPMs. There were two STM SiPMs installed in the setup and they were placed on the PI stage for most of the beam test. This allowed a quick repositioning of the SiPMs and thus measurement of bar response as a function of distance from the parallel cut edge.

A high voltage applied to the new MCP-PMT was tuned again to obtain the separation of the signal from the noise pedestal and 1870 V was determined as the optimum. The SiPMs were operated most of the time with the bias voltage of 30.7 V.

7.4.1 Comparison of signal amplitudes of different bars

All the LQbars were tested during the beam test in order to check how consistent is their response. One of the tests was the measurement of the pulse amplitude distribution for all the LQbars as plotted in Fig. 7.11. For this measurement, the bars were placed into the holder such that there is an empty space in between the A and B bars to reduce the light spillage from A to B bars.

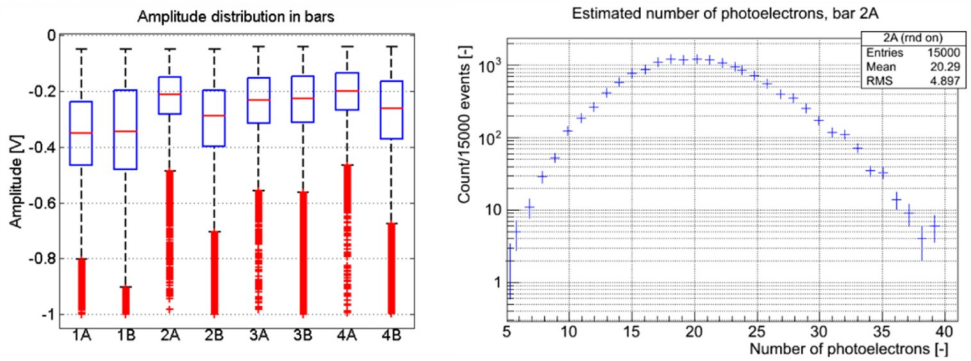

Figure 7.11: *Left:* Distribution of the amplitudes with the blue boxes representing the range from the 25 % to the 75 % quantile, the red line marking the mean value and the dotted line representing the distribution range excluding the outliers drawn as the red points. *Right:* Distribution of generated photoelectrons obtained from a Monte Carlo simulation [P3].

It is evident that the bars of the train 1 manifest larger mean amplitudes than the rest of the bars by about 30 %. This confirms the benefit of the taper. There are variations also between the remaining bars, mainly due to the non-uniform response of the PMT pixels (as confirmed by a laser measurement, see Sec. 8.2.1). The amplitude variation within one channel is caused by random processes in the signal forming — i.e. by emission of Cherenkov light, freeing photoelectrons at the MCP-PMT photocathode etc.

7.4.2 ToF performance

The time resolution of all the bars was measured and the time resolutions of two bar trains were determined. The bar resolutions were obtained from the distribution of times of a pion registration in a bar with respect to the SiPM1, as illustrated in Fig. 7.12. The time distribution was fitted by a Gaussian, the width of the Gaussian was extracted and the time resolution of the SiPM1 (12 ps) was subtracted in quadrature. For this measurement, the bars were placed again right next to each other.

The time resolution of a two bar train was determined from the time distribution of the averages of times determined by the two bars in the train (in each event, the time measured by the train is calculated as $t_{\mathrm{tr}} = \frac{1}{2}(t_{\mathrm{A}} + t_{\mathrm{B}})$).

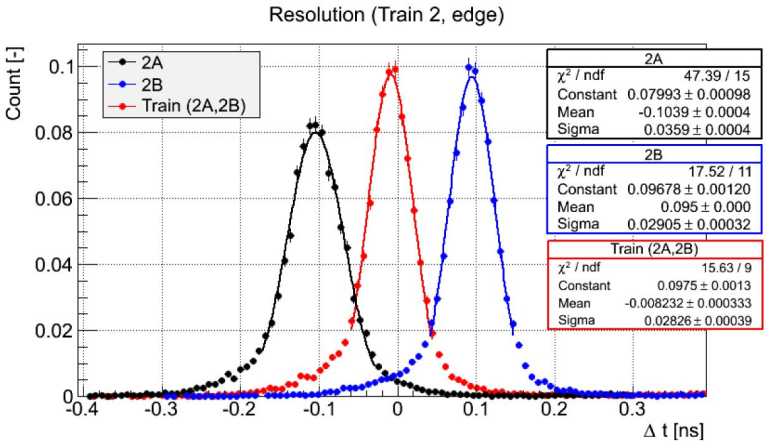

Figure 7.12: Time resolution distributions of the bars 2A and 2B, and of the two-bar train [P3].

The results for the cases of the SiPM aligned with the edge (i.e. covering the $3 \times 3\,\mathrm{mm}^2$ area of the bar ranging in x from the edge to 3 mm) and the SiPM positioned 5 mm from the edge (i.e. the x range of 5–8 mm) are listed in Tab. 7.1. The measurement error of ±2 ps was estimated from variation between 5 independent measurements.

Table 7.1: Resolution of bars and two-bar trains in picoseconds. Estimated uncertainty is ±2 ps [P9].

Train	Position	Bar A	Bar B	Whole train	(Bar A)/$\sqrt{2}$
1	edge	31	26	23	22
	5 mm from edge	40	31	28	28
2	edge	34	26	25	24
	5 mm from edge	42	31	33	30
3	edge	31	26	25	22
	5 mm from edge	41	31	34	29
4	edge	33	26	27	23
	5 mm from edge	42	29	33	30

The performance near the edge is consistently superior to the 5 mm from the edge with differences 3–10 ps. The parallel cut at the edge reflects part of the Cherenkov cone that would be lost otherwise and therefore increases light yield from a charged particle. This is effective up to about 4 mm, as shown by a simulation in Fig. 7.13b, and therefore the timing performance is degraded further from the edge. The taper of train 1 aids to reduce the impact of the lowered light yield further from the edge, as is visible especially from the train time resolutions. The overall performance of the train 1 is better by 2–6 ps.

The B bars show better time resolution both at the edge (by 5–8 ps) and at the 5 mm from the edge (by 9–13 ps). The reason for this behavior is that a part

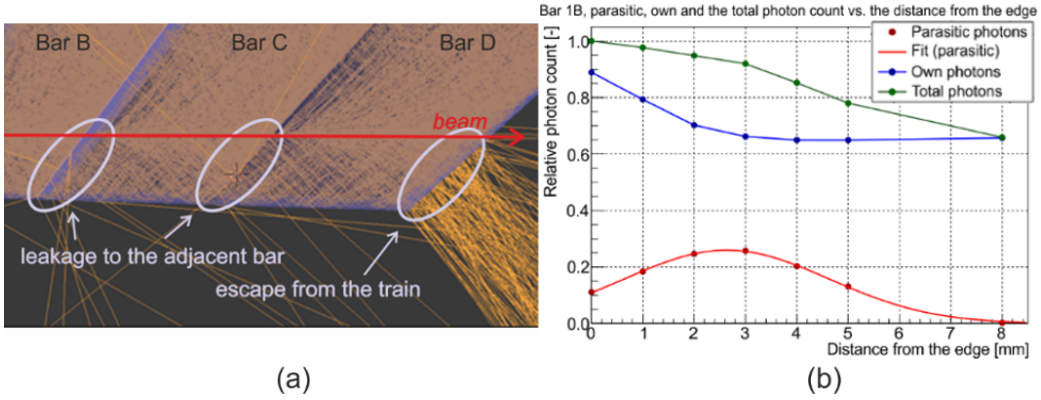

Figure 7.13: Optical leakage between bars near the train edge, (a) visualization in Geant4, (b) contribution of the own and the parasitic fractions to the total hit count in the sensor [61].

of a Cherenkov cone generated in one bar in a train leaks into the following bar in the same train. The process is visualized in Fig. 7.13 and the graph shows that the fraction of leaked photons increases up to about 3 mm, as the amount of photons reflected on the edge cut decreases, and then falls down and disappears about 8 mm from the edge.

The train time resolution ranges 23–34 ps. In theory, N consecutive independent time measurements, each with the resolution σ, yields a combined measurement with the resolution $\sigma_{comb} = \frac{\sigma}{\sqrt{N}}$. As the B bars benefit from the additional light provided by the A bars, one could argue that the measurements are not independent and without this benefit, the B bars are expected to perform as the A bars. This can be supported by a fair agreement of the train time resolution with $\frac{\sigma_A}{\sqrt{2}}$ (0–4 ps difference). However, the point of origin of the photons impacting one MCP-PMT pixel must be irrelevant, since they are all produced by the same primary charged particle and their time of propagation through the different bars is compensated by the design of the bars. This suggests a correlation of bar measurements within one train that originates further in the signal formation chain.

The results in Tab. 7.1 were obtained with the new MCP-PMT loaned by Photonis. The previously used MCP-PMT from UTA was also tested during one day of this beam test. A different bar placement[1] was used and these data cannot be used for the determination of train resolutions, however single bar resolutions were compared, where possible, with 10 % improvement for the bars of train 1 and about 30 % improvement for the remaining bars.

[1]The A and B bars were separated by a gap to measure the time resolutions of B bars without the light leakage from the A bars. The A bars were kept at their nominal place on the MCP-PMT surface, but the B bars were moved by one MCP-PMT pixel column. This bar configuration was used for both MCP-PMTs.

7.4.3 SiPM time resolution

The SiPMs did not perform the same throughout the beam test. Initially the SiPMs were installed as they were dismounted from the previous beam test. They were tested and it turned out their time resolution is worse than in the previous beam test. It was found out that the optical grease between the fused silica bar and the SiPM chip degraded. The optical grease is a transparent compound with a very similar refractive index as the fused silica and serves to optically connect the quartz bar and the SiPM front window, such that the loss of light due to reflections is minimized. To solve the issue, the SiPM and the bar were cleaned and a drop of glycerol was used as the optical grease.

SiPM time resolution deterioration was observed in the second week of the beam test. I analyzed the data and determined the time development of the combined time resolution of the two SiPMs, as this quantity is independent of changes in the ToF detector. Most of the time, only one SiPM was connected to trigger the oscilloscope and only smaller amount of measurements were performed with two SiPMs connected. I used the data with the two SiPMs and in addition I have also included the combined resolution of the SiPMs measured by the RCE. The result is plotted in Fig. 7.14.

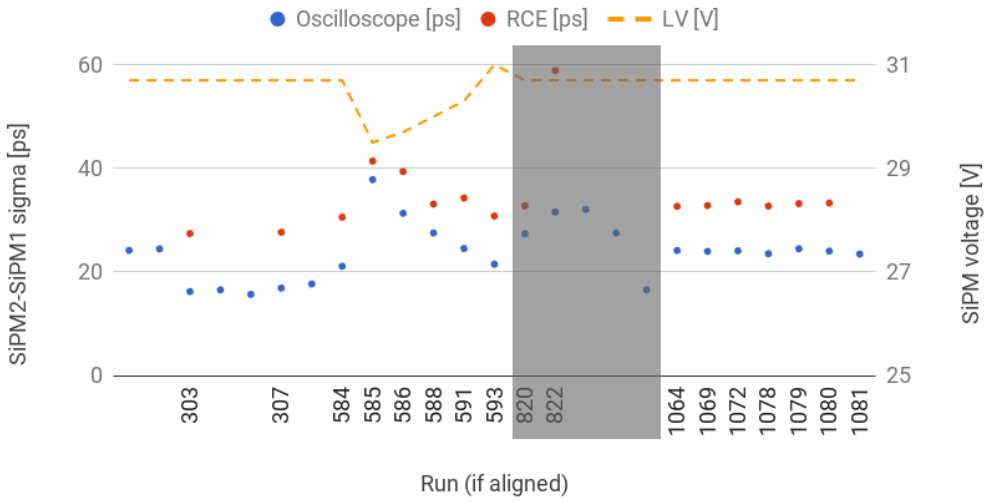

Figure 7.14: Time evolution of the combined resolution of two SiPMs throughout the beam test measured by oscilloscope and RCE (with HPTDC contribution). The supply voltage changed as indicated by the dashed orange line. Incremental RCE run numbers are used on the x axis for ordering of the measurements and pure oscilloscope measurements are placed in between appropriate RCE runs. The grayed area labels period when a coincidence unit was placed in the SiPM1 signal path introducing an additional timing jitter.

There are several regions in the figure. First two points represent measurements before the grease replacement followed by improvement of the time reso-

lution. The RCE run 584 marks the start of LV scan and it is visible that the time resolution improves with an increased LV, however already here the resolution is deteriorated, since it does not return to the values of RCE runs around 303–307. After the LV scan, a coincidence unit was added to introduce a dead time needed for the synchronous data taking of the RCE and the oscilloscope. This also introduced additional time smearing and it is not straightforward to interpret these measurements, e.g. the low point at the end of the grayed area corresponds purely to the coincidence unit jitter. The SiPM resolution stabilized again after the coincidence unit was removed from the setup, however the value was about 30 % higher than the best and at about the same level as before the grease replacement, suggesting degradation of the glycerol.

The degradation was further studied in JLO laser lab (see Sec. 8.3.1) and the effect was confirmed. A different grease was used (labeled OC-43[2]) and the SiPM resolution was monitored during the next beam tests.

7.4.4 RCE data

The oscilloscope data provide a baseline time resolution of the ToF system and it can be inferred from these data, what the resolution of the ToF with the full readout chain should be. The RCE data contain the full readout chain and the prediction can be compared to the results obtained from the RCE. The only significant contribution that is not included in the oscilloscope data is the HPTDC contribution, which was measured in a laboratory to be ∼16 ps.

I compared the resolutions of the bars obtained from the RCE with the results listed in Tab. 7.1. The time distributions obtained from the RCE were again fitted by a Gaussian and SiPM resolution was determined using time difference combinations of a bar and two SiPMs. The time distributions of bars w.r.t. SiPM1 were used as in the case of the oscilloscope data and SiPM1 resolution (23 ps) was subtracted. The results are listed in Tab. 7.2 together with the corresponding values of HPTDC contribution obtained as

$$\sigma_{\mathrm{HPTDC,i}} = \sqrt{\sigma^2_{\mathrm{RCE,i}} - \sigma^2_{\mathrm{scope,i}}}, \tag{7.4}$$

where $i \in \{A, B\}$ and the subscripts *RCE* and *scope* label the dataset from which the time resolution was determined.

Clearly, the HPTDC contributions were larger than expected and furthermore varied between channels. This needed further investigation in a laboratory as well as in the later beam tests. Partly, the worse performance was due to suboptimal calibration and in the later beam tests, the calibration was applied in the postprocessing rather than in the firmware as in this case, so that it can be easily corrected. Later, it was also shown, that inputs of a single HPTDC

[2]The OC-43 grease was provided by the SBU and I did not found out a proper reference for it. In beam tests since 2017, the Dow Corning (now DOWSIL) DC-4 grease was successfully used.

Table 7.2: Resolution of bars in the RCE measurements in picoseconds. The estimated uncertainty is ±2 ps.

Train	Position	Bar A	$\sigma_{\mathrm{HPTDC,A}}$	Bar B	$\sigma_{\mathrm{HPTDC,B}}$
1	edge	42	29	36	25
	5 mm from edge	46	24	38	22
2	edge	57	46	53	47
	5 mm from edge	61	44	51	40
3	edge	37	19	37	27
	5 mm from edge	49	27	40	25
4	edge	67	59	60	54
	5 mm from edge	67	53	58	51

chip interfere, which leads to a degradation of signals that arrive within a narrow time window (~ 0.5 ns), which is exactly the case of the signals from bars of one train. This was mitigated by a mapping of the HPTDC inputs to the ToF channels such that the bars of one train occupy HPTDC inputs as far apart as possible while spreading them across the three HPTDC chips.

7.4.5 Effect of an optical grease

The LQbars usually sit on top of the MCP-PMT faceplate without any optical bonding. This presents two steps in refractive index (fused silica → vacuum (air) → MCP-PMT faceplate (fused silica or borosilicate glass)) and causes that a fraction (about 4 % for the perpendicular direction) of photons is reflected on each transition. The light transmission can be improved by an optical grease with a similar refractive index as the fused silica.

The refractive index of the Suprasil fused silica ranges between 1.45 and 1.51 in the usable wavelength range [62]. Glycerol was used for the test of optical bonding of bars to the MCP-PMT, due to its favorable refraction index above 1.47 [63] and availability. A drop of glycerol was placed on all the bars at the light guide end and the bars were placed on top of the MCP-PMT. A comparison of the amplitude and time distributions for the bar 3A for the cases with and without glycerol is shown in Fig. 7.15.

The results confirm that the grease reduces light losses at the PMT window and therefore higher pulses are observed. The mean amplitude is higher by a factor of about 1.5 in both cases. The increased amount of light positively influences also time resolutions of bars — the resolutions are improved by 11 % for the bar 1A and by 21 % for the bar 3A. This can be compared to the expectation given by Eq. 6.7. The amplitude depends on the number of impacting photoelectrons approximately linearly and, neglecting the constant term in the equation, one

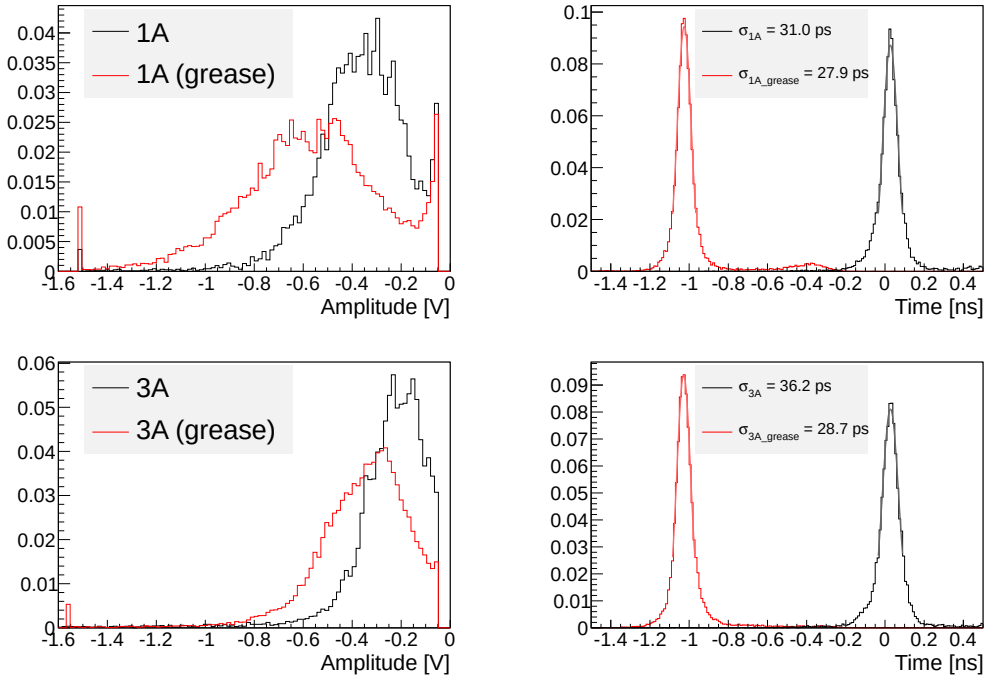

Figure 7.15: Comparison of amplitude (*left*) and time (*right*) distributions for bar 1A (*top*, with the taper), 3A (*bottom*, without the taper) with and without the grease with the loaned MCP-PMT at the HV of 1870 V. The SiPM contribution is subtracted in the time resolutions.

can obtain

$$\frac{\sigma_\mathrm{g}}{\sigma} = \frac{\cancel{\sigma_\mathrm{TTS}}\sqrt{N_\mathrm{pe}}}{\cancel{\sigma_\mathrm{TTS}}\sqrt{N_\mathrm{pe,g}}} \approx \sqrt{\frac{\bar{U}}{\bar{U}_\mathrm{g}}} = \sqrt{\frac{2}{3}} \approx 0.82, \tag{7.5}$$

where the subscript g denotes the values obtained with the grease and $\bar{U}$ is the mean amplitude. This yields expected improvement of about 18 %. This agrees well with the result for the bar 3A, but lower improvement is seen for the bar 1A, likely due to the neglected constant term in Eq. 6.7.

Although the test with grease shown significant improvement of the time resolutions, the grease was not used in further beam tests and the final detector. Reasons were mostly technical — operation of the detectors in vacuum demands use of a grease that does not evaporate or outgasses in vacuum and is radiation tolerant at the same time. Glycerol clearly cannot be used. The Epotek 305 glue used to bond the two parts of LQbars together presents a possibility. However, gluing the bars to the PMT is permanent and the bars would have to be replaced together with the MCP-PMT, while they can operate about 3 times as long.

7.4.6 Matte bars

Two pairs of newly produced LQbars were tested with sanded (matte) surfaces — one pair with matte sides of the light guide, keeping the radiator and the output face polished and the second pair with all the sides matte except for the output face and the parallel cut at radiator. The aluminum mirror on the 45° cut was preserved for both types of matte bars. These were designed to test whether only the Cherenkov photons traversing the full LQbar or the light guide of the LQbar without a reflection on its sides would be usable for proton timing. Such photons would have much smaller (essentially zero) time smearing caused by the variation of the path length and, hypothetically, should therefore provide a better time resolution.

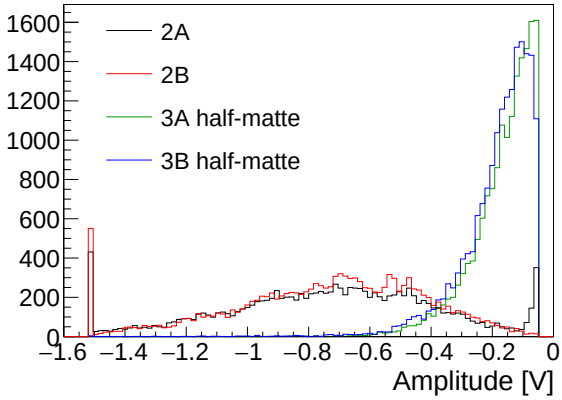

Figure 7.16: Signal amplitude distributions for bars of the train 2 (polished) and the train 3 (matte light guide). In both cases the HV was set to 1950 V. The negative polarity of the the signal originates from the MCP-PMT output polarity.

However, both the fully and partially matte bars proven to be too inefficient to be further considered. Figure 7.16 shows comparison of signal amplitudes for the case of polished bars (2A, 2B) and half matte bars (3A, 3B). In both cases, the HV was set to 1950 V and the triggering SiPM was aligned with the measured bars. The low amplitudes can be compensated by increasing the HV and therefore the gain of the MCP-PMT, but the timing performance is degraded due to a too low number of photoelectrons. The mean number of photoelectrons was estimated from a simulation (as shown in Fig. 7.11) to be about 20 ± 5 for the fully polished bars without the taper. As Fig. 7.16 shows, there is about 5 times less photoelectrons registered for the half-matte bars, which suggests about 3–5 photoelectrons produced by a half matte bar and even less by a fully matte bar. Therefore, the smearing due to the TTS in the MCP-PMT dominates the time resolution.

7.4.7 Bar correlations

Analysis of the oscilloscope data shown large correlations between times with respect to the trigger registered by two bars of the same train, as illustrated in Fig. 7.17. A correlation between 65–73 % was observed. In case of independent measurements, there should be no correlation.

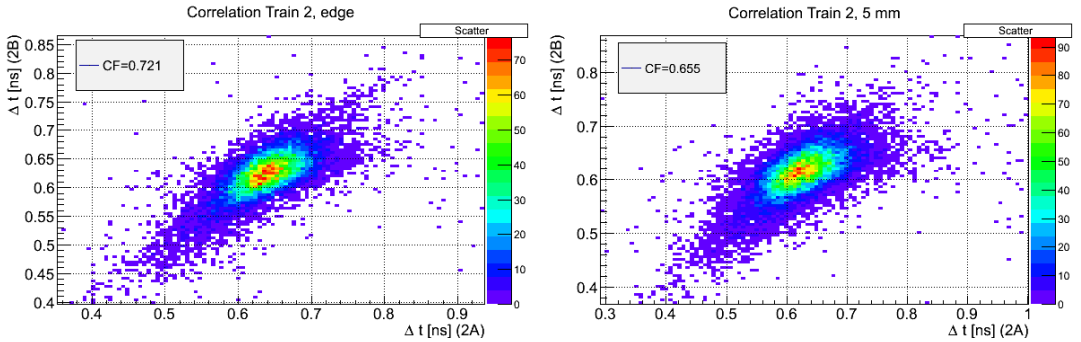

Figure 7.17: Example of bar correlations observed during the beam test — bars of train 2 (courtesy of Libor Nožka).

The major part of the correlation is however caused by the time reference, as I demonstrate below. What is happening is that the SiPM trigger itself is not perfect and manifests a finite time smearing (12 ps for the case of the measurement shown in Fig. 7.17). The time fluctuation of the trigger in an event is the same for all measured channels and therefore causes a correlation.

To confirm this hypotheses, I prepared a toy simulation. Simulated events were obtained by randomly generating three values — time registered by the first bar t_1, the second bar t_2 and by the trigger t_{trig}. These times correspond to the times measured with respect to the ideal clock, offsets between them (caused by the distance between the SiPM and the ToF and by different cable lengths) are neglected. The values were combined to obtain the quantities measured by the oscilloscope:

$$\begin{aligned} \Delta t_1 &= \Delta t_{2\text{A}} = t_1 - t_{\text{trig}}, \\ \Delta t_2 &= \Delta t_{2\text{B}} = t_2 - t_{\text{trig}}. \end{aligned} \tag{7.6}$$

A scatter plot is produced from the points $(\Delta t_1, \Delta t_2)$ and the correlation factor is calculated. The correlation clearly depends on the distributions used for the random generation of the values t_1, t_2 and t_{trig}. E.g. the Gaussian distributions would result in an ellipse, which does not correspond fully to the Fig. 7.17. Instead, a double Gaussian distributions, as introduced in Sec. 7.3.2, is utilized. Different parametrizations, based on fits of data distributions, are used for the times measured by bars and for the trigger time from SiPM

$$\begin{aligned} f_{\text{bar}}(t) &= G(t, 1, \mu, \sigma) + G(t, 0.05, \mu + \sigma, 2\sigma), \\ f_{\text{SiPM}}(t) &= G(t, 1, \mu, \sigma) + G(t, 0.1, \mu + 2\sigma, 4\sigma), \end{aligned} \tag{7.7}$$

where μ is the mean value of the distribution ($\mu = 0$ in the following), σ is the simulated time resolution and $G(t, a, \mu, \sigma) = \frac{a}{\sqrt{2\pi\sigma^2}} \exp -\frac{1}{2}\left(\frac{t-\mu}{\sigma}\right)^2$ is the Gaussian function.

The simulated time resolution for the bars is set according to results of the train 2 (see Tab. 7.1) to 34 ps and 26 ps for the 2A and 2B bar, respectively. The time resolution of the trigger is varied between 0 and 25 ps. The resulting time distribution simulated for bar 2A is illustrated in Fig. 7.18.

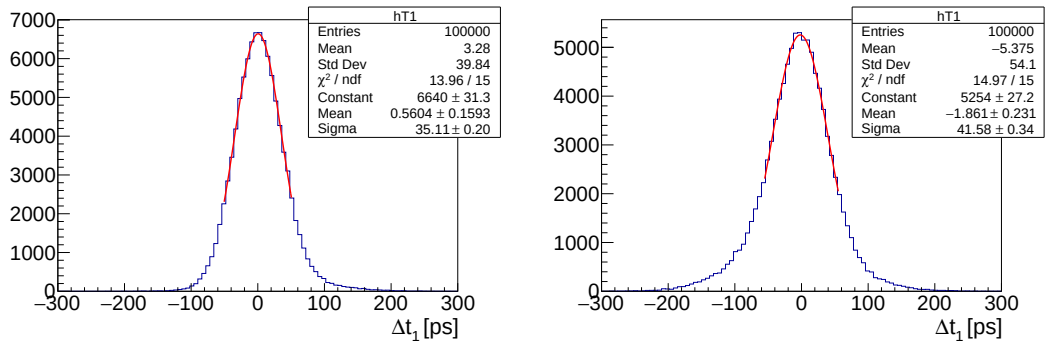

Figure 7.18: Simulated time distribution for bar 2A with the ideal trigger ($\sigma_{\text{trig}} = 0$, *left*) and for $\sigma_{\text{trig}} = 15$ ps (*right*).

The obtained correlation plots for four values of σ_{trig} are shown in Fig. 7.19. It is visible that the plots resemble the shape of the observed bar correlation from the data very well. However, a higher σ_{trig} than measured 12 ps is needed to obtain as high correlation as for the data, suggesting an existence of an additional correlation of the bars.

7.5 2016 beam tests

The year 2016 was filled with preparations for the installation of the second AFP arm and the ToF detectors. There were three ToF beam tests (in July, September and October, 5 weeks in total) and one tracker beam test (in April, one week) during this year. The tracker planes were successfully tested in their final assembly mounted on the tilted carbon fiber reinforced aluminum plates.

Full four-bar trains were tested for the first time in ToF. Also, the performance of new trains with 2 mm and 4 mm thick radiators was measured. For the purposes of the beam tests, these bars were labeled train 5 (2 mm radiator) and train 6 (4 mm), while the labels of the previously utilized trains were kept. The trains 5 and 6 were designed as replacements for the train 1 and 2, respectively.

During the July beam test, two ToF detectors were installed in the test setup. One was using a new miniPlanacon MCP-PMT (serial no. 9002053, with a reduced anode gap) with the almost final design of the bar and The PMT holder. The second detector was built of an older two inch Planacon MCP-PMT [64]

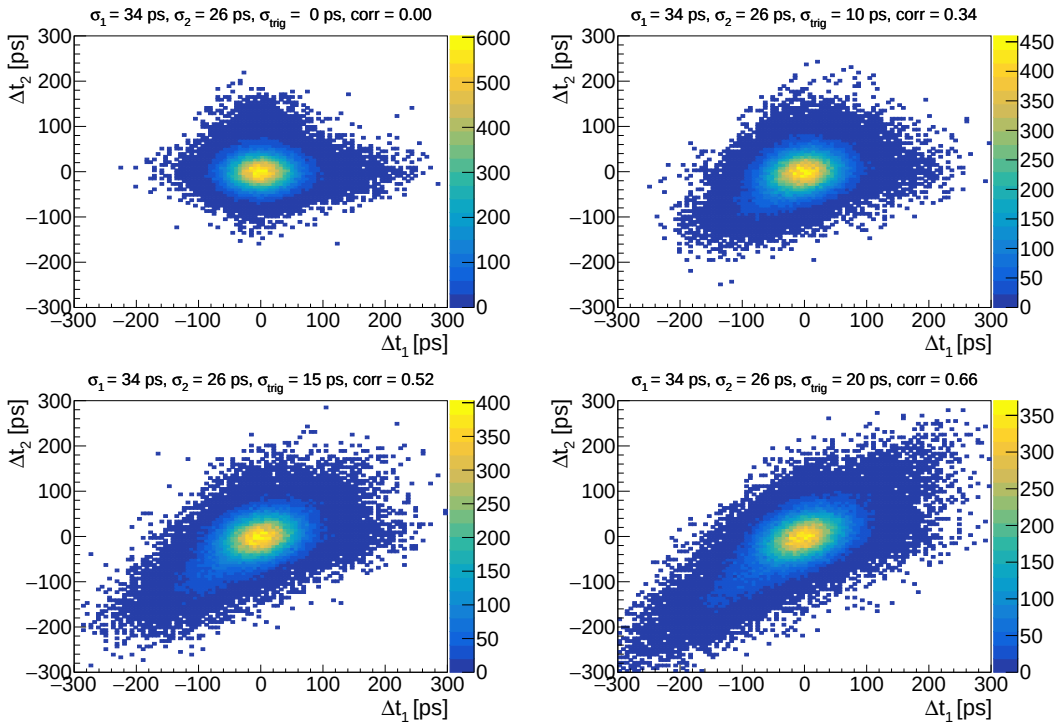

Figure 7.19: Correlation plots of simulated time distributions of two bars of a train for increasing time resolution of a trigger.

with 8×8 channels and the older bar holder with an adapted PMT holder. The miniPlanacon MCP-PMT was operated mainly at the HV of 2100 V, corresponding to the gain of $5 \cdot 10^4$, and the Planacon PMT at 2500 V, corresponding to a similar gain (the Planacon PMT manifested large gain variations between channels of up to 50 %). The ToF detector was also tested on the Roman pot flange for the first time during the autumn beam tests.

7.5.1 ToF performance

Several bar configurations were used in the beam test to understand the obtained time resolutions with the main focus on the full four-bar train resolution. The new miniPlanacon MCP-PMT was used in the presented measurements. The CFD threshold was set for all channels to −150 mV based on the transition between noise pedestal and signal in the distributions of signal amplitudes.

The time resolution of the SiPM trigger was again determined from the simultaneous measurement of three SiPMs. The SiPM1 used for the presented measurements had intrinsic resolution of $\sigma = 10$ ps (FWHM = 23 ps) during this beam test. The time resolution of the SiPM1 was periodically checked against SiPM2, so that any deterioration would be timely detected. The time resolutions were again determined from Gaussian fits (σ) and also in terms of FWHM of the time distribution. The time resolution of the SiPM1 was subtracted in

Table 7.3: Resolution of selected single bars at their edges. The estimated uncertainty is ±2 ps in σ and ±5 ps in FWHM [P14].

Bar	σ [ps]	FWHM [ps]	Bar	σ [ps]	FWHM [ps]
1B	22	54	5B	22	53
2A	24	58	6A	20	50
2B	24	58	6B	21	52
5A	23	60			

quadrature in the presented values. The presented uncertainties were obtained from 5 consecutive measurements of the same bar.

The time resolutions of selected individual bars without an influence of any other bars were obtained by placing only the bar of interest into the bar holder and keeping the remaining slots empty (aluminum dummy radiator bars were used to ensure the proper spacing of the holder plates). The results are listed in Tab. 7.3. The time resolutions are almost the same for the listed bars, with bars of train 2 being slightly worse (they are the only bars in the table without the taper) and train 6 slightly better, although in both cases the values agree within the uncertainty of the measurement.

The train time resolutions were determined from the time distribution of the average time measured by a train $t_{\text{avg}} = \frac{1}{4}(t_{\text{A}} + t_{\text{B}} + t_{\text{C}} + t_{\text{D}})$. An example of individual bar time distributions together with the t_{avg} distribution are plotted in Fig. 7.20.

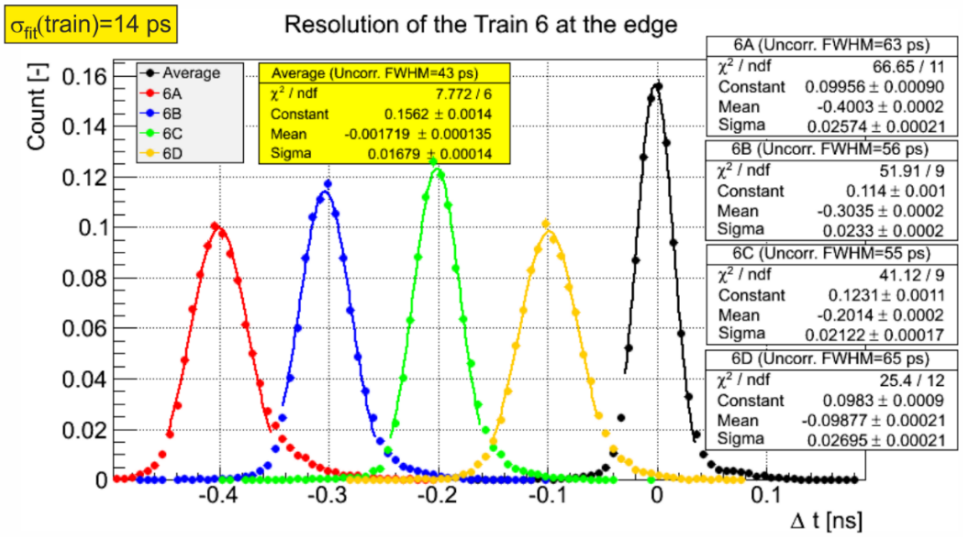

Figure 7.20: Time distributions of individual bars of train 6 and of the whole train (black) for the measurement at the edge, PMT 9002053. The *sigma* and *FWHM* values in the statistic boxes are not corrected for the SiPM contribution [P14].

The obtained time resolutions for all the 6 trains are presented in Tab. 7.4. The trains without the taper manifest consistently worse time resolution than

Table 7.4: Time resolution of trains. The estimated uncertainty is ±1 ps in σ and ±2 ps in FWHM [P14].

	edge of the ToF		5 mm from the edge	
Train	σ [ps]	FWHM [ps]	σ [ps]	FWHM [ps]
1	14	34	15	38
2	15	34	17	41
3	15	34	17	42
4	15	35	17	43
5	14	36	17	36
6	14	35	15	37

the ones with the taper, although within the uncertainty. The same applies to the measurements further from the edge with respect to the edge measurements. The trend of worsening the time resolution was also confirmed by scanning the distance from the edge in several steps from 0 up to 20 mm, as is shown in the left part of the Fig. 7.21.

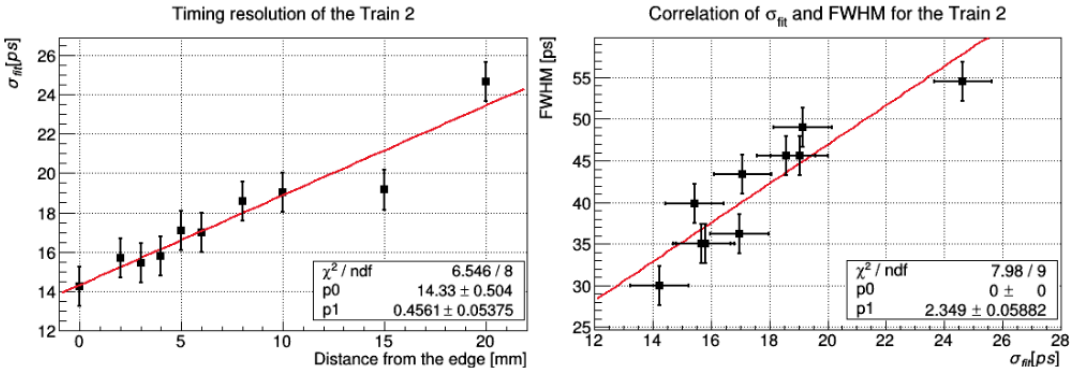

Figure 7.21: *Left:* Timing resolution of the Train 2 as a function of the distance from the edge; *right:* correlation of σ and FWHM measures of the timing resolution [P14].

The right part of the Fig. 7.21 plots the correlation of σ and FWHM measures of the time resolution. There is approximately a linear dependence between the two measures with FWHM $\approx 2.35\sigma$, which is the dependence expected for a Gaussian distribution. This result justifies the use of σ for the time resolution of bars and trains even though the distributions slightly differ from an ideal Gaussian.

7.5.2 ToF crosstalk

The main source of a crosstalk between ToF channels, as was shown earlier, is within the MCP-PMT. To asses the leakage of a signal from one channel to others, measurements with individual bars placed on top of the MCP-PMT were

performed. Two oscilloscopes were used for this measurement with a common trigger, so that 8 channels could be recorded. Since most of the ToF bars were removed from the setup, I will be referring to the MCP-PMT channels by their number, as illustrated in Fig. 7.22.

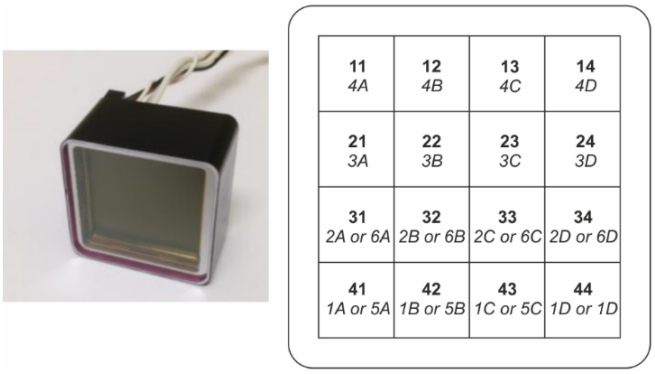

Figure 7.22: Pixels of miniPlanacon MCP-PMT with their designed bar occupancy [P14].

The results for bars 6A and 6B placed alone on the MCP-PMT are shown in Fig. 7.23. The channel occupied by the bar is in red and there are four values characterizing each measured channel — the mean amplitude of signals m and the level of crosstalk ci represented by the percentage of signals with amplitude below the given threshold of $-100\,\mathrm{mV}$, $-150\,\mathrm{mV}$ or $-200\,\mathrm{mV}$. The threshold of $-100\,\mathrm{mV}$ corresponds approximately to the limit of the noise pedestal, $-150\,\mathrm{mV}$ was used as the CFD threshold for the timing studies and $-200\,\mathrm{mV}$ is listed as a potential CFD threshold setting that would lead to a lower noise and crosstalk rate of the channels.

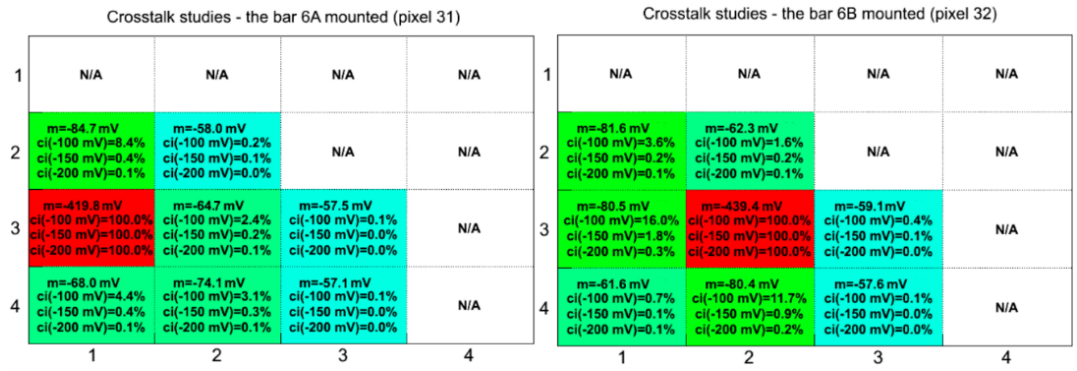

Figure 7.23: Leakage of the signal to adjacent pixels from the bar 6A (*left*), the bar 6B (*right*). The axes give the MCP-PMT pixel number, as shown in Fig. 7.22 [P14].

The results show decreasing amount of crosstalk for increasing absolute value of threshold from up to 16 % for $ci(-100\,\mathrm{mV})$ down to below 0.5 % for $ci(-200\,\mathrm{mV})$.

The crosstalk is enhanced if more bars are added to the setup, as illustrated for the case of bars 6A and 6C in Fig. 7.24. The crosstalk within the train is of the main interest here — the empty channel 32 (in between channels 31 and 32 occupied by bars) manifests 7 % of coincidences for the $ci(-150\,\mathrm{mV})$. The right part of the figure shows the amplitude distributions of the signals in pixel 32 for the empty MCP-PMT (pedestal only), the occupied pixel 31 and the two neighboring pixels occupied. The last case is relevant for estimating the amount of the crosstalk contribution from pixels within a train. The mean amplitude in the empty pixel 32 decreases by 43 mV (from −56 mV to −99 mV). This corresponds to 8 % crosstalk contribution, as the mean amplitude in the same pixel with all the bars from the train mounted is −523 mV. The main concern here is degradation of a train time resolution, as the crosstalk introduces correlation between measurements.

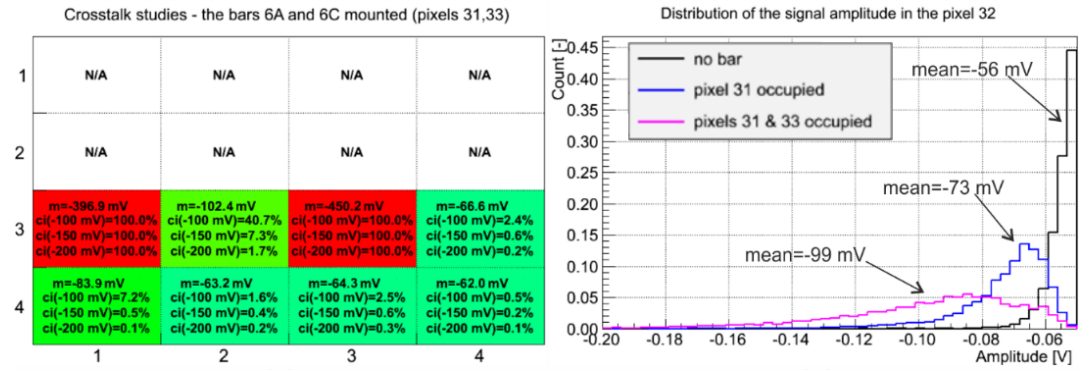

Figure 7.24: *Left:* leakage of the signal to adjacent pixels from the pair of bars 6A and 6C (the axes give the MCP-PMT pixel number, as shown in Fig. 7.22). *Right:* histogram of the signal amplitudes in the empty pixel 32 in different bars configuration [P14].

7.5.3 ToF efficiency

The efficiencies of ToF channels were determined from the RCE data. The events with a single track in SiT were selected and the efficiency was determined as the fraction of such events with the track pointing to a given ToF channel, in which the ToF channel responded. The efficiency at the selected operating HV of the PMT (2100 V for this PMT) and the CFD threshold (−150 mV) was of the main interest and is shown in Fig. 7.25.

The left part of the figure shows the efficiency of individual bars. It is clear that the train 1 performs notably better than the rest of the trains, as it is the only train with the taper in this configuration. Also, the A bars (except for 1A) manifest lower efficiency than the following bars in a train, since the B–D bars receive the additional photons from the preceding bar. Finally, small variations between channels can be attributed also to the non-uniformity of the MCP-PMT

response, as I confirmed in a laser lab measurement (see Sec. 8.2.1). However, the bar 4D manifests larger efficiency than can be attributed to these effects, possibly due to a noisy CFD channel.

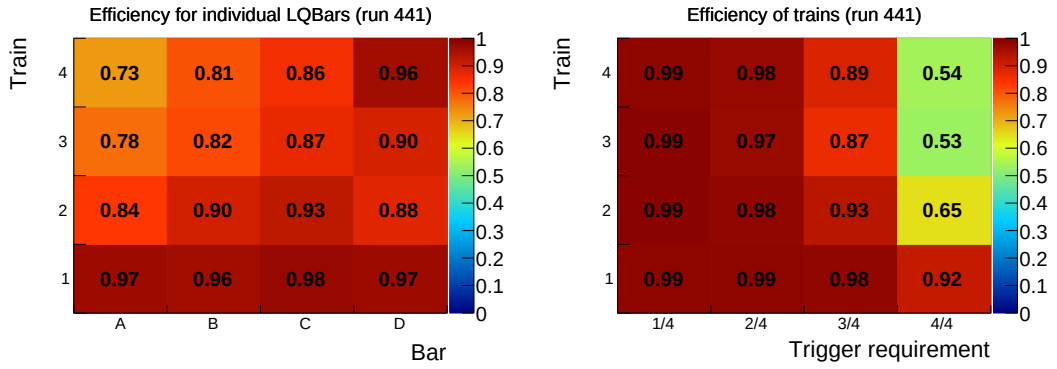

Figure 7.25: Efficiency of individual bars (*left*) and trains (*right*) for the HV of 2100 V and the CFD threshold of −150 mV.

The overall bar efficiency is high, mostly between 80–90 % in trains 2–4 and above 96 % in the train 1. The ToF should also provide a trigger for ATLAS CTP when a proton passes through the AFP, therefore, it was needed to estimate the trigger efficiency of trains. The trigger module should produce output when a selected number of bars (out of the total four) within a train responds. An estimate of the trigger efficiency for the four possible settings calculated from the RCE data is shown in the right part of Fig. 7.25. At least one bar fires in 99 % of events when a particle passes through any train. The efficiency decreases with increasing requirement on the number of fired bars, but at the expected requirement of 3 out of 4 bars (3/4) the efficiency is still above 87 %.

7.5.4 HPTDC contribution

The HPTDC did not behave as expected in the 2015 beam test. In the 2016 beam tests, the signals from each train were measured by a different HPTDC chip to avoid an interference. The signal polarity in each line between the CFD and the HPTDC modules was verified and all HPTDC modules were calibrated. These measures lead to a significant improvement, as illustrated in Tab. 7.5, where the resolutions of bars of the train 6, as measured by the oscilloscope and the RCE, are compared. The HPTDC contribution is again calculated using Eq. 7.4.

The HPTDC contribution for individual bars is in range 12–17 ps. The spread of measured contributions suggests a small variance in the performance of individual HPTDC channels, however it is within the uncertainty of measurement. The HPTDC contribution to the train resolution should be smaller than the individual bar contributions by approximately a factor of 2 (the factor would be exact for a constant bar contribution σ_{HPTDC} to all bars, as the contribution to the average train time is then $\frac{\sigma_{\mathrm{HPTDC}}}{\sqrt{4}}$). The result is sensitive to small variations

Table 7.5: Resolution of bars of train 6 as measured by the oscilloscope (σ_{scope}) and the RCE (σ_{RCE}). The contribution of the HPTDC σ_{HPTDC} is determined from these two values. The estimated uncertainty is ± 2 ps for the bar resolutions and ± 1 ps for the train resolutions.

Bar	σ_{scope} [ps]	σ_{RCE} [ps]	σ_{HPTDC} [ps]
6A	25	28	12
6B	21	26	15
6C	23	26	12
6D	28	32	17
train average	14	15	5

of the measured train resolutions. Considering the measurement uncertainty, the $\sigma_{\text{HPTDC}} = (5 \pm 1)$ ps for the train measurement is consistent with the contributions to the individual bars (with the estimated uncertainty of ± 2 ps), except for the bar 6D, where the values agree within 2 standard deviations.

7.5.5 First Sensor SiPM

A new SiPM was tested in the September 2016 beam test aiming to serve as an additional reference and as a spare in a case that any of the STM SiPMs would break. The new SiPM was purchased from the First Sensor company selling SiPM chips developed by Fondazione Bruno Kessler (FBK). The SiPM-NUV3S [59] chip capable of detecting light in near ultra-violet spectrum with the $40 \times 40\,\mu\text{m}^2$ cell size was selected.

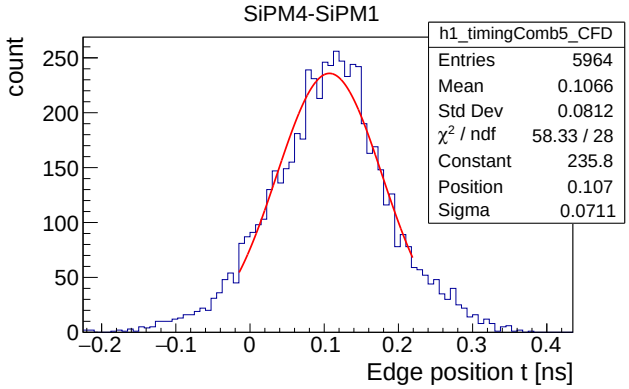

Figure 7.26: Time resolution of the First Sensor (FBK) SiPM.

The measured time resolution of the new SiPM was however too high, as is illustrated in Fig. 7.26: $\sigma = 70$ ps after the subtraction of the reference SiPM1 contribution.

7.6 2017 beam tests

The ToF detectors were installed in the LHC tunnel in April 2017 with Photonis miniPlanacon MCP-PMTs without the ALD coating with a short expected lifetime. Newly manufactured ALD coated miniPlanacon MCP-PMTs with the reduced anode gap and modified internal circuitry were tested during the beam tests in July and September 2017. The circuitry modifications were done by Photonis with the aim to reduce the electronic crosstalk and increase signal amplitudes and were based on modifications done by ALICE Fast Interaction Trigger group [65]. Also, the first prototype of the trigger module was tested.

ToF detectors in the LHC tunnel were not performing as expected and I describe the issues in detail in Chap. 9. During the beam test, the performance of the ToF in vacuum was verified and readout of the time-over-threshold (ToT) functionality of the CFDs was implemented in the HPTDC, calibrated and tested.

7.6.1 Performance of ALD coated MCP-PMTs

The high voltage scan was performed for the new MCP-PMTs and optimal values of 1900 V (PMT 9002096) and 1850 V (PMT 9002097) were found, corresponding approximately to gain of $5 \cdot 10^4$ (based on the gain values specified in the test results sheets of the PMTs).

Already during the HV scan, relatively large ringing (i.e. dampened oscillations in the waveform) was observed in the trailing edge of the pulses. The pulse shape is compared in Fig. 7.27, where the signals coming from the bar 3B after the passage of pions are overlaid for the previously used PMT 9002053 (operated again at HV of 2100 V) and the new PMT 9002096. A larger amplitude of the ringing is manifested in the pulses from PMT 9002096. The same behavior was present in all channels and also with the PMT 9002097.

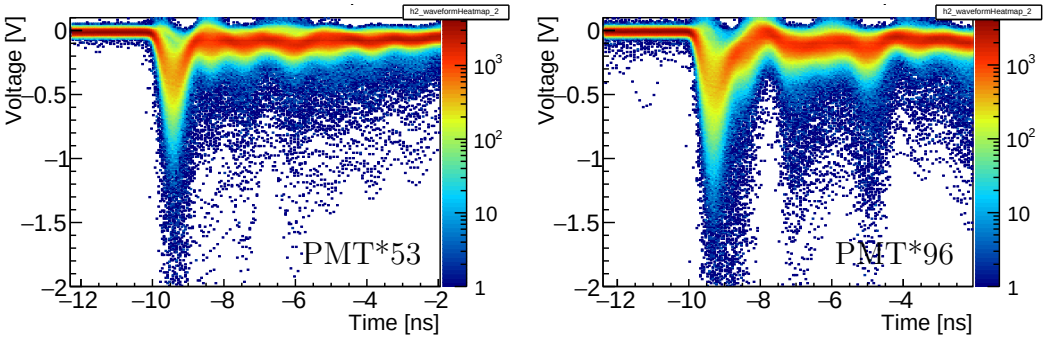

Figure 7.27: Raw signal waveforms in bar 3B for MCP-PMT 9002053 (*left*) and 9002096 (*right*). There are 32768 waveforms overlaid in each plot and the color map shows the amount of overlaid waveform points.

The crosstalk is illustrated in Fig. 7.28. Both the new PMTs manifest higher crosstalk amplitudes in the neighboring channels by up to 25 %.

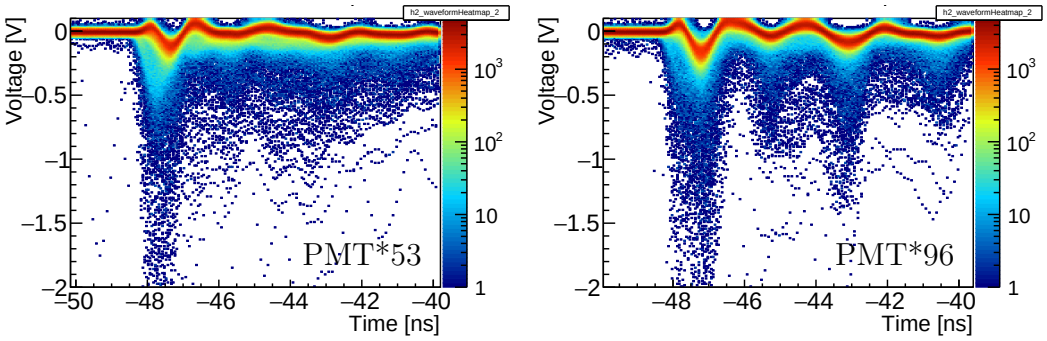

Figure 7.28: Raw crosstalk waveforms in bar 4B with signal in train 3 for MCP-PMT 9002053 (*left*) and 9002096 (*right*). There are 32768 waveforms overlaid in each plot and the color map shows the amount of overlaid waveform points.

Time resolution of train 3 was measured with both new PMTs and the result for PMT 9002097 is shown in Fig. 7.29. The time resolution of the whole train (i.e. the width of the distribution of the average from the 4 time measurements within the train) at the edge of the parallel cut of the radiator is (27 ± 1) ps for the PMT 9002096 and (25 ± 1) ps for the PMT 9002097. In both cases, the 14 ps contribution of SiPM2, used for triggering, is subtracted.

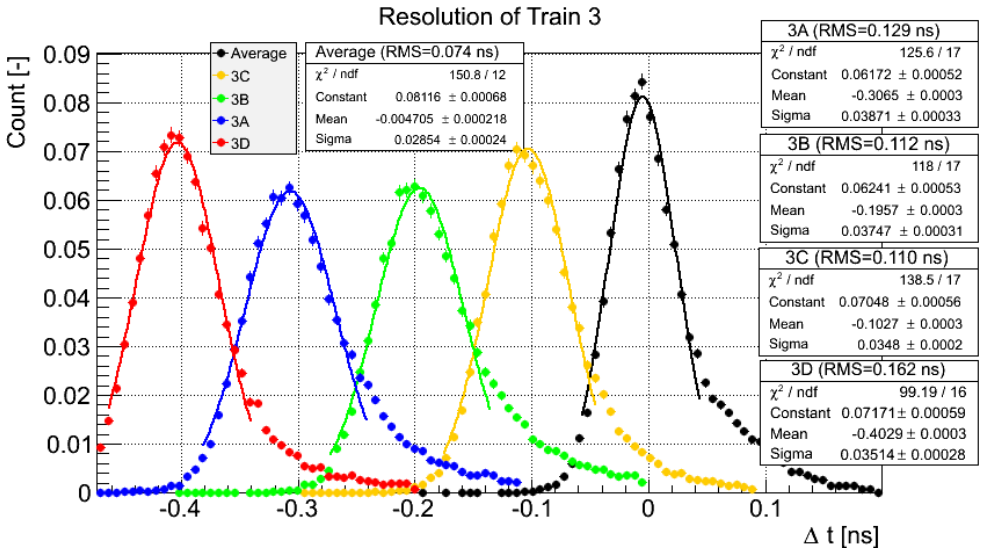

Figure 7.29: Time distributions of individual bars of train 3 and of the whole train (black) for the measurement at the edge, PMT 9002097. The *sigma* values in the statistic boxes are not corrected for the SiPM contribution.

The time resolutions are significantly worse from the ones measured in the beam tests in 2016. Comparing with Tab. 7.4, the resolutions are worse by at least 10 ps. This, together with the worse crosstalk performance of the new PMTs eventually lead to replacement of the new PMTs. They were tested in JLO laser laboratory and later also in UTA picosecond timing facility, which Photonis

acknowledges as their reference laboratory. The increased level of the crosstalk and the ringing was confirmed. The tests lead to the conclusion that the modified internal circuitry of the PMTs is causing the issues. E.g. the MCP output signal (not needed for use in ToF) was removed including the 1 MΩ resistor between the MCP output and the ground (see Fig. 7.30). However, simulations done by Vladimír Urbášek (JLO) shown that this reduced dampening of the ringing, causing the observed behavior. Also, a discussion with ALICE experts revealed that their modifications were more complex than what Photonis did in the case of the AFP.

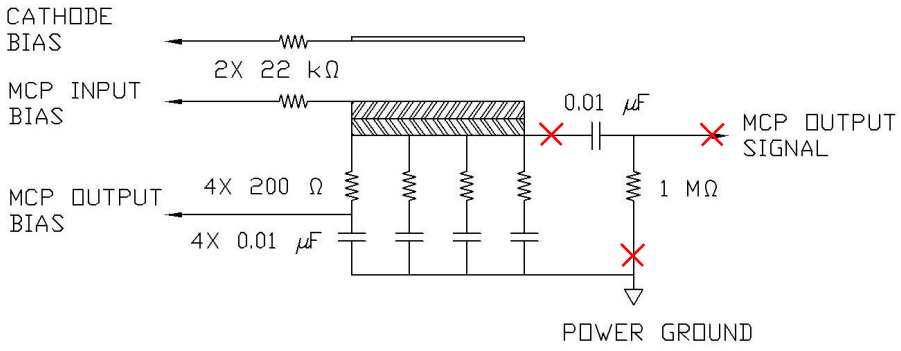

Figure 7.30: Schematic of the internal connections of Photonis miniPlanacon MCP-PMT [53]. The red crosses mark the removed MCP output and associated components of the modified MCP-PMT.

7.6.2 Trigger module

The AFP ToF trigger module has two functions:

- providing the trigger pulse for the ATLAS CTP when selected number of bars within a train responds and
- passing the CFD output signals (LVPECL) through only if the selected number of bars within the given train fires to limit the rates at the HPTDC input.

Both functions were tested during the July 2017 beam test.

Limiting of the CFD output rates was of the main interest. The trigger module was connected, as it should be placed, in the signal path between the CFD and the HPTDC. The RCE data were recorded for all the possible settings of the required number of bars that responded within a train. The options range from the passthrough, labeled as 0/4, (all the signals are let through) to 4/4 (either all signals from the train fire and are let through, or no signal from the train is let through). It was expected that the 0/4 and 1/4 settings should yield the same results, with the bar efficiency dropping for further increases of the

required number of fired bars according to the calculations shown in the right part of Fig. 7.25 and reaching the same value for all bars in the train for the 4/4 setting.

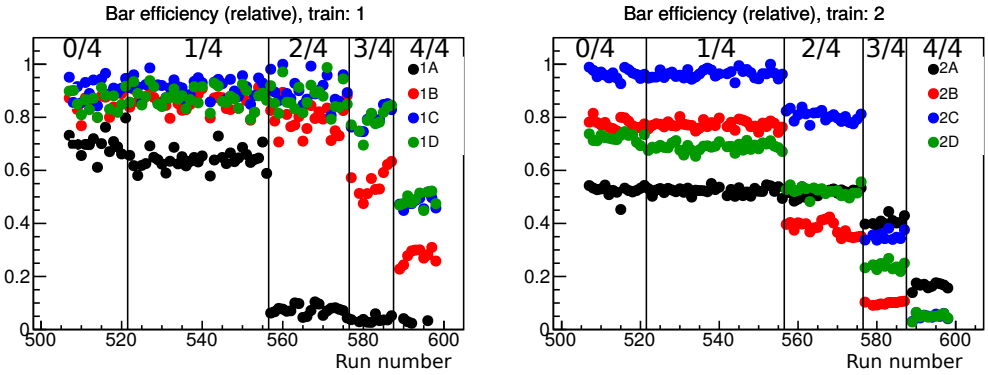

Figure 7.31: Efficiency of ToF channels for different settings of trigger requirement.

Figure 7.31 shows resulting efficiencies, I obtained in case of trains 1 and 2 for all the possible trigger requirements. The efficiencies were overall lower than in the previous beam test and larger variations between bars within a train were observed. The main reason was that only one SiT plane was available in this beam test, leading to high amount of fake tracks from noisy pixels of the SiT plane. I partially corrected for this by renormalizing the efficiencies to the maximum reached among the bars of a train, however the variations within the train were preserved. Still, these data are useful to assess the functionality of the trigger module and they show several issues with the module.

First, the expectation of the same efficiency for the 4/4 setting is not met for any train. A signal from some bars disappeared, as seen e.g. in the case of the bar 2B. The same performance at 0/4 and 1/4 settings is manifested for all displayed bars except for 1A. Furthermore, the efficiencies of bars 1C, 1D and 2A do not change between 1/4 and 2/4, while for 1A there is too large drop in the efficiency between the two settings and the efficiency essentially does not change for the increasing requirements.

These results led to a revision of the trigger module design. It turned out that the implementation of the N/4 selection by a power combiner followed by a threshold comparator is highly temperature dependent. Temperature stabilization was implemented and the voltage thresholds for individual N/4 requirements were fine tuned.

Also, a preliminary test of the output trigger pulse (common for the four trains) was performed during the beam test. The trigger module was to provide two output pulses — one when any of the four trains fulfill the N/4 requirement and second if a selected train meets the requirement. The first mentioned pulse worked, although the efficiency was affected by the temperature dependence of the threshold comparator. The second output was not fully prepared at the time.

7.6.3 ToF in vacuum

The main issue of ToF installed in the LHC tunnel was low efficiency (as is described in Chap. 9). One of the hypotheses, presented by Sune Jakobsen (CERN), was that the efficiency of the MCP-PMT can be affected by operating in vacuum. Since in all the previous beam tests the ToF was operated in air, a test with vacuum was conducted to see whether there is any effect. The ToF detector with one SiT plane were enclosed in the Roman Pot. First, data were taken with the air inside the pot and then the vacuum pump was turned on together with a cooling of the SiT plane.

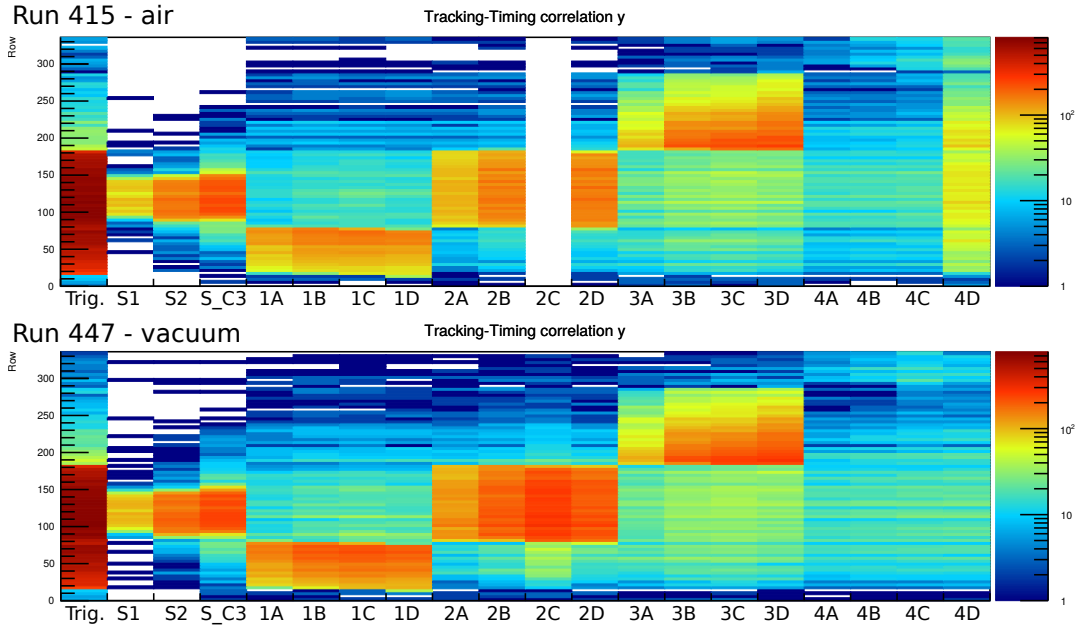

Figure 7.32: Correlation between response in ToF channels (and SiPMs) and y coordinate of the track registered by the SiT for runs with detectors in air (*up*) and in vacuum (*down*). Two channels were not functioning properly in the earlier — 2C (bad connection) and 4D (a low threshold on CFD).

The comparison of data taken with air and with the vacuum in the pot, shown no difference, as illustrated in Fig. 7.32. The issues with signal from bars 2C and 4D were observed in the run with air and they were fixed when the beam area was accessed to switch on the vacuum pump. Data with air were not retaken since the remaining channels shown no difference between the air and vacuum.

7.7 Summary

The ToF detector was extensively tested during the beam test campaigns and this chapter presented tests, measurements and analysis I performed or participated in.

The time resolution of ToF without the HPTDC contribution was measured and it was shown that the best achieved time resolution of individual bars was 20–30 ps depending on the bar position within the train and whether the bar had the taper. The trains with the taper manifested better time resolution by 5–15 %. The first bar within a train is always handicapped by the missing light leak that the consequent bars receive from their predecessors. The time resolution of the full trains starts at 14–15 ps.

The best time resolutions were achieved near the edge of the parallel cut of the radiator part of a bar. The dependence of the resolution on the distance from the edge was shown in Fig. 7.21. The dependence is approximately linear with the train 2 time resolution growing from 14 ps at 0 mm to 24 ps at 20 mm from the edge. As the bar geometry is the same on both the A and the C side of ATLAS and the ToF detector is rotated by 180° around the x axis between the two sides, the best time resolution is achieved for a different part of the diffractive protons hit pattern, as illustrated in Fig. 6.5.

The ToF detector was integrated into the common AFP readout that uses the RCE system. The time measurements were digitized using the HPTDC modules, which add an additional smearing to the measurement. As I shown in Tab. 7.5, the HPTDC contribution to the single channel time resolution was 12–17 ps. Combined ToF train resolution is therefore 15–30 ps over the AFP acceptance.

The crosstalk between bars was measured and it was shown that there is a negligible optical crosstalk, except for the light leaking from one bar to the next within a train. Within one train, the crosstalk between channels results in correlation of measurements in the train. Correlations of up to 20 % were observed in the RCE data (using different SiPMs as a reference for the bars being evaluated to avoid a trigger induced correlation). The crosstalk between bars of different trains reduces the ToF ability to handle a high pileup. E.g. in a case of two protons in one ToF arm within an event, the time measurement of the second proton is spoiled by the first one, if the crosstalk is large, even if they hit different trains. The results for an MCP-PMT with the reduced anode gap shown up to 12 % events with the crosstalk contribution above the noise pedestal to the neighboring channel. Typically the crosstalk pulse starts in the positive voltage (opposed to the negative signal pulse) followed by several dampened oscillations with amplitude of 8 % of the signal pulse causing it.

ToF channels manifested high efficiency of 80–98 % per bar and above 87 % efficiency when requiring 3 out of 4 bars within a train to respond. Bars with the taper performed significantly better, with efficiency above 96 % per bar and 98 % for the 3/4 requirement.

The ALD coated Photonis MCP-PMTs were tested during 2017 beam tests, promising an extended lifetime of about 10 C cm^{-2}, corresponding to about a year of operation in the AFP [10]. These performed significantly worse with train time resolutions above 25 ps and increased crosstalk. Therefore, these MCP-PMTs were not installed and they were replaced in 2018.

Chapter 8

Laser laboratory testing

The beam tests verified the performance of the whole ToF detector, comprising the LQbars, MCP-PMT detector and readout electronics. However, measurements of MCP-PMT and SiPM detectors using a controllable pulsed light source were needed to better understand contributions of individual components of the ToF system. Pulses with the width of the order of picoseconds, or narrower, were needed to characterize the detectors with time resolutions in the range 10–50 ps. The laser laboratory at the Joint Laboratory of Optics offered the possibility to perform such measurements.

In addition, an MCP-PMT illuminated by a pulsed laser provided a stable output pulses for tests of the readout electronics. A typical MCP-PMT pulse has rise time of 500 ps and width of less than 1 ns, which is beyond the capability of pulse generators commonly found in laboratories.

8.1 Measurement setup

The Coherent Mira 9000 laser system with 2nd (420 nm) and 3rd (280 nm) harmonics generation with the pulse width of 150 fs was used as the light source for measurements. The laser system operates at 50 MHz pumping frequency and, by default, a pulse is produced at the output port with 50 kHz rate.

Measurements needed to be performed in the dark. The lights in the laboratory were switched off for the measurements and the measurement setup was enclosed in a dark box build from a black foam core cardboard. The laser light was attenuated by a set of neutral density (ND) filters and coupled into an optical fiber after the harmonics generator and the fiber was routed into the dark box. Initially, the output end of the fiber cable was fixed to a holder and the device under test (DUT) was placed on a manually movable table allowing positioning of the DUT in the plane perpendicular to the laser beam axis, as shown for the case of miniPlanacon MCP-PMT in left part of Fig. 8.1. Later, a specialized encapsulation was manufactured by the JLO workshop for MCP-PMTs (illustrated in the right part of Fig. 8.1), consisting of aluminum frame and front plate with equidistant threaded holes matching the pitch of the MCP-PMT pixels.

An adapter for the optical fiber cable was prepared to enable a direct connection of the optical fiber to the front plate. The surface was anodized with a black dye. The encapsulation was made for two inch Planacon MCP-PMTs and an insert was manufactured for placement of one inch miniPlanacon MCP-PMTs.

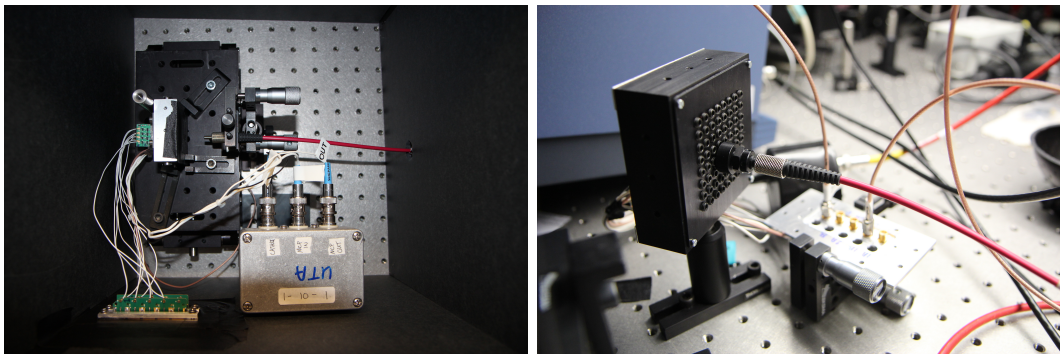

Figure 8.1: Photographs of the MCP-PMT in the custom dark box (*left*) and in the custom encapsulation (*right*).

The PAa preamplifiers, the PAb and the CFD modules of the AFP ToF were used for the output signal processing. The data acquisition was handled by a LeCroy WavePro 7200A oscilloscope with 2 GHz bandwidth and 10 GS/s sampling.

A low jitter trigger was needed for the timing measurements. The trigger output of the laser system was found to be insufficient. However, the laser system has an inbuilt fast PIN diode and it turned out to be feasible to split its signal output. Since the PIN diode provides pulses at 50 MHz rate, a two stage trigger scheme was utilized, using the laser trigger output to arm the trigger and the nearest PIN diode output pulse to produce the trigger. The described logic was set up in the oscilloscope. The full connection scheme is drawn in Fig. 8.2. The PIN diode signal amplitude was adjusted by a 3 dB attenuator and PAa and PAb amplifiers to match the CFD operational range. The jitter of this trigger scheme was measured to be (7 ± 1) ps.

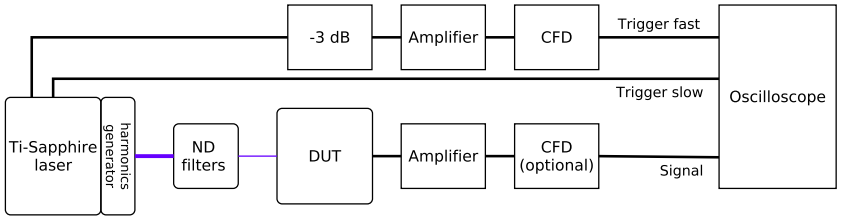

Figure 8.2: Measurement setup using the trigger output of the laser. The purple lines represent the laser beam, the boxes with round corners stand for optical components and the DUT, and the rectangles are used for the electronic devices.

The measurement scheme was improved over time. An SiPM was added to the

setup to serve as the trigger and additionally also as the output power monitor, as shown in Fig. 8.3. The laser beam was split in order to illuminate the second device. Initially a dichroic mirror was utilized and therefore the triggering SiPM was illuminated by 280 nm light when the DUT measured with 420 nm light and vice versa. This was further improved by using an optical fiber splitter (Y) cable with ND filters moved at the output of the DUT arm of the cable. The triggering SiPM (the STM NRD09_1) was installed mainly because it was sensitive to changes in the laser power output. This was needed as especially during the first hours of measurement, the laser tended to have unstable power output and its monitoring enabled to equalize the power between measurements and retake data if the monitoring pulse amplitude changed by more than 5 %. Since the SiPM was illuminated by the laser light attenuated only by the imperfect coupling to the fiber, it was sufficient to operate it at 27.5–28.5 V. Trigger jitter of the SiPM trigger was measured to be (4 ± 1) ps for the 420 nm light and (8 ± 1) ps for the 280 nm light.

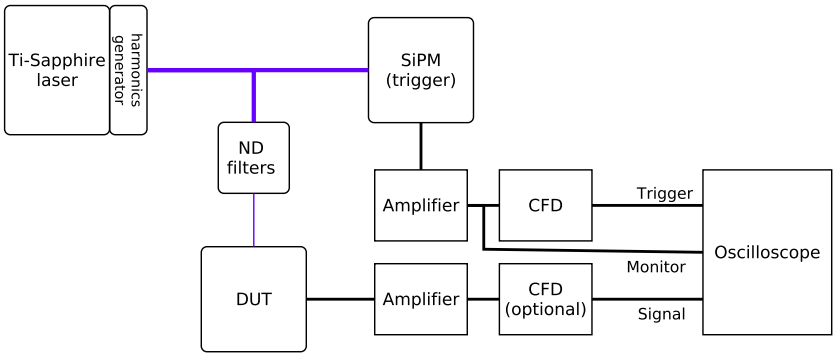

Figure 8.3: Measurement setup using the SiPM as the trigger. The purple lines represent the laser beam, the boxes with round corners stand for optical components, the SiPM and the DUT, and the rectangles are used for the electronic devices.

The low voltage power supplies GW Instek PSP-405 and TTi QL564TP were used for powering the SiPMs and the high voltage power supply CAEN N472 was used to power MCP-PMTs.

8.2 MCP-PMT characterization

8.2.1 Uniformity of pixel response

The gain of MCP-PMTs usually varies significantly (even more than by a factor of 2) across the active surface [66] and manufacturers are working on improvements. As this can influence performance of individual ToF channels in terms of efficiency as well as time resolution, the uniformity of response of individual

pixels was evaluated for the the MCP-PMT 9002053 before its use at the beam tests in 2016. The laser beam was split using the dichroic mirror and the SiPM was used for triggering on the 420 nm part of the laser light, while the individual MCP-PMT pixels were illuminated by the 280 nm light. The center of each pixel was illuminated by a 3 mm wide spot. The HV was set to 1870 V based on the experience with the two MCP-PMTs used in beam tests in 2014 and 2015, corresponding to gain of $1 \cdot 10^4$. The channel numbering is the same as presented before in Fig. 7.22.

As I mentioned earlier, the laser system output power tended to slowly change and this needed to be addressed for the uniformity measurement. The laser power was reduced by two ND filters with the total optical density value of 6 and a gradient ND filter wheel for fine adjustments. Initially, the power output was set such that the mean amplitude on the reference channel 11 was 500 mV. The amplitude of the monitoring SiPM was then read out and kept constant for the following measurements by adjusting the gradient ND filter wheel. The channels were measured in order along the columns in Fig. 7.22 and the channel 11 mean amplitude was checked at least once per MCP-PMT column and at the end of the measurement (to ensure stable light conditions). The channel 11 mean value varied by up to 28 mV, which determined the estimated uncertainty of 6 %. Both raw and CFD processed signals were recorded for each channel. The uniformity of the pulse amplitude (determined from the raw signals) and uniformity of time resolutions in terms of the FWHM (determined from the CFD signals) were evaluated and are presented in Fig. 8.4.

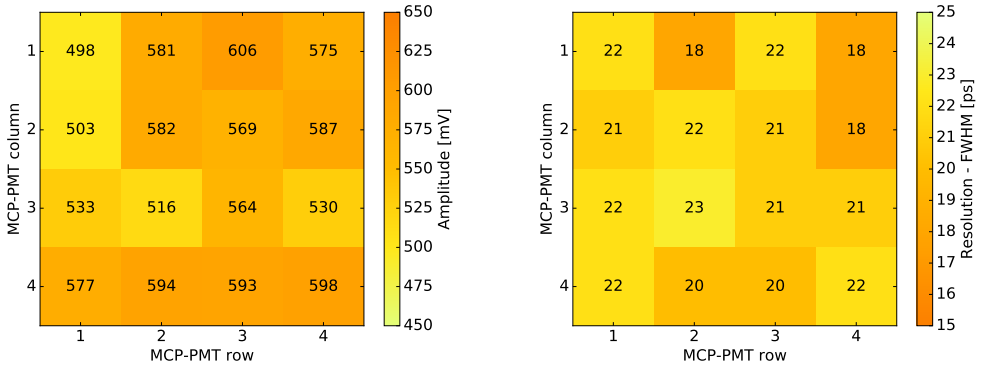

Figure 8.4: Uniformity of the MCP-PMT 9002053 response in terms of the output pulse amplitude (*left*) and the time resolution (*right*). The colormap is inverted between the two plots, as the resolution is expected to rise with decreasing amplitude.

The mean amplitude among pixels ranges 498–606 mV with the mean value of 563 mV. The ratio of the minimum to the maximum mean amplitude is 1:1.22. The time resolution varies between 18–23 ps with the mean value of 21 ps. Naively, one would expect an anticorrelation between the mean amplitude and the time resolution of a pixel. This would be true for the fixed gain and

varying amount of incident light, as indicated by Eq. 6.7. However in this case the amount of incident light is the same, while the gain varies. The gain can vary because of non-uniform quantum efficiency of the photocathode, which would result in varying N_{pe} and hence the anticorrelation, or because of non-uniformity at the MCP layers. As the anticorrelation is not observed in Fig. 8.4, the main source of non-uniformity is likely in the MCP layers.

8.2.2 Time transit spread

The time transit spread (TTS) is an important attribute of an MCP-PMT defining its timing performance, as discussed in Sec. 6.2. It characterizes its time resolution when only one photoelectron is produced per event.

I present here results of TTS measurements of three Photonis MCP-PMTs that I performed. The first one — an older two inch Planacon XP85012, with 8×8 channels, 25 µm pores and a nickname "Rachel" — was measured when the setup for the MCP-PMT characterization was being built at the JLO with help of prof. Brandt (UTA). It was a used MCP-PMT and it was needed to exceed its maximum recommended bias voltage by 50 V to reach a sufficient gain for the single photoelectron measurement. It was operated at 3050 V. At the time the setup with the trigger based on the laser system (Fig. 8.2) was used.

The second MCP-PMT was the miniPlanacon XPM85112 with 10 µm pores used in the 2015 beam test (BT). It was powered by the HV of 2100 V. The third was the 10 µm pore miniPlanacon XPM85112 with the reduced anode gap (the serial number 9002053) used in the 2016 beam tests. The HV was set to 2370 V. In both cases, the setup with the SiPM trigger (Fig. 8.3) was utilized with the laser beam split on the dichroic mirror and the SiPM illuminated by 280 nm light while the MCP-PMT was illuminated by 420 nm photons.

In all cases, the single photoelectron level was ensured by a very low light level corresponding approximately to one incident photon per event on average. The laser beam was attenuated by a set of ND filters down to the level when less than one in five events contained a PMT response. This scheme is based on the Poisson distribution of the photoelectron number, as for the mean value bellow 0.22 (corresponding to the one out of five events having a signal), the probability of an event with more than one photoelectron is less than 2 %. This level was reached iteratively with the HV increase following the increased ND filter value. The final HV was set such that the mean pulse amplitude is in range 300–500 mV, i.e. above the lower bound of the CFD optimal range. The CFD was used for the timing measurement with the threshold set to 100 mV.

Examples of obtained time distributions are displayed in Fig. 8.5, showing the TTS performance of the two inch Planacon tube and one of the newer miniPlanacon MCP-PMTs. A much more pronounced delayed peak caused by photoelectrons that bounced off the first MCP layer is present in the case of the two inch PMT, likely caused by the larger pore size.

The results for the measured channels of all three MCP-PMTs, with the

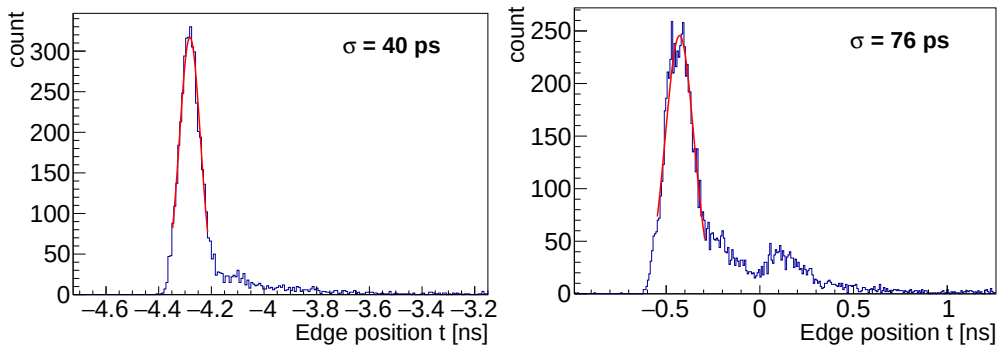

Figure 8.5: Time distributions at the single photoelectron level for the MCP-PMT from the 2015 beam test (*left*) and the 2 inch XP85012 (*right*).

Table 8.1: Time transit spread measurements of MCP-PMTs measured in the JLO laser lab. The estimated uncertainty is ±2 ps.

PMT	Channel	N_{pe}	HV [V]	σ_{TTS} [ps]
XP85012 (2 inch)	54	0.1	3050	75
BT2015	12	0.05	2100	43
	13	0.05	2100	41
	22	0.05	2100	39
BT2016 (9002053)	11	0.19	2370	46
	33	0.19	2370	49

trigger contribution subtracted, are listed in Tab. 8.1. There are small differences between different pixels of the same MCP-PMT and the best performance is observed in the case of the PMT from the 2015 beam test. This is, at first sight, contradicting the obtained time resolutions of bars at the beam tests with the two miniPlanacon tubes, where the PMT 2002053 performed better (compare Tab. 7.1 and 7.3). However, the TTS is only a part of the time performance for a given number of incident *photons*. A given number of photons is produced in an LQbar and Eq. 6.7 relates the TTS to time resolution for a given number of *photoelectrons* produced at the photocathode. The feature relating these two numbers is the quantum efficiency. Therefore, it can be inferred from the three tables (7.1, 7.3 and 8.1) that the PMT 9002053 has higher quantum efficiency than the one used in the 2015 beam test. Neglecting the constant term in Eq. 6.7, one can estimate that the quantum efficiency of the PMT 9002053 is better by a factor of about 1.6.

8.3 SiPM measurements

Silicon photomultipliers (SiPMs), or multipixel photon counters (MPPCs) as Hamamatsu calls them, are solid state detectors capable of detecting very low light down to single photon levels. An SiPM sensor is build from an array

of cells, consisting of an avalanche photodiode (APD) connected in series with a quenching resistor, as illustrated in Fig. 8.6 [67, 68]. All cells are connected in parallel and provide a single output. Different SiPM models provide a sensitivity to a specific wavelength range of incident light. UV sensitive models are of interest for Cherenkov timing applications. Typically the UV sensitive SiPM provide the sensitivity in the range 300–600 nm, with the peak detection efficiency around 400 nm.

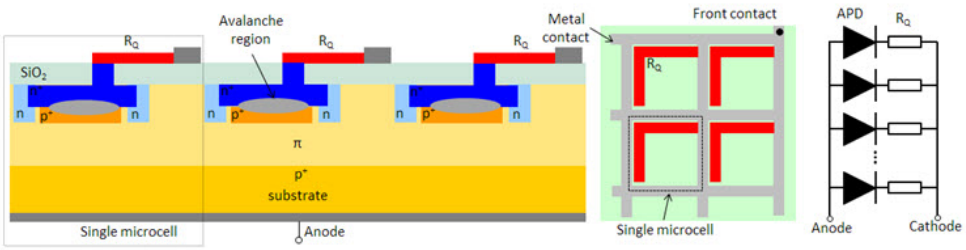

Figure 8.6: Schematic view of an SiPM structure. The left part depicts the cross section of the SiPM chip, the middle part is the schema of a placement of individual microcells and the right part is the circuit schema [67].

A bias voltage is applied over the SiPM in the reverse direction. The applied voltage is higher than the breakdown voltage of APDs, typically by an overvoltage of 1–6 V. A photon incident on an SiPM cell produces an avalanche of electrons, which reaches certain maximum for the given bias voltage and quenches. The cell therefore produces well defined current pulse. This way, a linear response of SiPM is ensured for multiple photons, given that the photons hit different cells. The maximum of the avalanche defines the *gain* of the SiPM, which is typically of the order up to 10^6.

In addition to the illuminated cell, also a neighboring cell may fire with a certain probability due to the *crosstalk*. The crosstalk happens when an avalanche electron hits the neighboring cell either directly (prompt crosstalk) or due to drift (delayed crosstalk) and causes another avalanche.

As the SiPMs are operated above their breakdown voltage, any electron freed in the avalanche region causes a current pulse at the SiPM output. This includes thermally freed electrons that are responsible for the *dark pulses* (or *dark counts*).

For the timing applications, an important characteristic is the time transit spread (TTS), often referred to as single photon time resolution (SPTR) in the case of SiPMs. Eq. 6.7 holds also in this case [69].

8.3.1 Optical grease effect

A deterioration of SiPMs time resolutions after about one week of running was observed in the 2015 beam test and it was attributed to degradation of the optical grease between the fused silica bar, serving as the Cherenkov radiator, and the SiPM sensor. The main evidence for this hypothesis was the value of the time

resolution after the first week, as it stabilized at the same value as was measured before the old grease was removed and glycerol was applied. To confirm the claim, I performed the set of measurements in a controlled environment of the JLO laser laboratory.

The setup with the laser system trigger (Fig. 8.2) was used for the test. First, the SiPM sensor and the radiator bar were cleaned and a drop of fresh glycerol was applied between the two. The SiPM was reassembled and the output of the optical fiber guiding the laser beam was coupled to the front face of the radiator bar. Initially, the fiber was pointing the laser beam along the radiator bar axis.

The 420 nm light was utilized and the laser output was tuned to 400 µW before the ND filters. The filters were set such that the mean pulse amplitude at the output of the SiPM, operated at 30.7 V, is about 600 mV. The value of 580 mV was reached for the filters with the total optical density of 4.5. Both raw and CFD processed signals were recorded. Then, the fiber was angled at about 45° (as it is close to 48° Cherenkov angle of highly relativistic particles in fused silica), as illustrated in Fig. 8.7. Glycerol was applied between the fiber output and the radiator bar in this case. Again, the raw and CFD processed signals were recorded.

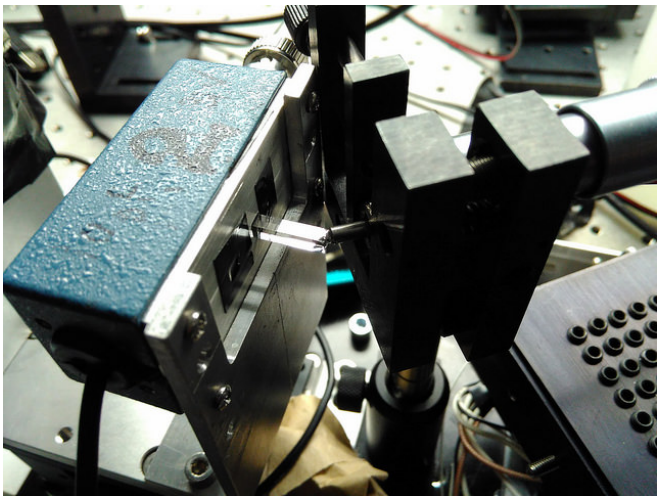

Figure 8.7: Photograph of the optical fiber coupled to the fused silica bar of SiPM detector for measurement of the glycerol aging effect.

The setup was then left in the laboratory at stable temperature of (23 ± 1) °C. After 11 days, a fresh glycerol was applied between the fiber output and the bar, while keeping the aged glycerol between the bar and the SiPM sensor. Data were recorded with the same illumination, first for the 45° case and then also for the 0°. Data were analyzed, trigger contribution subtracted and the time resolutions are compared in Tab. 8.2.

The results show deteriorated time resolution for the incident light at the 45°, while the light along the radiator bar axis provides very similar values. This is observed also in the mean pulse amplitude that essentially remains unchanged for

Table 8.2: Effect of the glycerol age on the time resolution of the SiPM.

Angle [°]	Time resolution [ps] after 0 days	11 days
0	13	14
45	14	20

the direct light and drops to 350 mV for the 45° case. A degraded optical grease, manifesting a change of the refractive index, influences the most a light incident at large angles, while the effect for the direct light is minimal, as governed by the Fresnel equations. The degradation itself can be explained in the case of the glycerol by the fact that the glycerol is hygroscopic, i.e. it absorbs water from the air, which causes decrease of its refractive index.

8.3.2 SiPM characterization

As I shown in the previous chapter, during the development of the ToF system of the AFP, a 3.5×3.5 mm^2 SiPM produced by STMicroelectronics (NRD09_-1, $58 \times 58\,\mu$m^2 cell size) coupled with a 3 cm long quartz Cherenkov radiator was utilized. This detector served as a timing reference and reached the time resolution of 11 ps [P10].

Since the STM NRD09_1 was not being produced anymore already during the first beam tests, possible replacement was investigated. The worry was that the so far used SiPMs might suddenly die, as their accumulated radiation dose increases. Increasing dark current was observed that supported this worry.

I did a research for possible options and I have selected a 3×3 mm^2 SiPM capable of detecting light in near ultra-violet spectrum, manufactured by FBK (SiPM-NUV3S [59], $40 \times 40\,\mu$m^2 cell size), as the first possible choice, based on its performance in the MEG II scintillation detector [70] and low price. It was purchased and assembled in June 2016.

I have then measured its properties in the JLO laser lab, with a focus on the time resolution under variation of the light intensity, an over-voltage and a wavelength of the light. I compared time resolutions of the FBK SiPM to the STM NRD09_1.

Cherenkov radiators produce light of wavelengths from below 250 nm and the light yield increases with decreasing wavelength down to a limit given by the radiator material [P9]. Therefore, it is important to know the timing properties not only near the peak efficiency (420 nm for the FBK SiPM-NUV3S) but also for the deeper UV region. Here I present a comparison of timing properties of the SiPMs for 420 nm and 280 nm wavelengths.

This section describes, in more detail, measurements that I documented in papers sent to Nucl. Inst. Meth. A [P15] and Jemná mechanika a optika (Fine Mechanics and Optics) [P16].

8.3.2.1 Methods

Measurement setup The setup with the SiPM trigger (Fig. 8.3) was used for this study. The laser beam was coupled into an optical fiber splitter (Y) cable. Coupling was adjusted such that the two outputs of the fiber splitter had an equal intensity (with observed deviation within 10 % of the output power). One part was fed into a reference SiPM (another STM NRD09_1) which was used as the trigger. The other output was attenuated by a set of neutral density (ND) filters and detected by the SiPM under test. A circular area with 3 mm diameter was illuminated for both SiPMs.

The output from both the measured and the triggering SiPM was amplified by the two-stage 32 dB low-noise broadband pre-amplifier (PAa+PAb). The third PAb amplifier with the amplification of 16 dB was added for the measured STM SiPM. The amplified signal from the triggering SiPM was split. One output was used for a direct monitoring and the other was processed by the CFD to reduce the trigger jitter. The SiPMs were powered by the TTi QL564TP power supply.

The second output of the triggering SiPM was used to ensure a stable laser output: the amplitude of the monitoring signal was kept constant between measurements and the shape of the monitoring signal was observed for a possible laser instability. The trigger jitter, including the readout of the reference SiPM, was determined to be (4 ± 1) ps for the 420 nm light and (8 ± 1) ps for the 280 nm light.

Measurements were performed in the air-conditioned laboratory at the temperature of 23 °C stabilized within 1 °C. The SiPMs were not thermally stabilized to keep the detector simple. Each SiPM was encapsulated in an aluminum box connected by an aluminum bracket to an optical breadboard, and the SiPMs were placed in a dark box with feedthroughs for cables and optical fibers.

Estimation of the number of photoelectrons The number of photoelectrons produced in an SiPM follows the Poisson distribution with the mean $N_{\mathrm{pe}}$and is given by the intensity of incident light, i.e the number of impacting photons, and photodetection efficiency. In case of a pulsed light source, the mean number of photoelectrons N_{pe}produced in the SiPM can be estimated from the Poissonian probability of a pedestal event (i.e. an event without any pulse above selected threshold). To determine this probability, it is needed to count the number of pedestal events N_{ped} while triggering on the light source output with the total number of triggers N_{tot}. Apart from the pulses caused by the light source, there are always also the dark pulses present and it is needed to correct for them by subtracting their contribution to the N_{pe}. To determine the dark pulses contribution, the SiPM is covered in such a way that there is no light impacting on its window and the number of pedestal events $N_{\mathrm{ped}}^{\mathrm{dark}}$ is counted with the total number of triggers $N_{\mathrm{tot}}^{\mathrm{dark}}$. The N_{pe}estimate is then calculated [71] from

$$N_{\mathrm{pe}} = -\ln \frac{N_{\mathrm{ped}}}{N_{\mathrm{tot}}} + \ln \frac{N_{\mathrm{ped}}^{\mathrm{dark}}}{N_{\mathrm{tot}}^{\mathrm{dark}}}, \tag{8.1}$$

The pedestal threshold was set to 0.5 photoelectron level, determined from the dark pulse amplitude for each bias voltage applied to the measured SiPM. However, it was not possible to determine the amplitude directly with enough precision due to the presence of an electronic noise. I have therefore, using the oscilloscope software, applied a bandwidth filter of 200 MHz (the software did not allow fine bandwidth limits) and averaged the pulse over 2000 events. This removed the noise contribution, but also distorted the pulse shape, which was now smeared with a lower amplitude. To correct for this and to find the correct amplitude for bandwidth value used later in analysis, I have established correction constants by the following procedure. For each SiPM type, I took a pulse obtained for high illumination with the amplitude bellow saturation of amplifiers (≈1.8 V). Such a pulse has very small shape distortion from the noise and can therefore serve as a template. I have then used a custom low-pass filter implemented in the analysis software and obtained the correction constant as the ratio of the pulse amplitude after the low pass filter using the optimal bandwidth value (as described bellow) to the pulse amplitude after the low pass filter set to 200 MHz.

Equation 8.1 is usable up to $N_{\mathrm{pe}} \approx 10$ due to the acquired total number of events from 10^4 to $3 \cdot 10^4$. For higher light intensities, I extrapolated the N_{pe} estimate based on the optical density value of the used ND filters. To extrapolate the N_{pe}, I first calculated the number of photons before each filter value for which it was possible to estimate N_{pe} (using Eq. 8.1) — $N = N_{\mathrm{pe}} \cdot 10^d$, where d is the optical desity value of the filter. I averaged N over all filter values, where the estimate was possible, except for the highest filter value (where the value was significantly higher due to the noise). Finally, I calculated the N_{pe} estimate for lower filter optical density value d' using the average number of photons before filters $\bar{N}$ from

$$N_{\mathrm{pe}} = \bar{N} \cdot 10^{-d'}. \tag{8.2}$$

The N_{pe} estimate is influenced by the pedestal threshold, determined from the dark pulse amplitude, which was measured with estimated uncertainty of 10 %. In order to calculate the uncertainty of the N_{pe} estimate, I have varied the pedestal threshold by ±10 % and determined how the N_{pe} estimate changes. The N_{pe} uncertainty was estimated as $\frac{1}{2}(N_{\mathrm{pe}}^{max} - N_{\mathrm{pe}}^{min})$ for the range of validity of the Eq. 8.1. For the higher N_{pe} values, the errors were propagated (based on Eq. 8.2) using[1]

$$\sigma^2_{N^d_{\mathrm{pe}}} = \frac{1}{N^2} \sum_{i=1}^{N} \sigma^2_{N^{f_i}_{\mathrm{pe}}} \cdot 10^{2f_i} \cdot 10^{-2d},$$

where N is the number of filters from which the N_{pe} value was calculated, f_i is the optical density value of the i-th filter, $\sigma^2_{N^{f_i}_{\mathrm{pe}}}$ is the corresponding uncertainty

[1]For the set of independent variables x_i ($i \in \{1, 2 \ldots, N\}$) each with the uncertainty σ_i, the uncertainty σ_X of the random variable $X = C \sum_i^N x_i$ ($C = \mathrm{const.}$) is $\sigma_x^2 = C^2 \sum_i^N \sigma_i^2$.

of the N_{pe} estimate and d is the optical density value of the filter for which the N_{pe} uncertainty is being determined.

Time resolution analysis I preprocessed the acquired waveforms in order to obtain the optimal timing performance and minimize the electronic jitter contribution. First, I applied a low pass filter to cut off high frequency interference. Then, the 0.5 photoelectron threshold was applied to remove events with the noise.

After the preprocessing, I used a constant fraction discriminator algorithm implemented in the analysis software (with the constant fraction set to 42% corresponding to the hardware CFD) to determine the time of the pulse detection with respect to the time of the trigger. The time resolution was obtained from the Gaussian fit to the signal time distribution.

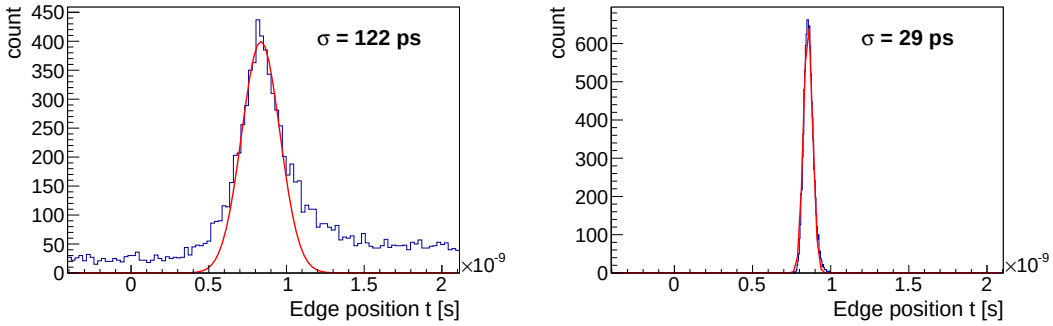

Figure 8.8: A typical time distribution for a single photoelectron (left) and a high number of photoelectrons (right). Histograms show time distributions for STM SiPM operated at 2.9 V overvoltage and illuminated by 420 nm laser light for $N_{\mathrm{pe}} = 1.2$ (left) and $N_{\mathrm{pe}} = 270$ (right). The Gaussian fit from which the time resolution was extracted is represented by the red line [P15].

Examples of time distributions are shown in Fig. 8.8. It is evident that, for the single photoelectron case, there are pronounced tails caused by delayed photoelectrons, uniformly distributed dark pulses and the electronic noise fluctuations superimposed to the time distribution of the photoelectrons generated by the laser. The Gaussian fit was performed iteratively around the central part of the distribution to measure the time resolution without the influence of delayed photoelectrons and dark pulses. This influence decreased with the increasing number of photoelectrons, as can be seen in the right part of Fig. 8.8.

The contribution of the trigger and the electronics jitter to the time resolution is subtracted in quadrature in the values and plots that follow.

I have optimized the low pass filter cut off frequency for each SiPM to obtain the best time resolution. I found the optimal value to be 900 MHz for the FBK SiPM and 1400 MHz for the STM device.

In the text below, I quote an overvoltage (OV) value $V_{\mathrm{OV}} = V_{\mathrm{bias}} - V_{\mathrm{BD}}$, where V_{bias} is the voltage applied to the SiPM and the breakdown voltage V_{BD} was measured to be 28.1 V for the STM SiPM and 26.6 V for the FBK device.

The time resolution is expected to behave as $\sigma_{\mathrm{TTS}} N_{\mathrm{pe}}^{-\frac{1}{2}}$ [69] with the saturation at high N_{pe} values. The saturation originates from the internal electronic jitter (labeled σ_{const} in the formula below) of an SiPM, which needs to be added in quadrature to describe the measured points as a function of N_{pe}. Therefore, I fit the graph of time resolution vs. N_{pe} by

$$\frac{\sigma_{\mathrm{TTS}}}{\sqrt{N_{\mathrm{pe}}}} \oplus \sigma_{\mathrm{const}} \equiv \sqrt{\frac{\sigma_{\mathrm{TTS}}^2}{N_{\mathrm{pe}}} + \sigma_{\mathrm{const}}^2}. \tag{8.3}$$

Time resolution uncertainty estimate I found that the influence of the electronic noise originating from electronic components, mostly two 1 kΩ resistors, in the SiPM connection and amplified by the pre-amplifiers cannot be neglected, especially for the single photoelectron illumination. This influence is the main source of a systematic uncertainty.

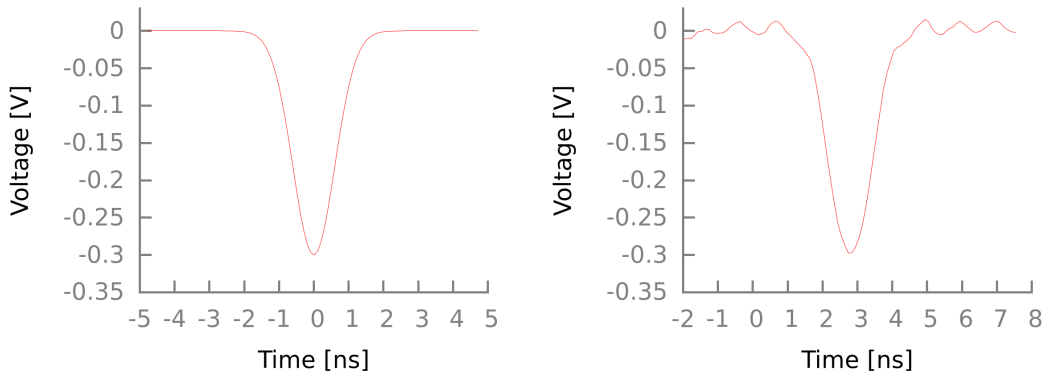

Figure 8.9: Illustration of the noise simulation. *Left:* a generated pulse, *right:* the same pulse with the superimposed noise [P16].

To evaluate the noise contribution to the time resolution, I utilized a Monte Carlo simulation. A set of waveforms with different mean pulse amplitudes was generated for each SiPM type. Gaussian pulses were used to approximate the SiPM output pulses with the rise time of 600 ps for the STM SiPM and 1 ns for the FBK SiPM. All pulses were generated at the fixed time with respect to the simulated trigger, i.e. with the zero time smearing.

The noise sample acquired for the given SiPM was then superimposed to each Monte Carlo sample and the time smearing was determined for each case. Figure 8.9 illustrates how the generated pulse was combined with the noise waveform.

The results are plotted in Fig. 8.10 together with fits. There is a good agreement between the results obtained using the noise samples from the two SiPMs,

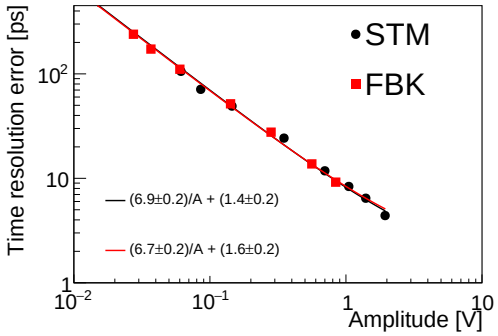

Figure 8.10: Time resolution uncertainty dependence on the mean pulse amplitude determined from the simulation [P16].

suggesting the same noise origin. This is expected, as the connection diagrams of the two SiPMs are the same.

8.3.2.2 Results

Time resolution Figure 8.11 plots the dependence of the time resolution on the N_{pe} and the SiPM overvoltage. Both SiPMs follow very well the $\sigma_{\mathrm{TTS}} N_{\mathrm{pe}}^{-\frac{1}{2}} \oplus \sigma_{\mathrm{const}}$ behavior (the lines in the figure show the fit results). Both SiPMs show a similar behavior for the two wavelengths.

To determine the best possible resolution with the available illumination, I removed the ND filters and subsequently obtained N_{pe} of the order 10^6 for 420 nm with corresponding time resolutions of (8 ± 1) ps and (4 ± 1) ps for the FBK and STM SiPM, respectively. For 280 nm, the N_{pe} was of the order 10^4 and the measurements of resolutions of (27 ± 1) ps (FBK) and (8 ± 1) ps (STM) were made. The SiPMs were operated just below the V_{BD} for this measurement.

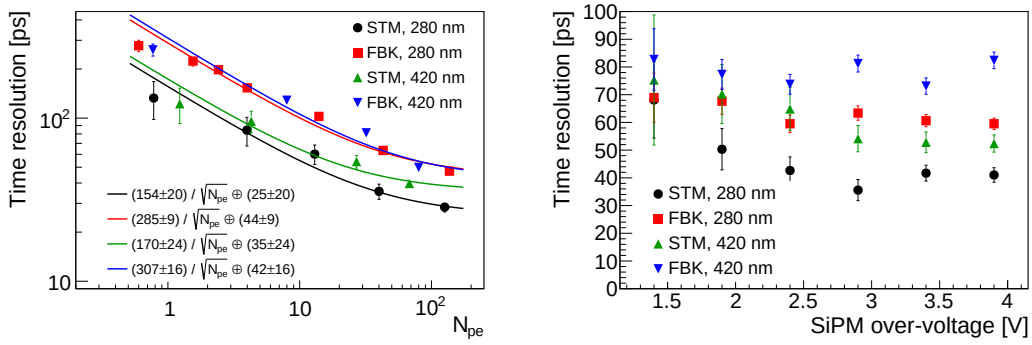

Figure 8.11: Time resolution dependence on N_{pe} for the overvoltage of 2.9 V (left); the resolution as a function of the overvoltage for N_{pe} in range 20–30 for 420 nm and 35–45 for 280 nm (right). N_{pe} calculation changes at $N_{\mathrm{pe}} \approx 10$, as described in section 8.3.2.1 [P15].

The right part of Fig. 8.11 shows the dependence of the time resolution on the increasing overvoltage. The STM detector resolution decreases up to $V_{\mathrm{OV}} = 2.9\,\mathrm{V}$ and levels off or slightly rises after this point. The maximum values of 68 ps and 75 ps for 280 nm and 420 nm, respectively, decrease down to 36 ps (280 nm) and 52 ps (420 nm). The FBK device shows quite significant changes for different overvoltages, but there is no clear monotonic trend. For 280 nm the minimum time resolution is 60 ps and the maximum is 69 ps. For 420 nm the minimum time resolution is 73 ps and the maximum is 83 ps. The results are not directly comparable between wavelengths, as the N_{pe} estimate is different for the two wavelength.

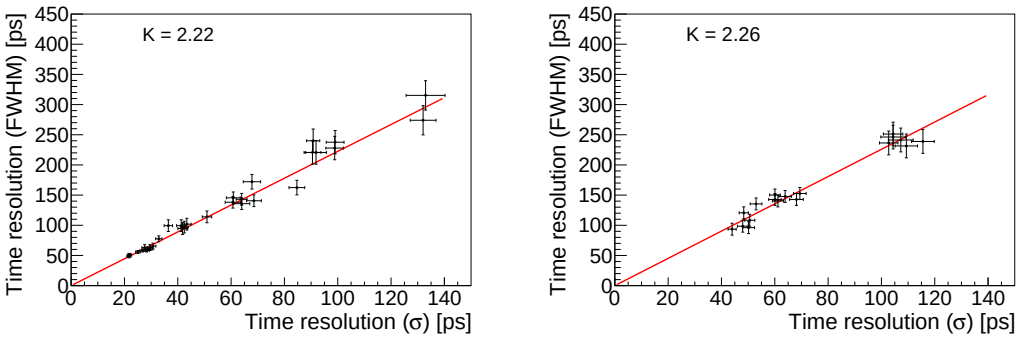

Figure 8.12: Correlation between the time resolution expressed in σ obtained from the Gaussian fit and the full width at half-maximum (FWHM) value of the time distribution. The values are fitted by FWHM $= K\sigma$. The fit is represented by the red line. *Left:* STM SiPM; *right:* FBK SiPM [P15].

Figure 8.12 plots the correlation between the time resolution expressed in σ obtained from the Gaussian fit and the full width at half-maximum (FWHM) value of the time distribution. For the ideal Gaussian, the linear fit FWHM $= K \cdot \sigma$ should yield $K \approx 2.35$. The values are lower for both SiPM types, but the deviation is small (below 5 %). The deviation is caused by the tails of the time distributions, as can be seen in Fig. 8.8, the tails slightly broaden the fit even in case of abundant photoelectrons (the peak of the distribution is visible above the fit line).

Single photon response Single photon measurements were performed for $N_{\mathrm{pe}} \approx 1$ in order to estimate σ_{TTS}. However, the level of the electronic noise was close to 0.5 photoelectron level of the SiPM signal and induced a significant smearing of the pulse amplitude as well as a time jitter. Therefore, it was not possible to select only 1 photoelectron events based on the signal amplitude. The time jitter was included as a systematic uncertainty based on the simulation described above.

Figure 8.13 plots measured single photon time resolution as a function of the overvoltage. The results show very similar values for both wavelengths with

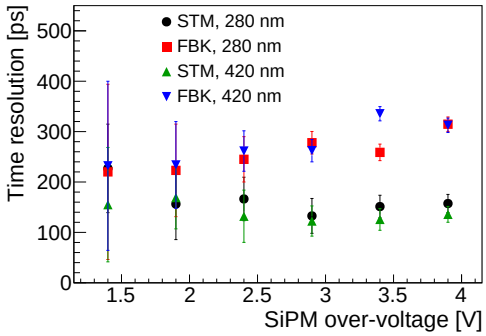

Figure 8.13: Time resolution dependence on the SiPM overvoltage for the single photoelectron level [P15].

minimal TTS of (223 ± 92) ps for FBK SiPM and (123 ± 30) ps for the STM one. The two SiPMs show a different behavior for increasing overvoltage: while the STM TTS is slightly improving up to $V_{OV} = 2.9$ V, the TTS of the FBK detector is increasing. In all cases, the decreasing size of the error bars illustrates mainly the increasing signal-to-noise ratio as the 1 photoelectron amplitude increases, although a contribution from increasing photodetection efficiency is also observed in the decreasing statistic uncertainty.

8.3.2.3 Discussion

As seen in Fig. 8.11, the time resolutions follow the $\sigma_{\mathrm{TTS}} N_{\mathrm{pe}}^{-\frac{1}{2}} \oplus \sigma_{\mathrm{const}}$ formula. For the σ_{TTS}, however, all measured points for $N_{\mathrm{pe}} \approx 1$ fall lower than the fit parameters suggest. The reason for this is that the points underestimate σ_{TTS}, since the time resolution for $N_{\mathrm{pe}} \approx 1$ comprises also contribution from events with more photoelectrons with probability given by the Poisson distribution with the mean value of 1. Due to the noise influence, it was not feasible to go lower with the light intensity. Therefore, the fit values provide more reliable measurement of σ_{TTS}.

The absorption length in silicon decreases from about 100 nm for 420 nm photons to about 10 nm for 280 nm photons [72]. Since the typical thickness of the top semiconductor layer is several micrometers, photons are absorbed on the same side of the P-N junction for both cases, with the 280 nm photons further away. This suggests a lower time smearing in the case of the 420 nm light. For high illumination levels, better results for the 420 nm light case are observed, yet results shown in Fig. 8.11 indicate the same or slightly better performance with the 280 nm light.

Overall, the FBK SiPM performance was consistently worse than that of the STM SiPM with time resolution 2–3 times higher. Considering 11 ps resolution achieved with STM SiPM during the beam test campaigns, expected beam test time resolution for the FBK device would be 20–35 ps. This is not good enough for the beam test purposes of the AFP ToF system, as it is at best the same

performance as the AFP ToF system, for which the SiPM should serve as the time reference.

8.3.2.4 Summary

I measured timing properties of SiPM detectors from the FBK and the STM producers. The devices manifested the TTS of (245 ± 10) ps (FBK) and (124 ± 22) ps (STM). The time resolution dropped with increasing N_{pe} as $\sigma_{\text{TTS}} N_{\text{pe}}^{-\frac{1}{2}} \oplus \sigma_{\text{const}}$ with the best time resolutions, achieved for N_{pe} of the order 10^6 for 420 nm, of (8 ± 1) ps and (4 ± 1) ps for the FBK and STM SiPM, respectively.

The results for the two wavelengths were very comparable, with 280 nm providing worse results at very high illumination: (27 ± 1) ps (FBK) and (8 ± 1) ps (STM) at N_{pe} of the order 10^4.

The STM SiPM has already proved to be a great detector for Cherenkov time-of-flight systems, reaching 11 ps when combined with 3 cm quartz radiator [P10]. However, the FBK device was found to provide worse resolution by a factor of 2–3.

The worse resolution was confirmed also during a beam test, where the resolution of 70 ps was measured (see Sec. 7.5.5), exceeding the estimated resolution, likely due to worse photodetection efficiency for the UV light.

During the search for possible SiPMs, I have also found few SensL devices that were of interest. At that time, SensL was preparing a large scale manufacturing and they offered only ready-made detector package with thermal stabilization for a very high price (about $1000). Later, the SensL MicroFC-SMA-30050 [60] borrowed from the HGTD group was successfully tested in a beam test with the measured time resolution of 15 ps. Three pieces of SensL MicroFC-SMA-30050 were purchased and assembled in June 2017 and tested during beam tests in 2017. I did not repeat the set of presented measurements in the laser lab with the SensL SiPM due to different priorities and the fact that it performed well during the beam tests.

Chapter 9

Installation and commissioning

The AFP ToF detector was installed for the first time during the year end technical stop (YETS) starting at the turn of 2016. The work on the installation finished by the end of April 2017 and the commissioning started in May 2017. I participated in the preparatory works before the installation and in the commissioning of the ToF detector.

Two ToF detectors were prepared for the installation with the newly prepared LQbars and mechanical holder construction. Two MCP-PMTs were foreseen for installation — serial number 9002053 previously tested in beam tests and a new 9002086, tested in the JLO laser laboratory by Tomáš Komárek (JLO). Both had a fused silica front window with a bi-alkali photocathode and 10 µm MCP pores.

9.1 Tests before installation

Further tests were needed before the installation in addition to what was done during the development and in the beam tests.

Signal path was validated for each ToF channel from the PAa to the HPTDC module. In the final configuration, the flat flexible cable (FFC) was used for the feedthrough between the Roman pot vacuum and the outside air (as illustrated in Fig. 6.12). The FFC was not used in any of the beam tests, therefore it needed to be tested in a laboratory. I performed a measurement of the FFC influence on a MCP-PMT-like signal obtained from a fast clock generator (SRS CG635) and shaped using a capacitive differentiator. The measurement shown acceptable added jitter of 2 ps and decreased signal amplitude by 20 %. The lowered amplitude was caused by an impedance mismatch, however, since the FFCs were already prepared and the impact on timing was negligible, the FFCs were kept for the installation.

The PAa and PAb amplifiers, the CFD modules and the HPTDC modules produce significant amount of heat that needs to be dissipated. The PAa preamplifiers are placed in the Roman pot vacuum and all the produced heat (about 3 W) is removed via the heatsink (Fig. 6.13). As the temperature at the MCP-

PMT backplane must not exceed 70 °C (as specified by the producer), measurements of PAa temperature with foam insulation and later also directly in vacuum were performed in a laboratory. Temperatures at the PAa boards were measured by four negative temperature coefficient thermistors (NTCs) placed next to one of the amplifier chips. The temperatures did not exceed 53 °C in both measurements.

The PAb, CFD and HPTDC modules, together with the trigger and clock modules are placed in a NIM crate cooled by a fan tray. The AFP DCS provides one channel per module for the temperature monitoring. As there are several cards in PAb and CFD modules, temperature maps were recorded using the infrared camera FLIR E4 and measurements were performed with up to 8 NTCs placed in the modules to obtain temperature distribution within the modules. An example of the temperature maps is shown in Fig. 9.1. The hottest cards in both PAb and CFD modules were located in the third slot from the top, reaching 40 °C (PAb) and 55 °C (CFD) with the fan tray running and the ambient temperature of 25 °C. The PAb module contains onboard NTCs placed next to each amplifier chip, while the CFD has only one NTC placed on the motherboard, further away from the main heat sources. Based on the measurements, the third NTC of PAb was used for the DCS monitoring and the offset of the temperature measured by the CFD onboard NTC to the hottest CFD card of 15 °C was determined.

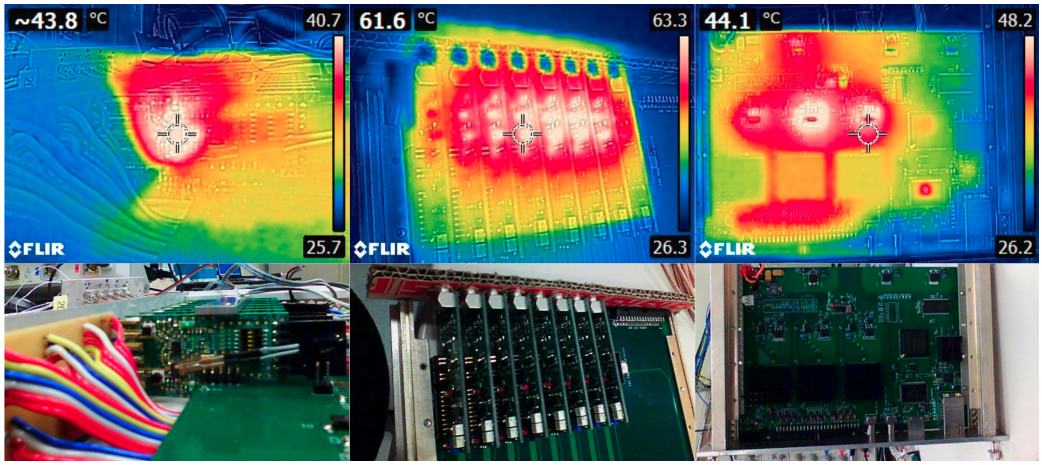

Figure 9.1: Temperature maps of PAb (*left*), CFD (*middle*) and HPTDC (*right*) module boards.

An automatic interlock system is necessary in the LHC environment to minimize the impact of a malfunction and to notify shifters and experts in case that a part of the system behaves outside of expected parameters values. There is a software interlock implemented in the DCS and a hardware interlock serving as a fail safe. Voltages, currents and temperatures are monitored in the ToF components and the presented measurements served as an input to define warning, error and fatal states of the components with appropriate actions to be taken

(SMS notification, affected systems to be shut down).

The MCP-PMT ability to operate in vacuum needed to be verified. There is a high vacuum inside the tube, so the pressure difference is not an issue. It is the applied high voltage that can cause problems, as the pressure inside the pot in the range 10–40 mbar represents the area on the Paschen curve for air of the breakdown voltage below 2 kV even at a distance of few centimeters. First tests were performed in a vacuum chamber at JLO, where also a dismantlable HV connection was developed and tested by Vladimír Urbášek (JLO). The tests before installation were performed in early February 2017 inside the AFP Roman pot using the dismantlable HV connection. During the tests, the HV was slowly ramped up to 2.4 kV and the current was observed with the maximum allowed value set to 600 µA (the expected current at the 2.4 kV was about 500–550 µA based on the beam test and laser laboratory measurements, with 400 µA current drawn by the HV divider). The test was successful in the case of PMT 9002086, but the PMT 9002053 failed at 2.0 kV.

A pair of MCP-PMTs with a borosilicate glass window was loaned to the AFP by Photonis as a replacement and the one labeled 9002089 was installed instead of the 9002053.

9.2 Commissioning

The commissioning of the newly installed AFP stations and the ToF detectors started with the LHC recommissioning at the beginning of May 2017. Initially, the LHC was filled with non-colliding beams and AFP stayed in its retracted position (the so-called *garage* position) most of the time. Stable beams collisions started in the second half of May with the intensity and the number of bunches steadily growing till the beginning of June. By the end of June, the AFP stations were being inserted on a regular basis shortly after the start of an ATLAS run.

In the beginning, the AFP detectors were mostly operated in the standalone mode, meaning that they were not part of any of the global ATLAS data streams and the AFP data were stored separately. The combined mode, in which the AFP operates as an ATLAS subdetector, was used for specific tests and later for common data taking.

Online monitoring was crucial for tests and debugging of detectors. Within ATLAS, so-called *GNAM histograms* are produced during the data taking and they are presented via Online Histogram Presenter service [73]. The GNAM histograms are produced on the best effort basis, meaning that events are not included into histograms, if a previous event is still being processed. I worked on ToF debugging, which included an implementation of ToF monitoring histograms during the commissioning as well as analysis of ToF performance from the acquired data. I present the key results in this section.

High voltage for ToF detectors on both sides was initially set to 2100 V and the CFD thresholds to 150 mV. The AFP can trigger on both the SiT detector and the ToF detector. As the trigger module was not installed, the trigger

output functionality was implemented by Paul Davis (University of Alberta) in the FPGA of the HPTDC module.

9.2.1 SiT-ToF correlation

A clear correlation between the track position reconstructed by the SiT and the response of ToF channels was observed in the RCE data during the beam tests (as shown e.g. in Fig. 7.32). It was, therefore, expected to be seen also in the data with the LHC proton beam. However, the correlation was initially not observed.

A possible explanation was that shower events are smearing the expected structure. In order to remove such events, I implemented a tighter selection in the GNAM histograms, requiring a clean "track" in SiT. As the track reconstruction was not available, I required that two selected planes of ToF had exactly 2 hits each (a minimum ionizing particle traverses 2 SiT plane pixels because of the 14° tilt) and the hit coordinates between the planes were at maximum 1 column (y coordinate, 250 µm) and 3 rows (x coordinate, 50 µm per row) apart. This selection yielded the expected correlation being visible, as illustrated in Fig. 9.2.

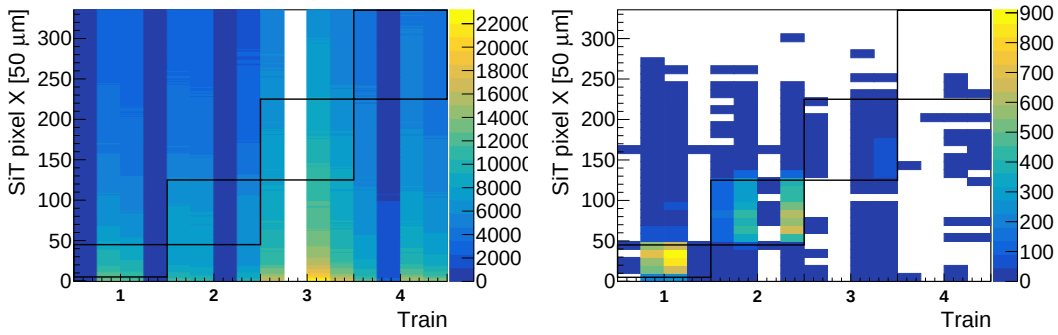

Figure 9.2: First observed SiT-ToF correlation in the run 327288, the C side ToF detector with a loose selection (*left*) and tight cuts (*right*). The black boxes illustrate expected signal regions.

Several ToF channels manifested low signal counts. This was investigated during the technical stop 1 (TS1) at the beginning of July 2017. Problems were identified in PAb and CFD channel cards and the problematic cards were replaced. This led also to improved SiT-ToF correlation plots, as shown in Fig. 9.3.

9.2.2 Efficiency

The need for the tight selection in the SiT-ToF correlation plots also suggested that efficiency of ToF channels might have been very low. First, I used GNAM histogramming and studied the relative efficiency of the possible N/4 selections

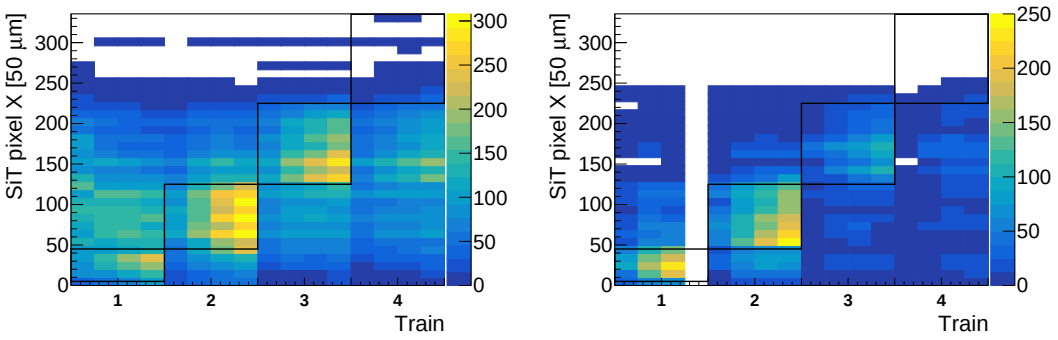

Figure 9.3: SiT-ToF correlation after TS1 with the tight selection for the A side (*left*) and the C side (*right*), run 328339. The black boxes illustrate expected signal regions.

of bars within a train with respect to the 1/4 selection. This did not reveal issues, however, the values were biased by the 1/4 requirement on a ToF train.

As GNAM provides only limited amount of events and it is not very straightforward to run GNAM code on already taken data, I moved to analysis of data taken in the standalone mode, as soon as the reconstruction of the raw data format into the ATLAS xAOD format became available.

I analyzed the AFP runs with the SiT trigger, so that the trigger would not bias the ToF efficiency. The efficiency was calculated as the fraction of events with a clean track in the SiT (the same clean track selection as in the SiT-ToF correlation was used) having the x pixel coordinate in the defined range (bins with the width of 5 pixel rows were used in the following plots) in which a given ToF channel responded. Results for all the ToF channels in the low μ part of the run 336505 (23rd September 2017) are shown in Fig. 9.4.

The observed efficiency within the x range corresponding to bars of a given train is 5–8 % for the A side and 1–3 % for the C side. Train 4 has low statistics due to the beam profile.

The reason of the low efficiency was investigated. There were three possible explanations being considered: a deteriorated MCP-PMT gain due to the collected charge, an insufficient rate capability of the MCP-PMT and threshold inefficiency caused by a too low HV or a too high CFD threshold.

The MCP-PMT photocathode is degraded with increasing charge collected by the MCP-PMT, mainly due to the bombardment by positive ions released from the MCP layer together with the electrons and accelerated towards the photocathode. The ALD coating of the MCP input layer addresses this issue and extends the lifetime of a tube. Non-ALD coated MCP-PMTs, such as the ones installed in the AFP in 2017, have expected lifetime in terms of collected charge of about 0.1 C/cm^2 [66], when the quantum efficiency drops by 30 % and continues falling rapidly, giving total collected charge expectancy of about 0.6 C for the miniPlanacon MCP-PMT with the active area of $25 \times 25\,\mathrm{mm}^2$. The

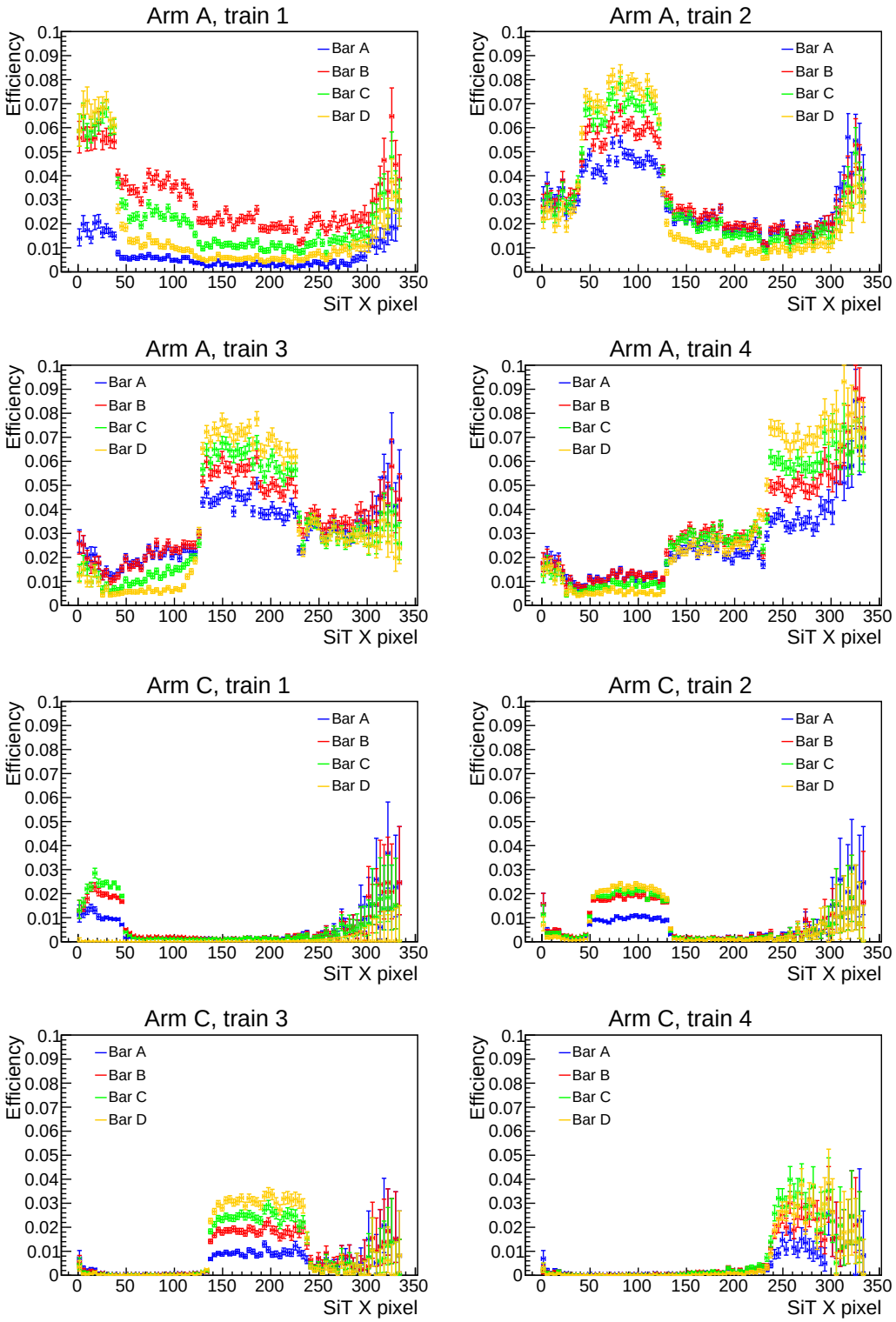

Figure 9.4: ToF efficiency as a function of SiT x coordinate in the run 336505.

collected charge of the ToF MCP-PMTs can be estimated as [74]:

$$Q = L_{\text{tot}} \sigma_{\text{inel}} \varepsilon N_{\text{pe}} G e, \tag{9.1}$$

where L_{tot} is the total recorded integrated luminosity, $\sigma_{\text{inel}} \approx 60\,\text{mb}$ is the inelastic cross section, $\varepsilon \approx 0.02$ is the AFP acceptance [56], $N_{\text{pe}} \approx 30$ number of photoelectrons per hit (based on an MC simulation [61]), $G \approx 1\text{–}2 \cdot 10^4$ is the MCP-PMT gain and e is the electron charge. The L_{tot} at a given point in time for year 2017 can be obtained from Fig. 9.5.

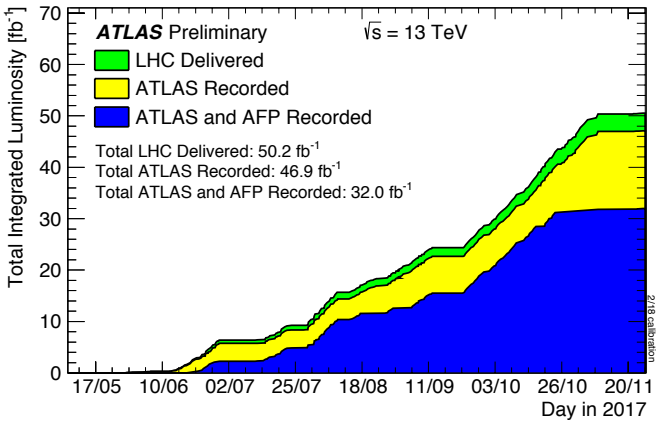

Figure 9.5: Total integrated luminosity delivered by LHC and recorded by ATLAS and AFP in 2017 [75].

The total integrated luminosity recoded by AFP reached $2\,\text{fb}^{-1}$ by the TS1, corresponding to 0.1–0.2 C of collected charge. By the end of the year, the collected charge reached 2–4 C. The expected lifetime value was probably reached by the end of July.

The MCP-PMT gain for a given HV starts to decrease at high signal rates (above ∼1 MHz, depending on the gain) [66]. The AFP expects rate of diffractive protons approximately 5 MHz [10], therefore the limited rate capability is of concern. The rate capability of new miniPlanacon tubes was tested by my colleagues using lasers at JLO and UTA and using a LED pulser at CERN. I investigated the effect in the data taken in 2017.

The rate R of protons impacting the ToF detectors depends on the pileup μ, AFP acceptance $\varepsilon \approx 0.02$, the fraction of diffractive events $\frac{\sigma_{\text{diff}}}{\sigma_{\text{tot}}} \approx 0.2$ [76] and the LHC collision rate $R_{\text{LHC}} = 40\,\text{MHz}$ approximately as

$$R \approx \mu \varepsilon \frac{\sigma_{\text{diff}}}{\sigma_{\text{tot}}} R_{\text{LHC}}. \tag{9.2}$$

This yields rate ranging between 16 kHz for $\mu = 0.1$ and 7 MHz for the nominal $\mu = 45$ in 2017. The actual average rate is lower due to gaps in the LHC filling scheme, the calculated values correspond to burst rates within one bunch train. I compared the efficiency in high-μ and low-μ runs in September 2017 and I observed no significant difference of the efficiency values.

9.2.3 HV and CFD threshold setting

The too low HV or too high CFD threshold settings were the third investigated possibility of the low efficiency. The two values are connected as increasing the HV raises the gain, which results in higher amplitudes. The two values should be set such that the amplitudes are within the optimal range for the CFD input while keeping the HV as low as possible (in order to extend the lifetime of the MCP-PMT). Initially, there was no possibility to obtain the amplitude distribution of the raw signals before the CFD from the HPTDC data. The HV was scanned between 1850–2000 V and the detector response was observed via GNAM histograms. A higher voltage of 2100 V was used only briefly during the May 2017 tests, however the readout of the HPTDC was not properly set yet and these data do not provide any useful insight.

The CFD modules provide time-over-threshold (ToT) functionality and the CFD output pulse length varies between 2 and 20 ns depending on the input pulse amplitude. The CFD output pulse length, however, needs to be digitized in the HPTDC module, which was implemented by Paul Davis (University of Alberta) in October 2017 in the FPGA of the HPTDC module.

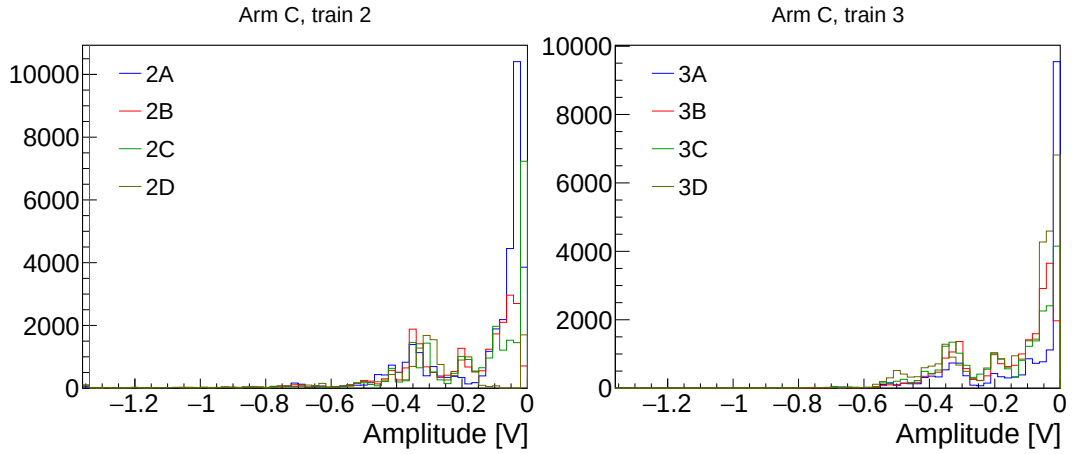

Figure 9.6: Amplitude distributions obtained from CFD ToT values at the HV of 2000 V for trains 2 and 3 on side C.

Examples of obtained amplitude distributions from the LHC data are shown in Fig. 9.6. Comparing e.g. to Fig. 7.16 with the beam test results, it is visible that the amplitudes are too low. It was found out that the HV setting was too low, which was confirmed later in laboratory tests. The gain corresponding to the HV of 2000 V was $1–2 \cdot 10^4$, instead of intended $5 \cdot 10^4$.

9.2.4 Timing performance

Despite the low efficiency, it was possible to determine time resolutions of ToF channels. I used data from the low μ part of the run 336505 with statistics of 13 million events.

I used distributions of time differences between the times measured by each pair of bars within one train ($t_i - t_j$, where $i, j \in \{A, B, C, D\}$, $i \neq j$), extracted widths of the distributions σ_{ij} and determined the time resolutions of individual bars from

$$\sigma_{ij} = \sqrt{\sigma_i^2 + \sigma_j^2}, \quad i, j \in \{A, B, C, D\}, \quad i \neq j. \tag{9.3}$$

There are six independent equations in total for the four values of bar time resolutions, as $\sigma_{ij} = \sigma_{ji}$.

The formula assumes that time resolutions σ_i and σ_j are independent variables, which is not necessarily true and the equations should read

$$\sigma_{ij} = \sqrt{\sigma_i^2 + \sigma_j^2 - 2\varepsilon_{ij}\sigma_i\sigma_j}, \quad i, j \in \{A, B, C, D\}, \quad i \neq j, \tag{9.4}$$

where ε_{ij} is the correlation of the two variables. However, it was not possible to reliably extract the correlation factors form the data, due to the low efficiency. Therefore, I neglected the correlation, which could lead to an underestimation of the bar time resolutions. Introducing 30 % correlation for all the bar pairs resulted in increase of the average time resolution by 5 ps, suggesting the magnitude of induced systematic error.

The time distributions of bar differences $t_i - t_j$ were obtained in each train on both sides from the events satisfying the clean track condition (in this case, I required 2–3 hits in two SiT planes in the corresponding station, with at least one hit from one plane at most 1 row apart and within the same column as one of the hits in the second plane) with the track pointing to the train and having a valid time record for the two bars, times of which are being subtracted. Examples of the distributions are shown in Fig. 9.7.

The σ_{ij} values were extracted from fits of the time difference distributions and they were plotted in a graph (illustrated in the bottom of the figure) with x coordinate of 0, 1, 2, 3, 4, 5, each corresponding to one combination AB, AC, AD, BC, BD, CD, respectively. The graph was then fitted on interval $(0, 6)$ by the multistep function

$$f(x - 0.5) = \sqrt{\sigma_i^2 + \sigma_j^2}, \quad \text{where } i = \begin{cases} x \div 3 & \text{if } x < 5 \\ 2 & \text{otherwise} \end{cases} \text{ and } j = (x - i) \div 1, \tag{9.5}$$

where $\div$ is the integer division operation. Fitting by this function realizes a minimization procedure for solving the overdetermined system of equations Eq. 9.3.

The results are listed in Tab. 9.1. The missing values are caused by missing 1A on side A and 1D on side C in the data and due to failed fitting procedure in case of 1C on side A and 4C on side C. There are few very low values of time resolutions bellow 20 ps, which are contradicting the beam test results and these suggest the total systematic error of determined values to be close to 10 ps. The average time resolution is 32 ps.

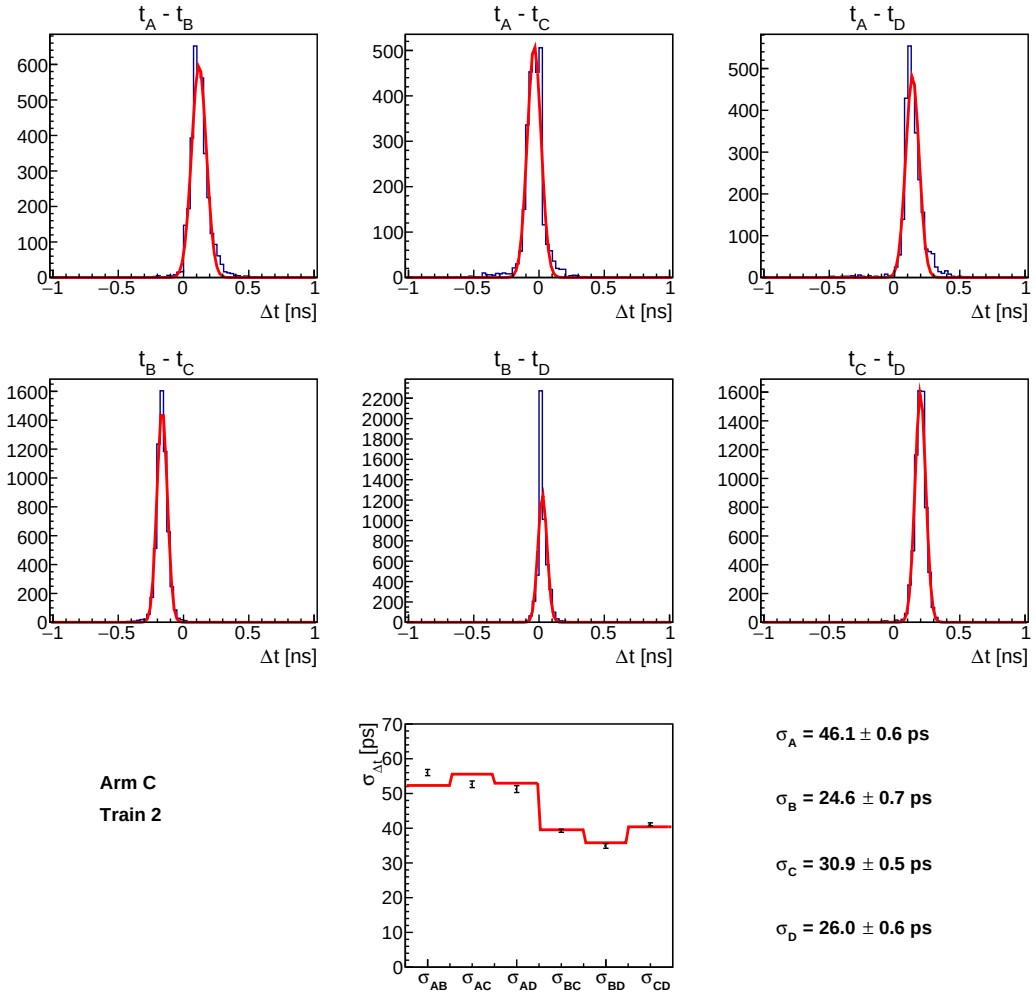

Figure 9.7: Time resolutions of bars of the train 2 on the C side in the run 336505.

Table 9.1: Resolution of bars from the LHC data in picoseconds.

	A side, bar:				C side, bar:			
Train	A	B	C	D	A	B	C	D
1	—	37	—	36	52	33	24	—
2	40	25	22	14	46	25	31	26
3	27	33	34	21	37	28	13	40
4	61	26	26	33	54	27	—	35

9.3 Summary and outlook

The AFP ToF detectors were installed together with the second arm of the AFP stations during the EYETS in the period of January–April 2017. The commissioning started at the beginning of May and at first the readout of the new SiT and ToF detectors was tuned and properly timed in.

The expected SiT-ToF correlation (Fig. 7.32) was not initially observed, however, after introducing tighter selection criteria, the correlation appeared.

The low efficiency of detectors was observed in both low and high μ runs. Two causes were identified: too low initial HV setting soon followed by reaching the expected MCP-PMT lifetime in terms of the total collected charge. While the later was expected to happen in order of months and will be addressed by the ALD coated MCP-PMTs, the HV setting was an error and needs to be set up more carefully in a future reinstallation. The CFD ToT functionality enabling to read MCP-PMT signal amplitudes was implemented and tested for the purpose of the proper HV setting and monitoring.

Despite the low efficiency, the time resolution values for bars provide rather optimistic estimate of the ToF performance, although they are affected by the neglected correlation and also due to the fact that only the MCP-PMT signals with a large amplitude were selected due to the HV and the CFD threshold settings. Still, the average time resolution of 32 ps is a good result, offering promising prospects for diffractive physics measurements, once the ToF is reinstalled and properly set up.

ToF detectors were removed at the end of 2017, because of the problems with the ALD coated MCP-PMTs measured during 2017 beam tests, that prevented the planned MCP-PMTs exchange. Several possibilities for replacement were investigated, including use of Hamamatsu MCP-PMTs with a similar form factor. A solution with new Photonis miniPlanacon MCP-PMTs was preferred as the pitch of pixels matches the LQbar design. The new Photonis tubes were available at the end of May 2018 and the foreseen installation should have happened during the TS1 at the end of July 2018. However, one of the tubes did not pass vacuum tests and the installation was abandoned.

Based on the rate performance of the miniPlanacon MCP-PMTs in the laboratory tests, a third stage of amplifier (PAc) was added to the signal chain. This, together with careful shielding of all ToF components up to PAb, enables to operate the MCP-PMTs at lower gain, which in turn allows to handle higher signal rates.

Conclusion

The work on this thesis comprised the software development, the data analysis, setting up and performing experiments and the detector hardware development.

The full simulation model of the ATLAS forward region was extended by orbit correctors and field transformations, further tuned and validated. The RP filler of ALFA stations was implemented.

The study of ATLAS central magnetic field influence on ALFA measurement at 7 TeV shown the effect on the four-momentum transfer t measurement of elastic protons of 0.3 % in Monte Carlo simulations. The comparison to data shown too large discrepancies between the model and the data to draw conclusions.

The simulation of multiple scattering and showers on the AFP thin entrance window demonstrated how much the tilt window, that was considered for the Hamburg beam pipe housing later replaced by Roman pots, affects the diffracted protons and AFP measurement. The scattering angle rose from 0.90–0.96 µm, for the window perpendicular to the beam, up to 1.61–1.81 µm for the window tilted at 11°. The fraction of showers was almost doubled between the two window angle limits.

The AFP ToF detector was successfully designed, manufactured and tested. Time resolution, crosstalk and efficiency of individual ToF channels were characterized.

The time resolution of ToF without the HPTDC contribution was measured and it was shown that the best achieved time resolution of individual bars was 20–30 ps. The trains with the taper manifested better time resolution by 5–15 %. The first bar within a train is always handicapped by the missing light leak that the consequent bars receive from their predecessors. The time resolution of the entire trains starts at 14–15 ps.

The best time resolutions were achieved near the edge of the parallel cut of the radiator part of a bar. The dependence of the resolution on the distance from the edge is approximately linear with e.g. the train 2 time resolution growing from 14 ps at 0 mm to 24 ps at 20 mm from the edge.

The ToF detector was integrated into the common AFP readout that uses the RCE system. The time measurements were digitized using the HPTDC module, which adds an additional smearing to the measurement. The HPTDC contribution to the time resolution was 12–17 ps. The combined ToF train resolution is therefore 15–30 ps over the AFP acceptance.

The crosstalk between bars was measured and it was shown that there is

a negligible optical crosstalk, except for the light leaking from one bar to the next within a train. Within one train, the crosstalk between channels results in a correlation of measurements in the train. The correlations of up to 20 % were observed in the RCE data (using different SiPMs as a reference for the bars being evaluated to avoid the trigger induced correlation). The crosstalk between bars of different trains reduces the ToF ability to handle a high pileup. E.g. in case of two protons in one ToF arm within an event, the time measurement of the second proton is spoiled by the first one, if the crosstalk is large, even if they hit different trains. The results for the MCP-PMT with the reduced anode gap showed up to 12 % events with the crosstalk contribution above the noise pedestal to the neighboring channel. Typically the crosstalk pulse starts in the positive voltage (opposed to the negative signal pulse) followed by several dampened oscillations with the amplitude of 8 % of the signal pulse causing it.

ToF channels manifested high efficiency of 80–98 % per bar and above 87 % efficiency when requiring 3 out of 4 bars within a train to respond. Bars with taper performed significantly better, with efficiency above 96 % per bar and 98 % for the 3/4 requirement.

The ALD coated Photonis MCP-PMTs were tested during 2017 beam tests, promising extended lifetime of about $10\,\mathrm{C\,cm^{-2}}$, corresponding to about a year of operation in the AFP [10]. These performed significantly worse with train time resolutions above 25 ps and increased crosstalk. These MCP-PMTs were not installed and they were replaced in 2018.

The measurements in the laser laboratory provided a useful insight into the MCP-PMT characteristics and performance of SiPMs. A good miniPlanacon MCP-PMT uniformity with the pixel variations in both mean signal amplitude and time resolution of less than 27 % was measured. The time transit spread, as the characteristic determining the timing performance of an MCP-PMT with a given detection efficiency, was measured in the range 39–49 ps for the channels of Photonis miniPlanacon XPM85112 tubes.

The STM and the FBK (branded as First Sensor) SiPMs were characterized with the focus on the time resolution under various illumination by two light wavelengths: 280 nm and 420 nm. The devices had the TTS of (245 ± 10) ps (FBK) and (124 ± 22) ps (STM). The time resolution dropped with increasing N_{pe} as $\sigma_{\mathrm{TTS}} N_{\mathrm{pe}}^{-\frac{1}{2}} \oplus \sigma_{\mathrm{const}}$ with the best time resolutions, achieved for N_{pe} of the order 10^6 for 420 nm, of (8 ± 1) ps and (4 ± 1) ps for the FBK and STM SiPM, respectively. The FBK SiPM was intended to serve as a replacement in case of a failure of one of the STM SiPMs. However, due to the significantly worse timing performance, confirmed also in a beam test, a different spare SiPMs had to be found. Later, the SensL MicroFC-SMA-30050 SiPMs were chosen.

The AFP ToF detectors were installed together with the second arm of AFP stations during the EYETS in the period of January–April 2017. The commissioning started at the beginning of May. ToF detectors worked, however low efficiency at the level of 1–8 % was observed. This was caused by too low HV setting and by the soon reached lifetime of MCP-PMTs. A monitoring of MCP-

PMT signal amplitude was implemented to avoid the low HV in the future. Even though the efficiency was low, the timing performance was evaluated and an average bar time resolution of 32 ps was measured, promising good prospects once the ToF is reinstalled and set up properly.

Currently, the ToF detectors are not installed in the LHC tunnel. They were removed at the end of 2017 and were not reinstalled due to the issues with the ALD coated PMTs measured in 2017 beam tests. Replacements for these tubes were obtained, however issues with operation in vacuum arose.

The AFP ToF detectors need a further development in order to keep up with the increasing luminosities in the LHC Run 3. The foreseen replacement of the HPTDC by the picoTDC should improve the $\sim$5 MHz limitation at the readout and the added PAc amplifier and the ToF shielding allows to handle higher rates due to the lowered gain of the MCP-PMT. In addition, glue-less bars are being developed at the JLO, promising about 20 % more light at the MCP-PMT window and less deterioration due to an irradiation. This could allow to reduce the MCP-PMT gain even further and to improve time resolutions. Also, the MCP-PMTs are still improving. However, the current ToF design is not the only option. Low gain avalanche detectors (LGADs) show very promising results [P13] and diamond detectors or fast silicon detectors can be an option as well, if they prove to be enough radiation tolerant.

Appendix A

List of figures

1.1 CERN accelerator complex [5]. 6
1.2 Bunch disposition of LHC, SPS and PS [2]. 7
1.3 Visualization of the beam crossing at the IP1 [6]. 8
1.4 Event display of a $Z \to \mu\mu$ candidate with 24 accompanying vertices. Red lines represent tracks of reconstructed muons from the event of interest, while the blue lines show other reconstructed tracks. The grey horizontal stripes illustrate ATLAS tracker planes (ATLAS Experiment © 2018 CERN). 8
1.5 ATLAS experiment with a cut out part to see the inner composition of detector layers [1]. 9
1.6 Placement of LUCID, ZDC and ALFA detectors in the forward region of ATLAS (one side) with a visualization of each detector. [1]. 10
1.7 ATLAS coordinate system. 12
1.8 Schema of the ALFA placement. The lower part indicates the station names and positions in Run 1 [P11]. 13
1.9 ALFA Roman pot [P11]. The two rectangular extensions at the top cover the OD detectors, while the MD is placed in the large box beneath with the sensitive area behind the diamond-shaped thinned wall. 14
1.10 *Left:* Schematic view of the ALFA station instrumentation (copyright CERN, CC-BY-4.0 license). *Right:* Photograph of the ALFA detector assembly [P11]. 14
1.11 Modifications of the ALFA pot and station to lower RF heating. *Left:* RP filler placed on the original pot; *middle:* ferrite ring attached to the station flange; *right:* added copper inside the pot to improve heat transfer [P11]. 15
1.12 Hamburg beam pipe with QUARTIC detectors enclosed in the secondary vacuum vessel [11]. 16
1.13 Schema of the AFP placement and instrumentation [12]. 17
1.14 *Left:* Schematic view of the AFP far station instrumentation [12]. *Right:* Photograph of the AFP detector assembly [12]. 17

1.15 View of the Roman pot inserted in the beampipe [12]. 18

2.1 Schema of magnets in the forward region between the IP and about 270 m [16]. 19
2.2 *Left:* Differential elastic cross section measured by ALFA with the fit using the theoretical prediction with free parameters σ_{tot} and B. The lower part shows the relative difference between the fit and the data with the yellow area representing the total uncertainty and the hatched area the statistical uncertainty. *Right:* Compilation of total and elastic cross section results as a function of the center-of-mass energy [P8]. 24
2.3 Proton-proton elastic cross section as a function of t for various energies in a collision. P stands for the momentum of the incoming proton in a fixed target experiment and $\sqrt{s}$ is the center-of-mass energy in pp collision [21]. 25
2.4 Illustration of elastic scattering, single and double diffractive dissociation [10]. 25
2.5 Illustration of central diffraction with (a) intact protons, (b) single dissociation, (c) double dissociation [10]. 26
2.6 Feynman diagrams of hard diffraction processes — (a) diffractive deep inellastic scattering (DDIS), (b) double pomeron exchange (DPE), (c) central exclusive production (CEP) [10]. 26
2.7 Feynman diagrams of processes with a potential to probe beyond the Standard Model physics. From left to right: diphoton production of diphoton, WW or ZZ; diphoton production of an invisible particle X; CEP of an invisible particle X. 28
2.8 Geometric (*left*) and mass (*right*) acceptance of the AFP [26]. . . 28

3.1 Illustration of the field transformation. Input parameters for the transformation are marked — start point, end point and rotation angle around the magnet axis. Point in the center shows the point around which the magnet is rotated. 34
3.2 Visualization of recticircular volume with flats on top and bottom. 34
3.3 Visualization of the forward region model — one side with ALFA, AFP and ATLAS. 35
3.4 Positions of protons with $\eta = 10$ and different energy after the transport by the `ALFA_BeamTransport` at $z = 237.403$ m. Axes are not to scale. The cut top and bottom are caused by apertures of beam elements (for the given optics, mostly by the aperture of the Q6 magnet). 37
3.5 Histograms of the differences between the full simulation and `ALFA_BeamTransport` in x (up) and y (down) for the beam 1 (left) and the beam 2 (right). 38

3.6 Histograms of the differences between the full simulation and ALFA_BeamTransport in r for the beam 1 (left) and the beam 2 (right). 38
3.7 Histograms of the differences between the full simulation and ALFA_BeamTransport in x (up) and y (down) with corresponding coordinate value for the beam 1 (left) and the beam 2 (right). . . 39
3.8 Histograms of the differences between the full simulation and ALFA_BeamTransport in r with corresponding value of r for the beam 1 (left) and the beam 2 (right). 39
3.9 Transported protons positions at position of the first AFP station ($z = 204\,\mathrm{m}$), $\xi = 0.29, 0.26, 0.23, 0.20, 0.17, 0.14, 0.11, 0.09, 0.06, 0.03, 0$, $p_\mathrm{T} = 2$ GeV with purged physics list (transport only). The blue rectangle represents the AFP geometrical acceptance, the green cross marks center of the beam. 41
3.10 Transported protons positions at position of the first AFP station ($z = 204\,\mathrm{m}$), $\xi = 0.29, 0.26, 0.23, 0.20, 0.17, 0.14, 0.11, 0.09, 0.06, 0.03, 0$, $p_\mathrm{T} = 2$ GeV with default physics list. The blue rectangle represents the AFP geometrical acceptance, the green cross marks center of the beam. 41
3.11 Visualization of the Q2 magnet field map. Contours show the value of the magnetic induction, arrows show the value and direction of the magnetic induction in the mesh points of the map. . . 42
3.12 Difference between the magnetic induction value calculated by interpolating the field map and that of the ideal (analytical) quadrupole for $x = 0$. 42
3.13 Differences in transported positions between Mad-X and the full simulation using 7 TeV, $\beta^* = 0.55$ m optics with a beam crossing. 44

4.1 VP1 [39] visualization of the ALFA Roman pot (light gray in the foreground) with the RP filler (dark grey). 45
4.2 Persint [41] visualization of the ATLAS magnetic field — $y = 0$ plane. 47
4.3 Persint [41] visualization of the ATLAS magnetic field — $z = 0$ plane. 47
4.4 Transported protons of beam 1 at the end of cavern, for the magnetic field of ATLAS switched on (green) and for the field off (red). The bottom picture is the zoomed in central part of the upper picture. Two points are circled to provide a reference. . . . 49
4.5 Differences of proton positions at the end of cavern for the magnetic field of ATLAS switched on and for the field off. 50
4.6 Transported protons at the 237 m from the IP, beam1 for the magnetic field of ATLAS switched on (green) and for the field off (red). The bottom picture is the zoomed in central part of the upper picture. Two points are circled to provide a reference. . . . 51

4.7 Differences of proton positions at the 237 m from the IP for the magnetic field of ATLAS switched on and for the field off. 52
4.8 ALFA chain block diagram. 53
4.9 Alignment illustration. Left to right: horizontal offset, rotation angle, vertical distance and offset. 53
4.10 Comparison of x distributions of hits passing selection criteria for the sample with the field off (black) and on (green). Bottom graph under each histogram plots ratio in a given bin (excluding empty bins). 56
4.11 Comparison of y distributions of hits passing selection criteria for the sample with the field off (black) and on (green). Bottom graph under each histogram plots ratio in a given bin (excluding empty bins). 56
4.12 Event-by-event comparison — the difference between hit position in the field on and the field off sample ($\Delta x = x_{\text{fieldOff}} - x_{\text{fieldOn}}$). . 57
4.13 Event-by-event comparison — the difference between hit position in the field on and the field off sample ($\Delta y = y_{\text{fieldOff}} - y_{\text{fieldOn}}$). . 57
4.14 Event-by-event x difference for the pot 0 with the real fiber placement (left) and the ideal fiber placement (right). 58
4.15 Positions of hits in events with a 4/4 track in the field off sample, but no 4/4 track in the field on sample (red), and in events with a 4/4 track in the field on sample, but no 4/4 track in the field ff sample (green). 58
4.16 Raw t comparison. Left: reconstructed t spectrum for both samples without corrections. Right: event-by-event comparison of the reconstructed t values. 59
4.17 Migration between the true (generated) t values and the values reconstructed by the ALFA detectors for the two samples with the field off and on. 60
4.18 Raw t spectrum reconstructed from the true positions of transported protons. Left: reconstructed t spectrum for both samples without corrections; ratio subplot has now smaller scale. Right: event-by-event comparison of the reconstructed t 60
4.19 Raw t spectrum reconstructed from the true positions of transported protons in the range ALFA uses for fitting. Left: reconstructed t spectrum for both samples without corrections. Right: event-by-event comparison of the reconstructed t for $-t \in [0.05, 0.15)$ GeV^2. 61
4.20 Illustration of the beam screen edge effect – the edge fitting procedure returns 1 mm different beam screen edge position (which is used to cut the y distribution) for data (green) and MC sample (black) in detectors on the left side. 62
4.21 EasyTracker [43] visualization of the Q6 beam screen edge. Top: horizontal projection, bottom: vertical projection. 63

4.22 Effect of the B slope on the x distribution of hits in ALFA pot 0 in the MC sample (black) compared to the data sample (green). The bottom part of each histogram shows ratio of the counts in each bin for MC over data. 64
4.23 Comparison of the MC and the 191373 data distributions. Upper row: x distributions; lower row: y distributions. Left column: MC sample with the field off; right column: MC sample with the field on. Black: MC; green: data. 65

5.1 Modified Hamburg beam pipe design. The orange area marks the thinned steel window [44]. 67
5.2 Scattering angle distributions after the last SiT plane (*left*) and the development of the mean scattering angle at individual SiT planes (*right*) for 0.3 mm thick window tilted at angles 11–90°. . 68
5.3 Fraction of events with showers as a function of the window tilt angle. 69

6.1 Illustration of a central diffraction event and two single diffraction events producing the same signature in AFP. 73
6.2 (a) Measured spectral transmissivity of Suprasil and Epotek 305 glue, (b) Light spectrum at the output of an LQbar (simulation) [P9]. 75
6.3 (a) Geometry of LQbars assembly in ToF, (b) LQbars with tracker planes (not in scale) [P14]. 75
6.4 Calculation of the time offset compensation. 76
6.5 Distribution of diffractive protons in AFP tracker acceptance (simulation) with overlaid ToF bars for the A side (*left*) and the C side (*right*). T1–T4 stand for train 1–4, solid blue line represents the edge cut and dashed blue line is placed at 5 mm from the edge. . 77
6.6 Light guide taper [P3]. 77
6.7 *Left:* Assembled ToF detector prototype with SiT tracker planes (with protective covers) on the Roman pot flange. *Right:* SketchUp [50] model of a holder plate with grooves. 78
6.8 Schema of an MCP-PMT. 79
6.9 Schematic structure of MCP [51]. 79
6.10 Time distribution of single photoelectron pulses produced by Photonis XPM85112 MCP-PMT illuminated by a femtosecond laser. 80
6.11 Photograph of a Photonis XPM85112 MCP-PMT. 81
6.12 Schema of ToF readout electronics. 81
6.13 The first stage preamplifier (PAa) board with the heat sink (courtesy off Vladimír Urbášek). 82
6.14 Feedthrough for signal lines and thermistors from the PAa. *Left:* outside of the Roman pot, *right:* whole feedthrough assembly with the inside of the pot at the top. 82
6.15 The PAb module. 83

6.16 Oscilloscope view of an MCP-PMT pulse (C1, yellow, 50 mV/div) and CFD output pulse (C2, magenta, 70 mV/div). Time scale set to 2 ns/div. 84
6.17 Simulation of the CFD constant fraction setting (labeled as the trigger level) impact on the time resolution of ToF (courtesy of Tomáš Komárek). The same set of MCP-PMT signal was processed using the software (SW) CFD with varying constant fraction setting for the pulse edge time extraction and the time resolution was evaluated for each setting. 84
6.18 The CFD module (*left*) and the trigger module (*right*). 85
6.19 The clock distribution reciever module under laboratory testing. 87
6.20 High Speed Input/Output board with Reconfigurable Cluster Element mezzanine (the small black board with the fan on top). . . 88

7.1 CERN North Area experimental site. 89
7.2 Monitoring screen of the SPS showing a course of a supercycle with two spills. The white line plots the field intensity of the SPS bending magnets and the yellow line the proton beam intensity [58]. 90
7.3 Beam test experimental setup [P14]. 91
7.4 Beam test area (H6B) overview. 92
7.5 November 2014 beam test experimental setup. 93
7.6 Oscilloscope screenshot from the CFD test. Two CFD output channels (magenta and cyan) and the trigger pulse (green) are recorded. The two histograms show time difference between the leading edge of the CFD output w.r.t. the trigger pulse leading edge (at 50 % level). 94
7.7 Oscilloscope screenshot from the HV optimization. The oscilloscope is triggered by an SiPM passed through the CFD (C4, green) and raw signals from two ToF bars are recorded (C1, yellow and C2, magenta). The two histograms represent the amplitude distribution of the C1 and C2 inputs with matching colors, each bin corresponds to 50 mV. Both histograms show an acceptable signal separation from the pedestal. 94
7.8 Correlation between the reconstructed SiT track position and response in ToF channels for the x (*right*) and y (*left*) coordinate. The MCP-PMT HV was set to 1800 V [P10]. 96
7.9 Example of time distribution obtained for bar 2B w.r.t. SiPM1 with Gaussian fit (*left*) and fit by sum of two Gaussians (*right*). . 96
7.10 Efficiency (*left*) and mean crosstalk from the neighboring channels (*middle*) and next-to-neighboring channel (*right*) as a function of HV for all bars [P10]. 98

7.11 *Left:* Distribution of the amplitudes with the blue boxes representing the range from the 25 % to the 75 % quantile, the red line marking the mean value and the dotted line representing the distribution range excluding the outliers drawn as the red points. *Right:* Distribution of generated photoelectrons obtained from a Monte Carlo simulation [P3]. 99
7.12 Time resolution distributions of the bars 2A and 2B, and of the two-bar train [P3]. 100
7.13 Optical leakage between bars near the train edge, (a) visualization in Geant4, (b) contribution of the own and the parasitic fractions to the total hit count in the sensor [61]. 101
7.14 Time evolution of the combined resolution of two SiPMs throughout the beam test measured by oscilloscope and RCE (with HPTDC contribution). The supply voltage changed as indicated by the dashed orange line. Incremental RCE run numbers are used on the x axis for ordering of the measurements and pure oscilloscope measurements are placed in between appropriate RCE runs. The grayed area labels period when a coincidence unit was placed in the SiPM1 signal path introducing an additional timing jitter. . . 102
7.15 Comparison of amplitude (*left*) and time (*right*) distributions for bar 1A (*top*, with the taper), 3A (*bottom*, without the taper) with and without the grease with the loaned MCP-PMT at the HV of 1870 V. The SiPM contribution is subtracted in the time resolutions. 105
7.16 Signal amplitude distributions for bars of the train 2 (polished) and the train 3 (matte light guide). In both cases the HV was set to 1950 V. The negative polarity of the the signal originates from the MCP-PMT output polarity. 106
7.17 Example of bar correlations observed during the beam test — bars of train 2 (courtesy of Libor Nožka). 107
7.18 Simulated time distribution for bar 2A with the ideal trigger ($\sigma_{\text{trig}} = 0$, *left*) and for $\sigma_{\text{trig}} = 15$ ps (*right*). 108
7.19 Correlation plots of simulated time distributions of two bars of a train for increasing time resolution of a trigger. 109
7.20 Time distributions of individual bars of train 6 and of the whole train (black) for the measurement at the edge, PMT 9002053. The *sigma* and *FWHM* values in the statistic boxes are not corrected for the SiPM contribution [P14]. 110
7.21 *Left:* Timing resolution of the Train 2 as a function of the distance from the edge; *right:* correlation of σ and FWHM measures of the timing resolution [P14]. 111
7.22 Pixels of miniPlanacon MCP-PMT with their designed bar occupancy [P14]. 112

7.23 Leakage of the signal to adjacent pixels from the bar 6A (*left*), the bar 6B (*right*). The axes give the MCP-PMT pixel number, as shown in Fig. 7.22 [P14]. 112
7.24 *Left:* leakage of the signal to adjacent pixels from the pair of bars 6A and 6C (the axes give the MCP-PMT pixel number, as shown in Fig. 7.22). *Right:* histogram of the signal amplitudes in the empty pixel 32 in different bars configuration [P14]. 113
7.25 Efficiency of individual bars (*left*) and trains (*right*) for the HV of 2100 V and the CFD threshold of −150 mV. 114
7.26 Time resolution of the First Sensor (FBK) SiPM. 115
7.27 Raw signal waveforms in bar 3B for MCP-PMT 9002053 (*left*) and 9002096 (*right*). There are 32768 waveforms overlaid in each plot and the color map shows the amount of overlaid waveform points. 116
7.28 Raw crosstalk waveforms in bar 4B with signal in train 3 for MCP-PMT 9002053 (*left*) and 9002096 (*right*). There are 32768 waveforms overlaid in each plot and the color map shows the amount of overlaid waveform points. 117
7.29 Time distributions of individual bars of train 3 and of the whole train (black) for the measurement at the edge, PMT 9002097. The *sigma* values in the statistic boxes are not corrected for the SiPM contribution. 117
7.30 Schematic of the internal connections of Photonis miniPlanacon MCP-PMT [53]. The red crosses mark the removed MCP output and associated components of the modified MCP-PMT. 118
7.31 Efficiency of ToF channels for different settings of trigger requirement. 119
7.32 Correlation between response in ToF channels (and SiPMs) and y coordinate of the track registered by the SiT for runs with detectors in air (*up*) and in vacuum (*down*). Two channels were not functioning properly in the earlier — 2C (bad connection) and 4D (a low threshold on CFD). 120

8.1 Photographs of the MCP-PMT in the custom dark box (*left*) and in the custom encapsulation (*right*). 124
8.2 Measurement setup using the trigger output of the laser. The purple lines represent the laser beam, the boxes with round corners stand for optical components and the DUT, and the rectangles are used for the electronic devices. 124
8.3 Measurement setup using the SiPM as the trigger. The purple lines represent the laser beam, the boxes with round corners stand for optical components, the SiPM and the DUT, and the rectangles are used for the electronic devices. 125

8.4 Uniformity of the MCP-PMT 9002053 response in terms of the output pulse amplitude (*left*) and the time resolution (*right*). The colormap is inverted between the two plots, as the resolution is expected to rise with decreasing amplitude. 126
8.5 Time distributions at the single photoelectron level for the MCP-PMT from the 2015 beam test (*left*) and the 2 inch XP85012 (*right*). 128
8.6 Schematic view of an SiPM structure. The left part depicts the cross section of the SiPM chip, the middle part is the schema of a placement of individual microcells and the right part is the circuit schema [67]. 129
8.7 Photograph of the optical fiber coupled to the fused silica bar of SiPM detector for measurement of the glycerol aging effect. . . . 130
8.8 A typical time distribution for a single photoelectron (left) and a high number of photoelectrons (right). Histograms show time distributions for STM SiPM operated at 2.9 V overvoltage and illuminated by 420 nm laser light for $N_{\mathrm{pe}} = 1.2$ (left) and $N_{\mathrm{pe}} = 270$ (right). The Gaussian fit from which the time resolution was extracted is represented by the red line [P15]. 134
8.9 Illustration of the noise simulation. *Left:* a generated pulse, *right:* the same pulse with the superimposed noise [P16]. 135
8.10 Time resolution uncertainty dependence on the mean pulse amplitude determined from the simulation [P16]. 136
8.11 Time resolution dependence on N_{pe} for the overvoltage of 2.9 V (left); the resolution as a function of the overvoltage for N_{pe} in range 20–30 for 420 nm and 35–45 for 280 nm (right). N_{pe} calculation changes at $N_{\mathrm{pe}} \approx 10$, as described in section 8.3.2.1 [P15]. . 136
8.12 Correlation between the time resolution expressed in σ obtained from the Gaussian fit and the full width at half-maximum (FWHM) value of the time distribution. The values are fitted by FWHM $= K\sigma$. The fit is represented by the red line. *Left:* STM SiPM; *right:* FBK SiPM [P15]. 137
8.13 Time resolution dependence on the SiPM overvoltage for the single photoelectron level [P15]. 138

9.1 Temperature maps of PAb (*left*), CFD (*middle*) and HPTDC (*right*) module boards. 142
9.2 First observed SiT-ToF correlation in the run 327288, the C side ToF detector with a loose selection (*left*) and tight cuts (*right*). The black boxes illustrate expected signal regions. 144
9.3 SiT-ToF correlation after TS1 with the tight selection for the A side (*left*) and the C side (*right*), run 328339. The black boxes illustrate expected signal regions. 145
9.4 ToF efficiency as a function of SiT x coordinate in the run 336505. 146

9.5 Total integrated luminosity delivered by LHC and recorded by ATLAS and AFP in 2017 [75]. 147
9.6 Amplitude distributions obtained from CFD ToT values at the HV of 2000 V for trains 2 and 3 on side C. 148
9.7 Time resolutions of bars of the train 2 on the C side in the run 336505. 150

Appendix B

List of tables

3.1 Coordinate system differences between `ALFA_BeamTransport` and the full simulation at the position of ALFA stations. 36

4.1 Results of horizontal alignment showing offset in mm for both samples. MC truth column contains offsets that were set in both simulations. 54
4.2 Results of horizontal alignment showing rotation angle in rad for both samples. MC truth column contains angles that were set in both simulations. 54
4.3 Results of vertical alignment showing optimized distance in mm for both samples. MC truth column contains distances that were set in both simulations. The reference station is underlined. . . . 54
4.4 Results of vertical alignment showing offset in mm for both samples. MC truth column contains offsets that were set in both simulations. The reference station is underlined. 54
4.5 Comparison of resolutions of the ALFA detectors in the simulation and in the data. 66

5.1 Mean scattering angle $\langle\theta\rangle$ after the last SiT plane for 0.3 mm and 0.4 mm thick window tilted at angles 11–90°. 68

6.1 The AFP trigger signal latency. 86

7.1 Resolution of bars and two-bar trains in picoseconds. Estimated uncertainty is ± 2 ps [P9]. 100
7.2 Resolution of bars in the RCE measurements in picoseconds. The estimated uncertainty is ± 2 ps. 104
7.3 Resolution of selected single bars at their edges. The estimated uncertainty is ± 2 ps in σ and ± 5 ps in FWHM [P14]. 110
7.4 Time resolution of trains. The estimated uncertainty is ± 1 ps in σ and ± 2 ps in FWHM [P14]. 111

7.5 Resolution of bars of train 6 as measured by the oscilloscope (σ_{scope}) and the RCE (σ_{RCE}). The contribution of the HPTDC σ_{HPTDC} is determined from these two values. The estimated uncertainty is ± 2 ps for the bar resolutions and ± 1 ps for the train resolutions. 115

8.1 Time transit spread measurements of MCP-PMTs measured in the JLO laser lab. The estimated uncertainty is ± 2 ps. 128
8.2 Effect of the glycerol age on the time resolution of the SiPM. . . . 131

9.1 Resolution of bars from the LHC data in picoseconds. 150

Appendix C

List of abbreviations

AFP ATLAS Forward Proton

ALD atomic layer deposition

ALFA Absolute Luminosity for ATLAS

APD avalanche photodiode

ATLAS A Toroidal LHC Apparatus

BD breakdown (of an APD or an SiPM)

BT beam test

BX bunch crossing (25 ns)

CD central diffraction

CEP central exclusive production

CERN European Laboratory for Nuclear Research

CFD constant fraction discriminator

CNM Centro Nacional de Microelectronica, Barcelona, Spain

CSC Cathode Strip Chamber

CTP Central Trigger Processor (of ATLAS)

DAQ data acquisition

DCS Detector Control System (of ATLAS)

DD double diffractive dissociation (double diffraction)

DDIS diffractive deep inelastic scattering

DPDF diffractive parton distribution function

DPE double pomeron exchange

DUT device under test

EM electro-magnetic

EYETS extended year end technical stop (of the LHC)

FBK Fondazione Bruno Kessler, Trento, Italy

FFC flat flexible cable

FPGA field-programmable gate array

FWHM full width at half maximum

HPTDC High Performance Time-to-Digital Converter

IBL Insertable B-layer

IP interaction point

JLO Joint Laboratory of Optics of Palacký University in Olomouc and Institute of Physics of the Czech Academy of Sciences

LAr liquid argon

LGAD low gain avalanche detectors

LHC Large Hadron Collider

LRG large rapidity gap

LS1 Long Shutdown 1 (of the LHC)

LS2 Long Shutdown 2 (of the LHC)

LSS1 Long Straight Section 1 (LHC section surrounding ATLAS)

LUCID Luminosity measurement using Cherenkov Integrating Detector

MAPMT multiple anode photomultiplier

MCP-PMT micro-channel plate photomultiplier

MD main detector (of ALFA)

MDT Monitored Drift Tube

MPPC multipixel photon counter

NTC negative temperature coefficient thermistor

OD overlap detector (of ALFA)

PAa first-stage pre-amplifier

PAb second-stage pre-amplifier

PAc third-stage pre-amplifier

pQCD perturbative quantum chromodynamics

PS Proton Synchrotron

QCD quantum chromodynamics

RCE Reconfigurable Cluster Element (a DAQ system)

RF radio-frequency

RP Roman pot

RPC resistive plate chamber

SBU Stony Brook University

SD single diffractive dissociation (single diffraction)

SiPM silicon photo-multiplier

SiT silicon tracker

SLAC Stanford Linear Accelerator Complex

SPS Super Proton Synchrotron

SPTR single photon time resolution

STM STMicroelectronics

TAN Target Absorber Neutral

TGC thin gap chamber

ToF time-of-flight

ToT time over threshold

TRT Transition Radiation Tracker

TS1 technical stop 1 (the first technical stop of the LHC in a given year)

TTS time transit spread

UTA University of Texas in Arlington

YETS year end technical stop (of the LHC)

ZDC Zero Degree Calorimeter

References

[1] ATLAS Collaboration. The ATLAS Experiment at the CERN Large Hadron Collider. *Journal of Instrumentation*. 2008, vol. 3, no. 08, pp. S08003. Available also from WWW: ⟨http://stacks.iop.org/1748-0221/3/i=08/a=S08003⟩.

[2] Evans, L.; Bryant, P. LHC Machine. *Journal of Instrumentation*. 2008, vol. 3, no. 08, pp. S08001. Available also from WWW: ⟨http://stacks.iop.org/1748-0221/3/i=08/a=S08001⟩.

[3] R. D. Heuer. *General Meeting January 2013* [online]. 2013 [visited on 2018-06-01]. Available from WWW: ⟨https://indico.cern.ch/event/219327/attachments/355208/494765/address-Jan2013.pdf⟩.

[4] F. Gianotti. *New Year Presentation* [online]. 2018 [visited on 2018-06-01]. Available from WWW: ⟨https://indico.cern.ch/event/660352/attachments/1583505/2502838/Jan-2018-talk.pdf⟩.

[5] Mobs, Esma. The CERN accelerator complex. Complexe des accélérateurs du CERN. 2016. General Photo. Available also from WWW: ⟨https://cds.cern.ch/record/2197559⟩.

[6] *Collisions*. [online]. [visited on 2018-06-01]. Available from WWW: ⟨https://lhc-machine-outreach.web.cern.ch/lhc-machine-outreach/collisions.htm⟩.

[7] Steerenberg, R. *LHC report: full house for the LHC* [online]. [visited on 2018-10-10]. Available from WWW: ⟨https://home.cern/cern-people/updates/2017/07/lhc-report-full-house-lhc⟩.

[8] Avoni, G.; Bruschi, M.; Cabras, G., et al. The new LUCID-2 detector for luminosity measurement and monitoring in ATLAS. *Journal of Instrumentation*. 2018, vol. 13, no. 07, pp. P07017. Available also from WWW: ⟨http://stacks.iop.org/1748-0221/13/i=07/a=P07017⟩.

[9] Phipps, M. W. A New ATLAS ZDC for the High Radiation Environment at the LHC. 2018. Available also from WWW: ⟨https://cds.cern.ch/record/2319880⟩.

[10] Adamczyk, L.; Banaś, E.; Brandt, A., et al. *Technical Design Report for the ATLAS Forward Proton Detector*. 2015. Available also from WWW: ⟨https://cds.cern.ch/record/2017378⟩.

[11] Pinfold, J. *AFP-QUARTIC Mechanics* [online]. 2012 [visited on 2018-07-03]. Presentation on AFP review. Available from WWW: ⟨https://indico.cern.ch/event/206644/contributions/1495802/⟩.

[12] *AFP Figures, twiki page*. [online]. [visited on 2018-06-01]. Available from WWW: ⟨https://twiki.cern.ch/twiki/bin/view/Atlas/AFP_Figures⟩.

[13] Lange, J.; Areste, M. Carulla; Cavallaro, E., et al. 3D silicon pixel detectors for the High-Luminosity LHC. *Journal of Instrumentation*. 2016, vol. 11, no. 11, pp. C11024. Available also from WWW: ⟨http://stacks.iop.org/1748-0221/11/i=11/a=C11024⟩.

[14] Lehmann, A.; Böhm, M.; Eyrich, W., et al. Lifetime of MCP-PMTs and other performance features. *Journal of Instrumentation*. 2018, vol. 13, no. 02, pp. C02010. Available also from WWW: ⟨http://stacks.iop.org/1748-0221/13/i=02/a=C02010⟩.

[15] Rijssenbeek, M.; AFP Collaboration, et al. ATLAS Forward Proton Detectors: Time-of-Flight Electronics. *Acta Phys. Pol. B Proc. Suppl.* 2014, vol. 7.

[16] Faus-Golfe, A.; Efthymiopoulos, I.; Grafstrom, P.; Rijssenbeek, M.; Haguenauer, M. A Very High-beta Optics to be used for an Absolute Luminosity Determination with Forward Detectors in ATLAS. In. *9th European Particle Accelerator Conference (EPAC 2004)*. 2004, pp. 1282–1284. Available also from WWW: ⟨http://hal.in2p3.fr/in2p3-00126110⟩.

[17] Jiráková, K. *Finding of optics improving the acceptance of the ALFA detector for diffractive protons* [online]. 2014 [visited on 2018-06-01]. Bachelor's thesis. Available from WWW: ⟨https://theses.cz/id/klr241/⟩.

[18] Wiedemann, H. *Particle Accelerator Physics*. 2015. Graduate Texts in Physics. ISBN 9783319183176.

[19] Herr, W.; Muratori, B. Concept of luminosity. 2006. Available also from WWW: ⟨https://cds.cern.ch/record/941318/files/p361.pdf⟩.

[20] Barone, V.; Predazzi, E. *High-Energy Particle Diffraction*. Berlin Heidelberg: Springer-Verlag, 2002. Texts and Monographs in Physics. Available also from WWW: ⟨http://www-spires.fnal.gov/spires/find/books/www?cl=QC794.6.C6B37::2002⟩. ISBN 3540421076.

[21] Arneodo, M.; Diehl, M. Diffraction for non-believers. In. *HERA and the LHC: A Workshop on the implications of HERA for LHC physics. Proceedings, Part B*. 2005, pp. 425–446. Available also from WWW: ⟨arXiv: hep-ph/0511047 (hep-ph)⟩.

[22] ATLAS Collaboration. Dijet production in s=7 TeVpp collisions with large rapidity gaps at the ATLAS experiment. *Physics Letters B*. 2016, vol. 754, pp. 214–234. Available also from WWW: ⟨http://www.sciencedirect.com/science/article/pii/S037026931600040X⟩. ISSN 0370-2693.

[23] Kepka, O; Royon, C; Schoeffel, L, et al. *Physics Cases within the AFP project*. 2012. ATLAS note to be made public. Available also from WWW: ⟨https://cds.cern.ch/record/1454194⟩.

[24] ATLAS Collaboration. *Proton tagging with the one arm AFP detector*. 2017. Available also from WWW: ⟨https://cds.cern.ch/record/2273274⟩.

[25] Fichet, S.; Gersdorff, G. von; Kepka, O., et al. Probing new physics in diphoton production with proton tagging at the Large Hadron Collider. *Phys. Rev.* 2014, vol. D89, pp. 114004. Available also from WWW: ⟨http://dx.doi.org/10.1103/PhysRevD.89.114004arXiv: 1312.5153 (hep-ph)⟩.

[26] Trzebinski, M. *The ATLAS Forward Proton Detector*. 2017. CERN Detector Seminar. Available also from WWW: ⟨https://indico.cern.ch/event/682159/⟩.

[27] Agostinelli, S. et al. GEANT4: A Simulation toolkit. *Nucl. Instrum. Meth.* 2003, vol. A506, pp. 250–303. Available also from WWW: ⟨http://dx.doi.org/10.1016/S0168-9002(03)01368-8⟩.

[28] *Twiki page for ATLAS ForwardTransport*. [online]. [visited on 2018-06-01]. Available from WWW: ⟨https://twiki.cern.ch/twiki/bin/viewauth/Atlas/ForwardTransport⟩.

[29] Pelikan, D.; Pfeiffer, F.; Stenzel, H. *Beam transport simulation of elastically scattered protons in Athena*. 2010. Approval request after note revision. Available also from WWW: ⟨https://cds.cern.ch/record/1240360⟩.

[30] Bussey, P.; Sherwood, P. *FPTracker package* [online]. [visited on 2018-06-01]. Available from WWW: ⟨https://svnweb.cern.ch/trac/atlasoff/browser/ForwardDetectors/FPTracker⟩.

[31] Carquin, E. et al. *FNTracker package* [online]. [visited on 2018-06-01]. Available from WWW: ⟨https://svnweb.cern.ch/trac/atlasoff/browser/ForwardDetectors/FNTracker⟩.

[32] Boudreau, J.; Tsulaia, V. The GeoModel toolkit for detector description. In. *Computing in high energy physics and nuclear physics. Proceedings, Conference, CHEP'04, Interlaken, Switzerland, September 27-October 1, 2004*. 2005, pp. 353–356. Available also from WWW: ⟨http://doc.cern.ch/yellowrep/2005/2005-002/p353.pdf⟩.

[33] *AGDD volume types*. [online]. [visited on 2018-06-01]. Available from WWW: ⟨https://twiki.cern.ch/twiki/bin/viewauth/Atlas/AGDDVolumeTypes⟩.

[34] Baranov, S; Bosman, M; Dawson, I, et al. *Estimation of Radiation Background, Impact on Detectors, Activation and Shielding Optimization in ATLAS*. 2005. Available also from WWW: ⟨https://cds.cern.ch/record/814823⟩.

[35] *Virtual Point 1*. [online]. [visited on 2018-06-01]. Available from WWW: ⟨https://atlas-vp1.web.cern.ch/atlas-vp1/home/⟩.

[36] *Layout Database*. [online]. [visited on 2018-06-01]. Available from WWW: ⟨https://layout.web.cern.ch/⟩.

[37] *CERN Drawing Directory Server*. [online]. [visited on 2018-06-01]. Available from WWW: ⟨https://edms5.cern.ch/cdd/plsql/c4w.get_in⟩.

[38] *MAD-X — Methodical Accelerator Design*. [online]. [visited on 2018-06-01]. Available from WWW: ⟨http://madx.web.cern.ch/madx/⟩.

[39] Kittelmann, T.; Tsulaia, V.; Boudreau, J.; Moyse, E. The Virtual Point 1 event display for the ATLAS experiment. *Journal of Physics: Conference Series*. 2010, vol. 219, no. 3, pp. 032012. Available also from WWW: ⟨http://stacks.iop.org/1742-6596/219/i=3/a=032012⟩.

[40] Keck, T. *Background Simulation* [online]. 2013 [visited on 2018-09-01]. presentation on ALFA Physics meeting⟨https://indico.cern.ch/event/266616/contributions/1603083/attachments/476035/658762/thomas_keck_background_simulation_final.pdf⟩.

[41] Pomarede, D.; Virchaux, M. The Persint visualization program for the ATLAS experiment. *eConf*. 2003, vol. C0303241, pp. MOLT009. Available also from WWW: ⟨arXiv: cs/0305057 (cs-gr)⟩.

[42] Aleksa, M; Bergsma, F; Giudici, P -A, et al. Measurement of the ATLAS solenoid magnetic field. *Journal of Instrumentation*. 2008, vol. 3, no. 04, pp. P04003. Available also from WWW: ⟨http://stacks.iop.org/1748-0221/3/i=04/a=P04003⟩.

[43] Komárek, T. *Visualization of particle tracks in an accelerator magnetic field* [online]. 2013 [visited on 2018-06-01]. Bachelor's thesis. Available from WWW: ⟨https://theses.cz/id/ikzo0d/⟩.

[44] Brandt, A.; Bruschi, M.; Bussey, P., et al. *AFP progress report*. 2013. Available also from WWW: ⟨https://cds.cern.ch/record/1595300⟩.

[45] Bonnet, L; Pierzchala, T; Piotrzkowski, K; Rodeghiero, P. GASTOF: Ultra-fast ToF forward detector for exclusive processes at the LHC. *Acta Phys. Pol. B*. 2007, vol. 38, no. arXiv:hep-ph/0703320. CP3-06-18, pp. 477–482. 6 p. Available also from WWW: ⟨http://cds.cern.ch/record/1031111⟩.

[46] Čerenkov, P. A. Visible Radiation Produced by Electrons Moving in a Medium with Velocities Exceeding that of Light. *Phys. Rev.* 1937, vol. 52, pp. 378–379. Available also from WWW: ⟨https://link.aps.org/doi/10.1103/PhysRev.52.378⟩.

[47] Frank, I. M.; Tamm, I. E. Coherent visible radiation of fast electrons passing through matter. *Compt. Rend. Acad. Sci. URSS*. 1937, vol. 14, no. 3, pp. 109–114. [Usp. Fiz. Nauk93,no.2,388(1967)]. Available also from WWW: ⟨http://dx.doi.org/10.1007/978-3-642-74626-0_2,10.3367/UFNr.0093.196710o.0388⟩.

[48] *Epotek 305 datasheet*.

[49] Frühwirth-Schnatter, S. *Finite Mixture and Markov Switching Models*. 2006. Springer Series in Statistics. Available also from WWW: ⟨https://books.google.cz/books?id=f8KiI7eRjYoC⟩. ISBN 9780387357683.

[50] Inc., Trimble, *SketchUp Make 2016*. Sunnyvale, CA, 2016. Available also from WWW: ⟨https://www.sketchup.com/⟩.

[51] *MCP and MCP assembly*. 2016. Available also from WWW: ⟨https://www.hamamatsu.com/resources/pdf/etd/MCP_TMCP0002E.pdf⟩.

[52] Va'vra, J.; Ertley, C.; Leith, D.W.G.S.; Ratcliff, B.; Schwiening, J. A high-resolution TOF detector—A possible way to compete with a RICH detector. *Nuclear Instruments and Methods in Physics Research Section A: Accelerators, Spectrometers, Detectors and Associated Equipment*. 2008, vol. 595, no. 1, pp. 270–273. RICH 2007. Available also from WWW: ⟨http://www.sciencedirect.com/science/article/pii/S0168900208009947⟩. ISSN 0168-9002.

[53] *miniPLANACON XPM85112*. 2014. Available also from WWW: ⟨https://www.photonis.com/uploads/datasheet/pd/Mini-PLANACON-4x4-datasheet.pdf⟩.

[54] Mota, M.; Christiansen, J.; Debieux, S., et al. A flexible multi-channel high-resolution time-to-digital converter ASIC. In. *2000 IEEE Nuclear Science Symposium. Conference Record (Cat. No.00CH37149)*. 2000, pp. 9/155–9/159 vol.2. Available also from WWW: ⟨http://dx.doi.org/10.1109/NSSMIC.2000.949889⟩.

[55] *HCA78-50J 7/8" HELIFLEX Air-Dielectric Coaxial Cable datasheet*. 2007. Available also from WWW: ⟨http://www.rfsworld.com/WebSearchECat/datasheets/pdf/?q=HCA78-50J⟩.

[56] Trzebinski, M. *AFP Lessons from 2016 Data Taking* [online]. 2016 [visited on 2018-11-01]. Presentation on AFP Review. Available from WWW: ⟨https://indico.cern.ch/event/579496/⟩.

[57] Efthymiopoulos, I. *The EHN1 Beams* [online]. [visited on 2018-07-01]. Available from WWW: ⟨https://sba.web.cern.ch/sba/Documentations/docs/Training/ie_spstraining_ehn1.pdf⟩.

[58] *Vistars — SPS Page 1*. [online]. [visited on 2018-07-22]. Available from WWW: ⟨https://op-webtools.web.cern.ch/vistar/vistars.php?usr=SPS1⟩.

[59] *Near Ultraviolet (NUV) SiPMs*. 2015. Available also from WWW: ⟨http://www.first-sensor.com/cms/upload/datasheets/SiPM-NUV_501628.pdf⟩.

[60] *Low Noise, Blue-Sensitive Silicon Photomultipliers*. 2016. Available also from WWW: ⟨http://sensl.com/downloads/ds/DS-MicroCseries.pdf⟩.

[61] Komárek, T. *Simulation of optical part of high-energy particle time-of-flight detector and comparison with data* [online]. 2016 [visited on 2018-11-01]. Master's thesis. Available from WWW: ⟨https://theses.cz/id/zts9l9/⟩.

[62] *Suprasil UVL datasheet*. 2018. Available also from WWW: ⟨https://www.heraeus.com/media/media/hqs/doc_hqs/products_and_solutions_8/optics/Suprasil_UVL_synthetic_fused_silica_EN.pdf⟩.

[63] Rheims, J.; Köser, J.; Wriedt, T. Refractive-index measurements in the near-IR using an Abbe refractometer. *Measurement Science and Technology*. 1997, vol. 8, no. 6, pp. 601. Available also from WWW: ⟨http://stacks.iop.org/0957-0233/8/i=6/a=003⟩.

[64] *PLANACON XP85012*. 2013. Available also from WWW: ⟨https://www.photonis.com/uploads/datasheet/pd/PLANACON-8x8-datasheet.pdf⟩.

[65] Finogeev, D. A.; Grigoriev, V. A.; Kaplin, V. A., et al. Performance study of the fast timing Cherenkov detector based on a microchannel plate PMT. *Journal of Physics: Conference Series*. 2017, vol. 798, no. 1, pp. 012168. Available also from WWW: ⟨http://stacks.iop.org/1742-6596/798/i=1/a=012168⟩.

[66] Lehmann, A.; Britting, A.; Cowie, E., et al. Systematic studies of micro-channel plate PMTs. *Nuclear Instruments and Methods in Physics Research Section A: Accelerators, Spectrometers, Detectors and Associated Equipment*. 2011, vol. 639, no. 1, pp. 144–147. Proceedings of the Seventh International Workshop on Ring Imaging Cherenkov Detectors. Available also from WWW: ⟨http://www.sciencedirect.com/science/article/pii/S0168900210020954⟩. ISSN 0168-9002.

[67] Piatek, S. *What is an SiPM and how does it work?* 2016. Available also from WWW: ⟨https://hub.hamamatsu.com/us/en/technical-note/how-sipm-works/index.html⟩.

[68] Ghassemi, A.; Sato, K.; Kobayashi, K. *MPPC*. 2016. Available also from WWW: ⟨https://hub.hamamatsu.com/resources/pdf/ssd/mppc_kapd9005e.pdf⟩.

[69] Gundacker, S.; Auffray, E.; Vara, N. Di, et al. SiPM time resolution: From single photon to saturation. *Nuclear Instruments and Methods in Physics Research Section A: Accelerators, Spectrometers, Detectors and Associated Equipment*. 2013, vol. 718, pp. 569–572. Proceedings of the 12th Pisa Meeting on Advanced Detectors. Available also from WWW: ⟨http://www.sciencedirect.com/science/article/pii/S0168900213001393⟩. ISSN 0168-9002.

[70] Nishimura, Miki et al. Pixelated Positron Timing Counter with SiPM-readout Scintillator for MEG II experiment. In. *Proceedings, 4th International Conference on New Photo-Detectors (PhotoDet 2015): Moscow, Russia, July 6-9, 2015*. 2016, pp. 011.

[71] Eckert, P; Stamen, R; Schultz-Coulon, H -C. Study of the response and photon-counting resolution of silicon photomultipliers using a generic simulation framework. *Journal of Instrumentation*. 2012, vol. 7, no. 08, pp. P08011. Available also from WWW: ⟨http://stacks.iop.org/1748-0221/7/i=08/a=P08011⟩.

[72] Rajkanan, K.; Singh, R.; Shewchun, J. Absorption coefficient of silicon for solar cell calculations. *Solid-State Electronics*. 1979, vol. 22, no. 9, pp. 793–795. Available also from WWW: ⟨http://www.sciencedirect.com/science/article/pii/003811017990128X⟩. ISSN 0038-1101.

[73] Dotti, A.; Adragna, P.; Vitillo, R. A. The Online Histogram Presenter for the ATLAS experiment: A modular system for histogram visualization. *Journal of Physics: Conference Series*. 2010, vol. 219, no. 3, pp. 032037. Available also from WWW: ⟨http://stacks.iop.org/1742-6596/219/i=3/a=032037⟩.

[74] Rijssenbeek, M. *AFP ToF Issues in 2017 and Cures for 2018* [online]. 2018 [visited on 2018-07-03]. Presentation on AFP ToF Review. Available from WWW: ⟨https://indico.cern.ch/event/732415/contributions/3020226/attachments/1659925/2664609/AFP-2018-06-06_ToF-Review.pdf⟩.

[75] *Forward Detectors public results, twiki page.* [online]. [visited on 2018-06-01]. Available from WWW: ⟨https://twiki.cern.ch/twiki/bin/view/AtlasPublic/ForwardDetPublicResults⟩.

[76] Cartiglia, N. Measurement of the proton-proton total, elastic, inelastic and diffractive cross sections at 2, 7, 8 and 57 TeV. 2013. Available also from WWW: ⟨arXiv: 1305.6131 (hep-ex)⟩.

[77] Ronzhin, A.; Albrow, M.; Byrum, K., et al. Tests of timing properties of silicon photomultipliers. *Nuclear Instruments and Methods in Physics Research Section A: Accelerators, Spectrometers, Detectors and Associated Equipment.* 2010, vol. 616, no. 1, pp. 38–44. Available also from WWW: ⟨http://www.sciencedirect.com/science/article/pii/S0168900210002706⟩. ISSN 0168-9002.

[78] Achilli, A.; Godbole, R. M.; Grau, A., et al. Total cross section and rapidity gap survival probability at the LHC through an eikonal with soft gluon resummation. *Physics Letters B.* 2008, vol. 659, no. 1, pp. 137–143. Available also from WWW: ⟨http://www.sciencedirect.com/science/article/pii/S0370269307011495⟩. ISSN 0370-2693.

[79] De Roeck, A.; Katre, A.; Mermod, P.; Milstead, D.; Sloan, T. Sensitivity of LHC Experiments to Exotic Highly Ionising Particles. *Eur. Phys. J.* 2012, vol. C72, pp. 1985. Available also from WWW: ⟨http://dx.doi.org/10.1140/epjc/s10052-012-1985-2arXiv: 1112.2999 (hep-ph)⟩.

[80] Inc., Wolfram Research, *Wolfram Alpha.* Champaign, IL, 2018. Available also from WWW: ⟨http://www.wolframalpha.com⟩.

[81] Ellis, J. P. TikZ-Feynman: Feynman diagrams with TikZ. *Computer Physics Communications.* 2017, vol. 210, pp. 103–123. Available also from WWW: ⟨http://www.sciencedirect.com/science/article/pii/S0010465516302521⟩. ISSN 0010-4655.

[82] Brun, Rene; Rademakers, Fons. ROOT — An object oriented data analysis framework. *Nuclear Instruments and Methods in Physics Research Section A: Accelerators, Spectrometers, Detectors and Associated Equipment.* 1997, vol. 389, no. 1, pp. 81–86. New Computing Techniques in Physics Research V. Available also from WWW: ⟨http://www.sciencedirect.com/science/article/pii/S016890029700048X⟩. ISSN 0168-9002.

Publications

[P1] Chytka, L.; ATLAS Collaboration. Status of the ATLAS Forward Physics (AFP) project. *AIP Conference Proceedings*. 2013, vol. 1523, no. 1, pp. 316–319. Available also from WWW: ⟨https://aip.scitation.org/doi/abs/10.1063/1.4802176⟩.

[P2] Bussey, P.; Chytka, L.; Staszewski, R.; Sykora, T.; Trzebinski, M. *LHC and ATLAS Coordinate Conventions*. 2013. ATLAS internal note. Available also from WWW: ⟨https://cds.cern.ch/record/1596453⟩.

[P3] Nozka, L.; Brandt, A.; Chytka, L., et al. Design of Cherenkov bars for the optical part of the time-of-flight detector in Geant4. *Opt. Express*. 2014, vol. 22, no. 23, pp. 28984–28996. Available also from WWW: ⟨http://www.opticsexpress.org/abstract.cfm?URI=oe-22-23-28984⟩.

[P4] Cavalier, S.; Chytka, L.; Fassnacht, P., et al. *Measurement of the total cross section from elastic scattering in pp collisons at $\sqrt{s} = 7$ TeV with the ATLAS detector*. 2014. Internal draft of publication. Available also from WWW: ⟨https://cds.cern.ch/record/1700047⟩.

[P5] ATLAS Collaboration. Measurement of the total cross section from elastic scattering in pp collisions at $\sqrt{s} = 7$ TeV with the ATLAS detector. *Nuclear Physics B*. 2014, vol. 889, pp. 486–548. Available also from WWW: ⟨http://www.sciencedirect.com/science/article/pii/S0550321314003253⟩. ISSN 0550-3213.

[P6] *Full Simulation of the ATLAS Forward Region TWiki page*. [online]. [visited on 2018-06-01]. Available from WWW: ⟨https://twiki.cern.ch/twiki/bin/viewauth/Atlas/FullSimulationATLASForwardRegion⟩.

[P7] Chytka, L.; Moraa, K. D.; Sykora, R.; Sykora, T. *Full Geant4 simulation of the ATLAS forward region under the Athena framework*. 2016. Approved ATLAS note. Available also from WWW: ⟨https://cds.cern.ch/record/2239159⟩.

[P8] ATLAS Collaboration. Measurement of the total cross section from elastic scattering in pp collisions at $\sqrt{s} = 8$ TeV with the ATLAS detector. *Physics Letters B*. 2016, vol. 761, pp. 158–178. Available also from WWW: ⟨https://www.sciencedirect.com/science/article/pii/S0370269316304403⟩. ISSN 0370-2693.

[P9] Nozka, L.; Adamczyk, L.; Chytka, L., et al. Construction of the optical part of a time-of-flight detector prototype for the AFP detector. *Opt. Express*. 2016, vol. 24, no. 24, pp. 27951–27960. Available also from WWW: ⟨http://www.opticsexpress.org/abstract.cfm?URI=oe-24-24-27951⟩.

[P10] Lange, J.; Adamczyk, L.; Chytka, L., et al. Beam tests of an integrated prototype of the ATLAS Forward Proton detector. *Journal of Instrumentation*. 2016, vol. 11, no. 09, pp. P09005. Available also from WWW: ⟨http://stacks.iop.org/1748-0221/11/i=09/a=P09005⟩.

[P11] Khalek, S. Abdel; Allongue, B.; Anghinolfi, F., et al. The ALFA Roman Pot detectors of ATLAS. *Journal of Instrumentation*. 2016, vol. 11, no. 11, pp. P11013. Available also from WWW: ⟨http://stacks.iop.org/1748-0221/11/i=11/a=P11013⟩.

[P12] Pácalt, J.; Chytka, L.; Kvita, J.; Palička, J. Měření doby života mionů z kosmického záření. *Jemná mechanika a optika*. 2017, vol. 62, no. 3, pp. 84–86. ISSN 0447-6441.

[P13] Lange, J.; Carulla, M.; Chytka, L., et al. Gain and time resolution of 45 μm thin Low Gain Avalanche Detectors before and after irradiation up to a fluence of 10^{15} n_{eq}/cm^2. *Journal of Instrumentation*. 2017, vol. 12, no. 05, pp. P05003. Available also from WWW: ⟨http://stacks.iop.org/1748-0221/12/i=05/a=P05003⟩.

[P14] Chytka, L.; Avoni, G.; Brandt, A., et al. Timing resolution studies of the optical part of the AFP Time-of-flight detector. *Opt. Express*. 2018, vol. 26, no. 7, pp. 8028–8039. Available also from WWW: ⟨http://www.opticsexpress.org/abstract.cfm?URI=oe-26-7-8028⟩.

[P15] Chytka, L.; Hrabovsky, M.; Komarek, T., et al. Time resolution of the SiPM-NUV3S. Submitted to Nucl. Inst. Meth. A.

[P16] Chytka, L.; Komárek, T.; Nožka, L.; Sýkora, T.; Urbášek, V. Noise influence on time resolution of SiPM photodetectors. *Jemná mechanika a optika*. Accepted for publication. ISSN 0447-6441.